INVESTIGATION OF A NOVEL MULTIRESONANT BEAM ENERGY HARVESTER AND A COMPLEX CONJUGATE MATCHING CIRCUIT

A thesis submitted to The University of Manchester for the degree of

Doctor of Philosophy

in the Faculty of Engineering and Physical Sciences

2011

SHAOFAN QI

School of Electrical and Electronic Engineering

Table of Contents

Final word count: 38442

List of Figures

List of Tables

Abstract

The aim of the work described in this thesis is firstly to improve the collection of vibration energy for piezoelectric cantilever harvesters, by a mechanical technique, so that the devices can harvest energy over a wider bandwidth. Secondly to investigate a new circuit topology for achieving complex conjugate load matching to the piezoelectric harvester. The thesis has been divided into two parts – the mechanical approach and the electrical approach.

For the mechanical approach, a novel multiresonant beam, comprising piezoelectric fiber composites on a clamped-clamped beam and side mounted cantilevers, was proposed. The side cantilevers are tuned by tip masses to be resonant at different frequencies. A Rayleigh-Ritz model was developed to predict the vibration response of the proposed model multiresonant beam. This model showed that the bandwidth of the multiresonant beam was increased over that of a single cantilever harvester.

A multiresonant beam for energy harvesting was experimentally tested and compared with a single cantilever energy harvester. The transmissibility and voltage responses were investigated, the beam showed a wide frequency response between 14.5Hz and 31Hz, whereas the single cantilever only showed one resonant frequency. Therefore the multiresonant beam system is feasible for wide band energy harvesting.

For the electrical approach, the task was to investigate complex conjugate impedance matching for the piezoelectric energy harvesters, so that the output impedance from the piezoelectric harvester can be reduced, and maximum energy extracted from the device with a possibility of frequency tuning. A new amplified inductor circuit was proposed to enable the capacitive output impedance of the piezoelectric device to be cancelled. Experimental and software simulations are provided to verify the theoretical predictions.

A prototype amplified inductor circuit was simulated and tested. The results showed that a variable effective inductance was achieved. However the circuit is lossy due to imperfections within the system, and needs further work to eliminate these imperfections.

Declaration

No portion of the work referred to in the thesis has been submitted in support of an application for another degree or qualification of this or any other university or other institute of learning.

Copyright

Acknowledgements

I would like to thank my supervisor Dr. Roger Shuttleworth for his guidance and encouragement throughout my study. Without his support, the researches carried out in the past years would be very difficult to achieve.

To my parents and relatives whom given me their endless support during my study, thank you for all the helps and encouragements.

I would also like to express my special thanks to Prof. Jan Wright for his generous guidance in developing the theoretical and simulation models.

Furthermore, I would like to thank the School of Electrical and Electronic Engineering for providing me the partial scholarship and also EU FP6 DYNAMITE project for funding part of the research carried out in this thesis.

Nomenclature

Q_m	Mechanical quality factor
l	Beam length
w	Beam width
h	Beam thickness
ρ	Material density
E	Modulus of elasticity (Young's modulus)
M	Mass
$Z(t)$	Oscillatory input motion
k_j	Stiffness
b_e	Electrical damping terms
b_m	Mechanical damping terms
V	Shear force moment
N	Bending moment
I	Relevant second moment of area of the cross-section
EI	Flexural rigidity
ρA	Mass per unit length
$y(x,t)$	Mode shape deformation as a function of displacement and time
$Y_i(x)$	Mode shape function at position x
$T(t)$	Kinetic energy
$U(t)$	Strain energy
Q_j	External applied generalized force
$Q_i(t)$	Generalized force
$\tilde{M}$	Mass in matrix form
$\tilde{K}$	Stiffness in matrix form
$\tilde{C}$	Damping in matrix term
c	Ratio between second moment of area and damping matrix
C_i	Arbitrary constant
$\ddot{u}(t)$	Acceleration

K_{ij}^2	Generalized electromechanical coupling coefficient
$\tilde{S}$	Strain for piezoelectric material
$\tilde{T}$	Mechanical stress for piezoelectric material
$\tilde{E}$	Electric field strength for piezoelectric material
$\tilde{D}$	Electric field displacement for piezoelectric material
m	Mass per unit length of a cantilever beam
c_j	Cantilever location on the main beam for a Multiresonant Beam
M_j	Effective tip mass of side cantilever for a Multiresonant Beam
l_j	Side cantilever length for a Multiresonant Beam
l_{cc}	Main clamped-clamped beam length for a Multiresonant Beam
$\theta(x,t)$	Mode shape for torsion
G	Beam material shear modulus
J	Beam section torsion constant
GJ	Torsional rigidity
γ	Mass moment of inertia, in twist, per unit length
ξ	Dissipative function/damper contribution
δW	Incremental work done
F	Input force for a Multiresonant Beam
$\underline{\ddot{q}}_0$	Input excitation for a Multireonant Beam
$\ddot{w}$	Overall system output for a Multiresonant Beam
$\underline{T}$	Transmissibility for a Multiresonant Beam
M_{Beam}	Mass of the main clamped-clamped beam for a Multiresonant Beam
$q(t)$	Generalized coordinate
χ	Shape function for kinetic energy equation
ψ	Shape function for strain energy equation
d_j	Measurement location on the beam
λ_i	Coefficient of mode shape function
T_{SS}	Thickness of the stainless steel shim used in PFC material
W_{PFCB}	Width of the PFCB material
L_{PFCB}	Length of the PFCB material
T_{PFC}	Thickness of the PFC material

T_{PFCB}	Thickness of the PFCB
ρ_{SS}	Density of the stainless steel shim used in PFCB
E_{SS}	Young's modulus of the stainless steel shim used in PFCB
M_{PFCB}	Weight of the PFCB
R_{PZT}	Output resistance of the piezoelectric material
C_{PZT}	Output capacitance of the piezoelectric material
V_{PZT}	Output voltage of the piezoelectric material
R_L	Electrical load resistor
C_{PZT}^{real}	Real term of the complex piezoelectric output capacitance
C_{PZT}^{imag}	Imaginary term of the complex piezoelectric output capacitance
X_L	Inductive impedance
X_C	Capacitive impedance
V_{amp}	Voltage across the amplified inductor circuit
R_{amp}	Effective resistance of the amplified inductor circuit
L	Inductance
R_{POT}	Potentiometer
G_{POT}	Potentiometer setting in per unit
L_{TOTAL}	Total effective inductance of the amplified inductor circuit

Chapter 1 :

Introduction to Piezoelectric Materials, Energy Harvesting Theory and Models

1.1 Introduction

Low power electronic devices such as wireless sensors are usually powered by primary batteries. However, since the trend for such devices is to be manufactured in smaller and smaller sizes, consuming less and less power, researchers have been investigating methods that could be used to replace disposable chemical batteries, since these degrade and need frequent replacement adding cost.

Energy harvesting is the process of acquiring energy from the surroundings of a system and converting it into useable electrical energy [1, 2]. Energy harvesting devices, by taking energy from the surroundings and storing this in a capacitor or a rechargeable battery, can ensure that low power electronic devices do not need primary batteries. The field of energy harvesting has significantly grown over the past few years due to the increasing demand to produce remote electronic monitoring devices with an extended lifespan.

Several energy sources have been considered for their viability to power remote electronic devices including solar, wind, heat and vibration. The work described in this thesis is concerned with energy harvesting which extracts energy from vibrations. These devices usually amplify the vibrations with a mechanical system

such as a cantilever and the vibrations are then applied to an electrical generator. There are three types of electrical generator [3].

Firstly, electrostatic generation consists of two conducting plates separated by a dielectric to form a capacitor, these plates move relative to one another. As the plates move due to vibrations, the energy stored in the capacitor changes, thus providing the mechanism for mechanical to electrical energy conversion [4, 5]. This method of harvesting energy is easy to integrate with electronics, but a separate voltage source may be needed for excitation. This is usually done by applying an initial charge to the plates.

Secondly, electromagnetic power conversion results from the motion of an electrical conductor in a magnetic field, so that electrical energy is generated [6-13]. Separate voltage sources are not required, however the output voltage is typically less than $1V$, and the generated voltage thus needs boosting before it can be used.

Thirdly, piezoelectric electricity generation results from repeated mechanical stressing of piezoelectric material to transform mechanical strain to electrical energy. Piezoelectric generation provides a relatively high power density, therefore piezoelectric energy harvesting systems, have been seriously investigated over the last decade [1, 2, 14-37]. Piezoelectric generation does not require a separate voltage source to generate energy, and can produce output voltages up to hundreds of volts.

Piezoelectric energy harvesters have the highest energy density of all vibration energy harvesters and the simplest configuration in comparison to electrostatic and electromagnetic generators [1-3, 38-41]. Hence, piezoelectric materials have been widely chosen for energy harvesting applications [1-3, 33, 39]. Section 1.2 discusses the properties of piezoelectric materials.

For this project, the interested power level is around tens of milli Watts.

1.2 Review of Piezoelectric Materials

1.2.1 Types of Piezoelectric Materials

The piezoelectric effect occurs only in non conducting materials and these materials can be divided into two main groups: crystals and ceramics [42].

Table 1.1: Types of piezoelectric material

Type	Piezoelectric material
Ceramic:	*Lead zirconate titanate (PZT), BaTiO3 ceramic, PLZT*
Crystal:	Natural:
	Quartz (SiO2), Tourmaline, Rochelle salt, Topaz, Zincblende, Boracite
	Synthetic:
	Ethylene diamine tartrate (EDT), Barium titanate single crystal
Others:	*Ferroelectric polymers (PVDF), Ferroelectric composites*

In Table 1.1, the most common crystal types of piezoelectric material are Quartz (SiO_2) and Tourmaline. The ceramic type of piezoelectric material includes Barium titanate ($BaTiO_3$) and Lead zirconate titanate (PZT). Other types of material have also been developed, these include polymers such as Polyvinylidene Fluoride (PVDF) and ferroelectric composites such as PZT-polymer composite.

Piezoelectric ceramic materials have gained increasing importance over the last few years. This is because they have higher piezoelectric constants than single crystal materials and are manufactured by a simple sintering process [42, 43]. Currently, the most common industrial piezoelectric materials are Piezoelectric Fiber Composite (PFC) and lead zirconate titanate (PZT). The main differences between these two materials are that PZT has a higher density, but is unsuitable for applications where

flexibility is necessary. Although PFC material is very flexible and easy to shape, this can reduce the effective coupling between the mechanical and electrical domains, resulting in a reduced electrical output.

1.2.2 Properties of Piezoelectric Materials

As described in [42, 44], the physical constants for piezoelectric materials are tensor quantities. The relationship between the applied force and the subsequent response of a piezoelectric element generally depends on three factors:

- The dimensions and geometry of the element
- The piezoelectric properties of the material
- The direction of the mechanical or electrical excitation

The properties of piezoelectric ceramics are strongly influenced by their manufacturing processes. The conventional manufacturing process is shown in Figure 1.1:

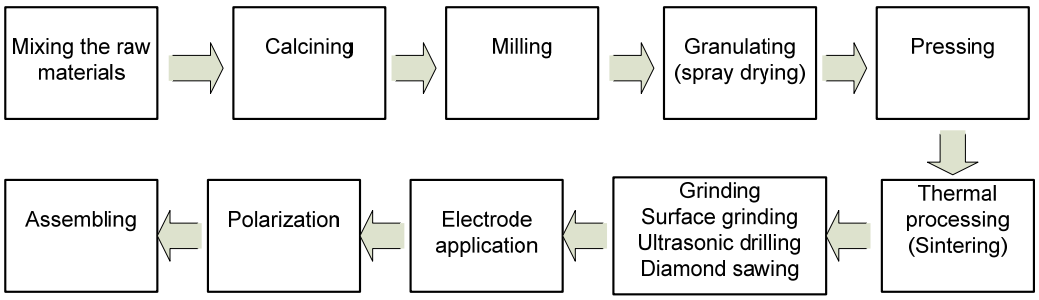

Figure 1.1: Manufacturing process of piezoelectric ceramics

During a typical piezoelectric ceramic manufacturing process, an appropriate amount of lead, zirconium and titanium oxides, together with a small amount of modifying additives are mechanically mixed with water. The mix then goes to calcining where it is heated to around 1000°C, to thermally decompose the material and drive off any moisture. This temperature is below the melting point. It is then milled to eliminate aggregations, spray dried and pressed into a block shape. The resulting block is next

sintered at a temperature between 1100°C and 1300°C for up to 2 hours in air. The material at this stage has a neutral polarity, so electrodes are applied and the material is poled by placing a high electric field across it, via the electrodes at a temperature above the Curie temperature, as shown in Figure 1.2. Note that the Curie temperature is much lower than the sintering temperature, typically around 300°C [42].

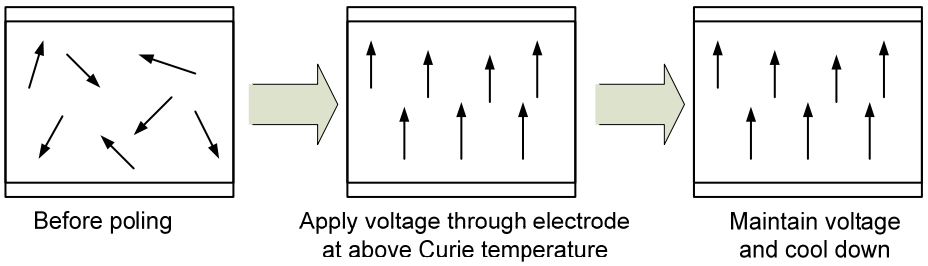

Figure 1.2: Polarization process of piezoelectric ceramics

Piezoelectric material constants are normally given two subscripts, representing both elasticity and permittivity (e.g. d_{33}). The first (or elasticity) subscript refers to the direction of stress. The second (or permittivity) subscript refers to the direction of electrical displacement and electric field. The direction of positive polarization is usually chosen to coincide with the *Z* axis of a rectangular system of crystallographic axes *X*, *Y*, *Z*. The various constants are then written with subscripts referring to these directions. This relation is shown in Figure 1.3, in which the directions *X*, *Y*, *Z* are represented by 1, 2 and 3 respectively and the shear about these axes by 4, 5 and 6 respectively.

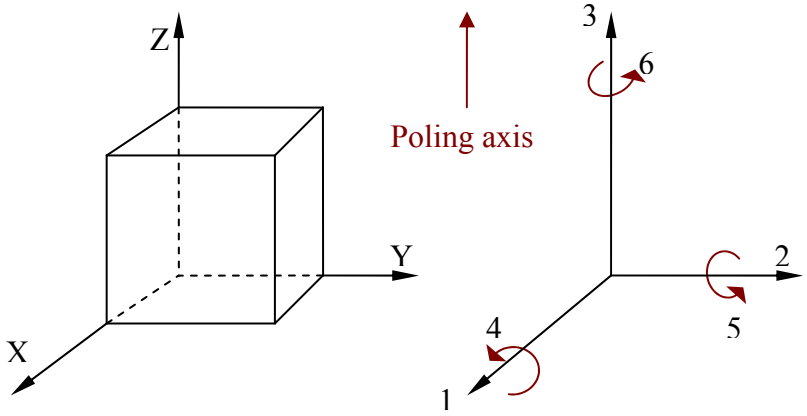

Figure 1.3: Designation of the axis and directions of deformation

When a piezoelectric device is active the material deformation is usually maximized at the mechanical resonance frequency. The maximum deformation depends on the mechanical losses as well as on the inertia and elastic compliance of the material.

1.2.3 PZT Type Materials

According to [42, 45, 46], PZT material is made soft by doping it with a small amount of Lanthanum, Neodymium or Niobium (*La*, *Nd* or *Nb*) which increases the compliance coefficients, dielectric constant or coupling factor. Potassium, Iron and Manganese (*Kp*, *Fe* and *Mn*) are hard dopants which give the material a higher quality factor, Q_m, and lower dielectric losses.

Hard type ceramics can withstand high levels of electrical excitation and mechanical stress, and due to the stability of the material, are suitable for use in high voltage transformers withstand around tens of kilo volts [42, 46, 47].

Soft type ceramics has higher domain mobility feature, higher sensitivity and permittivity than the hard type ceramics [42, 46]. However under high drive conditions they are susceptible to self-heating beyond their maximum operating temperature (Curie temperature) and the material then loses its piezoelectric properties. Soft materials are used in various sensors, low power motor type transducers and low power generators around milli watts [46].

Most applications for piezoelectric materials are based on their direct and converse effects [47], see Figures 1.4 and 1.5.

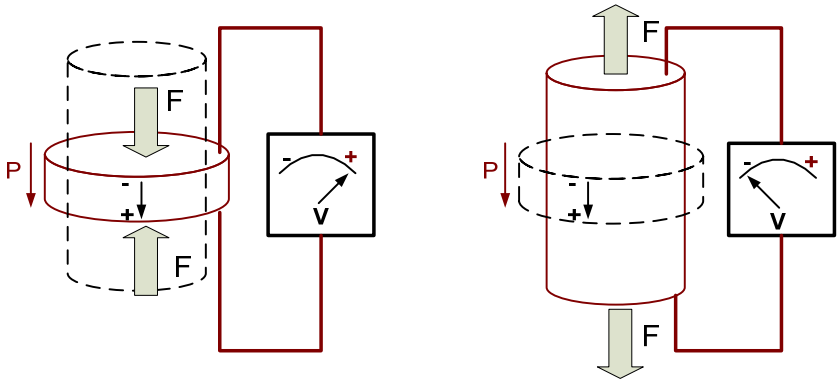

Figure 1.4: Direct effect of piezoelectric material

As shown in Figure 1.4, if the material is compressed by an external force, a voltage will appear between the electrodes in the same sense as the original polarizing field. Alternatively, if the material is stretched by an external force, the voltage across the electrodes has the opposite polarity. This phenomenon is known as a direct effect.

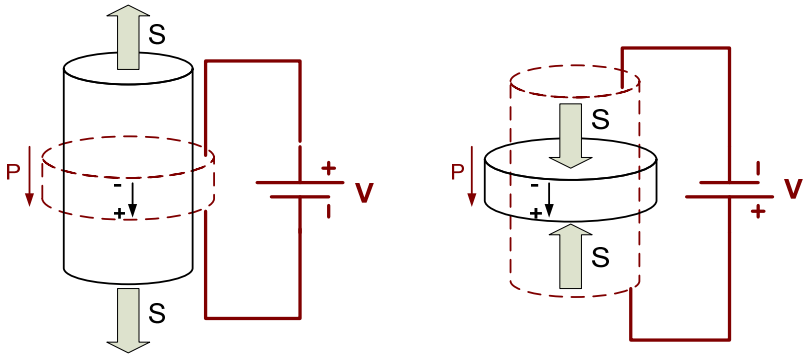

Figure 1.5: Converse effect of the piezoelectric material

In Figure 1.5, if a voltage is applied with a polarity opposite to that with which the material was poled, the material expands, so similarly, the material shrinks when a voltage is applied with the same polarity as the polarization. This phenomenon is known as a converse effect.

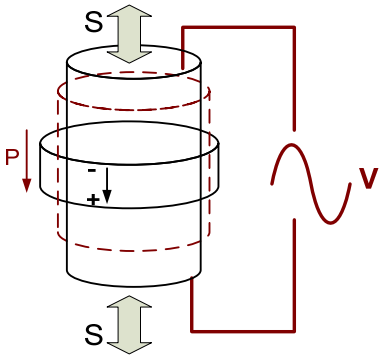

Figure 1.6: Piezoelectric material with an AC voltage applied

If an ac voltage is applied to the material, and the frequency of the voltage coincides with the mechanical resonant frequency of the piezoelectric ceramic, the ceramic will vibrate at the same frequency as the input signal with a greater displacement than it would at other frequencies. Figure 1.6 indicates the effects of extension and shrinking that would be seen if the AC voltage occurred at the mechanical, longitudinal, resonant frequency of a piezoelectric rod.

1.2.4 PFC Type Materials

In order to convert ambient vibration energy into electricity, piezoelectric films are now commonly incorporated into energy harvesting devices. Piezoelectric Fiber Composite (PFC) is one of the most commonly used piezoelectric films [43]. PFC uses an interdigitated electrode pattern to increase the effective ceramic volume as shown in Figure 1.7, allowing the piezoelectric primary axis to align with the fiber direction, permitting higher strain levels.

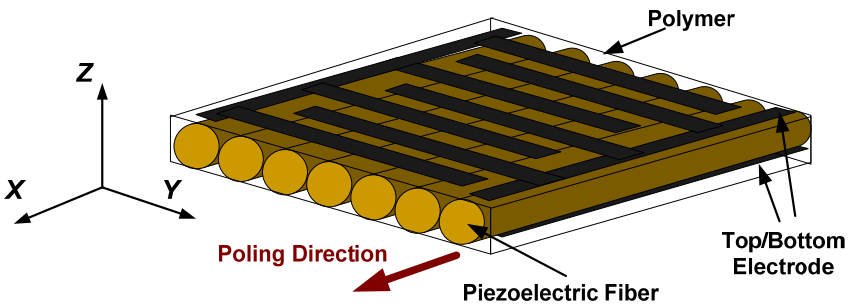

Figure 1.7: Geometry of Piezoelectric Fiber Composite (PFC) material

Figure 1.7 illustrates the geometry of the interdigitated electrode piezoelectric fiber composite device. Electrode patterns have fingers of alternating polarity, and are exact mirror images on the top and bottom faces. Poling is predominantly along the *X* axis [43]. Application of an electric field via the electrodes produces primary actuation along the fibers, and transverse actuation perpendicular to the fibers [48].

A Piezoelectric Fiber Composite Bimorph (PFCB), contains two layers of PFC material, mounted above and below a stainless steel shim, as shown in Figure 1.8. PFCBs are frequently employed in cantilever type energy harvesters, see later, because their construction naturally lends itself to this role.

Figure 1.8: Side view of Piezoelectric Fiber Composite Bimorph (PFCB)

The works described in this thesis are mainly involved with PFC and PFCB materials, due to their flexibility and ease of use. Most applications for piezoelectric materials are based on their direct effect [3, 47], see Figure 1.9.

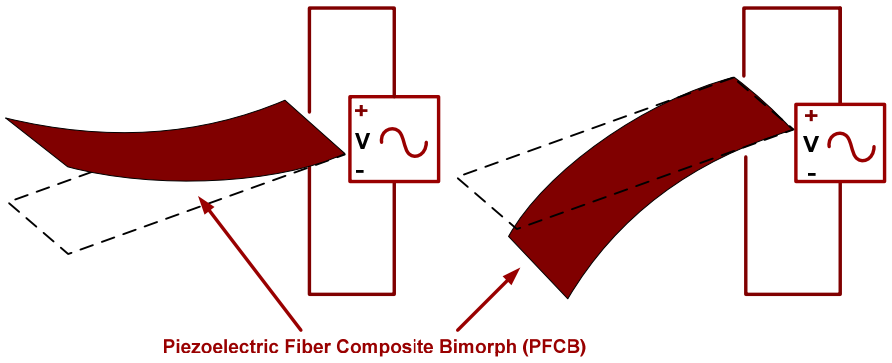

Figure 1.9: Direct effect of Piezoelectric Fiber Composite Bimorph (PFCB)

Figure 1.9 shows a PFCB vibrated by an external force, producing as a consequence a voltage between its electrodes. The PFCB material used was manufactured by Advanced Cerametrics Incorporated (ACI). A photograph of two PFCBs is shown in Figure 1.10. When operated at its resonant frequency, a PFCB can generate voltages

of over $400V_{pk\text{-}pk}$ according to the manufacturer [49]. However such voltage levels were found to be difficult to achieve by the author; the maximum open circuit voltage of a PFCB was measured to be around $130V_{pk\text{-}pk}$. Flexible piezoelectric devices such as PFCBs are attractive for energy harvesting applications, because of their ability to withstand high strain [48].

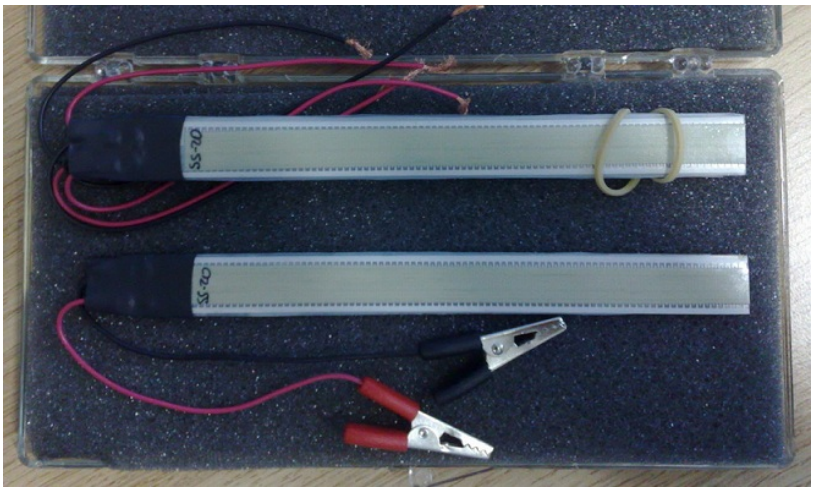

Figure 1.10: Piezoelectric Fiber Composite Bimorph (PFCB) from ACI

Unfortunately PFC material has a lower coupling coefficient than piezoelectric ceramic material such as PZT5A, which means it has a lower mechanical to electrical energy conversion rate [48]. However, its greater flexibility makes it more suitable for energy harvesting, where applications typically have resonant frequencies around $100Hz$ or below.

1.3 Literature Study of Piezoelectric Energy Harvesters

Several energy harvesting sources have been considered for their viability to power remote electronic devices. In [1, 2, 50, 51] a variety of ambient energy sources such as wind, light, thermal and mechanical vibration were studied. Among them, mechanical vibration was considered as a potential energy source, where there is insufficient light or thermal energy. Vibration sources can be easily found in accessible locations such as air ducts and building structures.

In 1996 Williams and Yates [52] proposed a piezoelectric device using a simple mass and damper system which generated electricity when embedded in a vibrating environment. This device has the dimension of $5mm$ in length and width, and $1mm$ of thickness, it also comprised a $15mg$ silicon mass. The amount of power generated was found to be proportional to the cube of the vibration frequency. Unfortunately the paper showed that the proposed generator performed poorly at low frequencies, and that a low damping factor was required to maximize power output, and allow a large deflection of the mass. For the device investigated the predicted power generation was $1\mu W$ at an excitation frequency of $70Hz$, and $0.1mW$ at $330Hz$.

Elvin et al [53, 54] and Ng and Liao [55] used the piezoelectric element simultaneously as a power generator and a sensor. They evaluated the performance of the piezoelectric sensor to power wireless transmission and validated the feasibility of the self-powered sensor system. A cantilever type of the system was used, with the piezoelectric material was mounted upon it, an average power of around $35\mu W$ was measured.

Techet et al investigated another harvesting scheme using long strips of piezoelectric polymers (also known as energy harvesting eels) in ocean or river-water flows in 2002 [56], see Figure 1.11.

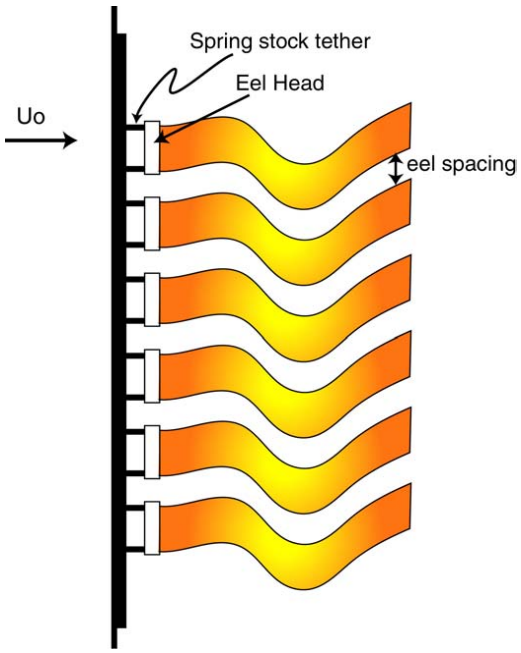

Figure 1.11: Piezoelectric eel harvester [56]

Priya [57, 58] used piezoelectric 'cymbal' transducers operating in the g_{33} mode and piezoelectric windmills for generating electric power from wind, see Figure 1.12.

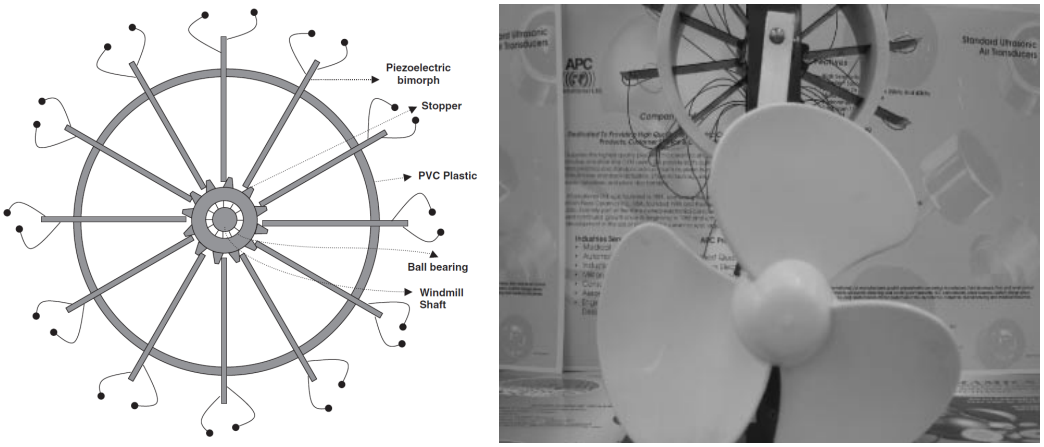

Figure 1.12: Piezoelectric windmill harvester [57, 58]

Research on MEMS scale piezoelectric based energy harvesters has also been expanded over the past years. Ramsey and Clark [28] conducted a design study which investigated the feasibility of using a piezoelectric transducer as power supply for a MEMS application in 2001. However the experimental results showed that the output power was small at around $2\mu W$ and too unreliable to power an electronic device.

Starner [59] performed an investigation into the amount of power expended for a vast range of human activities in 1996. His work brought to light the possibility of energy harvesting locations around the human body to the attention of many researchers, and the work in wearable power supplies began to grow. According to investigations carried out by Starner, energy generated by walking can also be collected. Assume a person weighs 68kg and is walking at 3.5mph, and that the fall of the heel is 5cm. Starner estimates that several watts of output power can be produced through the fall of the heel, assuming 100% efficiency.

Kymissis et al [60] studied the use of piezoelectric actuators located inside the sole of a shoe for power harvesting in 1998. Shenck [61] also demonstrated electrical energy generation from piezoelectric patches located in a shoe in the following year,

see Figure 1.13. Unfortunately the output power obtained was much smaller than expected. The patches produced around $1mW$ instead of the total theoretical estimated several watts power available from walking.

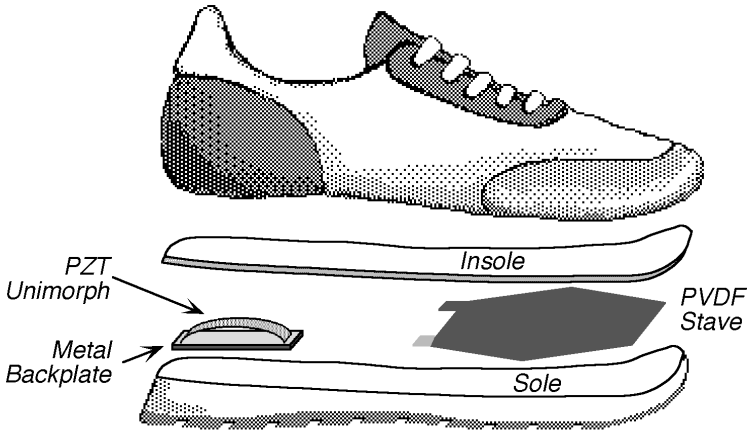

Figure 1.13: Kymissis and Shenck harvester model [60, 61]

Follow up research by Kymisis [60], Shenck [61] and others [15, 62] moved on to investigating the possible factors that limit the power output. The most important factor to limit power output is the generation efficiency, with piezoelectric elements operating in g_{31} and g_{33} modes. It is generally agreed that to increase the efficiency of piezoelectric energy harvesters, the mechanical quality factor and electromechanical coupling coefficients have to be increased and the dielectric losses decreased. Another factor which might limits the output power is that the devices tend to work at their non resonance frequencies, this leads to lower mechanical to electrical conversion ratio.

Among the different types of energy harvesting generators, the cantilever type is the most studied [1-3, 7, 29, 33, 38-40, 63-83]. This structure can generate a high strain and can be easily designed to oscillate at low frequencies around $100Hz$. Cantilever energy harvesters are described in the next section.

1.4 Cantilever Energy Harvester using PFC Material

1.4.1 Transverse Vibration of a Cantilever Beam Structure

A typical cantilever energy harvesting device, consists of a beam, clamped to a vibrating structure at one end, on which a piezoelectric film and a mass are mounted, as shown in Figure 1.14. This device is referred to as an energy harvester or a beam-mass system.

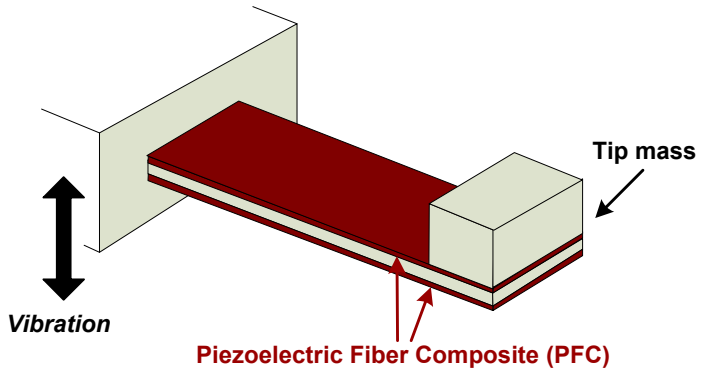

Figure 1.14: Piezoelectric cantilever harvester

An analysis of this was developed by Roundy [3] and this analysis is given in the next chapter. Only a short summary of the cantilever energy harvester is given here. The harvester consists of a beam, tip mass and piezoelectric fiber composite (PFC) material. When the system is mounted on a vibration source, the cantilever vibrates. This vibration is converted into electricity by the PFC. The tip mass is used to change the resonant frequency of the system. This is done by either altering its position on the cantilever or its mass. The resonant frequency for a linear dynamic system is the frequency where the maximum vibration occurs [3, 38-40, 48, 84, 85].

The vibration source generates a motion which is a function of time. To this motion there corresponds a power spectral density which is a function of frequency [84, 85]. The frequency at which the highest power spectral density occurs is known as the peak power frequency. When this frequency matches the resonant frequency of the

cantilever system, the energy harvesting device is most efficient. The efficiency of the system is very low otherwise, as is described in the next section.

1.4.2 Efficiency and Bandwidth of Cantilever Energy Harvester

The resonant frequencies of piezoelectric energy harvesters are designed to match the frequency of the ambient vibration, to achieve maximum output power [39, 51, 86].

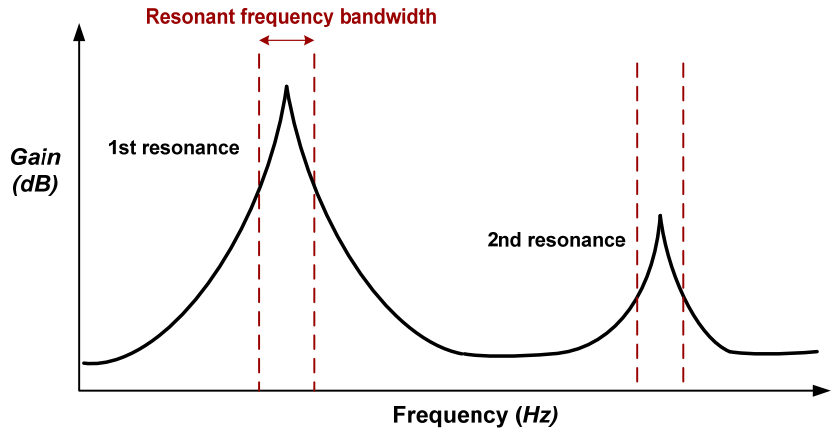

Figure 1.15: Estimated piezoelectric cantilever harvester output

The single cantilever model analysis mentioned in section 1.4.1, assumes a high Q, around 100 [87]. A cantilever will in practice have more than one resonant frequency, and the system is then known as having multiple degrees of freedom. Figure 1.15 shows the form of system output for a multiple degree of freedom system typical for a cantilever piezoelectric energy harvester. The system works most effectively at its first resonant frequency of perhaps around one hundred *Hz*, depending on cantilever stiffness and tip mass, see Chapter 2. The harvester is not suited to variable frequency vibrations due to its narrow bandwidth. It is reported that orders of reduction in output power occur even for a small deviation of vibration frequency from the resonant frequency [3, 38-40, 62]. This can be from around 50% (depending on the material's coupling coefficient) to as low as 2% (also depends on the amount of damping in the system).

Although it is possible to design an energy harvester in which the resonant frequency matches the vibration frequency, for variable speed industrial plant, vibrations often occur over a range of frequencies. For other plant the vibration frequency may be fixed but of indeterminate frequency, both these vibration sources will make the harvester device with one resonant peak less effective. Consequently interest has arisen in the design of an energy harvesting device which can operate over a wider frequency band, thus capturing vibration energy at any frequency within that band.

Another factor associated with the efficiency of piezoelectric materials is that piezoelectric energy harvesters have high capacitive output impedance. This high impedance (typically tens of kiloohms) significantly reduces potential power output, by limiting the load current.

Therefore the trend for development of piezoelectric energy harvesters has not only been to increase operating frequency range, but also to develop an electrical load circuit that optimizes electrical power output.

1.5 Project Motivation and Objectives

Industrial plant condition monitoring, is of high interest to process manufacturers as it can warn of impending machine failure and possible system deterioration, thereby permitting timely repairs and saving manufacturing costs. The availability of low cost sensors and low power signal processing devices allows condition monitoring to take place in a manufacturing establishment, maintaining industrial competitiveness. Where manufacturing plant is located over a wide area or large volume, the cost of wiring many condition monitoring sensors to a control/monitoring system can be excessive.

A possible solution to high wiring cost is to have wireless sensors, powered by energy harvesting devices. The wireless sensors are comprised of the condition monitoring sensors and low power radio transmitters (and in some cases receivers). The transmitters send the processed condition monitoring information to a distant

monitoring system completely eliminating the need for any wire connections. A typical condition monitoring system using wireless communications (e.g ZigBee, Bluetooth) is shown in Figure 1.16.

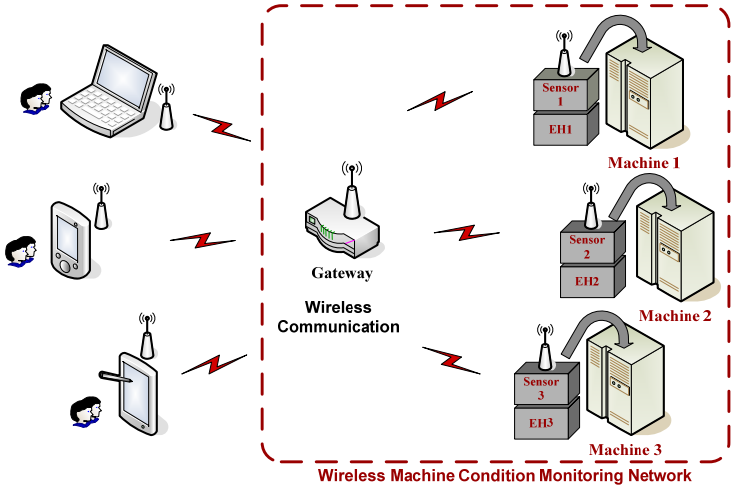

Figure 1.16: Wireless condition monitoring system schematic

Energy harvesters need to produce only low electrical powers, typically between 1 and $10mW$ to power condition monitoring sensors. The harvesters are often clamped to a machine bed plate and use the vibrations of the machine being monitored as the energy source [48].

Although sensing, processing and transmitting technologies are becoming well developed and highly efficient, nevertheless there exists scope for improvement in energy harvesting systems.

The objectives of the work described in this thesis have been towards the goal of firstly designing a form of cantilever which might have a wide bandwidth in comparison to cantilevers described so far in the literature. Secondly towards improving the circuit techniques used to extract energy from the piezoelectric device.

1.6 Thesis Outline

Chapter 1 gives an overview of the basic theory behind and the properties of piezoelectric materials and energy harvesting systems, and a literature review on piezoelectric energy harvesters. The project motivation and plans are also presented.

Chapter 2 introduces a literature study of piezoelectric cantilever energy harvesters in particular and research towards wideband/tunable energy harvesting devices. The analysis of the cantilever transverse vibration is a modification of the work described by Shahruz [84, 85], Warburton [88] and Blevins [89].

Chapter 3 introduces the multiresonant energy harvester concept proposed, the mathematical theory and the simulations results for the multiresonant energy harvester. Chapter 4 discusses the multiresonant beam harvester experimental test results.

Chapter 5 describes electronic circuits used previously with piezoelectric energy harvesters and Chapter 6 discusses the design, simulation and experimental results of the amplified inductor electronic circuit.

Chapter 7 gives the conclusions and future work.

Part of the work carried out in Chapter 2, 3 and 4 has been published as in [48, 90-92], see list of the publications in Appendix E. The analyses and experiment in these chapters are the modified and continuation work from the publications.

1.7 Conclusion

In this first chapter, different methods of energy harvesting including electrostatic, electromagnetic and piezoelectric have been discussed in Section 1.1. This section was followed by a review of different types of piezoelectric materials and

manufacturing processes in Section 1.2. A description of piezoelectric ceramic (PZT) and fibre (PFC) material operation were also given in Section 1.2.

A literature review of piezoelectric energy harvesters was carried out in Section 1.3. Among different types of piezoelectric energy harvesters, the cantilever harvester has been mostly studied due to its simple configuration.

In Section 1.4, a description a cantilever type piezoelectric energy harvester is given, and a discussion of its bandwidth limitations. It is concluded that the problem for such a type of harvester is its limited resonant frequency bandwidth, and the device is inefficient when the vibration frequency differs from its resonance frequency.

Section 1.5 gives the project motivations and objectives, describes the problems associated with existing piezoelectric energy harvesters, and the factors which cause this - the material's capacitive output impedance and its narrow bandwidth. The aims of the project are to develop solutions so that an energy harvester can harvest energy up to $10mW$ over a wide band and also maintain a reasonable efficiency.

Chapter 2 :

Cantilever and Piezoelectric Models, and Progress towards Wideband Harvesters

2.1 Introduction

This chapter initially describes the derivation of the standard cantilever mathematical model, which gives the resonant frequencies of the various cantilever modes. This is followed by a summary of piezoelectric electromechanical relationships, after which a literature review of wideband/tunable energy harvesters is given.

2.2 Rayleigh-Ritz Analysis of a Cantilever Energy Harvester

The most common techniques used in the analysis of vibrating structures are finite element and Rayleigh-Ritz analyses. For this initial investigation, a Rayleigh–Ritz analysis was adopted over a finite element analysis because it is more flexible, easier to change the cantilever configurations and because it enables a quick analysis of the system response [71, 84, 85, 93-95]. A finite element procedure, on the other hand, requires a longer time to change configurations, and to perform a steady state analysis.

The Rayleigh-Ritz analysis is a technique which can be used to estimate the responses of a vibration system that has more than one resonant frequency. To provide a better understanding of cantilever energy harvesters, a Rayleigh-Ritz analysis was carried out by Shahruz [84, 85]. Consider the beam-mass system shown schematically in Figure 2.1.

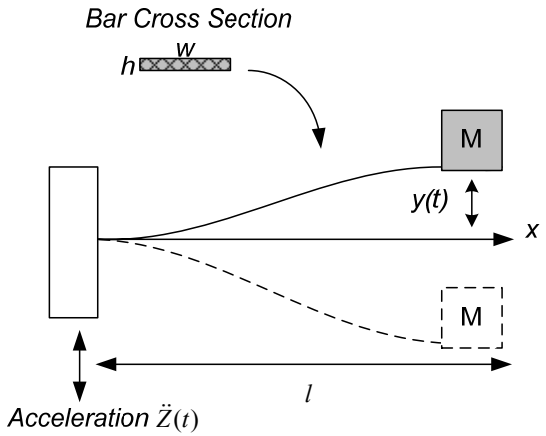

Figure 2.1: Schematic diagram of piezoelectric cantilever harvester

The length, width and thickness of the beam are denoted by l, w and h respectively. The density and modulus of elasticity (Young's modulus) of the beam are denoted by ρ and E. The proof mass is assumed to be a point mass M at the tip of the beam. The cantilever energy harvester system shown in Figure 2.1 can be modelled as the mechanical vibration system shown in Figure 2.2 [3, 39, 40, 84, 85, 93, 94].

With a cantilever energy harvester, the cantilever support bracket is subjected to an oscillatory motion $Z(t)$ and the response of the cantilever tip is a motion $y(t)$ with respect to the cantilever support. The cantilever is modelled in Figure 2.2 as a mass M, with a spring stiffness k, connecting the mass to the support bracket, and electrical and mechanical damping terms b_e and b_m. The electrical damping term arises by virtue of the piezoelectric device being attached to the cantilever beam and the electrical load connected to the piezoelectric material's terminals. It is assumed in this model that the cantilever beam itself has no mass.

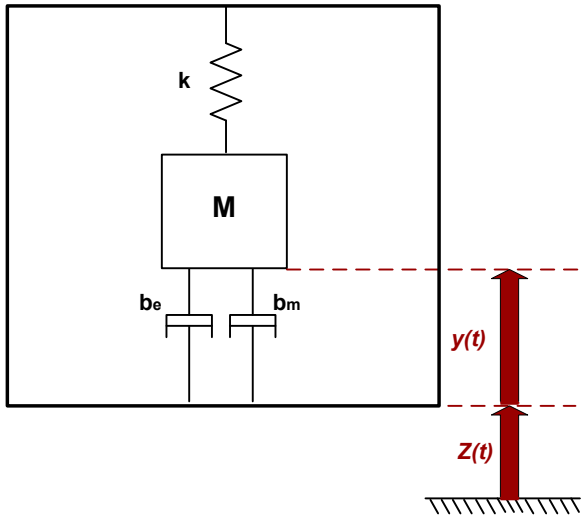

Figure 2.2: First order model of a resonant piezoelectric harvester

The equation representing the dynamic motion of the piezoelectric device is [3]:

$$M\ddot{y} + (b_e + b_m)\dot{y} + ky = -M\ddot{Z} \tag{2.1}$$

This model has been studied by many researchers [96-98], and has been used as a basis for developing a piezoelectric generator equivalent circuit.

According to [99], energy may be stored in the mass and the spring, whereas it is dissipated in the dampers (represented by terms b_e and b_m) as heat. These parameters are passive elements which are invariant with time. The external input *Z(t)* is the excitation of the system, also known as the active element, and its magnitude varies according to a function of time *t*. From [99], the mass, spring and damping terms shown in Figure 2.2 have the following characteristics:

The mass element is usually a rigid body and it executes a vibration, in which it gains or loses kinetic energy with velocity changes.

The spring element (beam) is assumed to have negligible mass and to possess elasticity. A spring force thus exists if there is a relative displacement between the

two ends of the spring. The work done in deforming the spring is equal to the strain energy stored.

The damping term applies if there is a relative motion between the two ends of the damper. A damper has neither mass nor elasticity. The work done to the damper is converted into heat and is therefore not recoverable.

According to [99], the number of degrees of freedom of a physical system is defined as the number of independent spatial coordinates necessary to define its configuration. The cantilever system shown in Figure 2.1 has one degree of freedom if the cantilever itself has negligible mass and the mass M is assumed to move vertically only. It is equivalent to the mass-spring-damper system shown in Figure 2.2.

However in a practical system, the beam will have mass and will not only move vertically. Similarly the mass will not only move vertically. Thus, in an analysis, the cantilever dimensions have to be considered, and the system has more than one degree of freedom and more than one natural frequency.

According to [88], when deriving the equation governing free undamped vibrations in flexure of cantilever beams, it is assumed that vibration occurs in one of the principal planes of the cantilever beam. The effects of transverse shear deformation and rotatory inertia are neglected in this analysis.

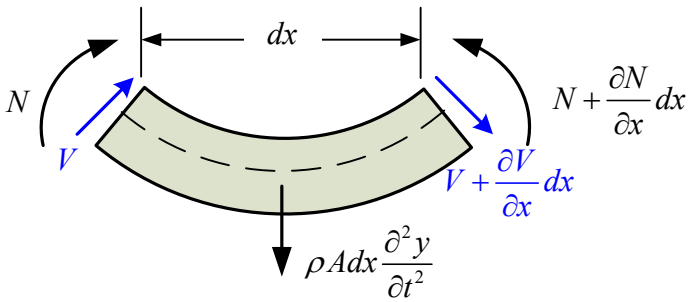

Figure 2.3: A short section of cantilever beam subject to bending

The effect of gravity forces are neglected by measuring the displacement from the position of static equilibrium of the beam. In Figure 2.3, the forces and moments on a beam element of length *dx* are shown. *V* and *N* are the shear force and bending moment seen by the element, the mass of the element is $\rho A dx$ and therefore the inertia force on the element is $\rho A dx \frac{\partial^2 y}{\partial t^2}$, where ρ is the density of the beam material and *A* is the beam cross-sectional area [88].

In Figure 2.4, the centre line of the cantilever beam during vibration is represented by *BC*, *y* is the displacement of any section *dx* at time *t*, and is a function of *x* and *t* in the *y*- direction [88].

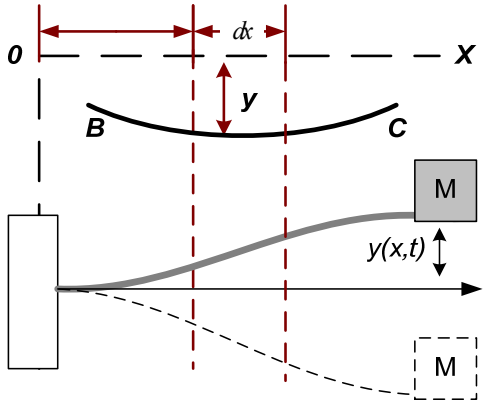

Figure 2.4: Schematic diagram of a cantilever beam with axis

Taking moments about the centre of the beam element and resolving for forces, yields:

$$V dx + N - \left(N + \frac{\partial N}{\partial x} dx \right) = 0 \tag{2.2}$$

thus

$$V = \frac{\partial N}{\partial x} \tag{2.3}$$

and resolving vertically

$$-V + \left(V + \frac{\partial V}{\partial x} dx \right) = \rho A dx \frac{\partial^2 y}{\partial t^2} \tag{2.4}$$

hence:

$$\frac{\partial V}{\partial x} = \rho A \frac{\partial^2 y}{\partial t^2} \tag{2.5}$$

Equation (2.6), relating bending moment N and displacement x, is given by [88], this is used to determine the static deflection of beams,

$$N = -EI \frac{\partial^2 y}{\partial x^2} \tag{2.6}$$

where E is Young's modulus and I is the second moment of area of the cross-section. Combining Equations (2.4), (2.5) and (2.6) [88], yields:

$$\frac{\partial^2}{\partial x^2} \left(-EI \frac{\partial^2 y}{\partial x^2} \right) = \rho A \frac{\partial^2 y}{\partial t^2} \tag{2.7}$$

Equation (2.7) can be used for uniform and non-uniform beams. For the non-uniform beams, the flexural rigidity EI and the mass per unit length ρA are functions of the coordinate x. For a uniform cantilever beam cross-section assumed in this analysis, Equation (2.7) [88] reduces to:

$$EI \frac{\partial^4 y}{\partial x^4} + \rho A \frac{\partial^2 y}{\partial t^2} = 0 \tag{2.8}$$

For free vibrations of the cantilever, $y(x,t)$ must be a harmonic function of time, i.e.

$$y(x,t) = Y(x) \sin(\omega t + \alpha) \tag{2.9}$$

Substituting Equation (2.9) in (2.8) [88]:

$$\frac{d^4Y}{dx^4} - \left(\frac{\rho A\omega^2}{EI}\right)Y = 0 \tag{2.10}$$

Equation (2.10) is of fourth order so the general solution will contain four constants [88] and is of the form:

$$Y = B_1 \sin\lambda x + B_2 \cos\lambda x + B_3 \sinh\lambda x + B_4 \cosh\lambda x \tag{2.11}$$

where

$$\lambda^4 = \frac{\rho A\omega^2}{EI} \tag{2.12}$$

Knowing the equations of the boundary conditions as in Table 2.1 [88], the natural frequencies of the cantilever can be determined.

For a clamped-free cantilever beam as shown in Figure 2.1, there are two boundary conditions shown in Table 2.1, each with its effect on the system. At the free boundary there is no associated bending moment and shearing force, where term $\frac{d^2Y}{dx^2}$ is related to the shear force V and $\frac{d^3Y}{dx^3}$ is related to the lateral loading of the cantilever [88, 100, 101]. The clamped boundary produces zero displacement and zero slope due to the clamp.

Table 2.1: Boundary conditions for a clamped-free beam structure

(Y is displacement see Equation (2.8))

Boundary Condition	Equation	Effect
Free Boundary	$\frac{d^2Y}{dx^2} = \frac{d^3Y}{dx^3} = 0$	Corresponds to no load on the beam
Clamped Boundary	$Y = \frac{dY}{dx} = 0$	Prevents beam from rotation and displacement

For a cantilever beam with the origin at the fixed end as shown in Figures 2.1 and 2.4, substituting the end conditions into equation (2.11) gives the following [88]:

At $x = 0$, $Y = 0$,

$$B_2 + B_4 = 0 \text{ and therefore } B_2 = -B_4 \tag{2.13}$$

At $x = 0$, $\frac{dY}{dx} = 0$,

$$\lambda B_1 + \lambda B_3 = 0 \text{ and } B_1 = -B_3 \tag{2.14}$$

At x = l, $\frac{d^2Y}{dx^2} = 0$,

$$-\lambda^2 B_1 \sin \lambda l - \lambda^2 B_2 \cos \lambda l + \lambda^2 B_3 \sinh \lambda l + \lambda^2 B_4 \cosh \lambda l = 0 \tag{2.15}$$

At x = l, $\frac{d^3Y}{dx^3} = 0$,

$$-\lambda^3 B_1 \cos \lambda l + \lambda^3 B_2 \sin \lambda l + \lambda^3 B_3 \cosh \lambda l + \lambda^3 B_4 \sinh \lambda l = 0 \tag{2.16}$$

Hence, substituting (2.13) and (2.14) into (2.15) and (2.16), yields:

$$B_1(-\sin \lambda l - \sinh \lambda l) + B_2(-\cos \lambda l - \cosh \lambda l) = 0 \tag{2.17}$$

and

$$B_1(-\cos \lambda l - \cosh \lambda l) + B_2(\sin \lambda l - \sinh \lambda l) = 0 \tag{2.18}$$

Eliminating B_1 / B_2, from (2.17) and (2.18), the frequency equation is found [88]:

$$(\sin \lambda l + \sinh \lambda l)(\sinh \lambda l - \sin \lambda l) - (\cos \lambda l + \cosh \lambda l)^2 = 0 \tag{2.19}$$

Using relationships $\cos^2 \lambda l + \sin^2 \lambda l = 1$ and $\cosh^2 \lambda l - \sinh^2 \lambda l = 1$, (2.19) can be simplified to:

$$\cos \lambda l \cosh \lambda l + 1 = 0 \tag{2.20}$$

The successive roots $\lambda_1 l, \lambda_2 l, \lambda_3 l....$ can be found by plotting equation (2.20), as shown in Figure 2.5.

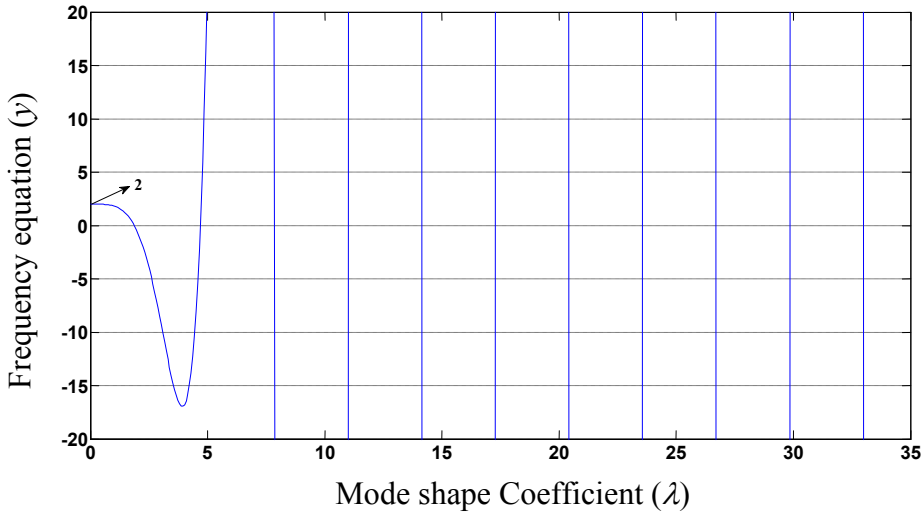

Figure 2.5: Plot of $y = \cosh\lambda l \cos\lambda l + 1$

As shown in Figure 2.5, the roots of the equation are where the curve crosses the zero axis. They occur at 1.8751, 4.6941, 7.8548, 10.9955, 14.1372, 17.2788, 20.4204, 23.5619, 26.7035 and 29.8451 for the first ten mode shapes, negative roots are ignored. This is also confirmed by several researchers [88, 89, 99, 102].

Also:

$$\omega_n = \lambda_i^2 \sqrt{\left(\frac{EI}{\rho A}\right)} \tag{2.21}$$

To obtain the general expression of the mode shape functions, equations (2.13) and (2.14) are substituted into (2.11), hence

$$Y = -B_3 \sin \lambda l - B_4 \cos \lambda l + B_3 \sinh \lambda l + B_4 \cosh \lambda l \tag{2.22}$$

and

$$Y = B_3(\sinh \lambda l - \sin \lambda l) + B_4(\cosh \lambda l - \cos \lambda l) \tag{2.23}$$

Rearranging (2.15), yields:

$$B_3 \sin \lambda l + B_4 \cos \lambda l + B_3 \sinh \lambda l + B_4 \cosh \lambda l = 0 \tag{2.24}$$

and

$$B_3(\sin \lambda l + \sinh \lambda l) + B_4(\cos \lambda l + \cosh \lambda l) = 0 \tag{2.25}$$

hence

$$B_3 = \frac{-B_4(\cos \lambda l + \cosh \lambda l)}{(\sin \lambda l + \sinh \lambda l)} \tag{2.26}$$

Substituting for B_3 in equation (2.23) gives:

$$Y_i(x) = B_4(\cosh \lambda_i x - \cos \lambda_i x) - \frac{B_4(\cos \lambda l + \cosh \lambda l)}{(\sin \lambda l + \sinh \lambda l)}(\sinh \lambda_i x - \sin \lambda_i x) \tag{2.27}$$

Therefore the shape of the *i*th mode, in terms of a single arbitrary constant, C_i, for a cantilever beam, is [88]:

$$Y_i(x) = C_i \left[\cosh \lambda_i x - \cos \lambda_i x - \left(\frac{\cos \lambda_i l + \cosh \lambda_i l}{\sin \lambda_i l + \sinh \lambda_i l} \right)(\sinh \lambda_i x - \sin \lambda_i x) \right] \tag{2.28}$$

where $i = 1, 2, 3, ...$, the shape function, $Y_i(x)$, is a mathematical function which models the structure's vibration mode shapes. λ_i is approximately $(2i-1)\frac{\pi}{2}$ after fifth mode [89].

The first three mode shapes of vibration are given in Figure 2.6. The associated natural frequencies for the first three mode shapes are (2.29-2.31) [88, 89]:

$$\omega_1 = \frac{3.516}{l^2}\sqrt{\left(\frac{EI}{\rho A}\right)} \tag{2.29}$$

$$\omega_2 = \frac{22.03}{l^2}\sqrt{\left(\frac{EI}{\rho A}\right)} \tag{2.30}$$

$$\omega_3 = \frac{61.70}{l^2}\sqrt{\left(\frac{EI}{\rho A}\right)} \tag{2.31}$$

From Equations (2.29-2.31) and the calculated roots from Figure 2.5, the frequencies of the first five modes are approximately in the ratios 1, 6.3, 17.5, 34.4 and 56.8. Therefore, it can be predicted that the second and third mode resonances are approximately 6.3 and 17.5 times higher than the first resonant frequency.

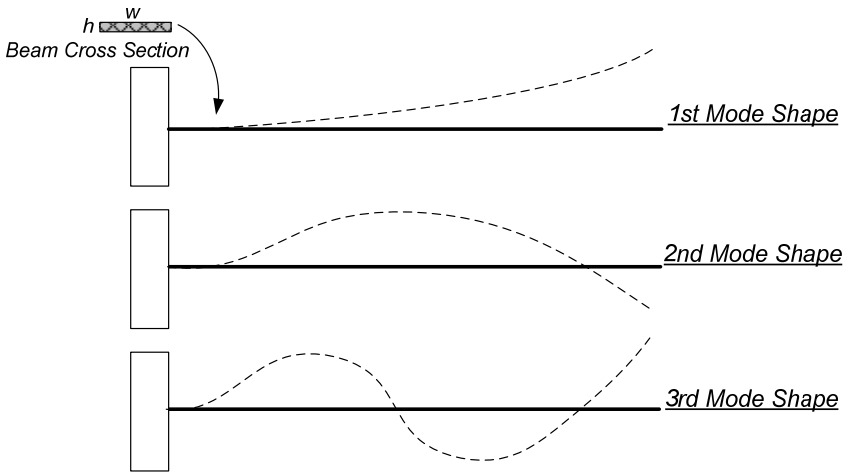

Figure 2.6: Mode shapes of a standard cantilever beam

Considering a freely vibrating beam, the total transverse deformation at any point along its length, is the sum of all its modal deformations and depends therefore on the number of natural frequencies it has.

Assume the total system deformation is a function of displacement with time $y(x,t)$, then the mode shape function $Y_i(x)$ describes the displacements at various positions on the cantilever, for each particular resonance frequency mode. According to [89], Equation (2.32) represents such a system. The subscript i in Equation (2.32) is associated with the number of flexural half-waves in the mode shape, so that for each i there is an associated natural frequency and mode shape.

$$y(x,t) = \sum_{i=1}^{n} A_i Y_i(x) \sin(2\pi f_i t + \theta_i) \tag{2.32}$$

In (2.32) $y(x,t)$ is the total transverse deformation and $Y_i(x)$ is the shape function given by equation (2.28), A_i is a constant, θ_i is the phase angle and f_i is the natural frequency [89, 102].

$$f_i = \frac{\lambda_i^2}{2\pi l^2}\sqrt{\left(\frac{EI}{m}\right)}; \qquad i = 1,2,3..., \tag{2.33}$$

In Equation (2.33), λ_i is a dimensionless parameter which is a function of the boundary conditions applied to the beam structure. l is the length of the beam, and m is the mass per unit length of the beam. E is the Young's modulus of elasticity, and I is the area moment of inertia and represents the beam cross section area during bending motion.

Considering the particular cantilever system shown in Figure 2.1, the vibration source exerts an acceleration which causes the cantilever beam to vibrate transversally. According to the single degree of freedom analysis by [84, 85], the transverse displacement of the beam is written as:

$$Y(x,t) = \tilde{y}_i^{\,T}(x) q_i(t) \tag{2.34}$$

where $\tilde{y}_i(x)$ is the mode shape function and $q_i(t)$ is the generalized coordinate function.

In the following analysis only the first two modes of free transverse vibration are represented, as shown in Figure 2.6, hence:

$$\tilde{y}(x) = \begin{bmatrix} \tilde{y}_1(x) \\ \tilde{y}_2(x) \end{bmatrix}, \; q(t) = \begin{bmatrix} q_1(t) \\ q_2(t) \end{bmatrix} \tag{2.35}$$

According to [99], for a multiple degree of freedom system, the variable is normally considered to be displacement, which in turn provides velocity and acceleration. However in practice, the system can have more than one set of independent geometric quantities. Such quantities are defined as generalized coordinates, and in this case are defined as $q(t)$.

If a tip mass is used in the cantilever system, then for $i=1,2$, λ_i will be a function of the ratio of proof mass to beam mass γ [84, 85, 93, 94, 102], where

$$\gamma = \frac{M}{\rho lwh} \tag{2.36}$$

where l, w and h are the length, width and thickness of the beam respectively. The beam mass density is ρ and M is tip mass. From equation (2.32) to (2.35), the mode shape function $\tilde{y}_i(x)$ with tip mass M is given by equation (2.37) [84, 85]:

$$\tilde{y}_i(x) = \cosh \lambda_i(\gamma)x - \cos \lambda_i(\gamma)x - \left(\frac{\cos \lambda_i(\gamma)l + \cosh \lambda_i(\gamma)l}{\sin \lambda_i(\gamma)l + \sinh \lambda_i(\gamma)l} \right) \left(\sinh \lambda_i(\gamma)x - \sin \lambda_i(\gamma)x \right) \tag{2.37}$$

The kinetic energy of the cantilever beam system due to its mass and spring are shown in equation (2.38) [84, 85].

$$T(t) = \frac{1}{2}\int_0^l \rho wh\dot{Y}^2(x,t)dx + \frac{1}{2}M\dot{Y}^2(l,t) \tag{2.38}$$

for $t \geq 0, \dot{Y} = \frac{\partial Y}{\partial t}$. In (2.38) the first term on the right hand side represents the kinetic energy of the beam mass and the second term is the kinetic energy due to the tip mass.

Putting equations (2.35-2.36) into (2.38), yields a simplified expression for kinetic energy [85]:

$$T(t) = \frac{1}{2}\dot{q}^T(t)(MH_1 + \rho lwhH_2)\dot{q}(t) \tag{2.39}$$

where H_1 and H_2 are given by equations (2.40-2.41) [85]:

$$H_1 = \begin{bmatrix} y_1^2(l) & y_1(l)y_2(l) \\ y_1(l)y_2(l) & y_2^2(l) \end{bmatrix} \tag{2.40}$$

$$H_2 = \begin{bmatrix} \int_0^1 \chi_1^2(z)dz & \int_0^1 \chi_1(z)\chi_2(z)dz \\ \int_0^1 \chi_1(z)\chi_2(z)dz & \int_0^1 \chi_2^2(z)dz \end{bmatrix} \tag{2.41}$$

and $\chi_i(z)$ is the mode shape function shown in (2.42) [85].

$$\chi_i(z) = \sin\lambda_i(\gamma)z - \sinh\lambda_i(\gamma)z - \left(\frac{\sin\lambda_i(\gamma) + \sinh\lambda_i(\gamma)}{\cos\lambda_i(\gamma) + \cosh\lambda_i(\gamma)}\right)\left(\cos\lambda_i(\gamma)z - \cosh\lambda_i(\gamma)z\right) \tag{2.42}$$

The strain energy of the system is given by (2.43) [84, 85]

$$U(t) = \frac{1}{2}\int_0^l EI\ddot{Y}^2(x,t)dx \tag{2.43}$$

for $t \geq 0$, $\ddot{Y} = \frac{\partial^2 Y}{\partial x^2}$ and second moment of cross section area I is:

$$I = \frac{wh^3}{12} \tag{2.44}$$

Substituting (2.44) into (2.43), yields:

$$U(t) = \frac{1}{2}q^T(t)\left(\frac{Ewh^3H_3}{12l^3}\right)q(t) \tag{2.45}$$

where H_3 is given by (2.46)

$$H_3 = \begin{bmatrix} \lambda_1^4(\gamma)\int_0^1 \psi_1^2(z)dz & \lambda_1^2(\gamma)\lambda_2^2(\gamma)\int_0^1 \psi_1(z)\psi_2(z)dz \\ \lambda_1^2(\gamma)\lambda_2^2(\gamma)\int_0^1 \psi_1(z)\psi_2(z)dz & \lambda_2^4(\gamma)\int_0^1 \psi_2^2(z)dz \end{bmatrix} \tag{2.46}$$

where [84, 85, 93, 94]:

$$\psi_i(z) = -\sin\lambda_i(\gamma)z - \sinh\lambda_i(\gamma)z + \left(\frac{\sin\lambda_i(\gamma)+\sinh\lambda_i(\gamma)}{\cos\lambda_i(\gamma)+\cosh\lambda_i(\gamma)}\right)\left(\cos\lambda_i(\gamma)z + \cosh\lambda_i(\gamma)z\right) \tag{2.47}$$

According to [99], a system with multiple degrees of freedom can be specified by a set of generalized coordinates. The Lagrange equation defines the motions of the system in terms of any generalized coordinates. The Lagrange equation is often used to express the generalized force (spring force, damping force and excitation force) as a function of the kinetic energy of the system written as:

$$\frac{d}{dt}\left(\frac{\partial T}{\partial \dot{q}_j}\right)-\frac{\partial T}{\partial q_j}+\frac{\partial \xi}{\partial \dot{q}_j}+\frac{\partial U}{\partial q_j}=Q_j \tag{2.48}$$

where q_j is the generalized coordinate chosen to describe the system geometric configuration, and $j=1,2,3....$, represents the number of generalized coordinates within the system.

In (2.48) the terms $\frac{d}{dt}\left(\frac{\partial T}{\partial \dot{q}_j}\right)$ and $\frac{\partial T}{\partial q_j}$ represents the kinetic energy within the system, the term $\frac{\partial \xi}{\partial \dot{q}_j}$ represents energy dissipated or loss, $\frac{\partial U}{\partial q_j}$ represents strain energy and Q_j is the external applied force.

If the system is conservative, which means the work done or total energy constant with time, there are no energy losses in the system. Equation (2.48) can then be simplified to (2.49):

$$\frac{d}{dt}\left(\frac{\partial T}{\partial \dot{q}_j}\right)-\frac{\partial T}{\partial q_j}+\frac{\partial U}{\partial q_j}=0 \tag{2.49}$$

In practice, the cantilever energy harvester is a non-conservative system and the generalized non-conservative forces applied to the beam in the absence of gravity is [84, 85]:

$$Q_i(t)=-\int_0^l \rho wh\ddot{u}(t)y_i(x)dx-M\ddot{u}(t)y_i(l) \tag{2.50}$$

where $\ddot{u}(t)$ is acceleration. Substituting the mode shapes (for $i=1,2$) shown in Equation (2.35) into the generalized force $Q_i(t)$ Equation (2.50), yields:

$$Q_i(t)=\begin{bmatrix}Q_1(t)\\Q_2(t)\end{bmatrix}=-\left[MH_4+\rho lwhH_5\right]\ddot{u}(t) \tag{2.51}$$

where H_4 and H_5 are

$$H_4 = \begin{bmatrix} y_1(l) \\ y_2(l) \end{bmatrix} \tag{2.52}$$

$$H_5 = \begin{bmatrix} \int_0^1 \chi_1(z)dz \\ \int_0^1 \chi_2(z)dz \end{bmatrix} \tag{2.53}$$

The equation of motion for a cantilever beam system derived from the Lagrange equation is given by [84, 85]:

$$\left[MH_1(\gamma) + \rho lwhH_2(\gamma)\right]\ddot{q}(t) + \left[\frac{Ewh^3 H_3(\gamma)}{12l^3}\right]q(t) = -\left[MH_4(\gamma) + \rho lwhH_5(\gamma)\right]\ddot{u}(t) \tag{2.54}$$

Therefore the mass and spring matrices $\tilde{M}$ and $\tilde{K}$ can be obtained from (2.54). Equation (2.54) ignores damping, yet in practice damping will be present. A damping term $\tilde{C}$ can be added and is here assumed to be a function of I the second moment of beam cross section area.

Using a state-space representation for the system [85]:

$$\tilde{M}\ddot{q}(t) + \tilde{C}\dot{q}(t) + \tilde{K}q(t) = -\tilde{F}\ddot{u}(t) \tag{2.55}$$

Therefore by comparing (2.54) with (2.55), the mass, stiffness, frequency and damping matrices $\tilde{M}$, $\tilde{K}$, $\tilde{F}$ and $\tilde{C}$ are shown in (2.56-2.59) [84, 85]:

$$\tilde{M} = MH_1(\gamma) + \rho lwhH_2(\gamma) \tag{2.56}$$

$$\tilde{K} = \frac{Ewh^3 H_3(\gamma)}{12l^3} \tag{2.57}$$

$$\tilde{F} = MH_4(\gamma) + \rho lwhH_5(\gamma) \tag{2.58}$$

$$\tilde{C} = cI \tag{2.59}$$

where c defines the relationship between second moment of area and damping matrix $\tilde{C}$. Using equations (2.56-2.59), the cantilever system can be converted into an electrical equivalent circuit as shown in Figure 2.7.

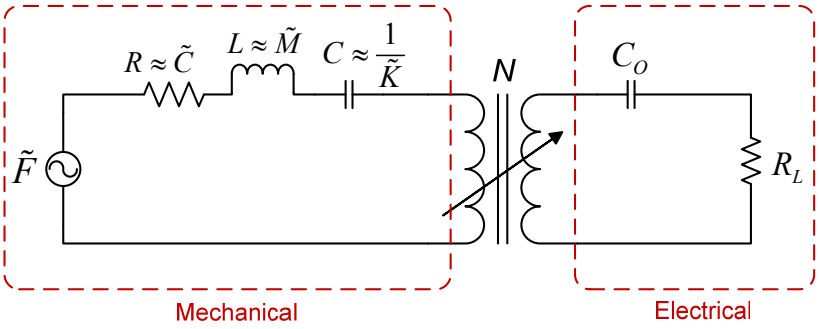

Figure 2.7: Electrical equivalent circuit of piezoelectric harvester

From Figure 2.7, the resistance R is equivalent to damping $\tilde{C}$, inductance L is equivalent to mass $\tilde{M}$ and capacitance C is equivalent to stiffness $1/\tilde{K}$. The non-ideal transformer is a simplified representation of the piezoelectric material and its mechanical to electrical coupling. The output impedance of the piezoelectric material is represented by C_O [11, 103-108].

The electromechanical coupling factor is an important parameter which needs to be considered for piezoelectric energy harvesters. According to [46], the coupling factor is the effectiveness of the piezoelectric effect, and represents the amount of mechanical energy that can be transferred to electrical energy and vice versa. The coupling factor is modelled by the transformer shown in Figure 2.7, where N is the transformer's electrical coupling factor and is less than 100%.

Since the mechanical mass, stiffness and damping terms are modelled in 3 dimensions [109], see Chapter 1, hence the electromechanical coupling coefficient of a piezoelectric material is also multi-dimensional. The coupling coefficient is usually represented as a generalized electromechanical coupling coefficient K_{ij}^2 [110], where

the subscripts i and j are the axis directions shown in Figure 1.3. The coupling factors for PFC material are given in Appendix A.

2.3 Electromechanical Behaviour of Piezoelectric Materials

This section describes the electrical relationships of piezoelectric material and parameters used when modelling the interlinking of mechanical and electrical fields.

The piezoelectric coefficient g_{ij} is generally described as in (2.60) [47].

$$g_{ij}^{\theta} = \begin{cases} = \left[\dfrac{\partial \tilde{S}_j}{\partial \tilde{D}_i}\right]_{\tilde{E},\theta} & = \left(\dfrac{m^2}{V}\right) \quad \text{Converse Effect (Actuator)} \\ = \left[-\dfrac{\partial \tilde{E}_i}{\partial \tilde{T}_j}\right]_{\tilde{S},\theta} & = \left(\dfrac{V \cdot m}{N}\right) \quad \text{Direct Effect (Generator)} \end{cases} \tag{2.60}$$

where $\tilde{T}$ and $\tilde{S}$ are the mechanical stress and mechanical strain at zero electric field strength. $\tilde{E}$ and $\tilde{D}$ are the electric field strength and electric field displacement of the unstressed medium under the influence of an electric field.

As stated by Morgan Ceramics [42] and [47, 111], the mechanical and electrical piezoelectric material relationships are :

$$\tilde{S} = s\tilde{T} \qquad \text{(Mechanical)} \tag{2.61}$$

$$\tilde{D} = \varepsilon \tilde{E} \qquad \text{(Electrical)} \tag{2.62}$$

where s is the compliance which is the strain produced in a piezoelectric material per unit of stress applied, and is the reciprocal of the modulus of elasticity (Young's modulus). ε is the permittivity.

For piezoelectric energy harvesting using the direct effect, the voltage constant g_{ij} relates electric field to applied stress and is given by the piezoelectric charge constant d_{ij} and relative dielectric constant K_T as shown in equation (2.63) [112],

$$g_{ij} = \frac{d_{ij}}{\varepsilon_0 K^T} \tag{2.63}$$

where ε_0 is the permittivity of free space. A more detailed review of different piezoelectric relationships and of the charge constant d_{ij} is given in Appendix A.

According to [112], the output voltage of piezoelectric material subject to a force F is:

$$V = \frac{g_{ij} F L_{PZT}}{A_{PZT}} \tag{2.64}$$

Where L_{PZT} is the length of the piezoelectric material and A_{PZT} is the cross sectional area of the material. Because the ratio L_{PZT}/A_{PZT} is high for piezoelectric fibre composite materials in comparison to piezoelectric ceramics, therefore fibre composite materials have a higher output voltage.

The electrical energy stored in a piezoelectric element, for a given applied force F, is:

$$Energy = VQ_{PZT} \tag{2.65}$$

where Q_{PZT} is the charge produced by the piezoelectric material produced. For the 33 vibration mode, the charge Q_{PZT} is Fd_{33}.

2.4 Summary

Sections 2.1 to 2.3 describe the Rayleigh-Ritz analysis of a cantilever system along with the piezoelectric electromechanical coefficient. Such a cantilever system has been used frequently as the standard piezoelectric energy harvester. It holds the advantages of being easy to configure, since its frequency can be tuned using tip masses, secondly it is easy to estimate its response, as there are well developed Rayleigh-Ritz or finite element analyses for cantilever vibration systems.

However, there are drawbacks for cantilever systems. For machine condition monitoring, a machine will often produce vibrations encompassing a range of frequencies and varying in frequency and amplitude as machine load and speed change. In these situations a single cantilever harvester is less effective and a harvester is needed instead which can work efficiently over a range of frequencies, adding damping is one means of broadening the response of a cantilever but the consequent loss of efficiency is undesirable, and for this reason the technique is hardly ever used [99, 113]. Hence, research towards developing a system to harvest energy from a wide frequency spectrum has been widely expanded over the past few years. A review of this is shown in next section.

2.5 Review and Discussion of Energy Harvesters for Broadband Resonance Frequency Response

2.5.1 Review of Research into Multiple Resonance Energy Harvesters

Shahruz [84, 85] was one of the first researchers to describe a wide band energy harvester. In his device an array of cantilevers is attached to a rigid body subjected to an input acceleration *ii* [48]. Each cantilever has a slightly different natural

frequency, as determined by dimensions and tip mass, and each has a piezoelectric device mounted upon it, see Figure 2.8.

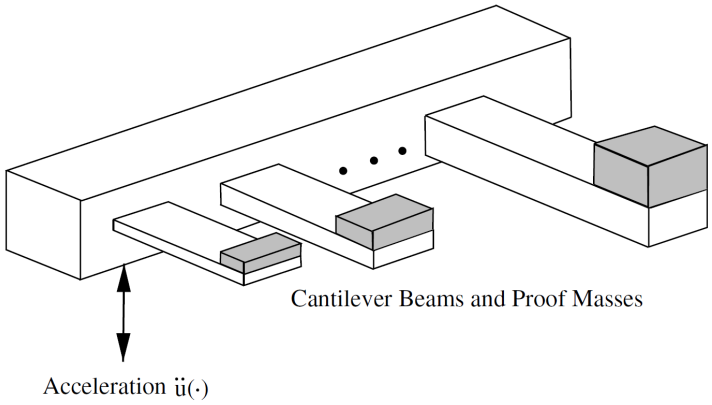

Figure 2.8: Shahruz harvester [84, 85]

The device is constructed so that it creates a band of closely spaced mechanical resonance peaks. The electrical outputs of each piezoelectric material are connected in parallel, to give a summated output. Figure 2.9 shows the predicted responses of the cantilevers. A paper describing a single degree of freedom model was published in 2006 [84] and an analysis of an improved multiple degree of freedom model was published in 2008 [85].

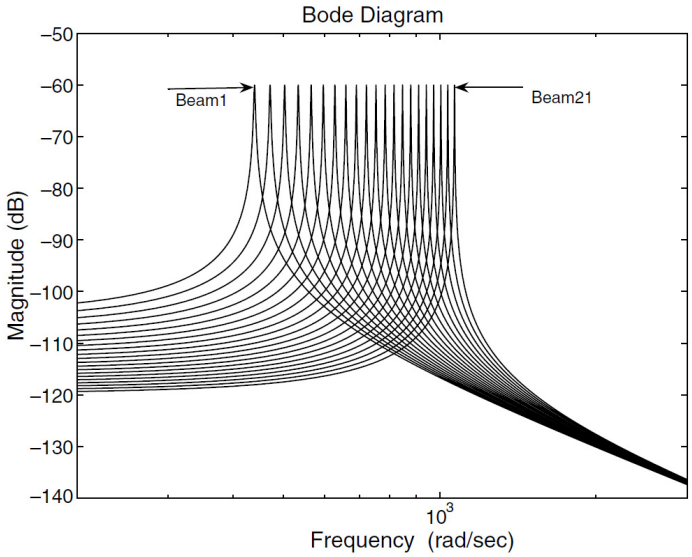

Figure 2.9: Responses of individual cantilevers by Shahruz harvester [84]

The frequency responses shown in Figure 2.9 result from 21 cantilevers with different beam dimensions and tip masses. The dimensions and tip masses were adjusted so that the resonance frequencies ranged from 70*Hz* to 170*Hz* for beam 1 to beam 21, in steps of 5*Hz*. Shahruz's theoretical predictions suggest that the device can harvest vibration energy over a wider range of frequencies than a single cantilever harvester i.e. 70*Hz* to 170*Hz*, when subject to transverse vibration. Shahruz's papers on this subject are however theoretical since no actual experimental results were presented.

Ferrari et al [114] also developed a multi-frequency piezoelectric generator as shown in Figure 2.10(a).

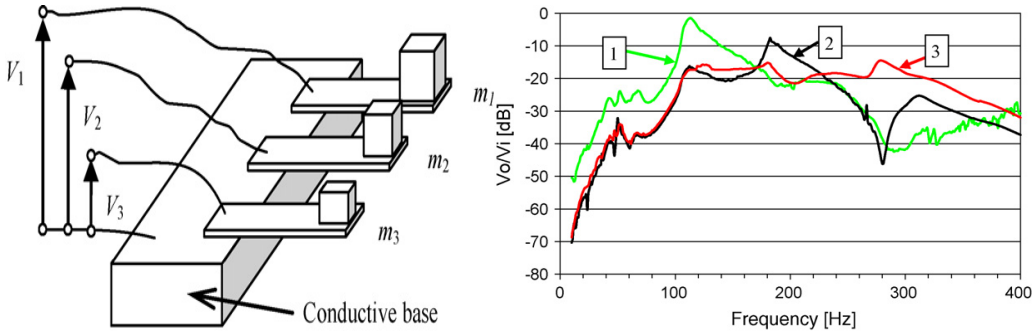

(a) (b)

Figure 2.10: Ferrari et al harvester [114] (a) piezoelectric cantilever array (b) cantilevers frequency responses

In this device, a set of three cantilevers having resonance frequencies of 113*Hz*, 183*Hz* and 281*Hz* were tested on a shaker, the result of which is shown in Figure 2.10(b). Note in Figure 2.10(b), curve 1 correspond to cantilever with m_1 of 113*Hz*, curve 2 correspond to cantilever with m_2 of 183*Hz* and curve 3 shows cantilever with m_3 of 281*Hz*.

The vertical acceleration from the shaker was around 1*g* peak. The peak electrical power output was measured as 89μW, 57μW and 57μW for the cantilevers with tip masses m_1, m_2 and m_3 respectively. Piezoelectric material was mounted on each cantilever in the same manner as that proposed by Shahruz. The device was used to charge a capacitor which in turn provided power for a sensor node. Preliminary test

results showed that the generator was able to trigger the transmission of the sensor when vibration occurred at its resonance frequencies.

Zhang et al [115] developed a magnetoelectric wideband energy harvester as shown in Figure 2.11(a). This is similar to the Shahruz model. The device uses multiple ferroelectric composite fibers which couple magnetic, electric and acoustic fields together. 40 fiber rods of various lengths, the longest being 10*cm*, were used. Rod diameters were not given in the paper.

The cantilever rods electrically were connected either in series or parallel to form a wide band response. Mathematical predictions from a single degree of freedom model are shown in Figure 2.11(b). The waveforms shown are response predictions for electrically parallel rods. The inset graph in Figure 2.11(b) shows predicted waveforms for when the rods are electrically connected in series.

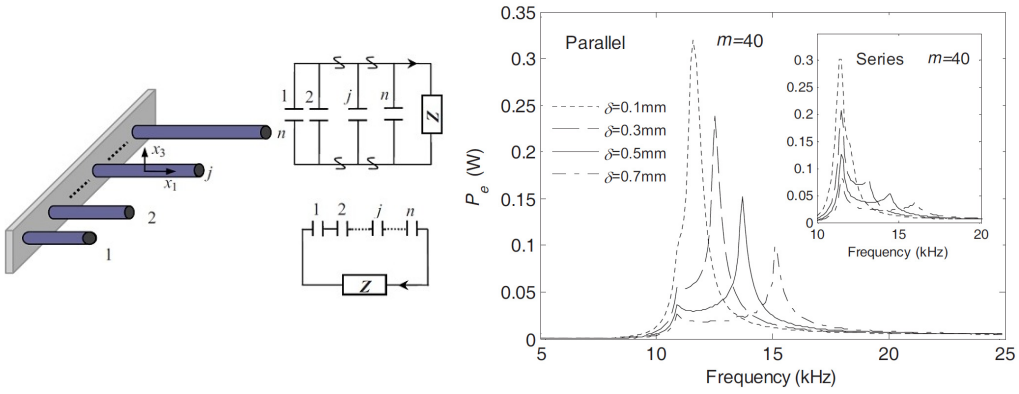

(a) (b)

Figure 2.11: Zhang et al harvester [115] (a) model with equivalent circuit (b) output power versus frequency curves

The power output was estimated from basic equations. It was concluded that increasing the number of fibers will widen the bandwidth of the device.

Liu et al 2008 [116] investigated a MEMS scale piezoelectric energy harvester which uses an array of cantilevers to form a wide band harvester, see Figure 2.12. Each cantilever comprised a piezoelectric device with metal electrodes on top and bottom, mounted on a silicon cantilever. Three cantilevers with resonant frequencies of 229*Hz*, 234*Hz* and 226*Hz* were tested. The length and width of the cantilevers

were 3000μm and 1000μm respectively. The power outputs from each cantilever were found to be 2.55μW, 2.1μW and 1.87μW.

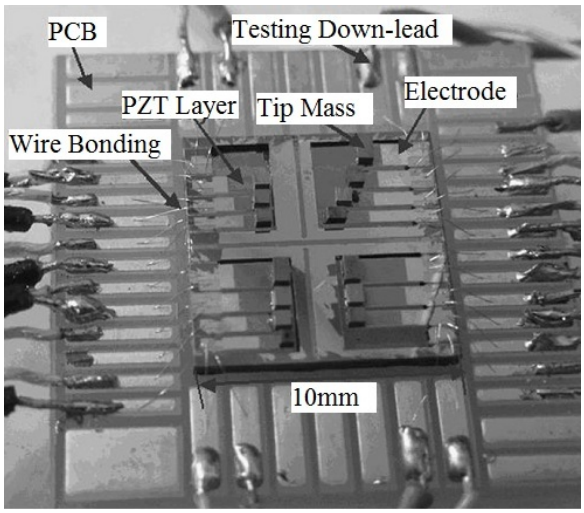

Figure 2.12: Liu et al harvester model [116]

It was concluded that the device showed the possibilities of MEMS scale multiple resonant frequency energy harvesting [116].

Chew et al [117] investigated MEMS scale piezoelectric energy harvester structures as shown in Figure 2.13. The device they constructed consists of several identical piezoelectric beams stacked together, with one beam end fixed onto the end of another beam to form a spiral system. Each beam is 15mm x 1.4mm x 0.6mm.

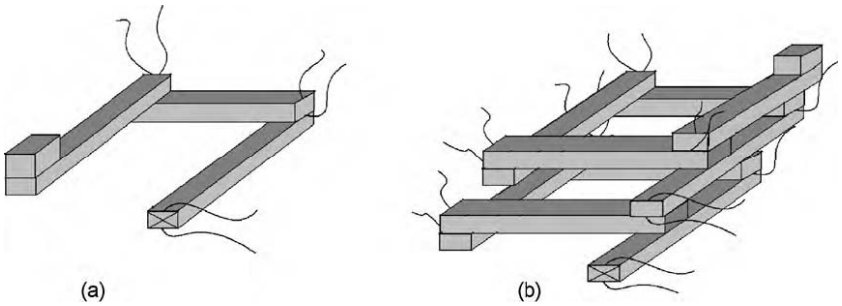

Figure 2.13: Chew et al harvester [117] (a) array of 3 beams (b) array of 9 beams

A graph of output voltage versus frequency for each cantilever of the 9 beam model is shown in Figure 2.14. During testing, beam 1 (the beam at the lowest tier in Figure

2.13(b)) was used as the input excitation source. Beams 2 to 8 were thus subject to the excitation force from beam 1.

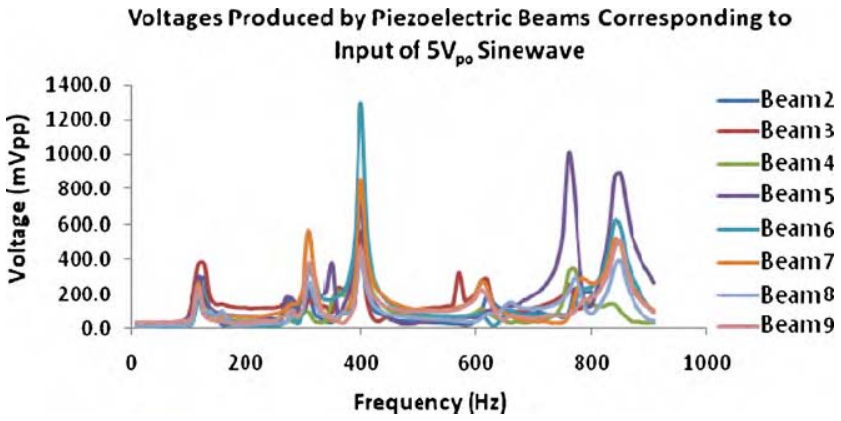

Figure 2.14: Chew et al harvester results for array of 9 beams [117]

The output connections from the piezoelectric beams were connected in parallel to provide optimum system performance. Seven resonance frequencies were obtained between 100*Hz* and 1000*Hz*.

Jung et al [118, 119] developed a buckled bridge energy harvester as shown in Figure 2.15(a). A proof mass with four (or more) cantilevers attached was mounted at the centre of the bridge. Each buckled bridge is about 1*mm* by 0.2*mm* in width and thickness respectively. The action of the device is as follows. An upwards acceleration of the base will cause the bridges to buckle and a snap downwards action results, the proof mass and cantilevers being rapidly accelerated downwards. The rapid downwards acceleration causes the cantilevers to transiently oscillate at their fundamental frequency of around 100*Hz*, producing an output voltage.

When downwards acceleration of the base exceeds a certain value, the bridges snap upwards, creating further cantilever oscillations and producing an output voltage. Thus, an output voltage is produced from the cantilever whenever the base acceleration exceeds a certain level.

The mass mounted at the centre of the bridges is much heavier than the total weight of the bridges. This helps to increase the swing and the vibrating forces of the bridge.

Because of the devices hysteretic operation it is not necessary to match the excitation frequency with the natural resonance frequency of the device.

Four designs were tested with different lengths of bridge, 25*mm*, 30*mm*, 35*mm* and 40*mm*. The horizontal lengths of the buckled bridges were approximately 22*mm* to 38*mm*. An increase in the lengths of the bridges results in a decrease of swing acceleration of at least 23m/s^2 for a proof mass of 2.7*g*. Acceleration however increases with a lighter proof mass.

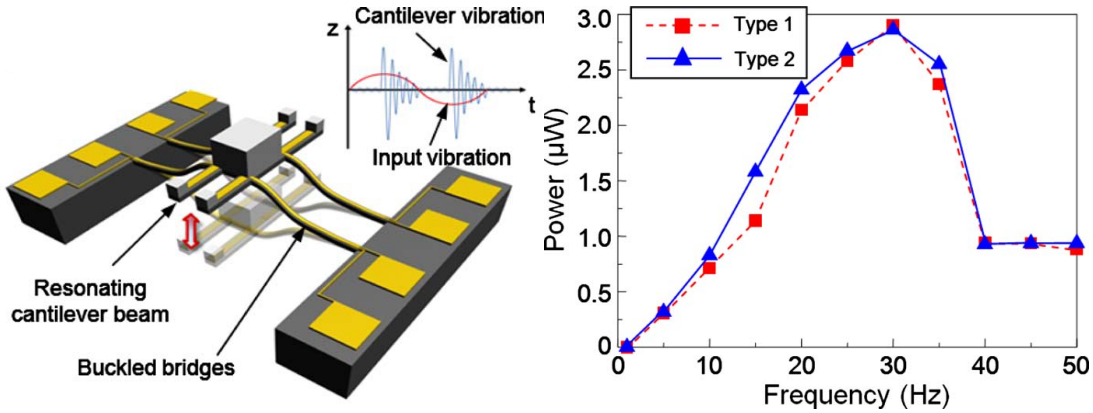

(a) (b)

Figure 2.15: Buckled bridge harvester [118, 119] (a) structure schematic (b) response curves

The device has a maximum power output at around 30*Hz* as shown in Figure 2.15(b). It has a wideband operation from 20*Hz* to 40*Hz*, and the input frequency can be lower than the resonant frequencies of the cantilevers. When the device was excited above its resonant frequency of around 35*Hz*, the bridge was not able to buckle resulting in a reduced power output and the discontinuity shown in the curve of Figure 2.15(b).

The device occupies a relatively large area and its ability to withstand large amounts of vibration remains to be further investigated. Additionally, an increase in vibration amplitude produces no more output power, once sufficient acceleration is provided to create the snap action.

Marinkovic et al [120] proposed a device which they claim can harvest energy between 160*Hz* and 400*Hz*, or over an even wider frequency range. The device, see Figure 2.16, consists of four thin beams which support a proof mass located in the centre. The ends of the beams are mounted to the base structure one end and to the proof masses at the other end. The device uses off resonance operation and so there is no need for resonance tuning. The proof mass is significantly heavier than the beams. Results are shown in Figure 2.16.

A prototype was built having beam thicknesses of only 5μm. The overall length and width of the device is 2300μm and 125μm respectively, and the centre mass weighs 9.3*mg*.

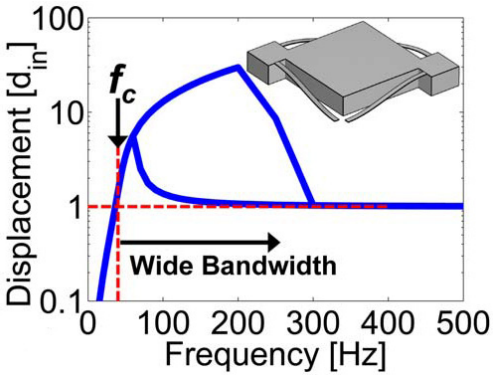

Figure 2.16: Marinkovic et al harvester model [120]

Piezoelectric material was mounted on each beam. The action of the device was such that the beams were stretched rather than vibrated transversally. However the active piezoelectric area is relatively small compared to the overall size of the device, which may lead to a low overall power density compared to that of a standard cantilever harvester. Other techniques based on nonlinearities are researched by [121-123].

Rather than try to harvest energy over a broadband, a different solution for the mismatch between excitation frequency and natural frequency of the device has been investigated by several researchers. The solution involves tuning the resonant frequency of the device by varying the stiffness of the cantilever.

Mansour et al [124] developed a cantilever harvester having two permanent magnets, see Figure 2.17. One magnet is mounted on the free end of the cantilever and the other is mounted nearby, so that they face each other. The polarity is such that they attract each other. By adjusting the gap between them, the attractive force between the two magnets can be altered to change the cantilever resonant frequency.

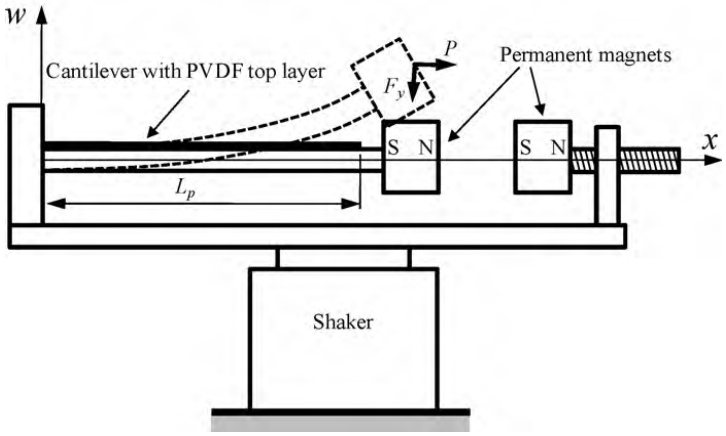

Figure 2.17: Mansour et al harvester model [124]

A steel cantilever beam of dimension 280*mm* x 26.7*mm* x 0.7*mm* was used to test the theory. Tests showed the magnet system to not only produce an axial force but also a transverse force onto the cantilever. The experimental results showed that the natural frequency of the cantilever can be tuned from around 3*Hz* to 12*Hz*, with a magnetic force of up to 3.35*N* at the tip of the cantilever beam, as shown in Figure 2.18.

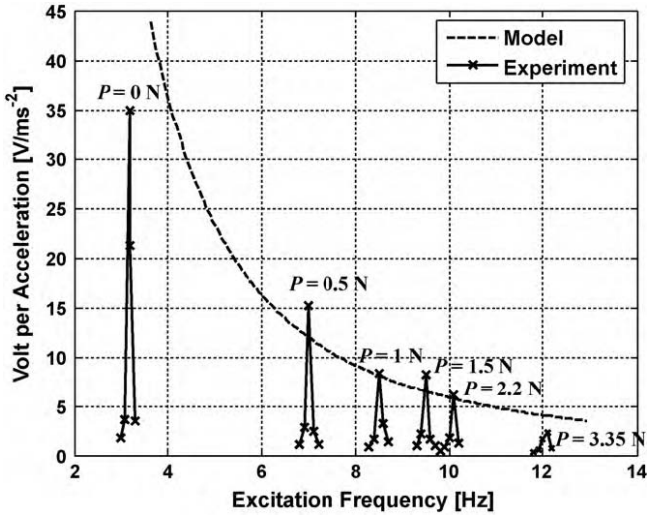

Figure 2.18: Mansour et al harvester voltage versus frequency response [124]

As shown in Figure 2.18, the output voltage of the device reduces with higher magnetic forces, since damping increases with a higher magnetic force. Hence, the system demonstrated a resonance frequency tuning method, however its drop in voltage output as frequency increases leads to a poor efficiency. Furthermore, frequency tuning is required which may be impractical for actual applications, and possibly results in energy loss.

Wu et al [125] developed a frequency adjustable device, shown in Figure 2.19(a). The resonant frequency is altered by moving the adjustable part of the tip mass m_1, inside the part m_0, which is attached to the end of the cantilever. This causes the centre of gravity of the tip mass to move resulting in a change of cantilever resonant frequency. The rod mass m, is 6mm in radius and 30mm long.

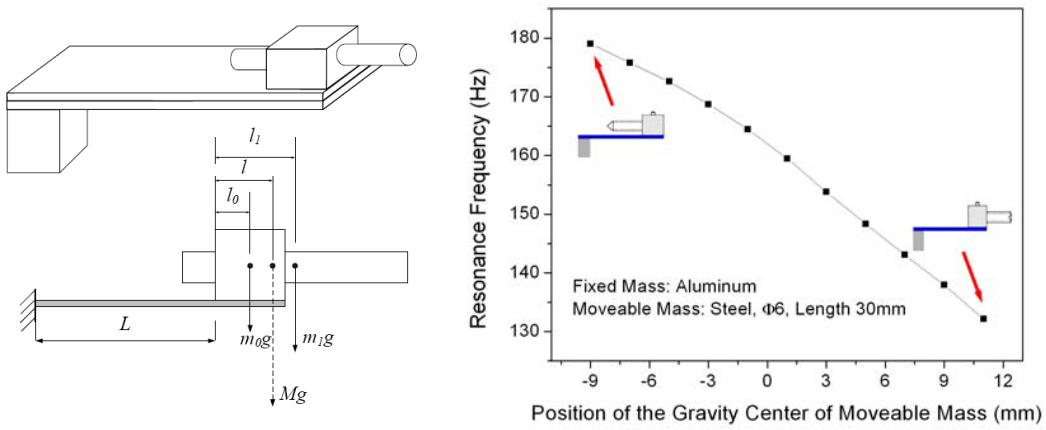

(a) (b)

Figure 2.19: Wu et al harvester [125] (a) cantilever with movable mass (b) results of frequency tuning

The resonant frequency can be adjusted between 130Hz and 180Hz as shown in Figure 2.19(b). However, in a practical device the adjustable part of the mass would need to be moved in an automatic manner to tune the device. It is difficult to envisage a practical, energy efficient system that could achieve this compensation.

Morris et al [126] describe a tuneable prototype energy harvester using PVDF sheet in a clamped-clamped structure, as shown in Figure 2.20. Two 28μm thick PVDF

sheets were attached to a seismic mass, one on the top and one on the bottom of a seismic mass as shown in Figures 2.20(a) and 2.21(a). The resonant frequency of the harvester is tuned by altering the preloading of the sheets. When the base is excited by an external force, the mass moves up and down, deflecting the PVDF sheets, and thereby converting mechanical energy to electrical energy.

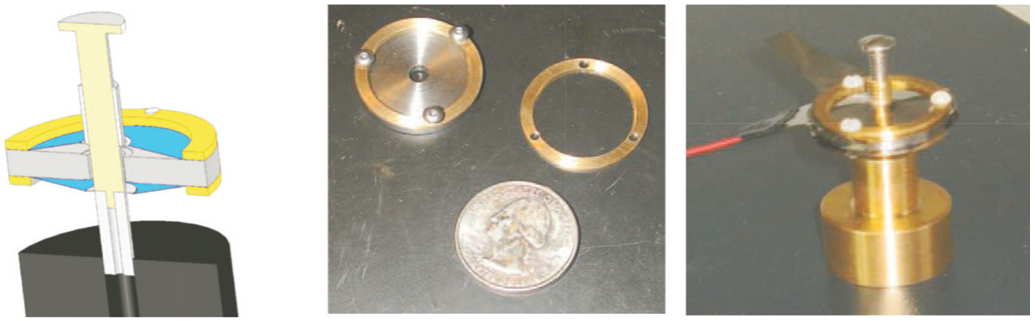

Figure 2.20: Morris et al harvester [126]
(a) cross-sectional drawing of the device (b) seismic mass and brass clamping rings (c) assembled device

The resonant frequency can be varied from 80*Hz* to 235*Hz*. Figure 2.21(b) shows the frequency response of three random preloading positions, achieved by adjusting the length of the preloading screw. The open circuit voltage was measured and it was shown that by changing the preloading screw position, the resonant frequency changed. Experiments showed that the results obtained are repeatable.

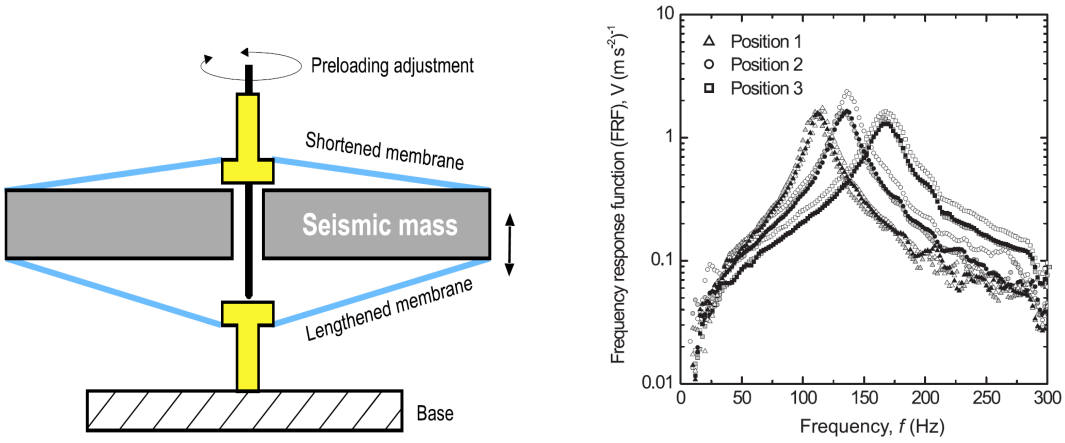

(a) (b)

Figure 2.21: Morris et al harvester [126] (a) cross sectional view of the device (b) frequency responses of different adjustment positions

As with the experiences of other researchers, Morris et al [126] found that the manual tuning of such a device can be complicated and energy consuming, making it unfeasible for practical use.

Soliman et al [127] investigated a cantilever with a stopper to limit the amplitude of vibration, see Figure 2.22, and showed that a 240% increase in bandwidth resulted from their device. The stopper was able to move along the cantilever.

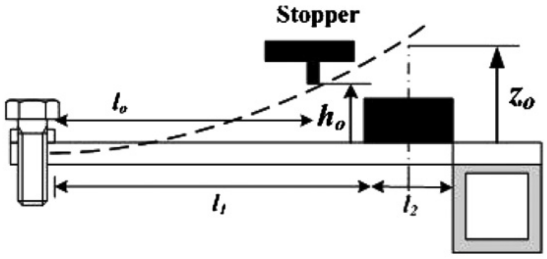

Figure 2.22: Soliman et al harvester model [127]

Sari et al [9] produced a micro harvester with a multiplicity of different length cantilevers, using electromagnetic generators (one coil per cantilever, all coils electrically in parallel) and a shared magnet, see Figure 2.23.

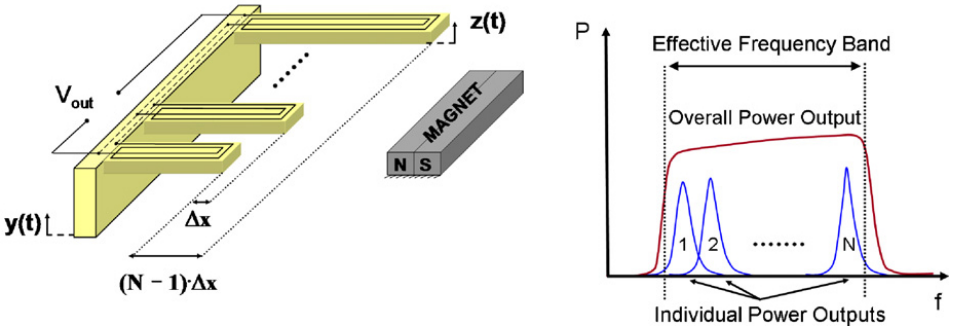

Figure 2.23: Sari et al harvester model [9]

The harvester showed a flat, wideband response, but it was considered that the output power density of $0.35\mu W/cm^3$ was low due to destructive interference between the signals generated by individual resonators [9]. Figure 2.24 shows Sari et al published simulation results.

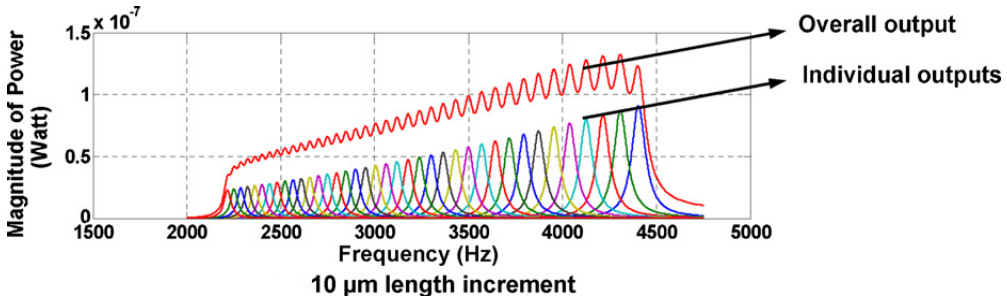

Figure 2.24: Sari et al harvester simulated power output results [9]

Zhu et al [128] produced a tunable harvester using magnetic tensioning of a cantilever shown in Figure 2.25. The generator is electromagnetic and the cantilever was tunable over a range of approximately 70*Hz* to 95*Hz*.

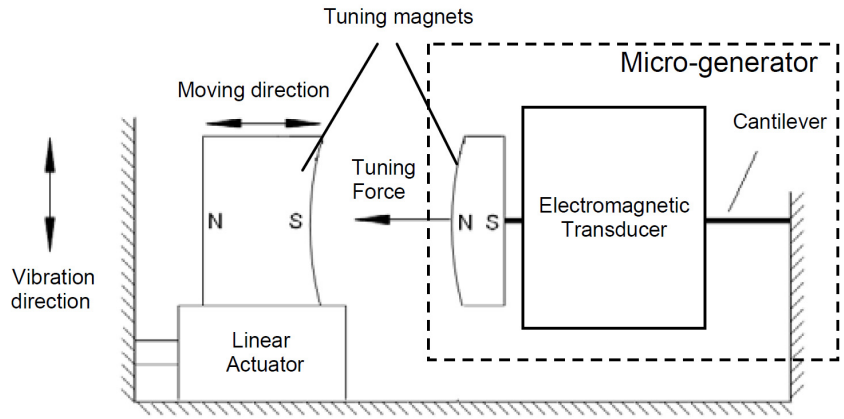

Figure 2.25: Zhu et al harvester model [128]

Zhu et al estimated the duty cycle for automatic tuning to be 230 seconds, this limit being imposed by energy consumption of the tuning device. This long response time limits the harvester to use in applications where vibration frequencies do not change rapidly. Figure 2.26 shows how the frequency changes when the distance between the two tuning magnets in altered.

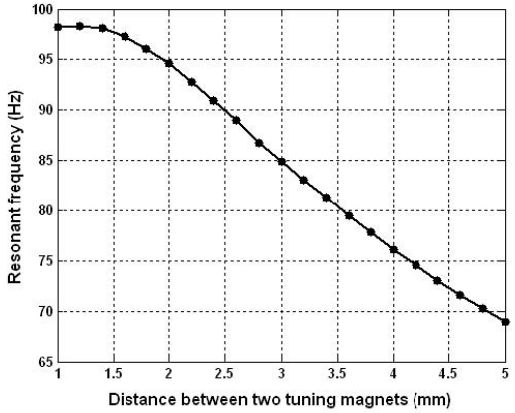

Figure 2.26: Zhu et al harvester [128] frequency responses

To summarise, most researchers have concentrated on varying the beam stiffness to achieve cantilever tuning. Other techniques such as capacitive loading have also been described [129].

The next section discusses the difficulties met with these various forms of wideband or tunable energy harvesters.

2.5.2 Discussion of the Problems Associated with Broadband Energy Harvesters, and Possible Solutions

Several multiple resonance frequency systems as described by various researchers, were summarised in the previous section. According to [41], the existing methods of frequency tuning of the harvester can be categorised as widening the system bandwidth, mechanical tuning and electrical tuning.

Consider the first category - widening the bandwidth of the harvester. To achieve this effect, the most popular method is to use an array of cantilevers. This method has been studied by several researchers, as reviewed in the previous section [9, 84, 85, 93, 94, 114-117, 130, 131]. In this technique several cantilevers having different resonant frequencies, each with a piezoelectric or electromagnetic mechanical to electrical converter, form an overlapping frequency response, and thereby a

broadband response. The method requires a summation of the outputs from the differently tuned cantilevers. These systems have the advantages of being easy to analyse.

It is relatively easy to obtain the desired bandwidth, when designing such a harvester. However, the output waveforms of piezoelectric generators are AC and not necessarily in phase when excited by a single frequency. Connecting the outputs of the piezoelectric materials in series or parallel will ensure energy flows between piezoelectric devices producing less than ideal system efficiency.

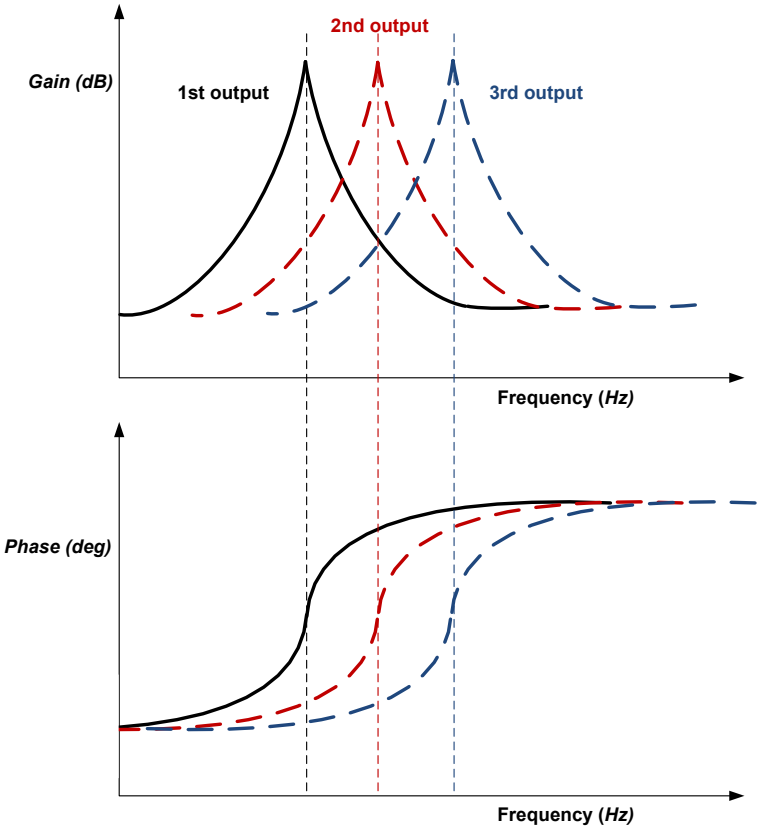

Figure 2.27: Estimated several cantilever energy harvester electrical outputs

Consider a harvester comprised of several individual cantilevers, each resonant at a slightly different frequency. When excited at a single frequency between the lowest and highest cantilever resonant frequencies, the voltages produced by each cantilever will have different amplitudes and different phases, see Figure 2.27. For those cantilevers with resonant frequencies higher than that of the excitation, the voltage

will lag the excitation, by a relatively small angle less than 90°, whereas for cantilevers with resonant frequencies below that of the excitation, the voltage will lag the excitation by an angle greater than 90°. If the electrical outputs are simply connected together, in series or parallel, phase cancellation will occur and the output voltage and power will be diminished.

Hence, simply connecting the piezoelectric outputs in series or parallel will not produce maximum output power. To overcome this problem, the output from each piezoelectric device should be rectified first before the outputs are summated. However, the rectification process adds cost, complexity and inefficiency, and given the low output voltages that may be produced with a low ambient excitation, may cancel out any benefits gained from adding after the rectification process. Furthermore, the cost of a harvester comprised of several cantilevers is high due to the number of piezoelectric devices used. Thus what is needed is a system that can provide wide band behavior at low cost.

Thus for optimum output power it is best to efficiently rectify the piezoelectric device output voltages before adding them together. For a harvester using around 20 or more beams as in Shahruz's work, over 20 efficient rectification circuits would be needed. There are some low power rectification circuits available in recent years [132], however a single rectification circuit will always hold its advantages over a large number of rectifiers. Piezoelectric devices have low output power, up to a few milli watts, and the designer must ensure that components used for rectification circuits do not overturn the gain in output power due to the rectification process.

However, to have say 20 cantilevers beams for the energy harvester will add 20 times to the cost of piezoelectric material and will add wiring cost. This can make the harvester expensive to manufacture.

Another method of widening the bandwidth is to use nonlinear generators and forced vibration [118-123]. Such solutions typically use a heavy proof mass, so that the natural resonance of the beam can be ignored. The devices operate in their off resonance region, and will always be able to respond to the excitation especially at

low frequencies. However such methods also produce a limited movement and power output which reduce the power density, and are also complex in design. Hence such methods are not yet feasible for wide band energy harvesting.

The second main category that has been intensively investigated is to use mechanical tuning. Such systems use stiffness tuning of the cantilever, either by moving the tip mass of the cantilever or by altering the force or preload acting on it. Other mechanical tuning methods include changing the centre of gravity of the cantilevers [125], using magnetic forces [124, 128] and straining the mechanical structure [126]. A method using a mechanical stopper has been investigated by Soliman et al [127]. This method is relatively easy to implement, but could decrease the amount of output power due to a decreased active area of piezoelectric material. Also in Soliman's paper the stopper was adjusted manually, and therefore it is unfeasible to use in practical applications where accessibility of the device is limited. Automatic tuning on the other hand would require a complex control system which consumes a relatively large amount of power, an amount which the energy harvester simply cannot supply [133].

Such devices have the advantages that for a certain excitation frequency, the device can be tuned to extract maximum energy from its input over a reasonable frequency range. However, such methods in general have high damping and are difficult to implement as they cannot be tuned while operating.

The last category to be considered is electrical tuning [134-139]. This is normally done by connecting a shunt external inductor across the harvester's output terminals to alter the cantilever's resonance [7, 110, 137, 140-146]. The method is more useful for application in vibration absorbers. However there is not yet an efficient solution to achieve this effect. A detailed review and analysis of the technique is given in Chapter 5.

2.6 Conclusion

This chapter has described a cantilever energy harvester and the researches undertaken on multiple resonant frequency energy harvesting.

Section 2.2 described a Rayleigh-Ritz study of a cantilever system subject to transverse vibration. Such a system has been widely investigated since it is the standard type of piezoelectric energy harvester. The cantilever structure allows the energy harvester to efficiently harvest energy at a specific resonant frequency, however for frequencies away from its resonance frequencies, the device is inefficient. The transverse vibration analysis was followed by a study of piezoelectric electromechanical coefficients in Section 2.3, in which the piezoelectric voltage coefficient g_{ij} was described. A summary is given in Section 2.4.

Section 2.5.1 gave a review of research towards multiple or tunable frequency energy harvesters, and a discussion of the problems that proposed designs have was given in Section 2.5.2. From the literature review, it was found that most researchers used multiple cantilevers to harvest energy over several frequencies, while others had investigated methods of altering the stiffness to change the resonant frequency of the device. The main difficulties of such solutions are that the piezoelectric materials are inefficient when connected directly together without rectification circuits and that in any case such electronic rectifiers consume energy. For stiffness tuning, the frequency cannot be altered automatically without a complex control algorithm and expand its use of energy in an actuator, and use of manual frequency tuning is unfeasible.

To summarise the problems discussed in Section 2.5.2, an ideal wide band piezoelectric harvester should not introduce an excessive amount of damping, should be cheap to manufacture, have simple electronic circuits to keep losses within the system to a minimum, should be easy to configure and scalable to suit different

applications. It was decided by the author that a particular form of multiresonant structure may suit these conditions. The structure is described in the next chapter.

Chapter 3 :

Mathematical Derivation and Simulation of Multiresonant Energy Harvester

3.1 Introduction to Proposed Multiresonant Beam Design

To achieve a wider piezoelectric energy harvester bandwidth, a multiresonant beam structure is proposed, as shown in Figure 3.1. The structure comprises a clamped-clamped beam which is accelerated equally at its clamped ends due to the ambient vibration. The beam supports several small cantilevers, each of which is tuned to a different frequency [48].

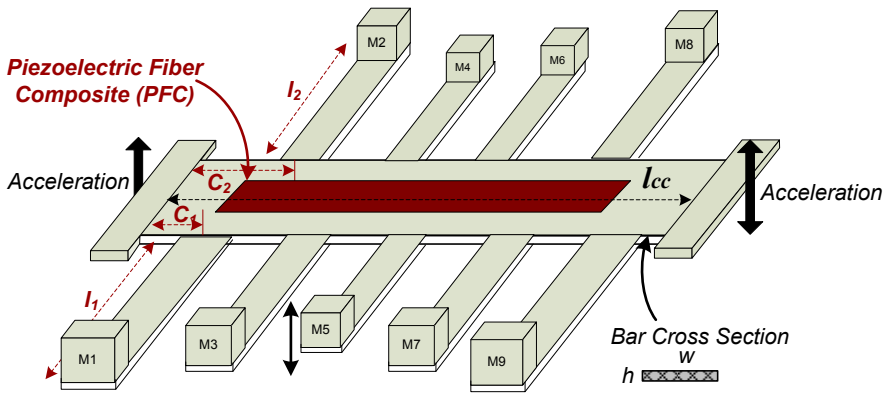

Figure 3.1: Proposed multiresonant beam structure

The system has therefore many resonant frequencies due to the many small cantilevers. The strains produced by the cantilevers when excited at their resonant frequencies by the ambient vibration are transferred to the clamped-clamped beam,

and converted to electrical form by a single PFC, which is mounted upon the clamped-clamped beam.

The resonant frequency of a cantilever depends primarily upon its stiffness and proof mass, therefore by adjusting one or both of these the cantilevers' resonant frequencies can be altered. As the cantilevers flex, they induce heave and torsion (see Figure 3.2) in the clamped-clamped beam, both of which will create voltages across the PFC.

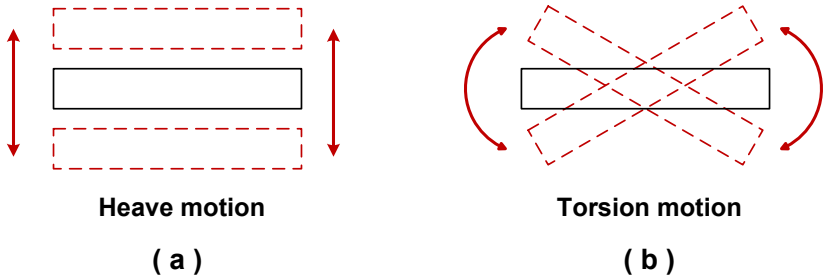

Figure 3.2: End view of a cantilever beam

Figure 3.2 gives the end view of a cantilever beam at their heave and torsion vibration motion. Torsion vibration can be understood as the amount of vibration in twist for a cantilever system. Although the excitation force is assumed to be in the transverse direction only, since the clamped-clamped beam has several cantilevers with different bending motions, the clamped-clamped beam will thus be bent and also twisted by the cantilevers. Torsion vibrations will add more strains onto the piezoelectric material attached to the clamped-clamped beam. The response of the PFC to the vibration acceleration at the end supports should thus have a multitude of resonance peaks, if the parameters are chosen appropriately.

Whereas a single cantilever system, as used for energy harvesting by previous researchers, has only one resonance peak at the fundamental mode, the proposed design should work over a wider bandwidth, enabling energy to be harvested over a wide spectrum. In addition, the design has only one PFC device, mounted on the clamped-clamped beam. This eliminates the need for electrical connections, as

would be required in harvesters comprising a multiplicity of individual cantilevers, reduces construction cost and has the benefit of simplicity.

Four of the several possible designs of the multiresonant structure were considered for suitability as shown in Figure 3.3. The cantilevers could be mounted on opposing sides of the beam, or on the same side, and the cantilevers can also have different lengths and different proof masses. Consequently the beam will be subjected to several sources of strain and the PFC will be subjected to several different resonances. Peak amplitudes of strain will occur at the clamped ends of the beam and also along the beam. By attaching the PFC on the beam so as to cover locations where strain peaks occur, i.e. where the cantilevers attach to the beam, so vibration energy can be harvested effectively. This is due to the multiresonant beam will not only be able to harvest energy from bending (heave) motion, but also from torsion.

As the PFC device is more effective in converting torsion motion to electricity than heave motion to electricity, so the device may be more effective than the multiple cantilever harvesters proposed by Shahruz [84, 85], which only harvest heave motion.

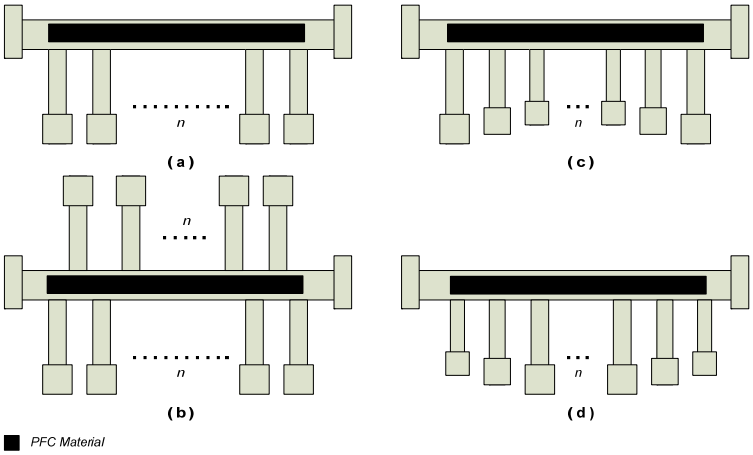

Figure 3.3: Multiple cantilever structures with PFCs
(a) cantilevers mounted on one side of the beam (b) cantilevers mounted at both sides of the beam (c) increasing cantilever lengths from middle to end of beam (d) decreasing cantilever lengths from middle to end of beam

An attractive concept is to have several shorter PFCs, placed on the clamped-clamped beam at the attachment points of the cantilevers. This approach can eliminate the mechanical phase cancellation (anti-resonance) problem described in Chapter 2, but would require summation using electronics and would add cost. For this reason the approach using a single PFC on the clamped-clamped beam is preferred.

The next section describes a Rayleigh-Ritz analysis of this topology, which was developed so that an optimised mechanical system could be created.

3.2 Rayleigh-Ritz Approximation of Multiresonant Beam Model

To determine if the concept is valid, a Rayleigh-Ritz mechanical analysis similar to that described in Chapter 2 for the analysis of a cantilever energy harvester, was carried out by author, the analysis of this proposed model has been published in [48, 90].

Since the cantilever beams can be mounted on either side of the main beam, the analysis started with a clamped-clamped beam having two cantilevers, one on each side as shown in Figure 3.4. The clamped-clamped beam is assumed to have only two mode shapes.

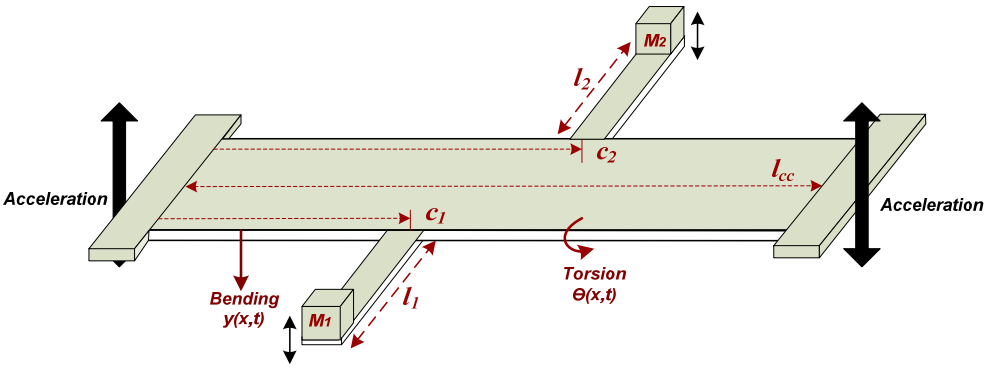

Figure 3.4: Clamped-clamped beam with two cantilevers

Further to the analysis of the standard cantilever in Chapter 2, torsional vibration of the beam is also considered. Figure 3.4 shows two cantilevers attached to the main beam at distances c_1 and c_2 from the left clamped beam end. M_1 and M_2 are the effective point masses, l_1 and l_2 are the cantilever lengths, and l_{cc} is the clamped-clamped beam length. Two mode shapes for bending $y(x,t)$ and torsion $\theta(x,t)$ of the beam, as given in equations (3.1) and (3.2), are assumed.

$$y(x,t) = q_0(t)\phi_0(x) + q_1(t)\phi_1(x) + q_2(t)\phi_2(x) \tag{3.1}$$

$$\theta(x,t) = b_1(t)\psi_1(x) + b_2(t)\psi_2(x) \tag{3.2}$$

In (3.1), $q_0(t)\phi_0(x)$ is the input acceleration and the other terms on the right hand side are the responses due to the first two modes. In (3.2), the two terms on the right hand side are the responses due to the first two torsional modes.

According to Warburton [88], the frequency equation for a clamped-clamped beam is

$$\cos \lambda_i l_{cc} \cosh \lambda_i l_{cc} - 1 = 0 \tag{3.3}$$

where the roots are $\lambda_1 l_{cc} = 4.730$, $\lambda_2 l_{cc} = 7.853$, $\lambda_i l_{cc} \approx (i + \frac{1}{2})\pi$ for $i \geq 3$.

Figure 3.5 shows the different mode shape forms for the clamped-clamped beam for bending only, as an example. In equations (3.4) and (3.5), $\phi_i(x)$ and $\psi_i(x)$ are the known shape functions, for a clamped-clamped beam, given by Blevins [89].

$$\phi_i(x) = \cosh\left(\frac{\lambda_i x}{l_{cc}}\right) - \cos\left(\frac{\lambda_i x}{l_{cc}}\right) - \left(\frac{\cosh \lambda_i - \cos \lambda_i}{\sinh \lambda_i - \sin \lambda_i}\right)\left(\sinh\left(\frac{\lambda_i x}{l_{cc}}\right) - \sin\left(\frac{\lambda_i x}{l_{cc}}\right)\right) \tag{3.4}$$

$$\psi_i(x) = \sin\left(\frac{i\pi x}{l_{cc}}\right) \tag{3.5}$$

where λ_i are the roots of the frequency equations as in (3.3), x is the positions along the beam length and l_{cc} is the beam length.

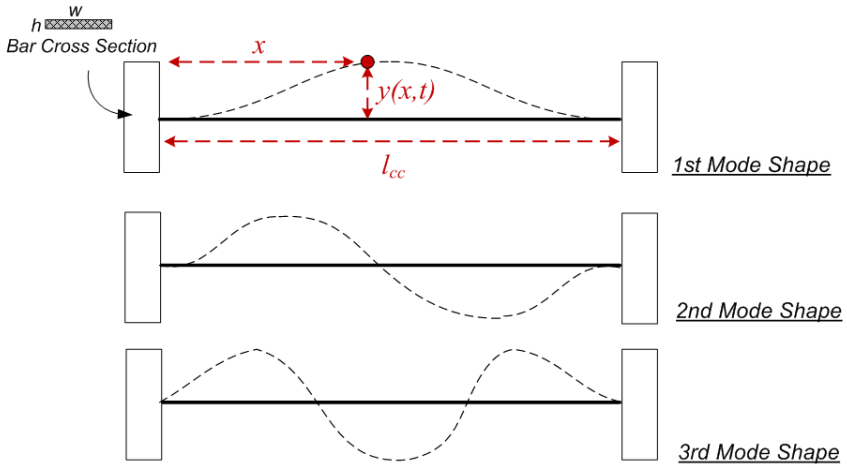

Figure 3.5: Clamped-clamped beam mode shapes

The strain energy U for the system is proposed by the author as in Equation (3.6),

$$U(t) = \frac{1}{2}\int_0^{l_{cc}} EI\ddot{y}^2(x,t)dx + \frac{1}{2}\int_0^{l_{cc}} GJ\dot{\theta}^2(x,t)dx + \frac{1}{2}\sum_{j=1}^{2} k_j y_j^{\,2} \tag{3.6}$$

where k_j is the stiffness of a cantilever, E is the material's Young's modulus, I is the second moment of inertia and the product EI is flexural rigidity. G is the material shear modulus, J is the section torsion constant and the product GJ is the torsional rigidity. Where $\ddot{y}(x,t)$ and $\dot{\theta}(x,t)$ are the assumed shape functions shown in (3.8) and (3.9).

The first term on the right hand side of (3.6) represents bending strain energy for the clamped-clamped beam, the second term is torsional strain energy due to twisting of the clamped-clamped beam and the third term is strain energy within the cantilevers mounted on the beam.

The kinetic energy equation of the system proposed by the author is given by (3.7),

$$T(t)=\frac{1}{2}\int_0^{l_{cc}} m\dot{y}^2(x,t)dx+\frac{1}{2}\int_0^{l_{cc}} \gamma\dot{\theta}^2(x,t)dx \\ +\frac{1}{2}\sum_{j=1,3,5}^{n} M_j\left[\dot{y}_j+\dot{y}(c_j)+l_j\dot{\theta}(c_j)\right]^2+\frac{1}{2}\sum_{j=2,4,6}^{n} M_j\left[\dot{y}_j+\dot{y}(c_j)-l_j\dot{\theta}(c_j)\right]^2 \tag{3.7}$$

where n is the total number of cantilevers, m is mass per unit length, M_j is the effective tip mass of each cantilever, γ is the mass moment of inertia, in twist, per unit length and c_j is the cantilever location along the main beam. The cantilevers have been divided into odd and even numbers, so that the system behaviour can be more easily studied. On the right hand side of equation (3.7), the first term corresponds to the kinetic energy of bending, the second term is kinetic energy due to beam torsion, the third term corresponds to kinetic energy of odd numbered cantilevers and the fourth term corresponds to kinetic energy of even numbered cantilevers.

Differentiating equation (3.1) twice with respect to x produces (3.8), and differentiating (3.2) once with respect to x produces (3.9)

$$\ddot{y}(x,t)=q_0(t)\ddot{\phi}_0(x)+q_1(t)\ddot{\phi}_1(x)+q_2(t)\ddot{\phi}_2(x) \tag{3.8}$$

$$\dot{\theta}(x,t)=b_1(t)\dot{\psi}_1(x)+b_2(t)\dot{\psi}_2(x) \tag{3.9}$$

(3.8) is the assumed shape function for bending and (3.9) is the assumed shape function for torsion.

By substituting (3.8) and (3.9) into (3.6), the system strain energy equation becomes:

$$U = \frac{1}{2}\int_0^{l_{cc}} EI\left[q_0(t)\ddot{\phi}_0(x) + q_1(t)\ddot{\phi}_1(x) + q_2(t)\ddot{\phi}_2(x)\right]^2 dx + \frac{1}{2}\int_0^{l_{cc}} GJ\left[b_1(t)\dot{\psi}_1(x) + b_2(t)\dot{\psi}_2(x)\right]^2 dx + \frac{1}{2}\sum_{j=1}^{2} k_j y_j{}^2 \tag{3.10}$$

Differentiating equation (3.1) once with respect to *t* this time gives:

$$\dot{y}(x,t) = \dot{q}_0(t)\phi_0(x) + \dot{q}_1(t)\phi_1(x) + \dot{q}_2(t)\phi_2(x) \tag{3.11}$$

and differentiating (3.2) once with respect to *t* gives

$$\dot{\theta}(x,t) = \dot{b}_1(t)\psi_1(x) + \dot{b}_2(t)\psi_2(x) \tag{3.12}$$

Now substituting equation (3.11) and (3.12) into (3.7) yields the kinetic energy equation (3.13), for the first two modes.

$$\begin{aligned} T = {} & \frac{1}{2}\int_0^{l_{cc}} m\left[\dot{q}_0(t)\phi_0(x) + \dot{q}_1(t)\phi_1(x) + \dot{q}_2(t)\phi_2(x)\right]^2 dx \\ & + \frac{1}{2}\int_0^{l_{cc}} \gamma\left[\dot{b}_1(t)\psi_1(x) + \dot{b}_2(t)\psi_2(x)\right]^2 dx \\ & + \frac{1}{2}M_1\left[\dot{y}_1 + \dot{q}_0(t)\phi_0(c_1) + \dot{q}_1(t)\phi_1(c_1) + \dot{q}_2(t)\phi_2(c_1) + l_1\dot{b}_1(t)\psi_1(c_1) + l_1\dot{b}_2(t)\psi_2(c_1)\right]^2 \\ & + \frac{1}{2}M_2\left[(\dot{y}_2 + \dot{q}_0(t)\phi_0(c_2) + \dot{q}_1(t)\phi_1(c_2) + \dot{q}_2(t)\phi_2(c_2) - l_2\dot{b}_1(t)\psi_1(c_1) - l_2\dot{b}_2(t)\psi_2(c_2)\right]^2 \end{aligned} \tag{3.13}$$

To provide the equation of motion using strain energy *U* and kinetic energy *T*, the Lagrange equation given by [89]:

$$\frac{d}{dt}\left(\frac{\partial T}{\partial \dot{q}_j}\right) - \frac{\partial T}{\partial q_j} + \frac{\partial \xi}{\partial \dot{q}_j} + \frac{\partial U}{\partial q_j} = Q_j = \frac{\partial(\delta W)}{\partial(\delta q_j)} \text{ for } j = 1,2...n \tag{3.14}$$

This equation is used in terms of the generalized coordinate q_j, where ξ is the dissipative function or damper contribution, Q_j is the generalized force, δW is the incremental work done, and δq_j is virtual displacement.

Assume the system is under free vibration, therefore the incremental work done term δW in (3.14) is zero, and derivations for the other terms in the equation are required. After determining each term in (3.14) by substituting equations (3.10) and (3.13), the Lagrange equation gives the equations of motion in matrix form as:

$$\tilde{M} \times \begin{bmatrix} \ddot{q}_0(t) \\ \ddot{q}_1(t) \\ \ddot{q}_2(t) \\ \ddot{b}_1(t) \\ \ddot{b}_2(t) \\ \ddot{y}_1 \\ \ddot{y}_2 \end{bmatrix} + \tilde{C} \times \begin{bmatrix} \dot{q}_0(t) \\ \dot{q}_1(t) \\ \dot{q}_2(t) \\ \dot{b}_1(t) \\ \dot{b}_2(t) \\ \dot{y}_1 \\ \dot{y}_2 \end{bmatrix} + \tilde{K} \times \begin{bmatrix} q_0(t) \\ q_1(t) \\ q_2(t) \\ b_1(t) \\ b_2(t) \\ y_1 \\ y_2 \end{bmatrix} = 0 \tag{3.15}$$

where $\tilde{M}$, $\tilde{K}$ and $\tilde{C}$ are the *7x7* matrices of effective beam mass, stiffness and damping. Assuming constant damping, each row and column of matrices $\tilde{M}$, $\tilde{K}$ can be filled, where q_0, q_1, q_2, b_1 and b_2 are the variables in the strain energy and kinetic energy equations (3.10) and (3.13).

Therefore, the multiresonant system transmissibility (ratio of output acceleration to the input excitation) can be predicted using the mass and stiffness matrices derived. Equation (3.15) can be rewritten as (3.16)

$$\begin{bmatrix} \tilde{M}_{00} & \tilde{M}_{01} \\ \tilde{M}_{10} & \tilde{M}_{11} \end{bmatrix} \times \begin{bmatrix} \ddot{q}_0(t) \\ \ddot{q}_1(t) \\ \ddot{q}_2(t) \\ \ddot{b}_1(t) \\ \ddot{b}_2(t) \\ \ddot{y}_1 \\ \ddot{y}_2 \end{bmatrix} + \begin{bmatrix} 0 & 0 \\ 0 & \tilde{K}_{11} \end{bmatrix} \times \begin{bmatrix} q_0(t) \\ q_1(t) \\ q_2(t) \\ b_1(t) \\ b_2(t) \\ y_1 \\ y_2 \end{bmatrix} = 0 \tag{3.16}$$

Matrices $\tilde{M}_{00}$, $\tilde{M}_{01}$ and $\tilde{M}_{10}$ are related to the excitation $\ddot{q}_0(t)$, thus $\tilde{M}_{00}$ is a *1x1* matrix, $\tilde{M}_{01}$ is a *6x1* matrix, $\tilde{M}_{10}$ is a *1x6* matrix and $\tilde{M}_{11}$ is a *6x6* matrix. There are no corresponding terms in the stiffness matrix $\tilde{K}$ relating to the excitation $\ddot{q}_0$, therefore, the first row and column of $\tilde{K}$ are zero vectors. The matrices $\tilde{M}_{00}$, $\tilde{M}_{01}$, $\tilde{M}_{10}$, $\tilde{M}_{11}$, $\tilde{K}_{11}$ are shown in equations (3.17-3.21):

$$\tilde{M}_{00}=\left[\int_0^{l_{cc}} M\phi_0^2(x)dx + m_1\phi_0^2(c_1) + m_2\phi_{02}^2(c_2)\right] \tag{3.17}$$

$$\tilde{M}_{01}=\begin{bmatrix} \int_0^{l_{cc}} M\phi_0(x)\phi_1(x)dx + m_1\phi_0(c_1)\phi_1(c_1) + m_2\phi_0(c_2)\phi_1(c_2) \\ \int_0^{l_{cc}} M\phi_0(x)\phi_2(x)dx + m_1\phi_0(c_1)\phi_2(c_1) + m_2\phi_0(c_2)\phi_2(c_2) \\ m_1l_1\phi_0(c_1)\psi_1(c_1) - m_2l_2\phi_0(c_2)\psi_1(c_2) \\ m_1l_1\phi_0(c_1)\psi_2(c_1) - m_2l_2\phi_0(c_2)\psi_2(c_2) \\ m_1\phi_0(c_1) \\ m_2\phi_0(c_2) \end{bmatrix}^T \tag{3.18}$$

$$\tilde{M}_{10}=\begin{bmatrix} \int_0^{l_{cc}} M\phi_0(x)\phi_1(x)dx + m_1\phi_0(c_1)\phi_1(c_1) + m_2\phi_0(c_2)\phi_1(c_2) \\ \int_0^{l_{cc}} M\phi_0(x)\phi_2(x)dx + m_1\phi_0(c_1)\phi_2(c_1) + m_2\phi_0(c_2)\phi_2(c_2) \\ m_1l_1\phi_0(c_1)\psi_1(c_1) - m_2l_2\phi_0(c_2)\psi_1(c_2) \\ m_1l_1\phi_0(c_1)\psi_2(c_1) - m_2l_2\phi_0(c_2)\psi_2(c_2) \\ m_1\phi_0(c_1) \\ m_2\phi_0(c_2) \end{bmatrix} \tag{3.19}$$

$$\tilde{M}_{11}=\begin{bmatrix} \tilde{M}_{11}(11) & \tilde{M}_{11}(12) & \tilde{M}_{11}(13) \\ \tilde{M}_{11}(21) & \tilde{M}_{11}(22) & \tilde{M}_{11}(23) \\ \tilde{M}_{11}(31) & \tilde{M}_{11}(32) & \tilde{M}_{11}(33) \end{bmatrix} \tag{3.20}$$

The sub-matrices of equation (3.20) are given in Appendix B, and $\tilde{K}_{11}$ is:

$$\tilde{K}_{11}=\begin{bmatrix} \int_0^{l_{cc}} EI\phi_1''^2(x)dx & \int_0^{l_{cc}} EI\phi_1''(x)\phi_2''(x)dx & 0 & 0 & 0 & 0 \\ \int_0^{l_{cc}} EI\phi_1''(x)\phi_2''(x)dx & \int_0^{l_{cc}} EI\phi_2''^2(x)dx & 0 & 0 & 0 & 0 \\ 0 & 0 & \int_0^{l_{cc}} GJ\psi_1'^2(x)dx & \int_0^{l_{cc}} GJ\psi_1(x)\psi_2(x)dx & 0 & 0 \\ 0 & 0 & \int_0^{l_{cc}} GJ\psi_1(x)\psi_2(x)dx & \int_0^{l_{cc}} GJ\psi_2'^2(x)dx & 0 & 0 \\ 0 & 0 & 0 & 0 & k_1 & 0 \\ 0 & 0 & 0 & 0 & 0 & k_2 \end{bmatrix} \tag{3.21}$$

Equation (3.16) can be rewritten as

$$\tilde{M}_{00}\underline{\ddot{q}}_0 + \tilde{M}_{01}\underline{\ddot{q}}_{00} = F \tag{3.22}$$

$$\tilde{M}_{10}\underline{\ddot{q}}_0 + \tilde{M}_{11}\underline{\ddot{q}}_{00} + \tilde{K}_{11}\underline{q}_{00} = 0 \tag{3.23}$$

where F is the input force on the structure. Since $\underline{\ddot{q}}_0$ is the excitation, therefore equation (3.22) is a force equation which generates $\underline{\ddot{q}}_0$, and equation (3.23) finds $\underline{q}_{00}$ representing the response due to excitation $\underline{\ddot{q}}_0$, where $\underline{q}_{00}$ is equivalent to the response vector shown in (3.24).

$$\underline{q}_{00}=\begin{bmatrix} q_1 & q_2 & b_1 & b_2 & y_1 & y_2 \end{bmatrix}^T \tag{3.24}$$

Assuming harmonic excitation for $\underline{\ddot{q}}_0$ and $\underline{q}_{00}$, that is

$$\underline{\ddot{q}}_0 = \ddot{A}_0 e^{i\omega t} \tag{3.25}$$

Since $\ddot{A}_{00} = -\omega^2 A_{00}$, thus:

$$\underline{q}_{00} = \underline{A}_{00} e^{i\omega t} \tag{3.26}$$

Substituting (3.25) and (3.26) into (3.22) and (3.23), yields Equations (3.27-3.28)

$$\left(\tilde{K}_{11} - \omega^2 \tilde{M}_{11}\right) \underline{A}_{00} = -\tilde{M}_{10} \ddot{A}_0 \tag{3.27}$$

Thus:

$$\ddot{\underline{A}}_{00} = \omega^2 \left(\tilde{K}_{11} - \omega^2 \tilde{M}_{11}\right)^{-1} \tilde{M}_{10} \ddot{A}_0 \tag{3.28}$$

Assuming overall system output is represented by $\ddot{w}$ and let $\ddot{w}(d_j) = \ddot{W}_j e^{i\omega t}$, the expression for $\ddot{w}(d_j)$ is:

$$\ddot{w}(d_j) = \ddot{q}_0 \phi_0(d_j) + \ddot{q}_1 \phi_1(d_j) + \ddot{q}_2 \phi_2(d_j) + b_1 \psi_1(d_j) + b_2 \psi_2(d_j) ... \tag{3.29}$$

where *j=1,2....*, d_j is the measurement location on the beam. On the right hand side of (3.29) the first term corresponds to the input excitation, and the second and third terms correspond to the bending responses due to the first and second mode shapes. The fourth and fifth terms correspond to torsion responses due to the first and second mode shapes.

Assuming the two mode shapes $\tilde{\phi}$ along the beam for locations of measurement, then from equations (3.28) and (3.29):

$$\underline{\ddot{W}} = \begin{bmatrix} \phi_0(d_1) \\ \phi_0(d_2) \end{bmatrix} \cdot \ddot{A}_0 + \tilde{\phi} \cdot \ddot{\underline{A}}_{00} \tag{3.30}$$

Thus,

$$\begin{Bmatrix} \ddot{W}_1 \\ \ddot{W}_2 \end{Bmatrix} = \begin{bmatrix} \phi_0(d_1) \\ \phi_0(d_2) \end{bmatrix} \times \ddot{A}_0 + \begin{bmatrix} \phi_1(d_1) & \phi_2(d_2) & 0 & 0 & 0 & 0 \\ \phi_1(d_1) & \phi_2(d_2) & 0 & 0 & 0 & 0 \end{bmatrix} \times \begin{bmatrix} \ddot{A}_1 \\ \ddot{A}_2 \\ \ddot{B}_1 \\ \ddot{B}_2 \\ \ddot{Y}_1 \\ \ddot{Y}_2 \end{bmatrix} \tag{3.31}$$

where $\begin{bmatrix} \phi_0(d_1) \\ \phi_0(d_2) \end{bmatrix}$ is the excitation force matrix at the main beam clamped ends. By substituting equation (3.28) for $\underline{\ddot{A}}_{00}$, equation (3.30) for the output response $\underline{\ddot{W}}$ becomes:

$$\underline{\ddot{W}} = \left\{ \begin{bmatrix} \phi_0(d_1) \\ \phi_0(d_2) \end{bmatrix} + \omega^2 \tilde{\phi} \left(K_{11} - \omega^2 M_{11} \right)^{-1} M_{10} \right\} \ddot{A}_0 \tag{3.32}$$

Therefore, the transmissibility of the multiple cantilever system is:

$$\underline{T} = \frac{\underline{\ddot{W}}}{\ddot{A}_0} = \frac{Output}{Input} = \begin{bmatrix} \phi_0(d_1) \\ \phi_0(d_2) \end{bmatrix} + \omega^2 \tilde{\phi} \left(K_{11} - \omega^2 M_{11} \right)^{-1} \cdot M_{10} \tag{3.33}$$

The analysis can also be applied to clamped-clamped beam structures where there are more than two added cantilevers, however as a consequence there is an expanded mass matrix $\tilde{M}$ and stiffness matrix $\tilde{K}$.

3.3 Summary

In this section, a Rayleigh-Ritz model design of the proposed multiresonant structure was described, the analysis describes the fundamental equations to be used in a multiresonant system simulation. The mathematical model built using these equations allows the main beam dimensions, side cantilever stiffness and the cantilever locations to be adjusted to provide the optimum wide band frequency response. The mathematical model constructed has significant advantages over a finite element model in terms of simulation time and flexibility. It enables the possibility of rapid system self optimization.

3.4 Introduction to Simulation Process

Following the Rayleigh-Ritz analysis of a multiresonant system, the next stage of system validation is to implement the equations obtained in a simulation package. Matlab was chosen for the purpose. The program code was written so that strain and kinetic energy matrices are obtained from which mass, stiffness and damping matrices, are generated, to predict transmissibility of the multiresonant system.

A flow chart of the simulation process is shown in Figure 3.6. The first stage of the simulation is to define dimensions, for both main clamped-clamped beam and side cantilevers. The second stage is to decide the input acceleration amplitude to the system, the number of mode shapes to be considered and the locations where the side cantilevers are to be mounted. Because the transmissibility will vary along the main beam, the number of measurement points along the beam is defined at the third stage along with the damping ratio of the system. The damping of the system is assumed to be a function of beam stiffness and small, around 1% [84, 85, 93, 94]. The fourth stage of the simulation is to generate mass and stiffness matrices from the strain and stiffness equations derived in Section 3.2. The final stage is to calculate and plot the system transfer function and transmissibility for analysis.

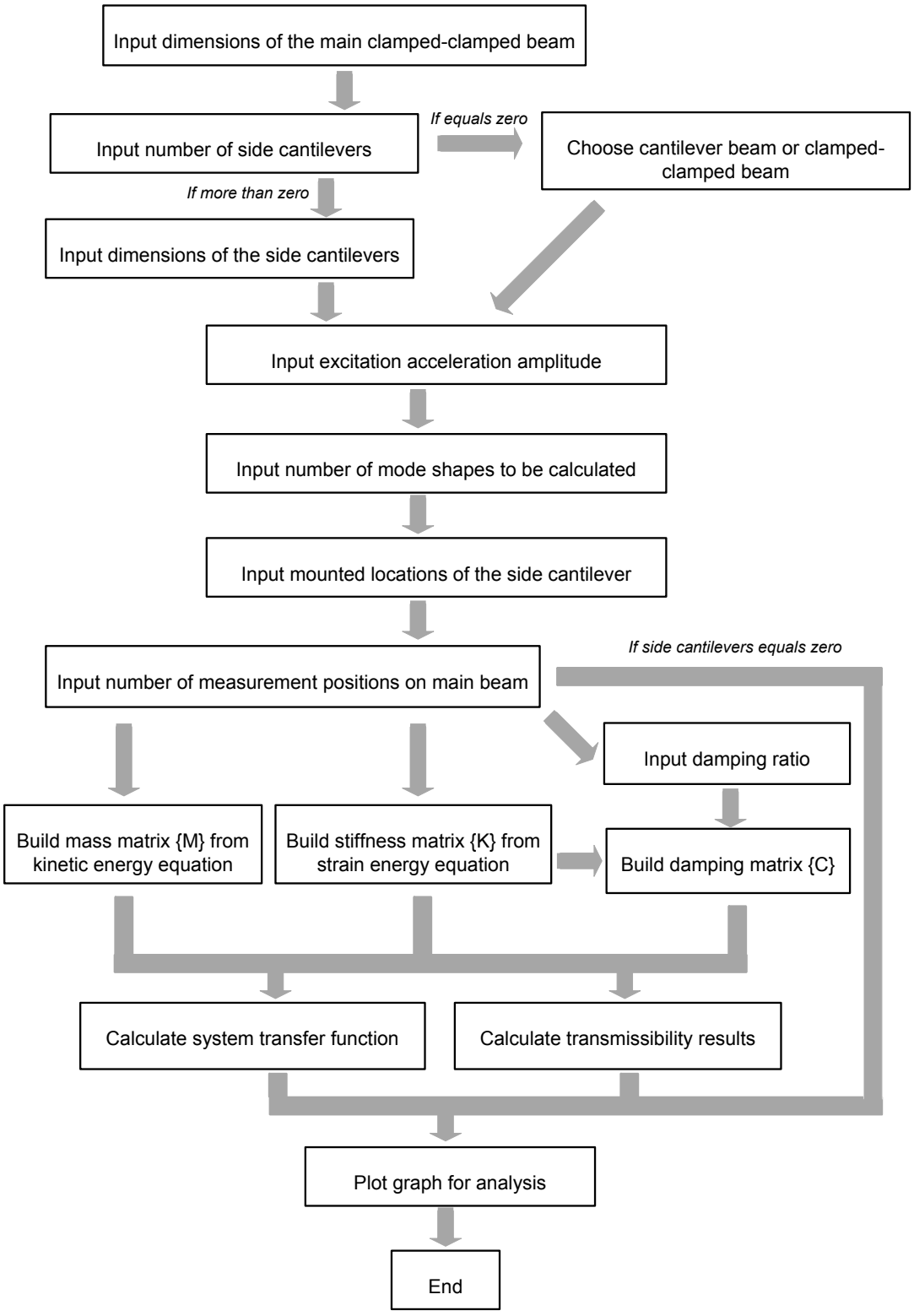

Figure 3.6: Flow chart of Matlab multiresonant beam simulation

3.5 Cantilever and Multiresonant Beam Mode Shape Test

In this section, the mode shape equations (2.37) and (3.4) for a cantilever beam and a clamped-clamped beam are plotted. This was achieved by calculating the deflection at 100 equally distributed locations along the beam length. The mode shapes $\tilde{y}_i(x)$ and $\phi_i(x)$ in equation (2.37) and (3.4) were normalised by calculating the response for various locations on the beam then dividing the response by the maximum response of $\tilde{y}_i(x)$ and $\phi_i(x)$ for each mode respectively.

3.5.1 Single Cantilever Mode Shape Test

For a cantilever beam, the first three mode shapes were calculated as shown in Figure 3.7. The clamped end of the cantilever is on the left hand side in these figures, and the right hand side is the free end of the cantilever. For the first mode shape shown in Figure 3.7, the greatest displacement occurs towards the free end of the cantilever. The displacement peaks occur at various locations along the beam for the second and third mode shapes. It can be seen that the first mode shape function always has the lowest resonant frequency. Normalising the response ensures that the free end of the cantilever is either at positive or negative unity.

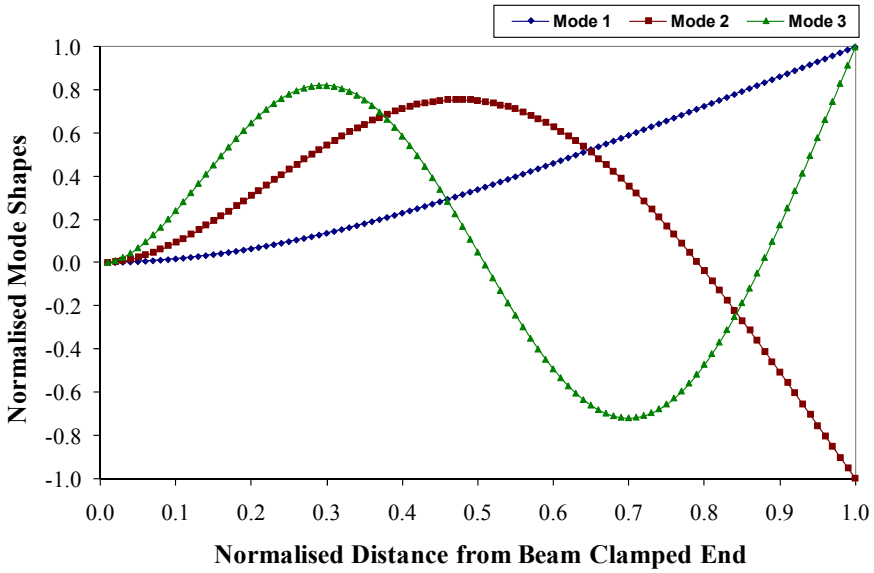

Figure 3.7: Normalised first three bending mode shapes of a cantilever beam

The calculated mode shapes are in general agreement with those calculated by Leissa et al [147](Figure 2) and the measurements presented by Jenkins et al [148](Figure 7). Higher mode shapes tend to have lower displacement amplitude, with the second and third modes having significantly lower amplitude than the first mode of vibration.

According to [149], the amplitude of cantilever displacement varies depending on the ratio between excitation frequency and fundamental resonant frequency. A displacement reduction is expected for mode shapes higher than the first. Using the equation given in [150], the maximum displacement of the first mode shape is approximately 13 times higher than the second mode, and 75 times higher than the third mode for a 8*cm* x 1*cm* x 0.1*cm* cantilever. Figure 3.8 gives the calculated beam displacement. The peak displacement of the first mode shape is estimated to be around 1*mm* which is close to that measured by S. O. Oyadiji [151], higher beam deflection occurs with a higher applied force. Calculations for a clamped-clamped beam mode shapes are given in the next section.

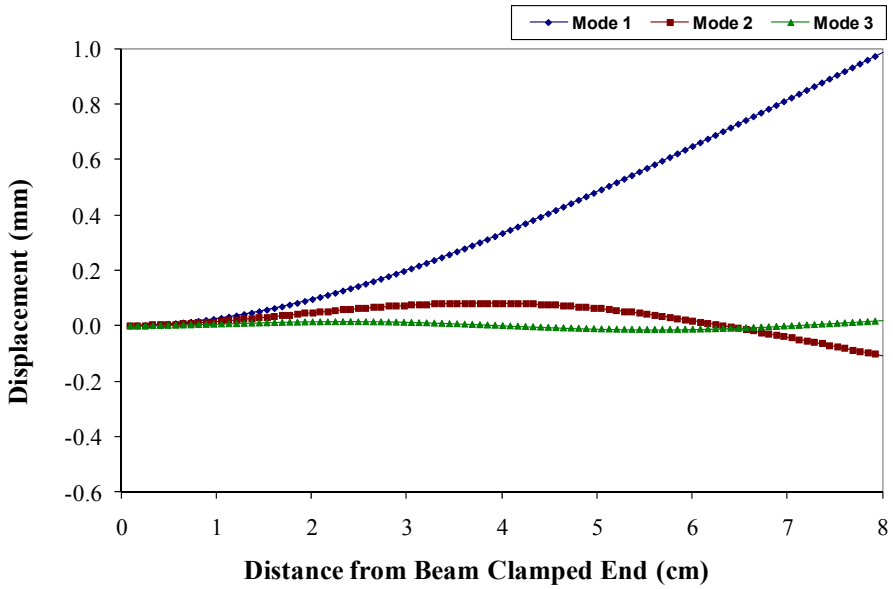

Figure 3.8: First three bending mode shapes of a cantilever beam

3.5.2 Clamped-Clamped Beam Mode Shape Test

The first three mode shapes of a clamped-clamped beam were also calculated, and the results are shown in Figure 3.9. It can be noted that for a clamped-clamped beam, the highest displacement of the first mode shape occurs at the middle of the beam. From the first three modes, it can be seen that the shapes are symmetrical for a clamped-clamped beam, and the amount of displacement is the same from either end of the clamped edge for each mode respectively, although not always in the same direction. The results are in general agreement with the mode shapes given by Blevins [89].

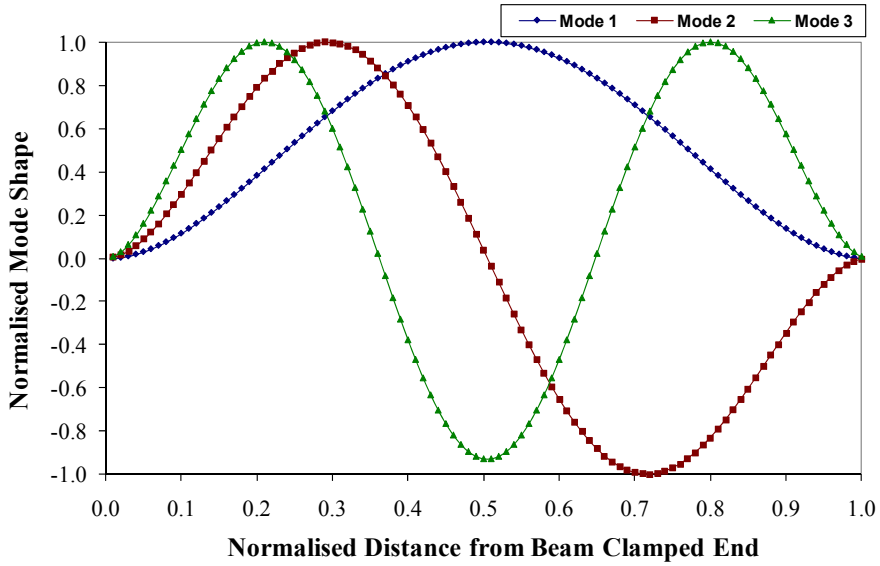

Figure 3.9: Normalised first three bending mode shapes of a clamped-clamped beam

In practice, the maximum displacement for the second and third mode shapes will be lower than that for the first mode of vibration. Figure 3.10 shows the calculated displacement for a 17*cm* x 2*cm* x 0.1*cm* clamped-clamped beam. The maximum displacement of the first mode shape is estimated to be around 0.1*mm* [151].

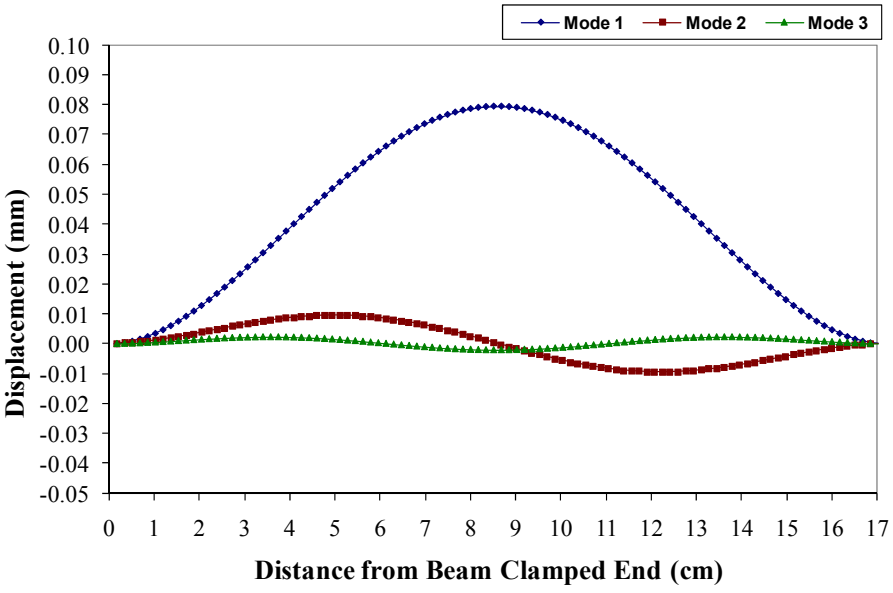

Figure 3.10: First three bending mode shapes of a clamped-clamped beam

3.6 Simulation Parameters and Initial Conditions

In Section 3.1 and 3.2, the dependency of the structures response upon the dimensions of the main clamped-clamped beam and the side cantilevers was discussed. It follows from this discussion that the dimensions, tip mass loading and boundary conditions of the beam and side cantilevers must be correctly specified if a multiresonant system with a designated frequency band is to be constructed.

The beam dimensions were chosen by using the beam's natural frequency equation (3.34)

$$f_n = \frac{\lambda_i^2}{2\pi L^2}\sqrt{\left(\frac{EI}{\rho A}\right)} \tag{3.34}$$

Where ρ is the material density of the beam, A is cross sectional area, L is the length of the beam, and I is the second moment of beam cross section area calculated by (3.35)

$$I = \frac{wh^3}{12} \tag{3.35}$$

In (3.35), w and h are the beam's width and thickness, see Figure 3.1. In the mode shape tables of [89, 102], a list of approximate resonant frequencies of the main clamped-clamped beam are given.

For a general vibration analysis, the first three mode shapes are usually considered to be the most influencing modes of vibration [14, 99-101, 113]. Investigation by the author of vibrations from several machines during an EU project, DYNAMITE, found that factory machines often produced vibrations around 50*Hz*, for this reason the first resonant frequencies of the cantilevers were chosen to be around 50*Hz*.

Ideally, the dimensions of the cantilevers should be kept small in comparison to the dimensions of the main beam, so that they will not significantly affect the main beam resonance. Figure 3.11 shows the parameters which can be adjusted during the design process, to achieve the required response. The side cantilevers can be mounted on either or both sides of the main beam. The spacing between side cantilevers can be adjusted so that they are close together, or equally spaced along the main beam, or asymmetrically distributed. Additionally, individual tip masses can be changed to modify the side cantilevers resonant frequencies. The tip masses used are all much greater than the mass of a side cantilever beam to ensure that the tip masses dominate the frequency equations [99-101, 113].

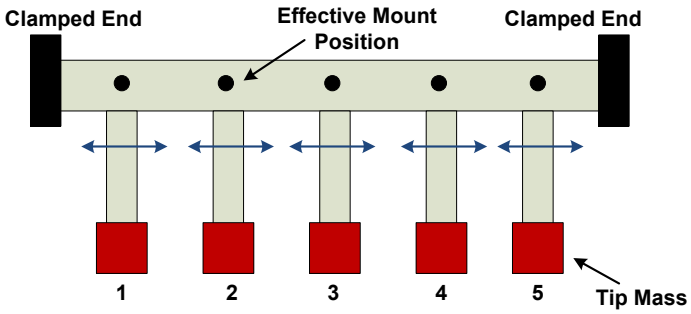

Figure 3.11: Simulation adjustable parameters of a multiresonant beam model

The first mode shapes of the side cantilevers and main beam are the most suitable for the proposed energy harvester, and were chosen so that their resonant frequencies are below $100Hz$. Higher resonance modes occur at higher frequencies, therefore only the first mode shapes were considered for this analysis to provide a better understanding of the system.

During testing an accelerometer is placed on the main beam, to measure the acceleration. The software allows the measurement position to be adjusted, so that the location of the best response can be found.

3.7 Multiresonant Beam Simulation Results

3.7.1 Simulation of Multiresonant Beam without Tip Masses

It was decided that the main beam would be 170*mm* long and 20*mm* wide, that the side cantilevers would be 80*mm* long and 10*mm* wide, and that the device would be constructed from 1mm thick stainless steel, as shown in Table 3.1. These dimensions are much bigger than those of other harvesters, to allow easy measurement, tuning and proof of principle. Since the energy harvester is linear, scaling to a smaller size can be done later, after proving the principle of operation.

Table 3.1: Geometric and material properties of multiresonant beam

	l (mm)	w (mm)	t (mm)	ρ (kg/m^{-3})	E (Gpa)
Clamped-Clamped Beam	170	20	1.0	7850	205
Cantilever 1	80	10	1.0	7850	205
Cantilever 2	80	10	1.0	7850	205
Cantilever 3	80	10	1.0	7850	205
Cantilever 4	80	10	1.0	7850	205
Cantilever 5	80	10	1.0	7850	205

The cantilevers are effectively mounted at 25*mm*, 55*mm*, 85*mm*, 115*mm* and 145*mm* respectively along the beam, and are thus equally distributed.

The predicted transmissibility curve for the beam using the Rayleigh-Ritz analysis without tip masses is shown in Figure 3.12. Resonance peaks occur over a frequency range of approximately 50*Hz* to 80*Hz*, due to the first modes of the five side cantilevers. The peak at 170*Hz* is due to the clamped-clamped beams first bending mode. 11 equally placed measurement positions were used along the beam, Figures 3.12 and 3.13 show transmissibility at positions 1, 3, 5 and 8.

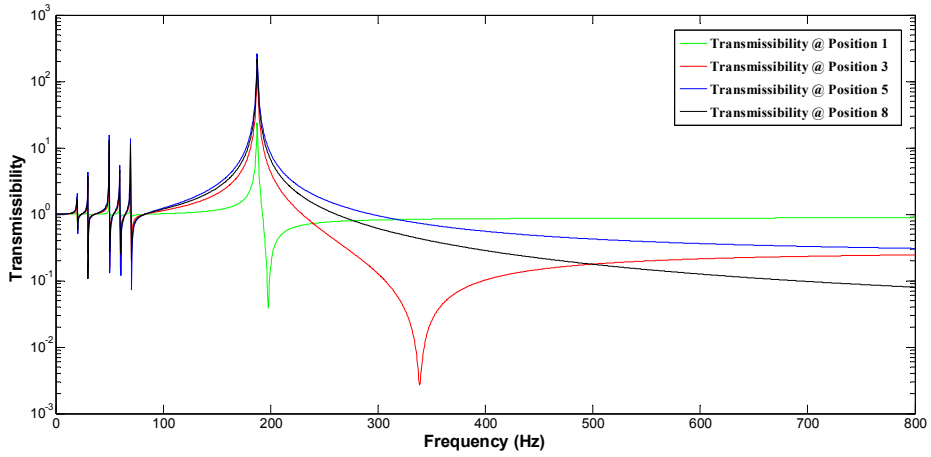

Figure 3.12: Transmissibility calculated at various positions of the multiresonant beam with no tip masses, first mode of vibration

It is considered that the second mode of the beam may be important. Figure 3.13 shows the transmissibility for two mode shapes. Higher amplitudes than would be achieved in practice are shown in Figures 3.12 and 3.13, which is due to the low damping ratio.

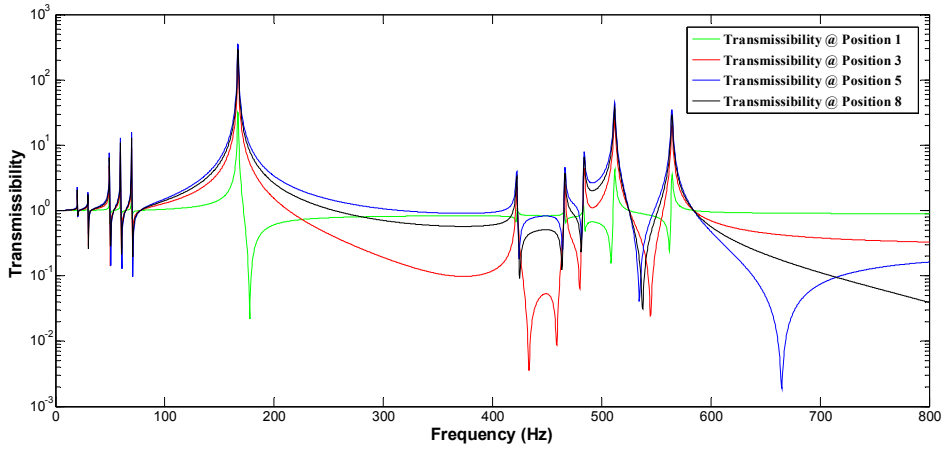

Figure 3.13: Transmissibility calculated at various positions of the multiresonant beam with no tip masses, first and second modes of vibration

The model assumes 1% damping ratio in the bending and torsion fields, see Section 3.4. The highest predicted waveform is at the centre position of the beam, where the highest deflections occur. However anti-resonances also occur in the system due to pole-zero cancellation [99-101, 113]. These anti-resonances decrease the transmissibility of the system, and will reduce the PFCB output.

3.7.2 Simulation of Multiresonant Beam with Tip Masses

According to [89, 102], the first five roots of the frequency equation for a clamped-clamped beam are λ_1=4.73, λ_2=7.853, λ_3=10.9956, λ_4=14.137 and λ_5=17.279. Considering the parameters which affect the natural frequency f_n, the beam's width w, length l and thickness h were chosen as shown in Table 3.1. Stainless steel was chosen again for the beam material, and a list of the calculated main beam natural resonant frequencies is shown in Table 3.2.

Table 3.2: Calculated resonant frequencies of clamped-clamped beam

Mode shape of the beam	Frequency (*Hz*)
1^{st} mode	181
2^{nd} mode	498
3^{rd} mode	977

By adjusting the beam dimensions shown in Table 3.1, the beam's mode frequencies can be varied. The first resonant frequency of the main beam will reduce slightly from that in Table 3.2 due to the side cantilevers added mass.

The mass of the main clamped-clamped beam M_{Beam} without any cantilevers mounted is about 63.4*g*. Table 3.3 gives the side cantilevers added masses and positions, and resulting first mode freuqnecies.

Table 3.3: Mounted side cantilevers parameters

Cantilever	Mass *(g)*	Mounted position *(cm)*	Frequency *(Hz)*
1	40	6*cm*	30*Hz*
2	40	8*cm*	35*Hz*
3	40	10*cm*	40*Hz*
4	40	12*cm*	45*Hz*
5	40	14*cm*	50*Hz*

The transmissibility, T, in the middle position of the beam was examined in this model.

Following the initial implementations in Section 3.6 and using the parameters shown in Tables 3.1 and 3.3, the transmissibility of the system was calculated using Matlab and is shown in Figure 3.14.

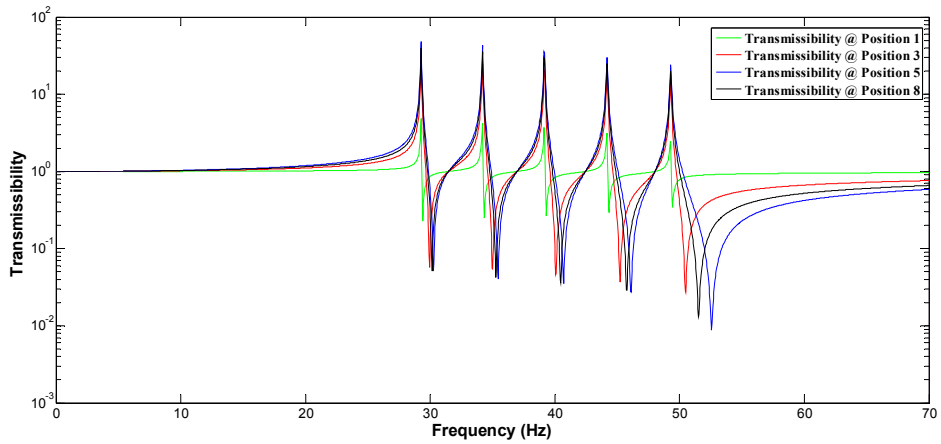

Figure 3.14: Transmissibility of a multiresonant beam model with tip mass

As shown in Figure 3.14, amplification peaks occur between 30Hz and 50Hz, producing high gains of around 20 or more. However there are also dips in gain between 30Hz and 50Hz. This effect is anti-resonance, or pole-zero cancellation of the transfer function. The effect decreases the transmissibility of the system, thus reducing the piezoelectric power output.

In practical cases, higher tip mass also causes higher damping, therefore damping should vary according to tip mass for each cantilevers, whereas in this simulation it is assumed to be constant.

3.8 Possible Solution to Anti-Resonant Frequency Effect

As anti-resonances occur in every resonant system, it is therefore impossible to remove these by varying the beam parameters. A possible means of reducing the

effects of anti-resonances is to have two separate clamped-clamped beams as shown in Figure 3.15, one on top of the other, perhaps, so that both are subject to the same vibration source, each having a number of cantilevers mounted upon it.

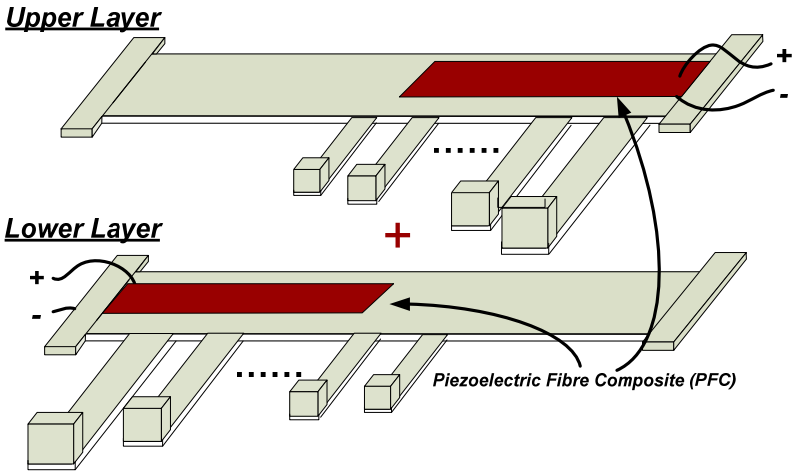

Figure 3.15: Stacked multiresonant beam solution

With appropriate beam parameters, the transmissibility of, say, the lower beam can be frequency shifted slightly with respect to the upper beam to produce a combined transmissibility as shown in Figure 3.16.

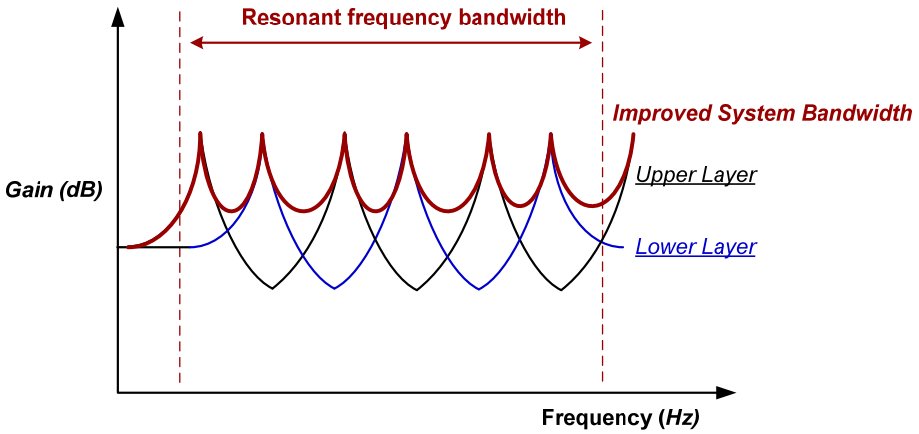

Figure 3.16: Output of two multiresonant beam design

In Figure 3.16 the lower and the upper beam transmissibilities are shown in thin and dashed lines. The peaks in the upper beam's transmissibility are placed so as to be at the same frequency as the anti-resonances of the lower beam and vice versa. Thus

the transmissibility of the system is improved to that of the upper curve shown in bold.

A simulation of such a double beam system is shown in Figure 3.17, where the "dips" of the first beam occurred at 31*Hz*, 35*Hz*, 42*Hz*, 47*Hz* and 53*Hz*. An improved transmissibility is now obtained with a second multiresonant beam (Red line) introduced.

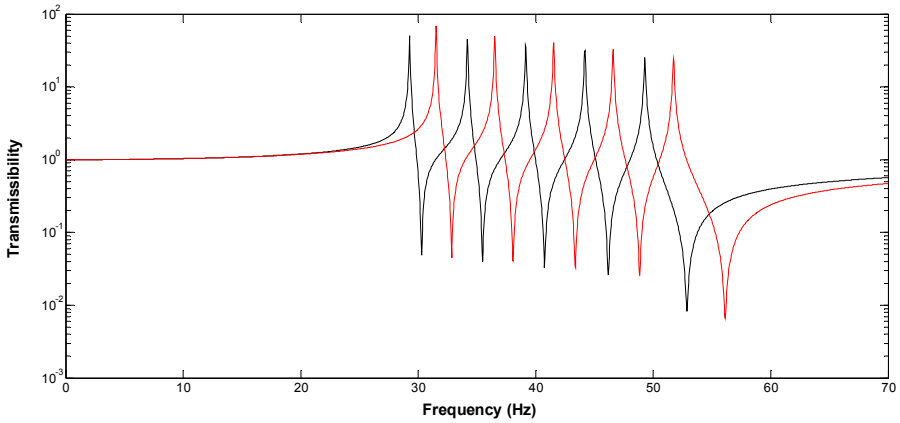

Figure 3.17: Transmissibility of two multiresonant beam model

3.9 Conclusion

In this chapter, a multiresonant beam structure was proposed, consisting of an array of cantilevers attached to a clamped-clamped beam, where the PFC material is mounted. Such a system could in theory harvest energy over a wider frequency spectrum than the standard cantilever system shown in Chapter 2. Also the system is more sensitive to strains produced from torsion, and therefore vibration energy can be harvested more efficiently.

A Rayleigh-Ritz analysis of the multiresonant system was carried out in Section 3.2. In addition to the cantilever analysis in Chapter 2, torsion vibration was considered in the analysis. Based on the mathematical theory, the system was simulated and the results were shown in this chapter.

The simulated mode shapes for cantilever and clamped-clamped beam are shown in Section 3.5, this is followed by the simulation results of the proposed system in Section 3.7. From the simulation results, several resonant frequencies were shown by the system, however the effects of anti-resonance prevent the system from having continuous transmissibility amplification. The effect was discussed in Section 3.8 along with a possible solution.

To conclude, the results show a multiple resonance frequency response from the proposed system in comparison to a cantilever energy harvester. The next chapter gives the results of an experimental test on both a standard cantilever and the multiresonant beam system.

Chapter 4 :

Cantilever and Multiresonant Beam Experimental Test Results

4.1 Introduction

In order to verify the proposed design simulated in Chapter 3, a clamped-clamped beam with attached cantilevers was constructed and tested in the Laboratory. A further objective of the laboratory work was to investigate the transmissibility behaviour of the multiresonant beam in comparison to a single cantilever energy harvester.

4.2 Laboratory Setup

Figure 4.1 shows the Laboratory measurement apparatus. It comprises a shaker/vibrator (4) with attached cradle (5) to which the harvester to be tested is attached. In this figure the multiresonant harvester (6) is shown attached to the cradle. Accelerometers (7, 8) measure the input and output accelerations. The accelerator signals are applied to a Solatron Instrument SI1260 impedance/gain-phase analyser (2) and a signal conditioning equipment (9, 10) which scales the signals to amplitudes that can be applied to the Solatron analyser without incurring saturation of the analyzer's input stages. A PC (1) is used to save the results obtained and a power amplifier (3) provides the shaker electrical drive [48].

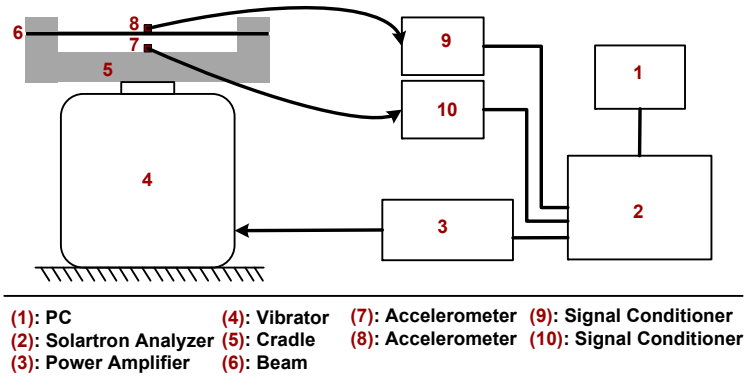

Figure 4.1: Laboratory measurement setup

During testing the Solatron analyser SI1260 provides a variable frequency, constant amplitude drive signal to the shaker power amplifier and thereby affects a frequency sweep over the frequency range of interest. The transmissibility was determined over this frequency range, from the measurements of beam acceleration divided by the acceleration measurements of the reference signal, to produce a dimensionless ratio between the acceleration at output and input. Initial tests were performed on PFCB cantilevers to provide a base set of tests, to which the multiresonant beam measurements can be composed.

4.3 Experimental Test Results

Several cantilevers, formed from PFCBs with added tip masses and the multiresonant system were tested using the same test apparatus. The results are discussed in this section.

4.3.1 Single cantilever array test

4.3.1.1 Transmissibility Test of Cantilevers

Initial work involved determining the resonant frequencies of PFCB single cantilevers with different tip masses. The approximate values of the required tip masses and their mounting locations for a particular first mode frequency were calculated using the standard mass-spring-damper system equation (4.1) [48, 90, 102].

$$f_i = \frac{1}{2\pi}\left(\frac{\lambda_i}{L}\right)^2 \sqrt{\left(\frac{EI}{\rho A}\right)} \tag{4.1}$$

where λ_i is the coefficient of mode shape function, E is Young's modulus, I is moment of inertia, ρ is the density of the cantilever material, A is the cantilever cross-sectional area, L is the cantilever length. The parameters of the PFCB are shown in Table 4.1. T_{SS} is the thickness of the stainless steel shim, and T_{PFC} is the thickness of each PFC layer mounted on the top and bottom of the PFCB. Note that $T_{PFCB} = T_{SS} + 2T_{PFC}$.

Table 4.1: PFCB cantilever dimensions

L_{PFCB} (mm)	W_{PFCB} (mm)	T_{SS} (mm)	T_{PFC} (mm)	T_{PFCB} (mm)	M_{PFCB} (g)	E_{SS} (Gpa)	ρ_{SS} (kgm^{-3})
80	10	0.4	0.3	1.0	7.5	205	7850

A set of tip masses weighing 8.5*g*, 15*g*, 21*g* and 30*g* were used for the investigation. According to [102], for the first mode of beam vibration, with 8.5*g* mass loading, λ_i is 1.202. For a 15g tip mass, λ_i is 1.076. For 21*g* and 30*g* tip masses, λ_i is 0.997 and 0.9174 respectively.

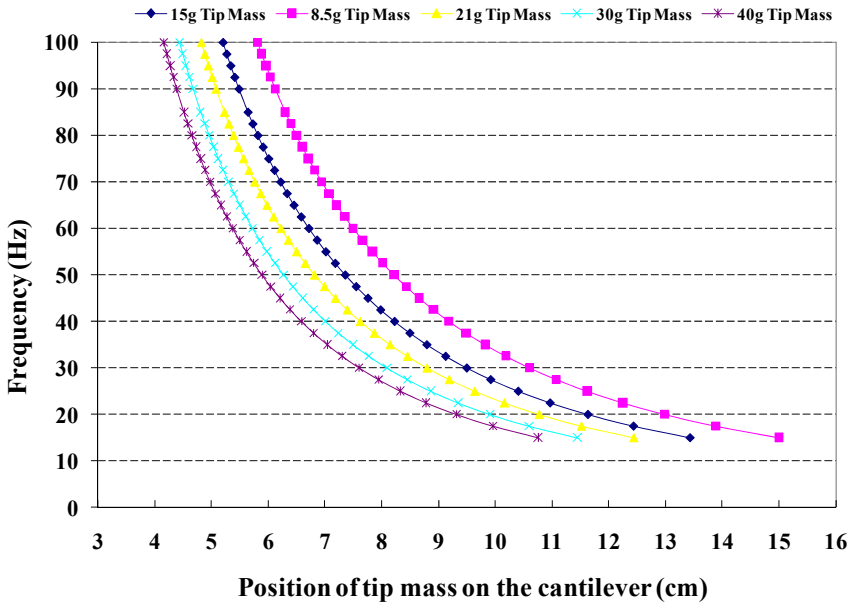

Figure 4.2: Estimated cantilever tip mass clamp position chart

Figure 4.2 shows how the calculated resonant frequency of a PFCB cantilever changes as the position of the mass on the cantilever is varied, for several different tip masses. Using this chart, a series of cantilever resonant frequencies can be configured.

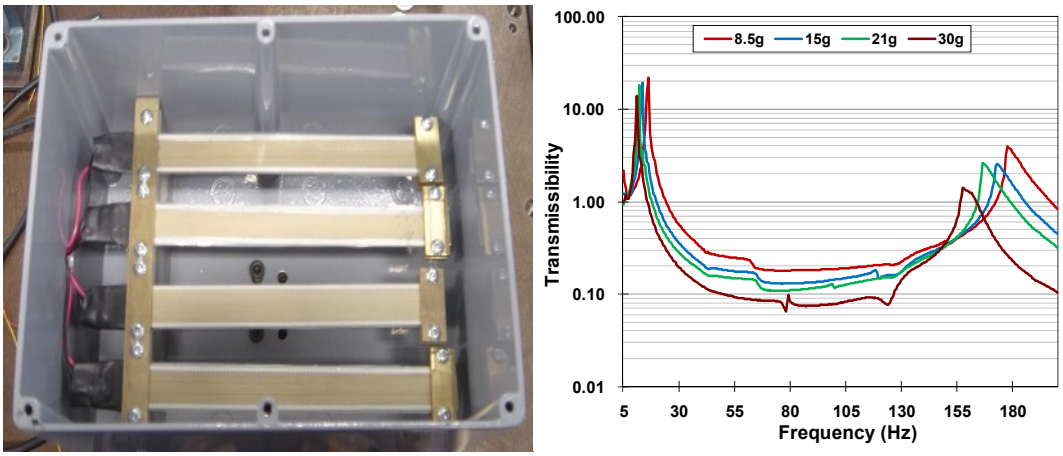

(a) (b)

Figure 4.3: Several cantilevers connected in parallel

(a) picture of a cantilever array [90-92] (b) measured transmissibility results

The curves in Figure 4.3(b) show the measured transmissibility curves of four PFCB cantilevers tuned with different tip masses. Also shown in Figure 4.3(a) is a photograph of the four cantilevers, in a box attached to the shaker cradle. By means of the different tip masses, the system transmissibility curves have been made to overlap between 10*Hz* and 20*Hz* and also between 150*Hz* and 175*Hz* where the first and second resonances modes occur respectively. These curves indicate that in practice the proposed broadened bandwidth concept can be applied to either the first or second (or possibly higher) resonance region. A more detailed frequency curve for the first mode of the four cantilevers is shown in Figure 4.4. Note that due to low frequency instrument noise, the results obtained below 5*Hz* are corrupted and have not therefore been plotted.

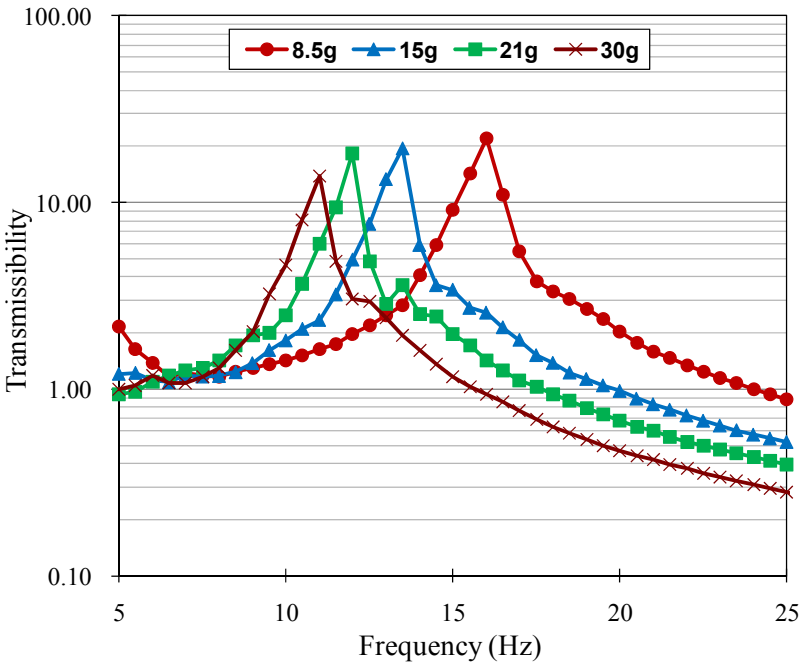

Figure 4.4: Measured cantilever transmissibility curves with different tip masses at first resonance

As shown in Figure 4.4, the four resonant frequency peaks occur between 10*Hz* and 20*Hz*. The range can be moved to higher or lower frequencies with different tip mass selections.

4.3.1.2 Electrical Output Test of PFCB Cantilever

The electrical output behavior of a PFCB cantilever energy harvester has also been investigated. The material properties of the PFC are shown in Appendix A [46, 49].

The output resistance and capacitance of the PFCB cantilever was measured using an Agilent 4284A network analyzer, see Figures 4.5 and 4.6.

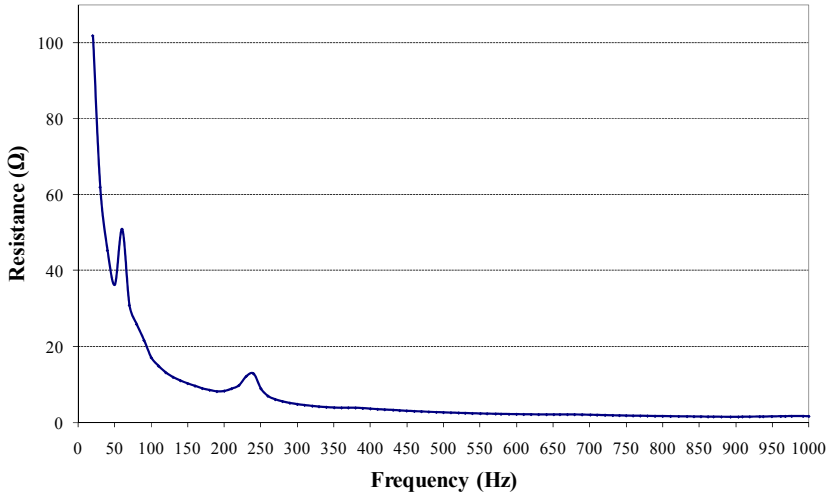

Figure 4.5: Measured output resistance of PFCB

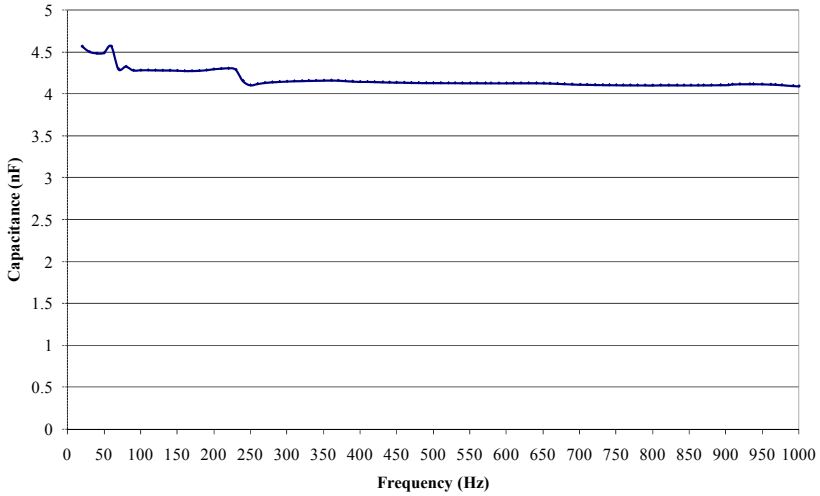

Figure 4.6: Measured output capacitance of PFCB

Figure 4.7 shows the voltage output from two electrically parallel PFCs mounted on a single cantilever structure top and bottom respectively (a single PFCB in effect), without any tip mass. Thus the resonant frequency is slightly higher than a cantilever of the same type that has a tip mass.

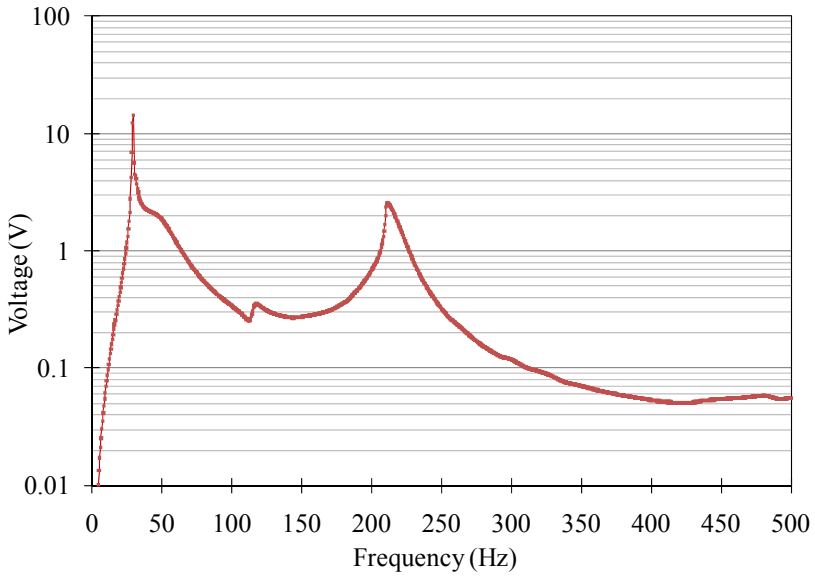

Figure 4.7: Measured PFCB cantilever output voltage

The open circuit voltage and short circuit current are around $10V_{pk-pk}$ and $0.01mA_{pk-pk}$ respectively at the lower resonant frequency when the support is subject to an excitation level of $10.47ms^{-2}{}_{pk-pk}$. The two resonant frequencies are around $34Hz$ and $220Hz$ [48].

These results are in good agreement with results achieved by other researchers on similar PFCs [152], between $15V$ to $36V$ with tip masses. Note that in Figure 4.7 the device was driven at an excitation level that is generally higher than would be met in practice when harvesting, in order to produce maximum harvester output.

4.3.2 Multiresonant Beam Structure Test

4.3.2.1 Transmissibility Test

A multiresonant beam system was constructed, and tested in the Laboratory as shown in Figure 4.8 with the dimensions outlined in Table 3.1 in Section 3.7, Chapter 3. Measured results are shown in Figures 4.9 and 4.10 without and with tip masses respectively.

By spacing the side cantilevers equally and by also making the main beam longer than is needed (so that main beam length is determined by adjustable end clamps). The design has the flexibility to simulate offset side cantilevers.

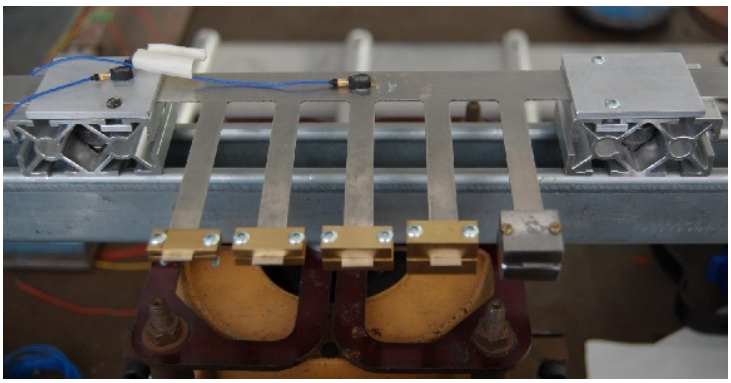

Figure 4.8: Experimental version of multiresonant beam [48, 90]

The side cantilevers could be attached to the main beam by for instance soldering, spot welding, rivetting or bolting. However all these attachment techniques will produce a variable thickness along the main beam which will modify the beam's parameters, and therefore the resonant frequencies of the system. To avoid this effect it was decided to construct the main beam and side cantilevers, by cutting both from one piece of stainless steel sheet, thus eliminating variations in thickness. The side cantilevers can therefore be tuned by adding tip masses. Since the beam is fastened by screws at each clamp, and these screws are not 100% rigid, so the beam clamps are slightly flexible and therefore imperfect.

Table 4.2: Calculated single cantilever resonant frequencies

	Tip Mass (g)
Cantilever 1	8.5
Cantilever 2	15
Cantilever 3	21
Cantilever 4	30
Cantilever 5	40

Figure 4.9 shows that when there are no tip masses, there are no resonances between 150*Hz* and 400*Hz*. The first mode resonances are seen to occur between 1*Hz* and 100*Hz*, the second mode resonance peaks are between 400*Hz* and 600*Hz*. The main beam is resonant at about 135*Hz*. When tip masses were added, as shown in Table 4.2, the result in Figure 4.10 was achieved. It is difficult to determine which resonances are due to which cantilevers and modes from Figure 4.10.

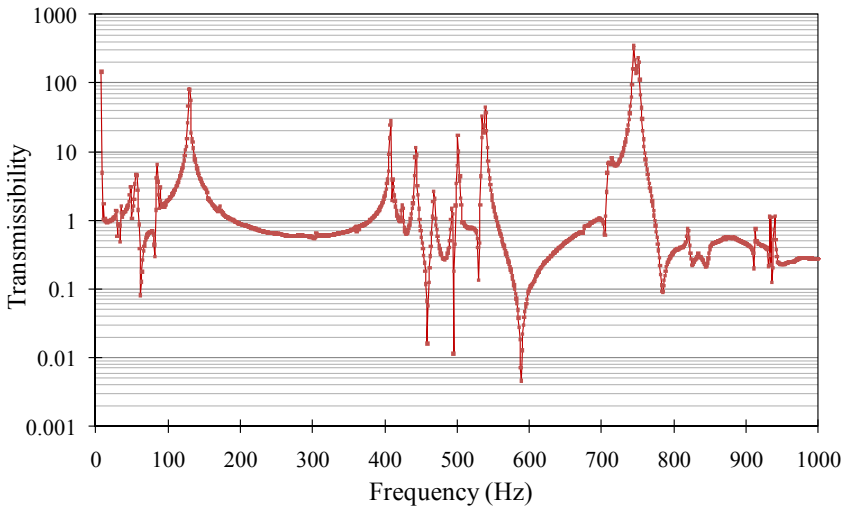

Figure 4.9: Measured transmissibility of multiresonant beam without tip masses

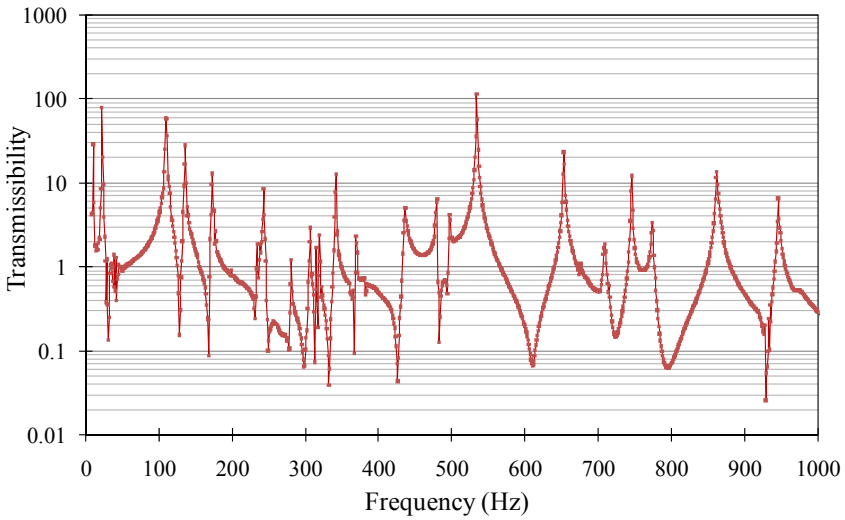

Figure 4.10: Measured transmissibility of multiresonant beam with tip masses

Figure 4.10 shows that the beam structure with multiple cantilevers attached, produces a multiple resonant frequency effect. It is reasonable to assume that by adjusting the side cantilevers tip mass position, and possibly changing the beam dimensions, some of these resonances could be engineered to produce a band of resonances centred around a particular frequency.

The transmissibility frequency response curve depends upon the position of the accelerometer on the clamped-clamped beam. Considering the main beam alone, as the frequency is increased from a low to high value, so the various modes of beam vibration will occur and so the transmissibility will vary depending upon the accelerometer position on the beam, see Figure 4.11.

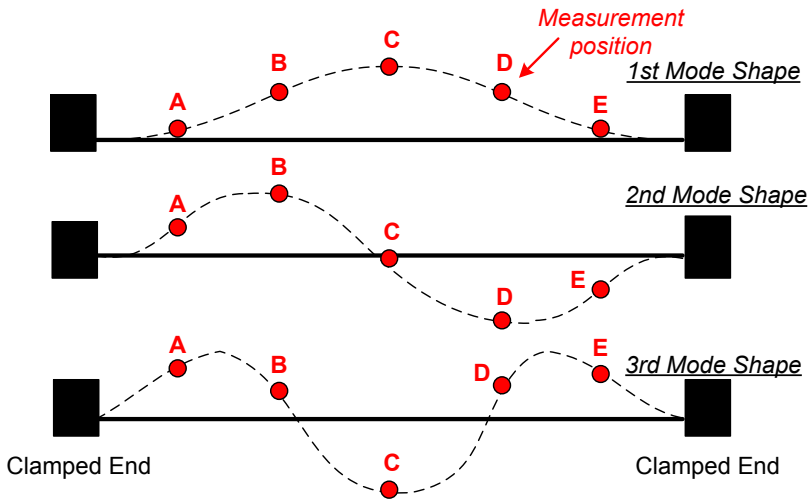

Figure 4.11: Measurement positions on a clamped-clamped beam for different mode shapes of vibration

The effect was demonstrated experimentally by placing an accelerometer at five locations as shown in Figure 4.11, on the clamped-clamped beam. These five locations were at the roots of the five side cantilevers. Figure 4.12 shows the transmissibilities measured at the five locations.

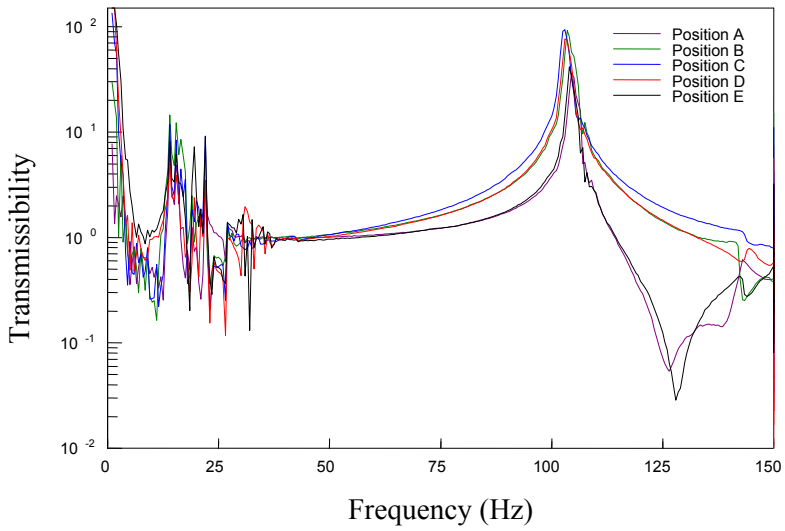

Figure 4.12: Multiresonant beam tansmissibilities measured at different locations

Figure 4.13 shows the transmissibilities up to 50*Hz*. Responses below 5*Hz* should be ignored since amplifier offset voltages and noise give spurious results. In Figure 4.13, the main resonances of the five cantilevers occur at around 15*Hz*, and there are also

resonances at 20*Hz* and 23*Hz* caused by the two cantilevers which have the lowest tip mass and are also closest to one clamped end of the beam.

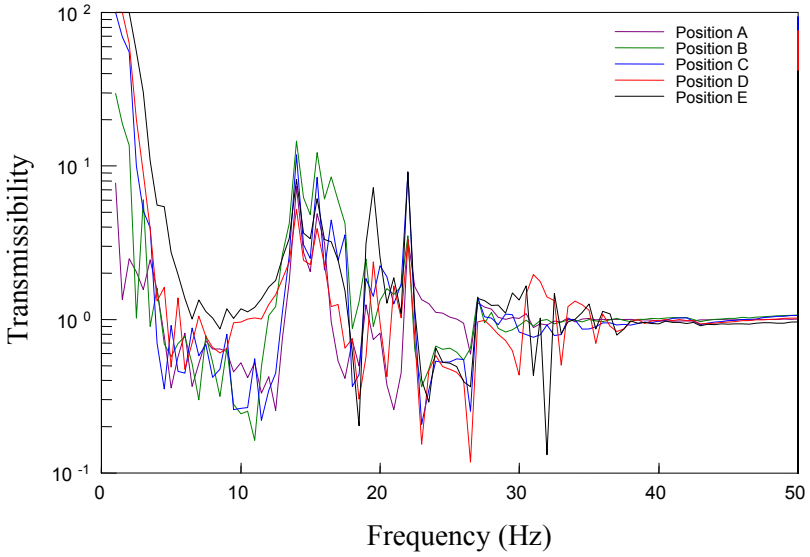

Figure 4.13: Multiresonant beam transmissibilities measured at different locations (detailed view)

Figures 4.12 and 4.13 demonstrate the complexity of the multiresonant system. The ultimate aim is to integrate all these responses to produce a wideband voltage response, by adding PFC material to the beam. The author's approach to this is described in the next section.

4.3.2.2 Piezoelectric Fiber Composite (PFC) Electrical Output Test

The behaviour of two PFCs electrically in parallel and attached to the main beam was measured, see Figure 4.14. The tip masses of cantilevers 1 to 5 in Figure 4.14 are shown in Table 4.2.

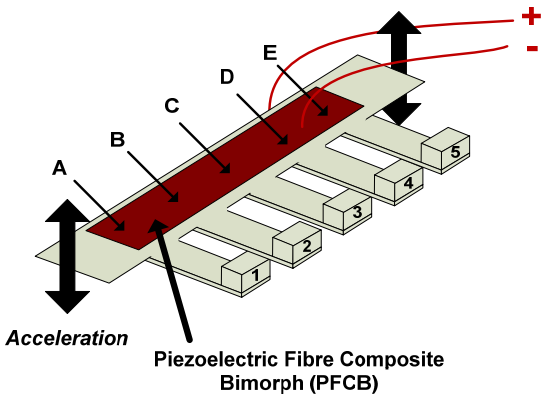

Figure 4.14: Test on multiresonant beam

The two PFCs are subjected to bending and twisting by the five side cantilevers, each of which resonates at a different frequency, and also to bending due to the clamped-clamped beam.

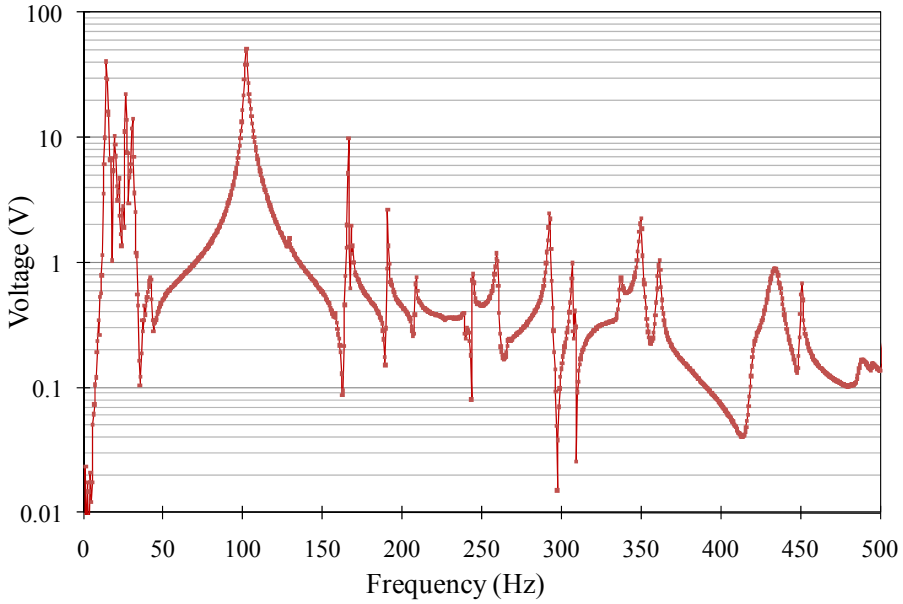

Figure 4.15: PFC voltage output from multiresonant beam

Figure 4.15 shows the measured voltage output from the two PFCs, electrically connected in parallel, mounted on the clamped-clamped beam. Concentrating only on the spectrum up to 50*Hz*, many resonances are seen to occur between 15*Hz* and

34*Hz*. The dips between the peaks are caused by anti-resonances, as described in Section 3.8.

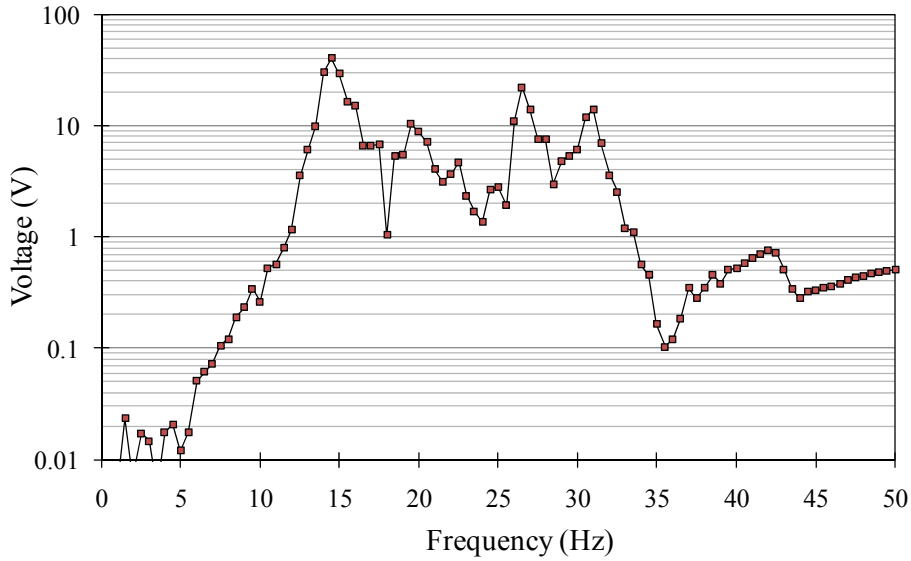

Figure 4.16: PFC voltage output on multiresonant beam (detailed view)

Figure 4.16 shows a more detailed view of the PFC voltage response between 1*Hz* and 50*Hz*. The PFC response is a voltage which bears similarities to the transmissibility results shown in Figures 4.12 and 4.13. This is because the PFC covers the five measurement positions which produced the curves in Figures 4.15 and 4.16. However in comparison to Figure 4.13, the PFC voltage output shows a wider frequency band. This is possibly due to strain induced in the clamped-clamped beam by torsion. Torsion in the main beam is not shown by the accelerometer.

4.3.3 Comparison of PFC Output for Single Cantilever and Multiresonant Beam Model

Figure 4.17 shows the voltage output from a PFCB single cantilever as described in Table 4.1.

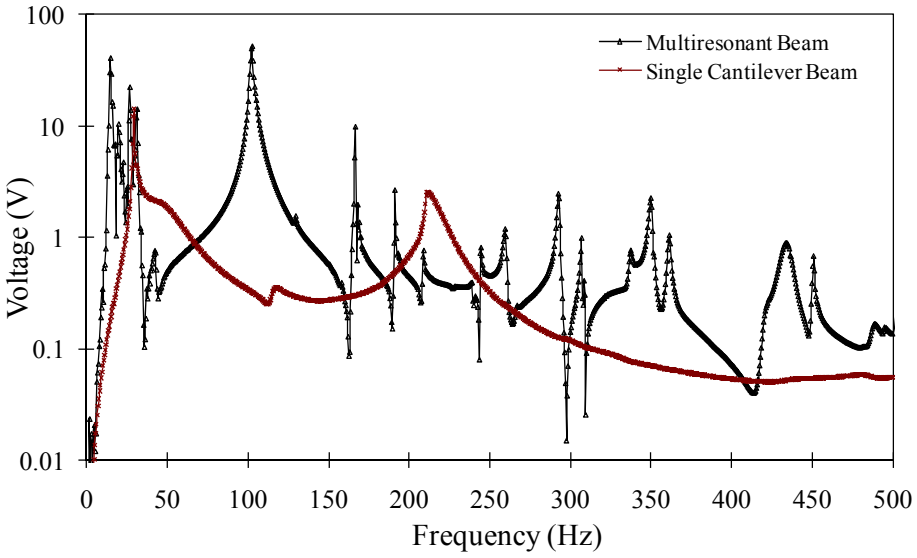

Figure 4.17: Voltage output comparason between PFCB cantilever and multiresonant beam

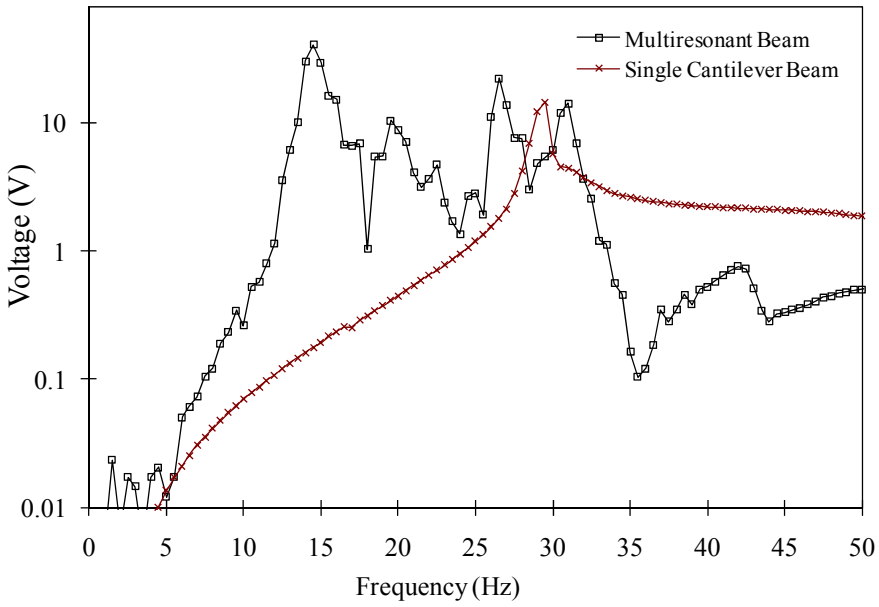

Figure 4.18: Voltage output comparison between PFCB cantilever and multiresonant beam (detailed view)

A more detailed comparison between the single and multiresonant beam structure covering the frequency range from 1*Hz* to 50*Hz* is shown in Figure 4.18. By using Equation (4.1) in Section 4.3.1.1 [102], the resonant frequency of each side cantilever attached to the clamped-clamped beam was calculated. These frequencies

are shown in Table 4.3. Also shown in Table 4.3 are the measured resonant frequencies of the side cantilevers, found by exciting the clamped-clamped beam and observing the amplitude of the side cantilevers motions.

Table 4.3: Calculated and measured resonant frequencies of side cantilever

	Calculated Resonant frequency (*Hz*)	Measured Resonant frequency (*Hz*)
Cantilever 1	37.4007	31
Cantilever 2	29.9782	26.5
Cantilever 3	25.7285	22.5
Cantilever 4	21.7281	19.5
Cantilever 5	19.2281	14.5

Table 4.3 shows the resonant frequencies of each side cantilever can be identified in Figure 4.18. There are disagreements between the predicted and measured frequency magnitudes. This is probably because the predicted frequencies are based on the assumption that the side cantilevers are fixed to a rigid body, which is not the case as the clamped-clamped beam is flexible.

According to Table 4.3, the first mode resonance in Figure 4.19 is due to cantilever 1, and the second, third, fourth and fifth mode resonances are due to cantilevers 2, 3, 4 and 5 respectively.

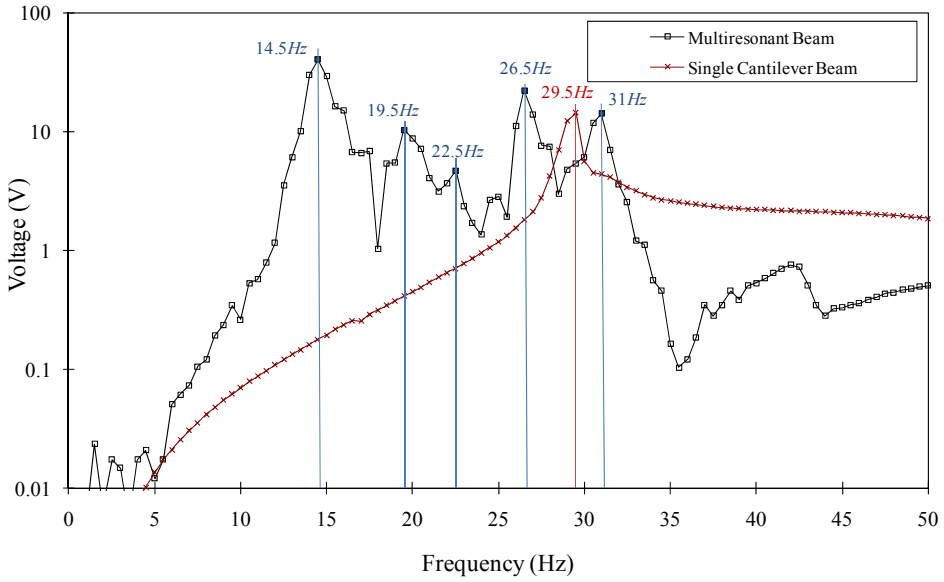

Figure 4.19: Voltage output comparison between PFCB cantilever and multiresonant beam highlighting the resonant frequencies

From Figure 4.19, the average open circuit voltage of five resonant peaks is found to be around $18V_{pk\text{-}pk}$. The measured results show that the multiresonant structure has multiple resonant peaks compared to the single cantilever model, which has only a single resonance around $29.5Hz$. Hence the multiresonant model is more suitable for harvesting variable frequency vibrations.

4.4 Conclusion

Laboratory test results were given in this chapter, the laboratory setup was described in Section 4.2.

In Section 4.3.1, the test result of a cantilever array using different tip masses was measured. Such a model was studied by many researchers including Shahruz [84, 85], however there are no experimental results shown by him.

The multiresonant beam was built and tested in the laboratory as described in Section 4.3.2. The results prove that the multiresonant beam can harvest energy from a wide frequency spectrum compared to a standard cantilever system. The advantage of the multiresonant beam system is that, for the same amount of piezoelectric materials as a standard cantilever, a much wider bandwidth is produced. This was later discussed in Section 4.3.3.

The multiresonant system tested in this chapter has not been optimised. Further optimization can be made to the multiresonant system to improve this continuous amplification. This could be achieved by altering the weight of the tip masses and size of the beam. However such a study will need to be a part of future work which could also involve the automatic optimization of the computer model of system. This will be discussed in Chapter 7.

Chapter 5 and Chapter 6 will investigate the electronic circuits for piezoelectric energy harvesters, which would also allow the frequency tuning electrically mentioned in Chapter 2.

Chapter 5 :

Electronic Circuit for Energy Harvesting Devices

5.1 Introduction and Piezoelectric Harvester Equivalent Circuit

This chapter reviews piezoelectric energy harvester equivalent circuits and the requirements of electronic circuits needed to convert the piezoelectric output energy to a form suitable for use by load circuits. Often a harvester will work discontinuously, in which case its output energy must be stored in, for instance, a rechargeable battery or super capacitor. Piezoelectric generators have a capacitive output impedance, which at the vibration frequencies of interest, (less than say 150*Hz*) has a high value. Therefore the design of the electronic circuit to extract the piezoelectric energy is of paramount importance if the extraction is to be done in an efficient manner.

The electrical equivalent circuit of a piezoelectric device at its resonant frequency is often treated as a voltage source in series with a resistor and capacitor [22, 87, 107, 109, 110, 153-159], as shown in Figure 5.1(a). The external load is modelled as a resistor R_L, although in practice this would usually be a power electronic converter. Figure 5.1(b) shows a phasor diagram for this circuit. The phasor $-jX_CI_L$, representing the voltage drop across C_{PZT}, is not drawn to scale and in practice would be much longer than shown here. As a consequence of the high capacitive impedance, current flow is limited and the resistor load receives little power.

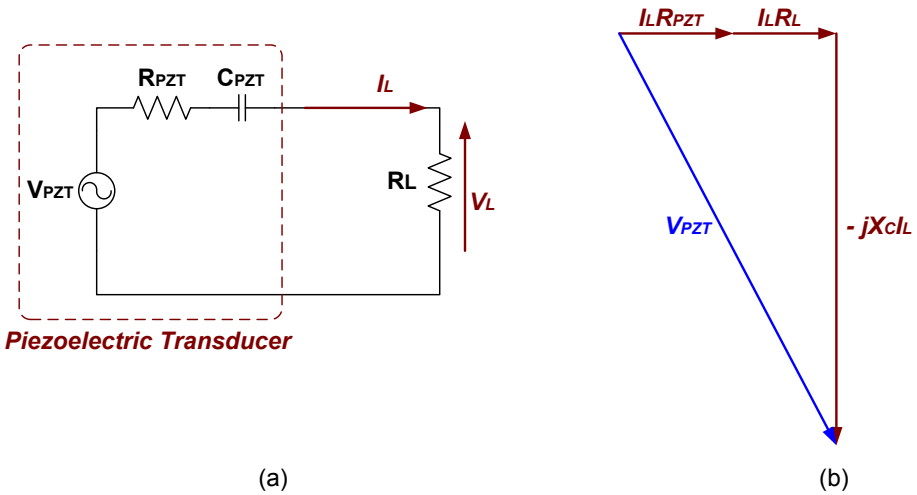

Figure 5.1: Piezoelectric transducer equivalent circuit with a load

(a) Piezoelectric transducer equivalent circuit with load

(b) Phasor diagram of harvester equivalent circuit at resonance

Anderson et al 1994 [160] investigated the behaviour of piezoelectric transducers and in particular the behaviour of the capacitance (C_{PZT} in Figure 5.1(a)) as the resonance frequency mode is changed. According to [160], the output capacitance is not ideal due to hysteresis loss in its dielectric. Thus the capacitance C_{PZT} in Figure 5.1 is complex, see Equation (5.1):

$$C_{PZT} = C_{PZT}^{real} + jC_{PZT}^{imag} \tag{5.1}$$

where C_{PZT}^{real} and C_{PZT}^{imag} are the real and imaginary term of capacitance C_{PZT}. The imaginary term represents a loss and is often ignored in most piezoelectric analyses, but can have a significant influence when the resonant frequency varies. Therefore the capacitance will change as the frequency changes.

A more general circuit model, shown in Figure 5.2 simulating higher resonance modes, was investigated by Campolo et al 2003 [161]. In this model the authors split the equivalent impedance of the piezoelectric material. Thus C_0 represents the primary capacitance and the capacitances C_i, where $i=1,....n$, represent the

capacitances that are effective at different resonant frequencies of the piezoelectric transducer.

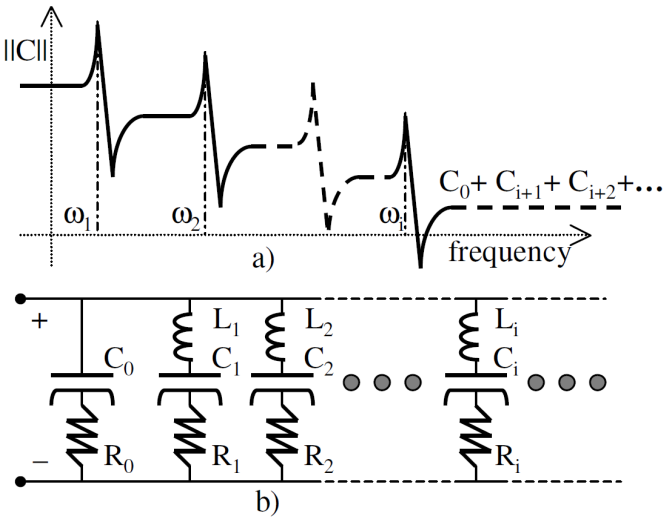

Figure 5.2: Complex piezoelectric equivalent model [161]

The aim of the work described in this thesis was to investigate and analyse the behaviour of piezoelectric material only around the fundamental cantilever resonant frequency. Therefore a single resonant frequency model (Van Dyke circuit [153]) as shown in Figure 5.1(a) was used.

5.2 Review of Different Circuit Topologies

Due to the high capacitive output impedance of piezoelectric materials, electronic circuits to improve the harvester output power have been widely investigated. Several researchers have been working on improving the resistive impedance matching in recent years. Viana et al, Lesieutre and others [110, 135, 138, 140-144] investigated the effect of connecting various load circuits to the piezoelectric material.

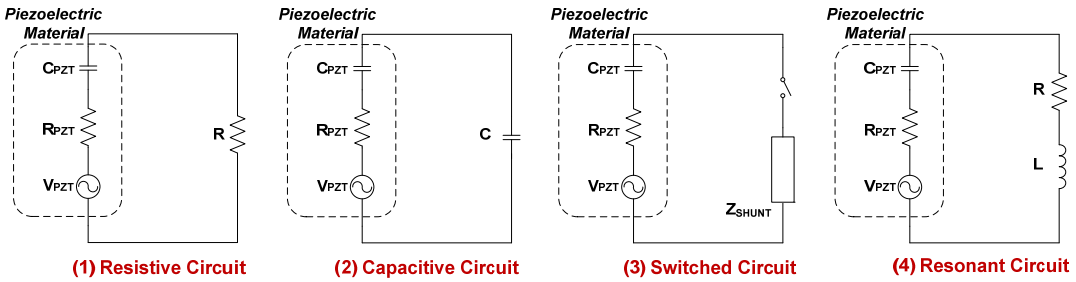

Figure 5.3: Different load circuit designs for piezoelectric transducer [110]

Figure 5.3 shows four load topologies investigated [110]. The first topology, the resistive circuit, will be described in Section 5.4. The second topology, the capacitive circuit, does not absorb energy since the capacitor is a non-dissipative element. However the capacitor load will alter the stiffness of the piezoelectric transducer. The third topology, the switched circuit, is non-linear and has been investigated by several researchers. The fourth topology, the resonant circuit, can reduce or negate the capacitive impedance of the piezoelectric device and has also been investigated. The second topology produces no power, and will not be considered further. The switched and resonant circuit topologies however are described and discussed in Sections 5.5, 5.6 and 5.7.

5.3 Resistive Load Matching Circuit Analysis

According to [22, 110, 142, 156], from the circuit shown in Figure 5.1(a), Equation (5.2) is given:

$$V_{PZT} = I_L R_{PZT} + I_L R_L - jX_C I_L \tag{5.2}$$

where $X_C = \dfrac{1}{\omega C_{PZT}}$.

Hence:

$$I_L = \frac{V_{PZT}}{R_{PZT} + R_L - jX_C} \tag{5.3}$$

and

$$|I_L| = \frac{|V_{PZT}|}{\sqrt{(R_{PZT} + R_L)^2 + X_C{}^2}} \tag{5.4}$$

Therefore the power in R_L is:

$$P_L = |I_L{}^2| R_L = \frac{|V_{PZT}|^2 R_L}{(R_{PZT} + R_L)^2 + X_C{}^2} \tag{5.5}$$

The condition for maximum power transfer can be obtained by differentiating the output power as in (5.5), to yield (5.6) [22, 110, 142, 156]:

$$\frac{dP_L}{dR_L} = \frac{|V_{PZT}|^2}{(R_{PZT} + R_L)^2 + X_C{}^2} - \frac{2|V_{PZT}|^2 R_L (R_{PZT} + R_L)}{\left[(R_{PZT} + R_L)^2 + X_C{}^2\right]^2} \tag{5.6}$$

The maximum power condition is found by putting $\frac{dP_L}{dR_L}$ equal to zero:

$$\left[(R_{PZT} + R_L)^2 + X_C{}^2\right] - 2R_L R_{PZT} - 2R_L{}^2 = 0 \tag{5.7}$$

$$R_{PZT}{}^2 + 2R_{PZT}R_L + R_L{}^2 + X_C{}^2 - 2R_L R_{PZT} - 2R_L{}^2 = 0 \tag{5.8}$$

$$R_L{}^2 = R_{PZT}{}^2 + X_C{}^2 \tag{5.9}$$

Hence from (5.9), the maximum power in the load is achieved when:

$$R_L = \sqrt{R_{PZT}{}^2 + X_C{}^2} \tag{5.10}$$

Figure 5.4 shows a photograph of a piezoelectric fiber transducer, type P876.A11, from PI Ceramics. The output resistance R_{PZT} and capacitance C_{PZT} were measured

over a range of frequencies using an Agilent 4284A network analyzer, as shown in Figures 5.5 and 5.6.

Figure 5.4: P876.A11 piezoelectric transducer

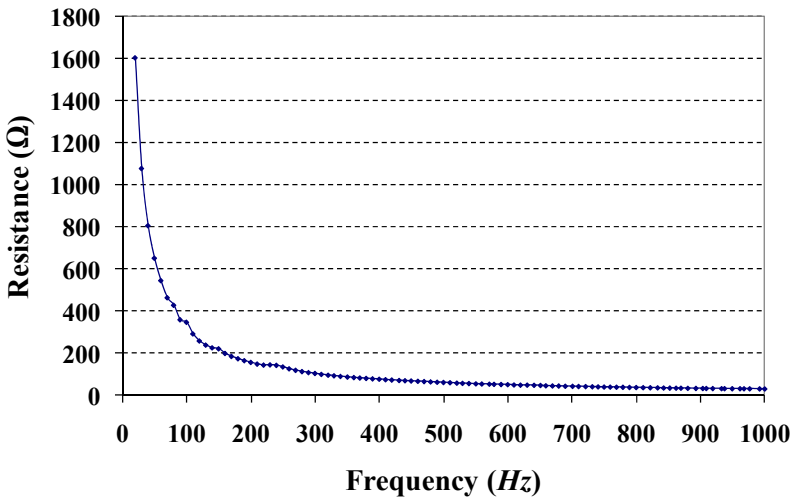

Figure 5.5: Measured output resistance of P876.A11

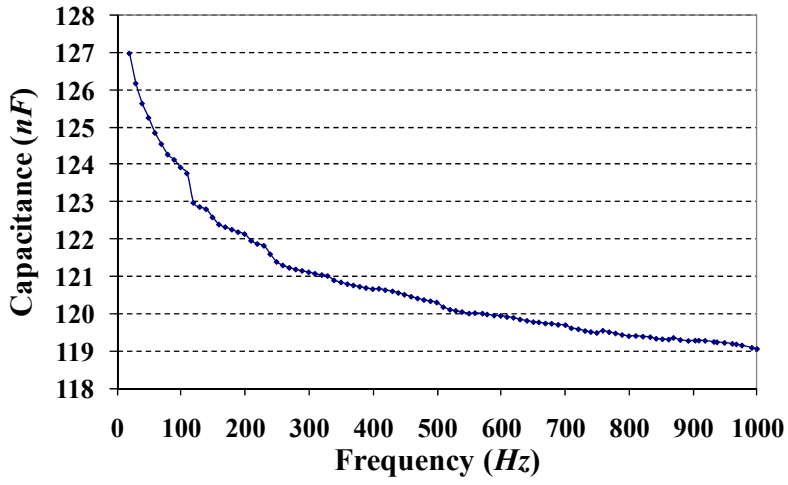

Figure 5.6: Measured output capacitance of P876.A11

Figures 5.5 and 5.6 show a general decrease of resistance and capacitance with frequency. There are several possible reasons for the decrease. For instance the piezoelectric coefficient and the permittivity of the piezoelectric material might decrease at higher frequencies due to a frequency dispersion effect from the material [162]. Another possibility is that due to the hysteretic nature of the material, the higher order harmonics produce a phase error at the output. Thus the capacitance term at higher frequencies becomes complex, and since the imaginary term of the capacitance cannot be directly measured from the network analyzer [160], so the capacitance appears to decrease.

As an example, assume the P876.A11 device produces an AC voltage of amplitude of $1V$ and frequency $70Hz$. The corresponding resistance and capacitance values of the P876.A11 device are 466Ω and 125nF, from Figures 5.5 and 5.6

Using these parameters, a simplified equivalent circuit of the P876.A11 transducer can be obtained as shown in Figure 5.7(a). The phase angle in Figure 5.7(b) is obtained by Equation (5.13). In practice, the coupling factor would also affect the parameters slightly.

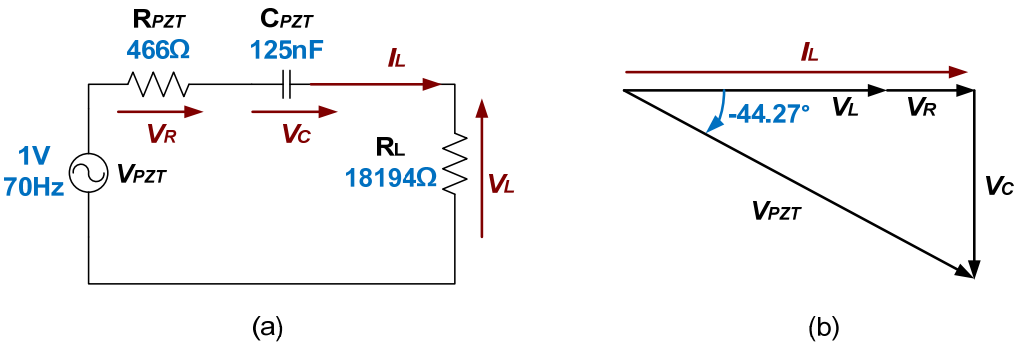

Figure 5.7: Piezoelectric harvester resistive loading circuit (a) equivalent circuit model of P876.A11 piezoelectric transducer (b) phasor diagram of P876.A11

The reactance of C_{PZT} can be calculated using Equation (5.11).

$$X_C = \frac{1}{\omega C_{PZT}} = \frac{1}{2\pi f C_{PZT}} = \frac{1}{2 \times \pi \times 70Hz \times 125nF} = 18189\Omega \qquad (5.11)$$

The optimum load is 18194Ω as calculated in (5.12)

$$R_L = \sqrt{R_{PZT}{}^2 + X_C{}^2} = \sqrt{466\Omega^2 + 18189\Omega^2} = 18194\Omega \qquad (5.12)$$

and V_{PZT} lags I_L by

$$\tan^{-1}\left(\frac{-18189}{466+18194}\right) = -44.27° \qquad (5.13)$$

By inserting these values into the equivalent circuit (Figure 5.7), the circuit model can then be simulated in an electronic circuit simulation package. Using Orcad Pspice, the average power P_L for the optimum resistor value R_L was found to be around 13μW. It was found that increasing or decreasing R_L from this value reduced the power output from the simulation.

5.4 Review of Resistive Circuit Topologies

The previous circuit dissipates energy in the load resistor, but is not suitable for powering most electronic circuits, because such circuits need a DC supply. This section reviews two practical methods of resistive load matching which produce a DC output for use by electronic loads.

5.4.1 Standard Rectification Circuit

Figure 5.8 shows the most common load circuit for a piezoelectric harvester, which is a bridge rectifier to convert the AC voltage to DC, a reservoir capacitor C_L and the load R_L, which simulates the electronic circuit being supplied.

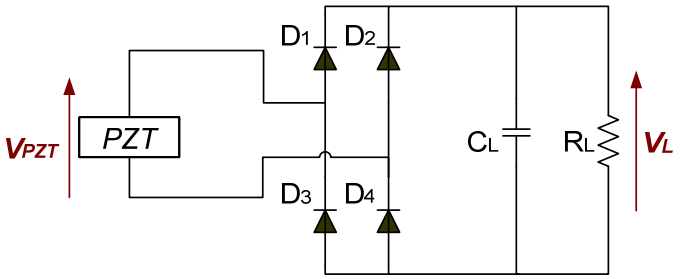

Figure 5.8: Standard piezoelectric transducer interface

Although this is the simplest rectification method, the piezoelectric output capacitive impedance is present, and therefore the circuit does not extract the maximum power available from the piezoelectric harvester. This circuit has been extensively analysed in the literature [16, 23, 24, 26, 86, 163-165] and is frequently used as a bench mark for comparison with other circuits.

5.4.2 Voltage Multiplier Circuit

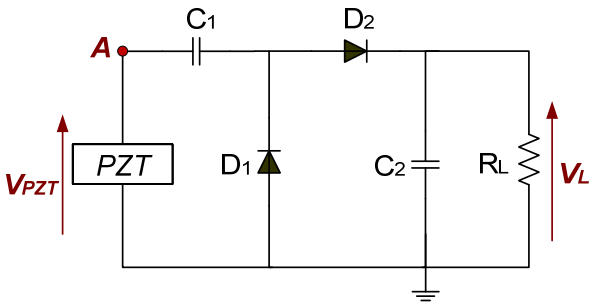

Figure 5.9: Voltage doubler circuit for piezoelectric transducer

A voltage multiplier circuit can both rectify and increase the piezoelectric output voltage, to produce a DC voltage approximately two or more times the peak input AC voltage. There are several different voltage multiplier circuits available [26, 166-168]. A typical voltage doubler circuit is shown in Figure 5.9.

The multiplier operates in the following manner. Assume the peak output voltage from the PZT source is $\tilde{V}_{PZT}$. Thus point A will have a sinusoidal voltage of peak values $\pm\tilde{V}_{PZT}$. When point A goes negative, diode D_1 conducts and C_1 is charged so

that its right hand side is at $+\tilde{V}_{PZT}$ (ignoring diode voltage drop) with respect to its left hand side. When point *A* goes positive, D_2 conducts and charge from C_1 transfers to C_2. After several cycles of operation, C_2 ends up with $+2V_{PZT}$ across it. If more stages are added, higher voltage increases can be obtained. In practice C_1 is formed from the output capacitance of the piezoelectric device, C_{PZT}.

Although the voltage can be increased, the output voltage ripple increases as more stages are added, and also the output current decreases. Hence the circuit cannot extract more power than an ordinary resistor load, from the piezoelectric harvester, and again the material's capacitive impedance limits the output current and therefore power [24, 26, 165].

5.4.3 Summary

Two resistive piezoelectric load circuits have been discussed in this section. Resistive loading of the piezoelectric material is not the best solution for impedance matching, since the capacitive output impedance severely restricts the maximum power output that can be obtained. In addition, both circuits have diodes which produce voltage drops and reduce conversion efficiency. Some researchers have investigated switched circuits to enhance the electrical output of piezoelectric devices and these circuits are discussed in the next section.

5.5 Review of Switched Circuit Topologies

5.5.1 Synchronized Switch Harvesting on Inductor (SSHI) Circuit

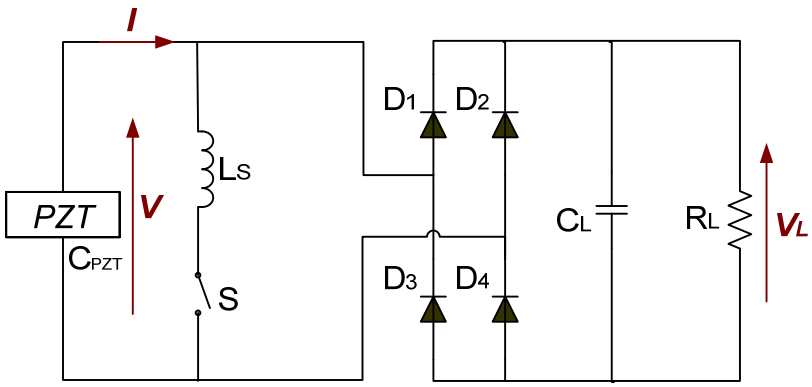

Figure 5.10: Synchronized switch harvesting on inductor (SSHI) circuit

The synchronized switch harvesting on inductor circuit (SSHI) was originally proposed by Richard et al [169] and later modified by Guyomar et al [163]. The circuit is shown in Figure 5.10. The switch S switches on and off at maximum and minimum input vibration displacement u, see Figure 5.11, assuming the displacement u is sinusoidal at resonance. Note V_M represents the amplitude of voltage V.

The closure of switch S when V reaches V_M produces a current which flows from C_{PZT} through L_S. The components C_{PZT} and L_S form a resonant circuit, and so a sinusoidal voltage swing is produced across the piezoelectric energy harvester when S closes. When the sinusoidal current tries to reverse, switch S is opened, clamping the voltage V at $-V_M e^{-\pi/2Q}$. The process is repeated later when V reaches $-V_M$. Thus V is increased as shown in Figure 5.11 and more power is provided to the load R_L.

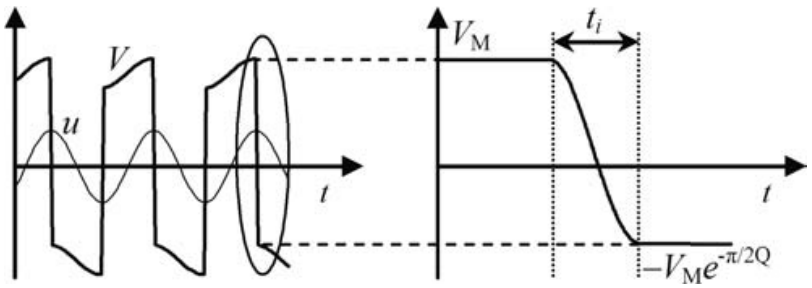

Figure 5.11: Inversion process of SSHI circuit [16]

The inversion time t_i is given by [16]:

$$t_i = \pi\sqrt{L_S C_O} \tag{5.14}$$

A high value of inductance is not required so that t_i is very short compared to the displacement period.

A SSHI circuit using two switch circuits in parallel with the piezoelectric energy harvester was investigated by Qiu et al [26], this is shown in Figure 5.12.

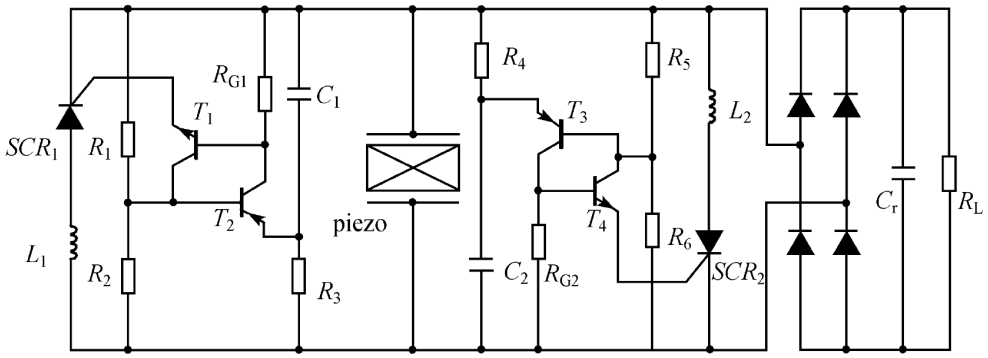

Figure 5.12: SSHI solution by Qiu et al [26]

In Figure 5.12, there are two inductors L_1 and L_2, and the switches are formed by SCR_1 and SCR_2. T_1, T_2 and T_3, T_4 form the trigger circuits for the SCRs [26, 31, 32]. When the vibration displacement is at a maximum one SCR is turned on, and when the displacement is a minimum, the other SCR is turned on. The SCRs naturally turn off when the resonant current tries to reverse.

Another form of SSHI circuit was also investigated by Ben-Yakkov et al [170], as shown in Figure 5.13.

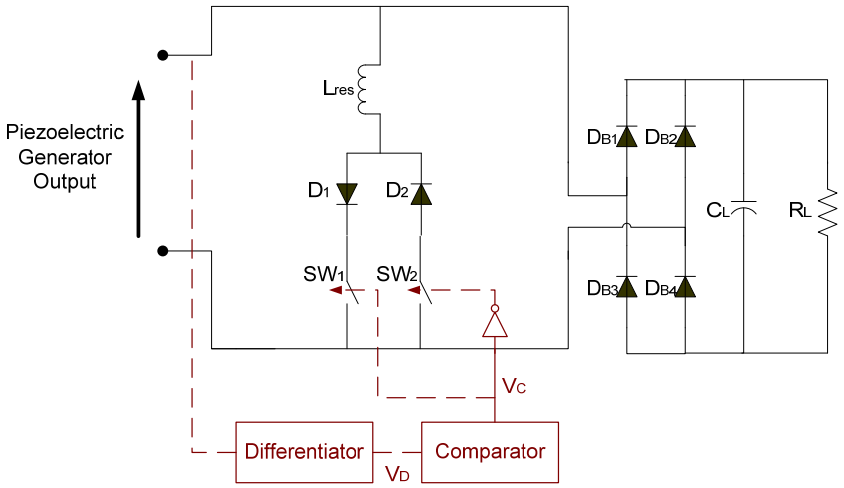

Figure 5.13: Ben-Yaakov circuit model [170]

The circuit uses an inductor and the piezoelectric capacitance to form a resonant network controlled by switches. An external voltage source was used to power the comparator in his experiment.

The SSHI topology provides a significant improvement over the standard resistive load circuits described in the previous section. According to [16], a measured power increase of 400% was found to occur over a standard resistive load circuit, when using the SSHI topology.

However, the SSHI circuit is not an easy circuit to design. Firstly, the trigger circuits for the SCRs are designed to be optimum at one frequency. If the frequency changes, the circuit will no longer be optimal. Secondly, the transducer voltage changes rapidly when the switches conduct. This rapid voltage change can inject energy back into the mechanical system creating an energy loss [16]. Thirdly, the method is based on the assumption that the input vibration displacement is sinusoidal and the vibration amplitude is known, whereas in practical systems the piezoelectric transducer internal voltage may not be sinusoidal, since the displacement may not be sinusoidal, and the amplitude is variable.

5.5.2 Synchronous Charge Extraction Circuit

The synchronous charge extraction circuit was proposed by Lefeuvre et al in 2005 [23, 24], and has been studied by many researchers including Qiu et al [26], see Figure 5.14(a). Waveforms for V_{PZT}, I and displacement u are shown in Figure 5.14(b) [86].

The circuit is, in essence, a rectifier with a buck-boost circuit connected to its DC output terminals. The buck-boost circuit switch turns on when the rectifier DC voltage reaches a maximum and turns off when the rectified voltage becomes zero. The value of L_S is chosen so that all the charge on C_{PZT} is removed in a time much shorter than the period of displacement. Lefeuvre et al [23, 24, 86, 165] claims that this topology can theoretically produce four times more power than the circuit of Figure 5.8.

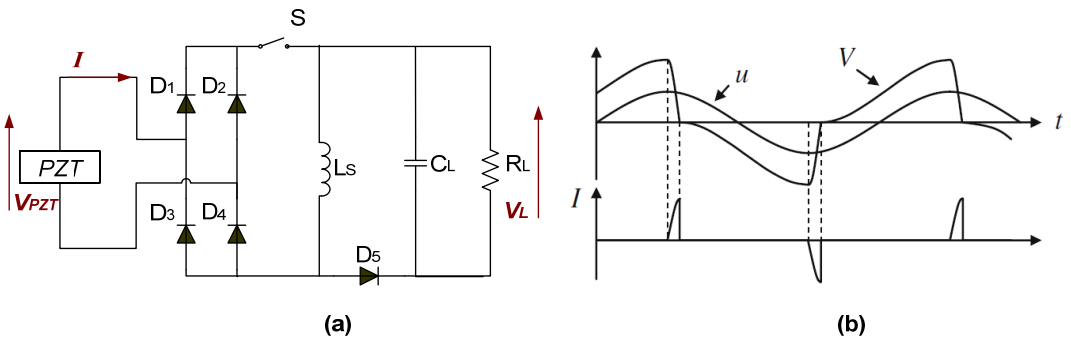

Figure 5.14: Synchronous charge extraction circuit for piezoelectric harvester [26, 86]
(a) circuit schematic (b) waveforms

The circuit operates in a similar manner to the SSHI circuit. The switch opens and closes at the minimum and maximum input vibration displacement. Hence the topology will have difficulties similar to that of the SSHI circuit.

5.5.3 Summary

This section, 5.5, has reviewed two different switched circuits for piezoelectric energy harvesters. These circuits are difficult to implement and control, and although energy gains are possible, the circuits only partially compensate for the impedance of C_{PZT}. The trigger circuits depend on there being a known value of displacement frequency, whereas in practice this may not be the case. The next section analyses the method of load matching by inserting an external inductor into the harvester's load circuit.

5.6 Inductive Load Matching Circuit Analysis

The capacitive impedance of a piezoelectric energy harvester is high, which limits the power output. Many researchers have looked at compensating the capacitive output impedance by means of an inductor in shunt or series with the resistor load. This section investigates the effect of such an inductor on the piezoelectric harvester.

Kong et al, Niezrecki et al, Viana et al and Park et al [22, 110, 145, 156] investigated the effects on an equivalent circuit when an inductor L_S was connected in series or parallel with a piezoelectric energy harvester load.

For any parallel *RL* circuit, as shown in Figure 5.15 there is an equivalent series *RL* circuit which behaves identically.

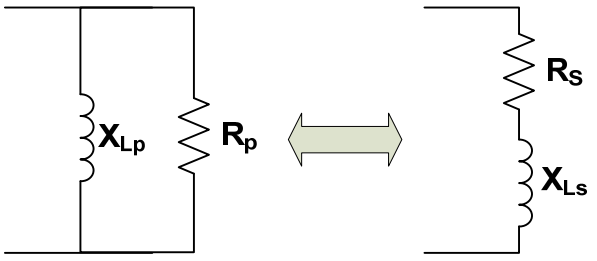

Figure 5.15: Inductor connected in parallel and series with a resistor

It can be shown that

$$R_S = \frac{X_{Lp}^2 R_p}{\left(R_p - X_{Lp}\right)^2} \tag{5.15}$$

and

$$X_{LS} = \frac{X_{Lp} R_p^2}{\left(R_p - X_{Lp}\right)^2} \tag{5.16}$$

Thus it is not necessary to analyse both parallel and series connections of L_S with the load since mathematically they can be made equivalent. For this reason only the series L_S case is considered here. Figure 5.16 shows an inductor L_S connected in series with a piezoelectric energy harvester and a load.

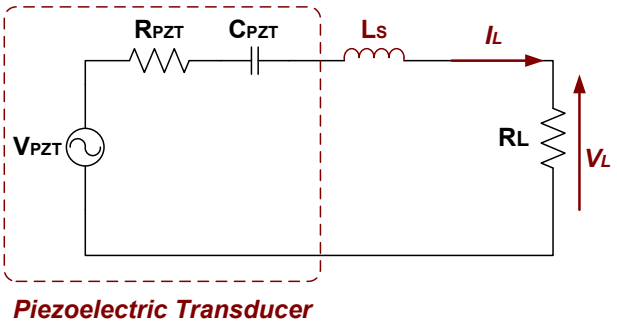

Figure 5.16: Inductor connected in series with piezoelectric generator

According to [22, 171], Figure 5.16 can be reduced to the circuit shown in Figure 5.17. The maximum power transfer of a resonant circuit occurs when the load impedance is the complex conjugate of the source impedance.

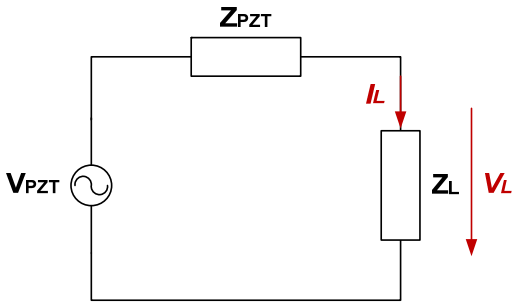

Figure 5.17: Inductive component in series piezoelectric transducer [22]

Assume an AC voltage source V_{PZT} and a piezoelectric harvester output impedance Z_{PZT} of R_{PZT}-jX_{PZT}. For maximum power output the complex load impedance Z_L must be R_L+jX_L, where $R_L=R_{PZT}$ and $|X_L|=|X_{PZT}|$. The maximum power that can be delivered to the load is [22]:

$$P_L = \left| \frac{V_{PZT}}{Z_{PZT} + Z_L} \right|^2 R_L = \frac{V_{PZT}^2 R_L}{(R_{PZT} + R_L)^2 + (-X_{PZT} + X_L)^2} \tag{5.17}$$

Since the load impedance equals the complex conjugate of the source impedance, therefore Equation (5.17) becomes Equation (5.18) [22]:

$$P_L = \frac{V_{PZT}^2}{4R_{PZT}} \tag{5.18}$$

In Figure 5.18(b), the phasor diagram shows that the capacitive component $-jX_CI_L$ has been cancelled out by jX_LI_L.

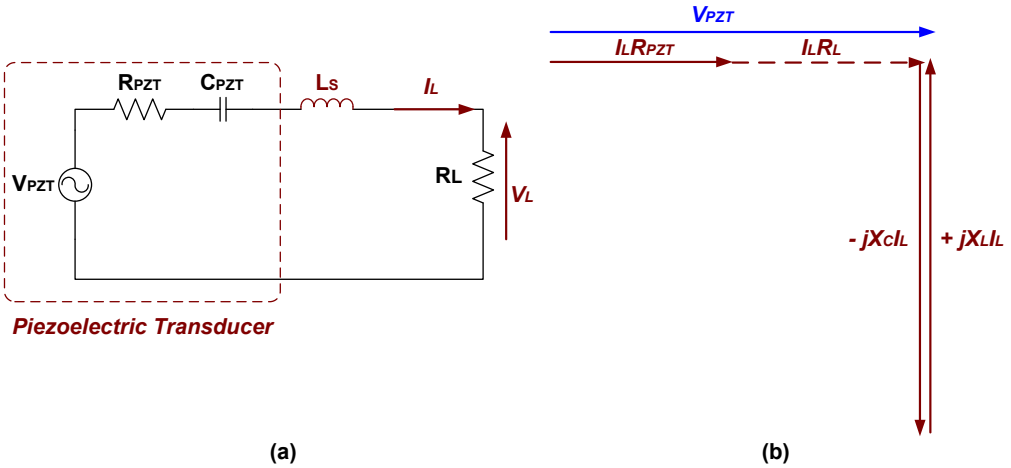

Figure 5.18: Inductor in series connection with piezoelectric harvester and an optimum load (a) circuit diagram (b) phasor diagram

Using the parameters measured for the P876.A11 transducer at $70Hz$, the required value of L_S can be calculated from Equation (5.19):

$$L_S = \frac{1}{\omega^2 C_{PZT}} = \frac{1}{(2\times\pi\times 70Hz)^2 \times 125nF} = 41.356H \qquad (5.19)$$

The equivalent circuit of the P876.A11 transducer with a series connected inductor L_S of this value is shown in Figure 5.19.

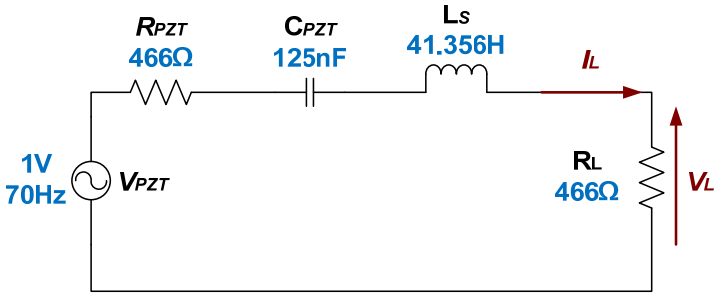

Figure 5.19: An inductor in series connection with P876.A11 transducer and load R_L

The circuit shown in Figure 5.19 was simulated using Orcad Pspice, and it was found that the averaged power P_L is around $255\mu W$. The inductive impedance

matching method has therefore improved the power output by a factor of almost 20 compared to the power output of a standard resistive load.

According to [22, 171, 172], complex conjugate impedance matching of piezoelectric material is impractical since the inductor required is prohibitively large, and this has limited the use of this matching method.

5.7 Review of Resonant Circuit Topologies

Although the complex conjugate matching technique is claimed to be impractical, nevertheless its benefit of a much increased power output is very attractive. For this reason it was decided by the author to further investigate the technique.

Several circuits which might produce the inductance required for a piezoelectric harvester complex conjugate impedance matching, were investigated by the author, and these are discussed in the following sections.

5.7.1 Inductor

Taking the P876.A11 transducer as an example, this requires an inductor of about $41H$ to obtain matching at $70Hz$, as shown in Figure 5.19.

Table 5.1 gives the inductor values required for this transducer at other frequencies, assuming its capacitance is fixed at $125nF$.

Table 5.1: Inductance required for 125nF capacitance C_{PZT} at various frequencies

Inductance L (H)	Frequency f (Hz)
2026.4	10
81.1	50
20.3	100
5.1	200
2.3	300

For vibration frequencies below, say 100Hz, an inductor is required having a value greater than approximately 20H. Although it is possible to make an inductor of this value, its physical size would be prohibitively large when considering the harvester design objectives of low mass and volume. In addition, a fixed inductor can only give complex conjugate matching at one frequency.

5.7.2 Synthetic Inductor/Gyrator

In an attempt to overcome the need for a prohibitively large inductor, circuits which simulate inductors using operational amplifiers have been studied by many researchers [110, 146, 173-175]. Viana et al [110] analysed various synthetic inductor circuits for piezoelectric energy harvesters in 2006.

To analyse the feasibility of such circuits, a simpler synthetic inductor circuit, developed by Torres et al [176] and Muthuswamy et al [177] was analysed, see Figure 5.20. The circuit was initially proposed by Chua [178].

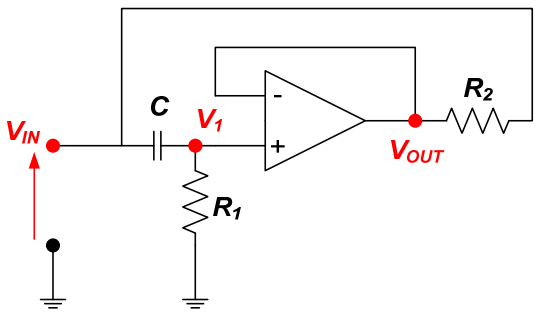

Figure 5.20: Chua's synthetic inductor circuit [176, 178]

Assuming the operational amplifier has infinite input impedance, then:

$$Z_{IN} = \frac{V_{IN}}{I_{IN}} = \frac{V_{IN}}{\left[\frac{V_{IN}}{R_1 + (1/j\omega C)}\right] + \left(\frac{V_{IN} - V_{OUT}}{R_2}\right)} \tag{5.20}$$

In practice operational amplifier are not ideal. Assume the gain of the amplifier to be A where A is close to, but not equal to, unity. Thus:

$$V_{OUT} = AV_1 = \frac{AV_{IN}R_1}{R_1 + (1/j\omega C)} \tag{5.21}$$

Substituting (5.21) into (5.20), yields:

$$Z_{IN} = \frac{V_{IN}}{I_{IN}} = \frac{R_2\left[R_1 + (1/j\omega C)\right]}{\left[\frac{R_2}{R_1 + (1/j\omega C)}\right] + 1 - \left[\frac{AR_1}{R_1 + (1/j\omega C)}\right]} \tag{5.22}$$

Simplifying (5.22):

$$Z_{IN} = \frac{j\omega CR_1R_2 + R_2}{1 + j\omega C\left[R_2 + R_1(1 - A)\right]} \tag{5.23}$$

From (5.23), it can be seen that the numerator represents a practical inductor of value CR_1R_2, having a resistance R_2. The denominator shows that the inductance and resistance will decrease as the input frequency increases. R_1 is typically 10^4 times greater than R_2, so that the gain of A is critical if the simulated inductor is to function correctly at higher frequencies. Thus the gyrator circuit has a limited operating frequency above which it will not function correctly.

According to Viana et al [110], there are two main types of synthetic inductor circuits, one proposed by Antoniou [173, 179, 180] and another proposed by Riordan [174]. The circuit diagrams of these are shown in Figure 5.21.

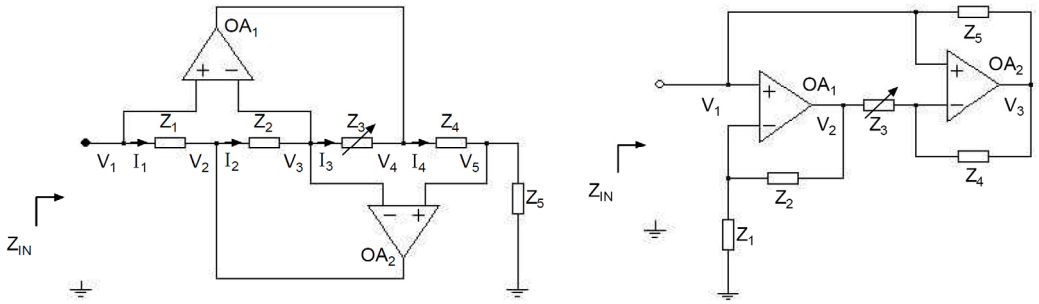

(a) (b)

Figure 5.21: Synthetic inductor (a) Antoniou circuit (b) Riordan circuit [110]

Both circuits have the same equations for input impedance, which is [110, 173, 174, 179, 180]:

$$Z_{IN} = \frac{Z_1 Z_3 Z_5}{Z_2 Z_4} \tag{5.24}$$

and this input impedance is made to appear inductive by choice of Z_1, Z_2, Z_3, Z_4 and Z_5. The impedance components Z_1, Z_2, Z_3, Z_4 and Z_5 are given as:

$$Z_1 = R_1;\;\; Z_2 = R_2;\;\; Z_3 = R_3;\;\; Z_4 = -\left(\frac{j}{\omega C_4}\right);\;\; Z_5 = R_5; \tag{5.25}$$

Thus the input impedance Z_{IN} is:

$$Z_{IN} = j\omega L_S \tag{5.26}$$

Substituting (5.25) into (5.24), and comparing with (5.26), yields [110]:

$$L_S = \frac{R_1 R_3 C_4 R_5}{R_2} \tag{5.27}$$

The analyses given by Antoniou [173, 179, 180] and Riordan [174] are simplistic and ignore operational amplifier imperfections, which produce resistances in parallel and series with the synthetic inductance. In general the resistance associated with the synthetic inductor increases as the inductance increases. Viana et al [110] measured the associated resistance of the synthetic inductor as shown in Figure 5.22, between electrical resonance frequencies of 20*Hz* and 400*Hz*.

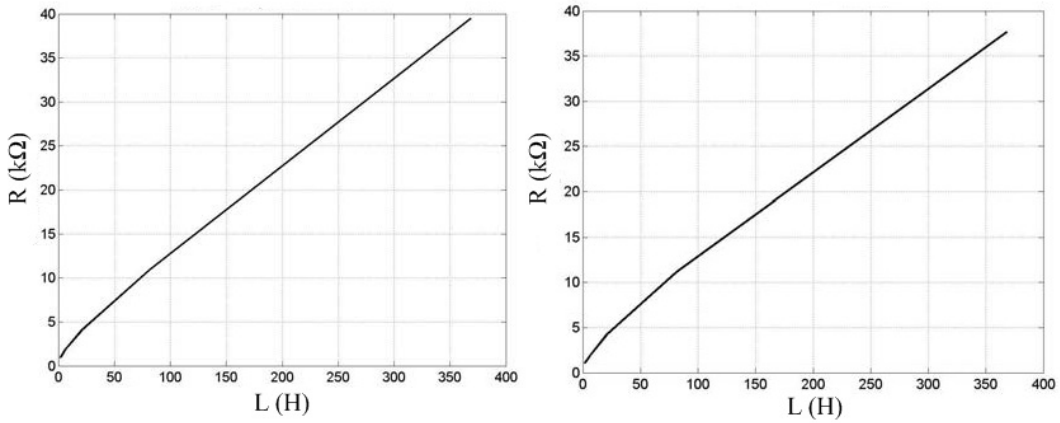

(a) (b)

Figure 5.22: Resistance versus inductance of synthetic inductor (a) Antoniou circuit (b) Riordan circuit [110]

The parasitic series resistance of these two circuits is around 7.5*k*Ω for a simulated inductance of 50*H*, which is too high for most piezoelectric harvesters.

5.7.3 Summary

In this Section, 5.7, two techniques that might be suitable for piezoelectric inductive impedance matching have been reviewed. The possibilities of using an inductor and the gyrator circuit were reviewed and discussed. These techniques all have problems and are unlikely to produce any improvement in harvester power output.

5.8 Conclusion

This chapter reviewed and investigated different load matching circuits for piezoelectric energy harvesters. Section 5.1 describes the standard equivalent circuit for piezoelectric energy harvesters.

Section 5.4 investigated different methods of resistive load matching for the harvesters. This includes the basic bridge rectifier and voltage multiplier circuits. It was shown that the standard circuits cannot extract maximum energy from the harvester due to its high capacitive output impedance and that an inductor is needed at the output stage to increase the power harvested.

Sections 5.5 to 5.7 show several circuits which could reduce the high inductance requirement from the piezoelectric harvester circuit and several possible solutions for inductive loading have been considered by the author. Possibilities include using an inductor, gyrator, SSHI circuit or synchronous charge extraction circuit. It was found by author that for a piezoelectric transducer such as P876.A11, there would be a 20 times power amplification by using output capacitance cancellation in comparison to a standard resistive load circuit. However, problems exist with all the investigated circuits, such as high resistance loss (gyrator), impractical physical size (inductor) and uncertainties over control of switches (SSHI/Synchronous charge extraction circuit). Hence, these difficulties limit the circuits, preventing the extraction of maximum power from the device.

In searching for alternative circuits, the author concluded that a circuit similar to a gyrator was needed, since such circuits do not rely on a knowledge of the source voltage. In the next chapter the author proposes an amplified inductor circuit which does not need a measure of voltage, but which potentially may have less resistive losses than a gyrator circuit. The circuit to the author's knowledge has never been contemplated as an energy harvester load circuit.

Chapter 6 :

Amplified Inductor Circuit Theory, Simulation and Experimental Results

6.1 Introduction

This chapter investigates a new circuit for piezoelectric energy harvester complex conjugate impedance matching. From the review in Chapter 5, to be able to work with piezoelectric harvesters, a simulated inductor circuit should have the following characteristics. Firstly, the circuit should simulate an inductor over a wide range of harvester output voltage amplitude and frequency. Secondly, the simulated inductor circuit should have a low loss at the harvester's frequency. Thirdly, the inductor simulation circuit should provide an energy gain which is greater than any losses arising from within the circuit or its use. Finally the circuit should give easy control of the simulated inductance value so that complex conjugate matching can be achieved over a range of frequencies.

The technique described here has not to the author's knowledge, yet been investigated for piezoelectric energy harvesters. The concept of the circuit is described in the next section. It is basically an amplifier which augments the voltage across an inductor and adds the augmented voltage to the end of the inductor, thereby increasing the effective inductance.

6.2 Literature Study of Amplified Inductor Circuit

The amplified inductor system is based on the circuit for a micromachine time constant regulator [181-185]. Similar systems were also developed to provide electrical compensation for transformers, see [186-189]. A micromachine is an alternator that has some per unit characteristics of a large (e.g 330*MW*) alternator. Micromachines were used to simulate electrical power systems of perhaps several 1000*MW* size, yet these machines have only low power ratings of perhaps 3*kW*.

The difficulty with micromachines is that the per unit resistance of the field and damper windings cannot be easily made identical to the full scale machine. The per unit winding resistances of the micromachine are inherently higher than those of a typical power station alternator giving untypical responses.

A technique for correcting these responses was developed which used a time constant regulator. A time constant regulator uses analogue feedback circuits and a power amplifier to modify the time constant of a winding making the micromachine behave in a manner similar to that of a full scale machine [181-185]. A simplified schematic of the circuit is shown in Figure 6.1.

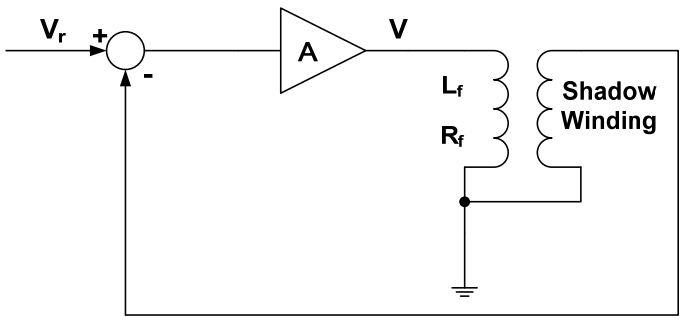

Figure 6.1: Time constant regulator schematic

In Figure 6.1, V_r is the reference voltage into the amplifier A, R_f is the resistance of the winding, and L_f is the winding inductance.

6.3 Amplified Inductor Circuit Concept for Piezoelectric Energy Harvester

The circuit shown in Figure 6.1 has been redrawn, see Figure 6.2, to show how it might be used with a piezoelectric energy harvester.

The method has the advantage that the source voltage V_{PZT} does not need to be measured, whereas for switched circuits such as SSHI, the amplitude and frequency of V_{PZT} needs to be known.

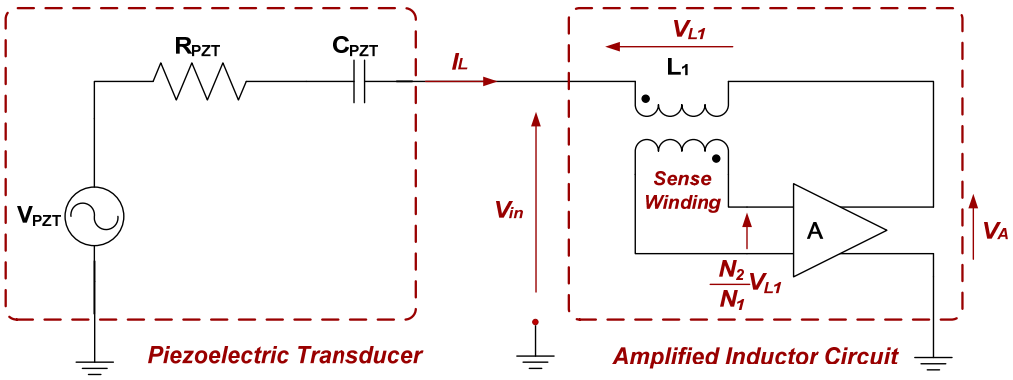

Figure 6.2: Concept of amplified inductor using ideal amplifier

As shown in Figure 6.2, L_1 is an inductor with a sense winding wound on the same core. The sense winding provides a measure of the $L_1\left(\frac{dI_L}{dt}\right)$ voltage across the inductor. The sense winding is connected to the input of the amplifier, gain A, and the output of the amplifier is connected to the right hand side of L_1. The ground terminal of the harvester is connected to the ground of the amplifier.

The voltage across L_1 is given by $V_{L1} = L_1\left(\frac{dI_L}{dt}\right)$ and the sense winding voltage is:

$$\frac{N_2}{N_1}V_1 = L_1\frac{N_2}{N_1}\left(\frac{dI_L}{dt}\right) \tag{6.1}$$

where N_1 is the number of inductor turns and the N_2 is the number of sense winding turns.

The voltage output from the amplifier is:

$$V_A = AL_1 \frac{N_2}{N_1}\left(\frac{dI_L}{dt}\right) \tag{6.2}$$

This voltage V_A is connected to the right hand side of L_1. The voltage seen by the piezoelectric harvester, V_{in}, is given by:

$$V_A = L_1 \frac{dI_L}{dt} + AL_1 \frac{N_2}{N_1}\left(\frac{dI_L}{dt}\right) = L_1\left(1 + A\frac{N_2}{N_1}\right)\left(\frac{dI_L}{dt}\right) \tag{6.3}$$

Hence the total inductance of the system becomes:

$$L_{TOTAL} = L_1\left(1 + A\frac{N_2}{N_1}\right) \tag{6.4}$$

Figure 6.3 shows an amplified inductor circuit and piezoelectric transducer, connected in series with a load R_L, and the phasor diagram associated with it, when gain A is adjusted so that:

$$\omega = \sqrt{\frac{1}{L_1\left(1 + A\frac{N_2}{N_1}\right)C_{PZT}}} \tag{6.5}$$

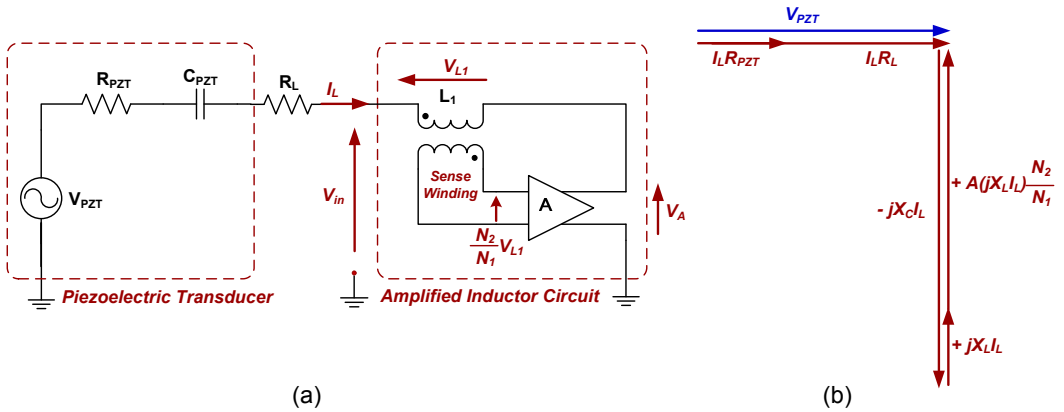

Figure 6.3: Amplified inductor circuit with load (a) circuit (b) phasor diagram

As shown in Figure 6.3(b), the voltage drop caused by the output capacitance C_{PZT} is cancelled by the voltage drop due to L_{TOTAL}, so that the power in the load is increased, assuming the only circuit losses are in R_L and R_{PZT}.

6.4 Amplified Inductor Circuit Implementation Considerations

In considering the design of an amplified inductor circuit, several important factors need to be considered. When resonance occurs, as shown in Figure 6.3, the current taken from the piezoelectric device increases greatly. Using the P876.A11 transducer as an example, at $70Hz$, R_{PZT} is 466Ω and X_C is 18189Ω. If A is adjusted to provide electrical resonance and R_L equals R_{PZT}, then the voltage across C_{PZT} is:

$$V_C = jX_C I_L = \left(\frac{18189\Omega}{2\times 466\Omega}\right) V_{PZT} \approx 19.5 V_{PZT} \tag{6.6}$$

If V_{PZT} is $1V$, then V_{in} will also be $19.5V$. The amplifier has to provide a high proportion (η_{amp}) of this voltage, as can be seen from Equation (6.7).

$$\eta_{amp} = \frac{\left(A\frac{N_2}{N_1}\right)}{\left(1 + A\frac{N_2}{N_1}\right)} \tag{6.7}$$

Equation (6.7) is derived from Equation (6.3) and η_{amp} is the proportion of V_{in} which comes from the amplifier.

Operational amplifiers are not suitable for the scheme proposed here, since they are linear amplifiers and therefore lossy and have a limited output voltage range.

A switched mode amplifier may be suitable since it can be designed to withstand a higher voltage than an operational amplifier and can usually provide a high efficiency, 90% or more being achievable. However, whether such a high efficiency can be maintained for a piezoelectric harvester load circuit is as yet unknown.

For switch mode amplifiers, since feedback will be present in the circuit, a low pass filter is essential to prevent circuit instability due to switching voltages being fed back into the modulator.

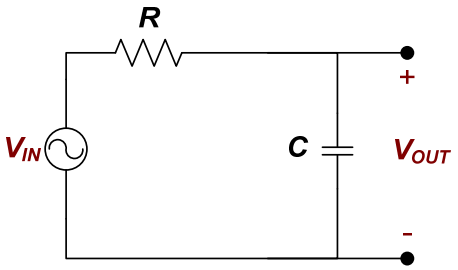

Figure 6.4: Low pass filter schematic

For a RC low pass filter as shown in Figure 6.4:

$$\frac{V_{OUT}}{V_{IN}} = \frac{1}{1 + j\omega T} \tag{6.8}$$

where T is the time constant and is equal to RC. Incorporating the RC filter into Figure 6.3 produces Figure 6.5, and its phasor diagram is shown in Figure 6.6.

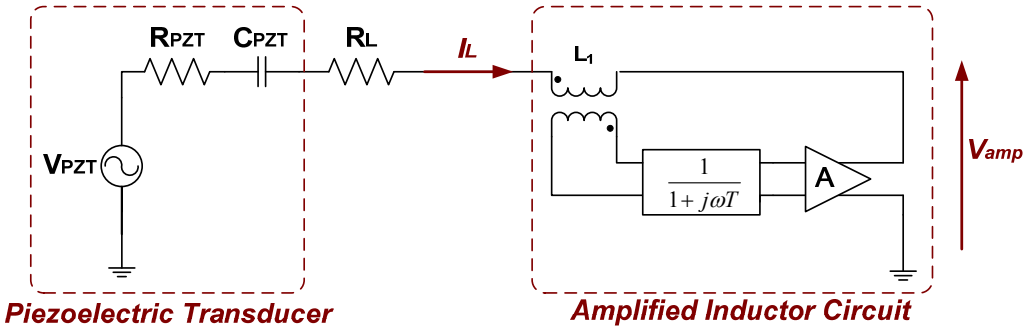

Figure 6.5: Schematic diagram of amplified inductor circuit

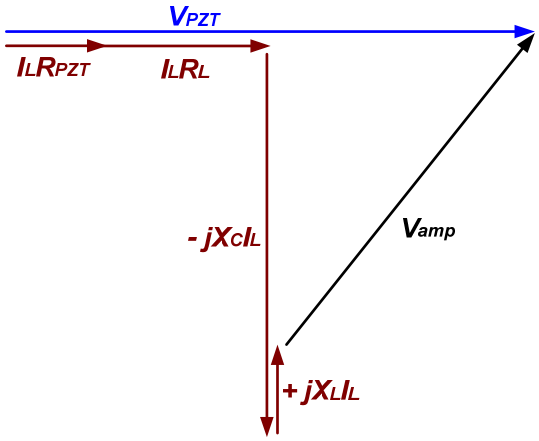

Figure 6.6: Phasor diagram of amplified inductor circuit

In Figure 6.6, V_{PZT} is the maximum available output voltage from the piezoelectric energy harvester, $I_L R_{PZT}$ represents the resistive voltage drop in the piezoelectric material, $I_L R_L$ represents the voltage across the load R_L, $jX_C I_L$ represents the voltage across the output capacitor C_{PZT}. The term $jX_L I_L$ is the voltage across the inductance L_1, and V_{amp} is the voltage from the amplifier.

Figure 6.7 shows how V_{amp} can be split into two components: $I_L R_{amp}$ in phase with V_{PZT} and $+A(jX_L I_L)\frac{N_2}{N_1}$ in quadrature with V_{PZT}.

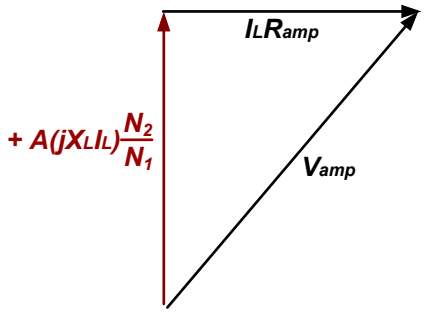

Figure 6.7: Phasor diagram of the amplifier

Redrawing Figure 6.6 then produces Figure 6.8:

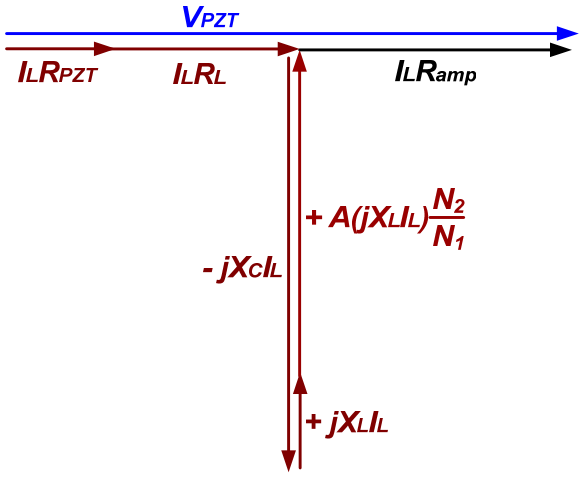

Figure 6.8: Detailed phasor diagram of the amplified inductor circuit

In Figure 6.8 the phasor $A(jX_L I_L)\frac{N_2}{N_1}$ represents a purely reactive voltage drop and does not expend energy. The phasor $I_L R_{amp}$ is produced by the phase shift of the RC filter, and represents an effective resistance in the amplifier. The effective resistance R_{amp} is a fictitious component created to explain the operation of the circuit. The term $I_L^2 R_{amp}$ is the power going into the amplifier from the harvester. This was verified by simulation using OrCad Pspice. Thus the harvester will produce power in both R_L and R_{amp}. It is therefore sensible to eliminate R_L and instead take harvester power through the amplifier.

Let $N_r = \frac{N_2}{N_1}$ and ignoring the load R_L, Figure 6.5 can now be drawn as Figure 6.9.

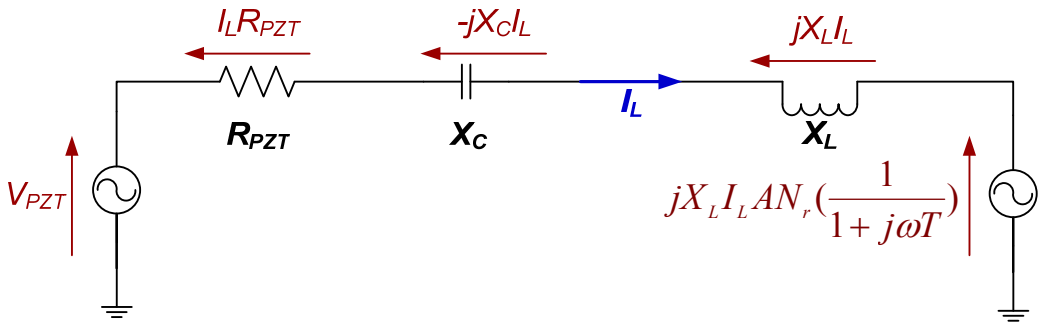

Figure 6.9: Amplified inductor circuit schematic

In Figure 6.9, term $jX_L I_L AN_r\left(\frac{1}{1+j\omega T}\right)$ is the voltage from the amplifier, hence:

$$V_{PZT} = I_L R_{PZT} - jX_C I_L + jX_L I_L + \left(\frac{jN_r X_L I_L A}{1+j\omega T}\right) \tag{6.9}$$

Equation (6.9) can be rearranged as:

$$\frac{V_{PZT}}{I_L} = R_{PZT} + \left(\frac{AN_r X_L \omega T}{1+\omega^2 T^2}\right) + j\left[\left(1+\frac{AN_r}{1+\omega^2 T^2}\right)X_L - X_C\right] \tag{6.10}$$

Replacing X_L by ωL_1, the amplified inductor resistance R_{amp} is given by:

$$R_{amp} = \frac{\omega^2 L_1 AN_r T}{1+\omega^2 T^2} \tag{6.11}$$

From Equation (6.11), by adjusting the gain A and time constant T, the effective resistance and inductance of the amplified inductor circuit can be controlled. To obtain the appropriate inductance L_{TOTAL} in Equation (6.4) and thereby cancel the voltage drop across C_{PZT}, the gain of the amplifier A can be altered accordingly. R_{amp} can then be adjusted via T to match the harvester output resistance R_{PZT} and achieve

maximum power transfer. The next section discusses design considerations of the circuit.

6.5 Prototype Amplified Inductor Circuit Design

6.5.1 Design Considerations

An amplified inductor circuit using an amplifier incorporating Pulse Width Modulation (PWM) is proposed, as a potential method of producing complex conjugate load matching, the block diagram of which is shown in Figure 6.10.

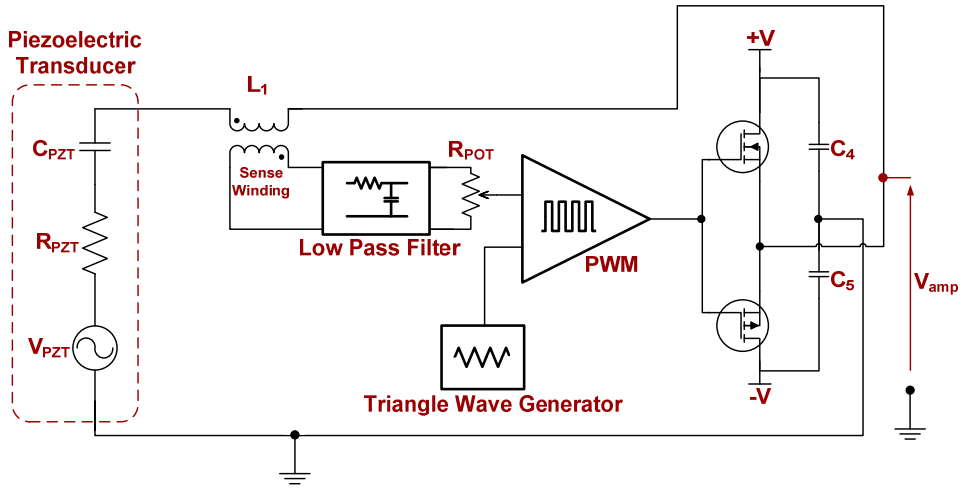

Figure 6.10: Amplified inductor circuit block diagram

In this circuit the sense winding output voltage is filtered by the low pass filter, and is attenuated by R_{POT} and turned into a PWM signal by the PWM block. The triangle wave generator determines the switching frequency f_s. The PWM block drives the output transistors, which are a complementary pair of MOSFETs, directly. This topology avoids the need for isolated gate drives, ensuring fast turn on and off of the output transistors, minimising switching losses. The low pass filter, triangle wave generator and PWM block are powered by a $5V$ battery in this prototype design.

The square wave output voltage V_{amp} is applied to the right hand side of inductor L_1, the left hand side of L_1 being connected to the piezoelectric device. The piezoelectric device comprises elements V_{PZT}, R_{PZT} and C_{PZT}, and its other terminal is connected to the junction of C_4 and C_5 which provide an AC earth point. A DC earth point is not provided for the piezoelectric device since this can, if V_{amp} has a DC offset, cause gradual depolarisation.

The complementary MOSFET output transistors have inherent anti-parallel diodes across them (not drawn). This is an inherent property of any MOSFET. The diodes provide thereby a means by which energy can flow from the harvester into the power supply rails of the amplifier.

In this prototype circuit, it was decided to make the inductance of L_1 as high as possible, so that the gain-bandwidth product of A is as small as possible and therefore switching losses can be minimised. Figure 6.11 shows how the gain-bandwidth product of the amplifier $\frac{A}{2\pi T}$ relates to the switching frequency.

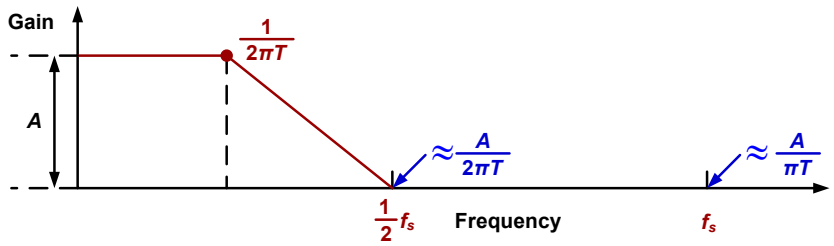

Figure 6.11: Gain bandwidth plot of switching frequency and RC constant

In Figure 6.11, T is the RC time constant of the low pass filter and A is the amplifier gain. For stability it is necessary to have an amplifier gain less than unity at half the switching frequency [190, 191]. Thus f_s must be greater than or equal to twice the gain-bandwidth product, i.e. $\frac{A}{\pi T}$.

6.5.2 Circuit Schematic and Operation

Figure 6.12 gives a full circuit diagram of the amplified inductor circuit. Approximate values for R_{PZT} and C_{PZT} for the P876.A11 transducer at $70Hz$ have been added. Note that R_{PZT} is 60Ω instead of 466Ω. This is because the circuit was tested, see later, with a function generator having an output resistance of 60Ω.

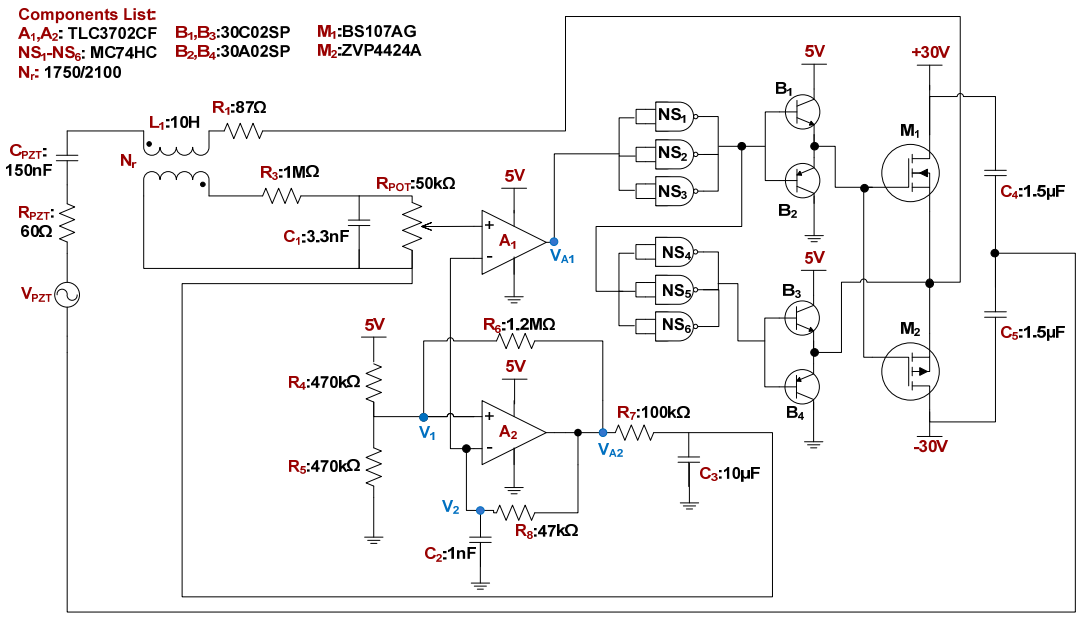

Figure 6.12: Circuit schematic of amplified inductor circuit proposed

It was decided for this initial test that L_1 would be $10H$, this being about the highest inductance value that could be constructed on an ETD59 core, without an excessive winding resistance. An inductor was designed and wound, see Appendix C. Its resistance was 87Ω and this is included in Figure 6.12. R_3, R_{POT} and C_1 form a low pass filter to eliminate switching voltages from the feedback path. R_{POT} is a ten turn potentiometer and also controls the gain of the amplifier.

Amplifier A_2 is the triangle wave generator and its operation is as follows. Assume V_{A2} is a $5V$ square wave as shown in Figure 6.13. The voltage V_1 is an attenuated version of V_{A2} due to the potential division of resistors R_4, R_5 and R_6, with a mean value of $2.5V$, and a peak to peak value of around $1V$.

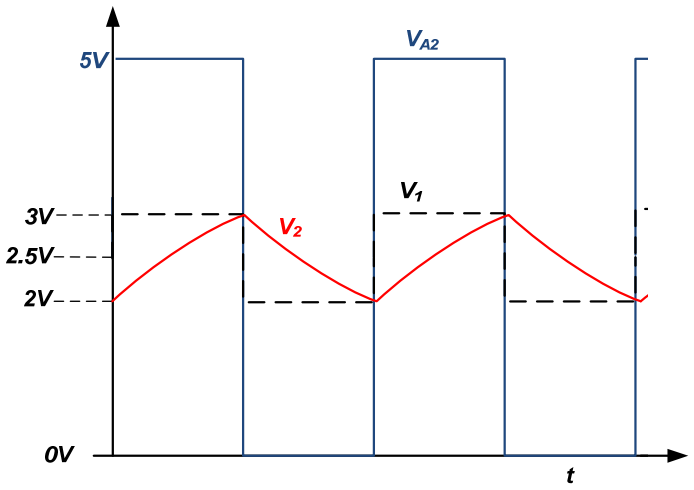

Figure 6.13: Triangle wave voltage and amplifier output

When V_{A2} is positive C_2 is charged via R_8 and its voltage V_2, rises. When V_2 reaches V_1 which is around $3V$, the comparator A_2 switches and V_{A2} goes to zero volts. C_2 is now discharged via R_8, and V_2 falls. When V_2 reaches the new value of V_1, around $2V$, the comparator switches again and V_{A2} becomes $+5V$. Thus the circuit is an oscillator which has a square wave output at V_{A2} and a triangle wave V_2. The triangle wave V_2 thus has an amplitude equal to V_1 and a frequency determined by the values of C_2 and R_8. Amplifier A_1 has no feedback components and is operated as a comparator, to perform PWM by comparing the triangle wave from A_2 with the signal from R_{POT}.

A_1 and A_2 are type TLC3702 micropower comparators, and share the same dual-in-line package. The PWM output from A_1 is inverted by 3 parallel connected NAND gates and this signal is again inverted by another 3 parallel connected NAND gates. The output voltages from the 2 sets of NAND gates are further buffered by emitter follower connected bipolar transistors, and then applied to the gates and sources of the 2 output MOSFETs, so that the MOSFETs are switched in sympathy with the PWM output of A_1.

For A_2, the amplitude of the triangle wave voltage is:

$$V_1 = \left(\frac{5V}{2}\right) \times \left[\frac{\left(\frac{470k\Omega}{2}\right)}{1.2M\Omega + \left(\frac{470k\Omega}{2}\right)}\right] = \pm 0.409V \tag{6.12}$$

The half period of the switching frequency t_s is:

$$t_s = \frac{1nF \times (0.409 \times 2)V_{pk-pk}}{\left(\frac{2.5V}{47k\Omega}\right)} = 15.43\mu s \tag{6.13}$$

Therefore the switching frequency is around $32kHz$. To minimise DC offsets the output of A_2 is integrated by R_7 and C_3 to provide a $2.5V$ reference signal. This reference signal is added to R_{POT}, so that when R_{POT} is set to zero, the $2.5V$ reference signal ensures the mean value of V_{amp} is almost zero.

The MOSFETs chosen have a low Q_g estimated to be around $3nC$, low on resistances $R_{DS(on)}$ of 6.4Ω and 8Ω, and drain voltages around $200V$. The MOSFET supply voltage is $\pm 30V$.

The voltage gain of the amplifier from the slider of R_{POT} to the source connections of the two MOSFETs is determined by the amplitude of the output square wave voltage divided by the amplitude of the triangle wave and is therefore $60V/0.818V$=73.35.

6.6 Prototype Amplified Inductor Circuit Simulations

The circuit shown in Figure 6.12 was simulated using OrCad Pspice, to check its correct operation and also prove that the analysis in Section 6.4 is correct. The simulated triangle wave from A_2 and its output voltage V_{A2} are shown in Figure 6.14(a). The amplitude of the simulated triangle wave is $0.86V_{pk\text{-}pk}$ which is close to

the $0.818V_{pk\text{-}pk}$ estimated in Section 6.5, and the frequency is $30.5kHz$ which is close to the estimated $32kHz$. Figure 6.14(b) shows the comparator/PWM block output voltage with R_{POT} set to zero.

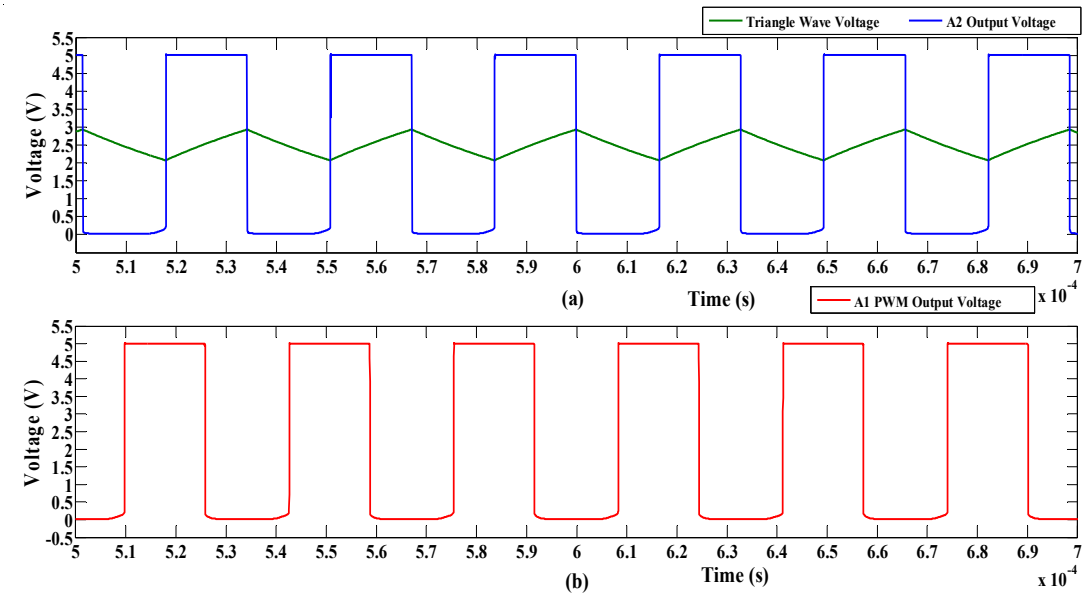

Figure 6.14: Simulated waveforms (a) simulated triangle wave and square wave generated by A2 (b) PWM block output voltage

The maximum low frequency gain of the inductor, sense winding and amplifier, A, can be estimated from the component values and is given by:

$$A=\left(\frac{R_{POT}}{R_3+R_{POT}}\right)\cdot\left(\frac{V_{Supply}}{V_1}\right)\cdot\left(\frac{N_2}{N_1}\right)=\left(\frac{50k\Omega}{1M\Omega+50k\Omega}\right)\cdot\left(\frac{60\text{V}}{0.818\text{V}}\right)\cdot\left(\frac{1750}{2100}\right)=2.9 \tag{6.14}$$

The gain A can be set at any value between zero and 2.9 by adjusting R_{POT}. Let G_{POT} be the per unit setting of R_{POT}, so that when G_{POT}=1, A is 2.9 and when G_{POT} =0, A=0.

Thus the total effective inductance seen by the piezoelectric transducer is

$$L_{TOTAL}=L_1+G_{POT}AL_1\left(\frac{N_2}{N_1}\right)=L_1\left[1+G_{POT}A\left(\frac{N_2}{N_1}\right)\right] \tag{6.15}$$

The effective gain, inductance and resonant frequency for values of G_{POT} between 0 and 1 are shown in Table 6.1.

Table 6.1: Effective inductance and resonant frequency estimation

Potentiometer turns G_{POT}	Effective Gain $G_{POT}A$	Effective Inductance L_{TOTAL} (H)	Estimated Resonant Frequency f (Hz)
0	0	10	129.95
0.1	0.29	12.43	116.58
0.2	0.58	14.85	106.63
0.3	0.87	17.28	98.87
0.4	1.16	19.70	92.58
0.5	1.46	22.13	87.36
0.6	1.75	24.56	82.93
0.7	2.04	26.98	79.12
0.8	2.33	29.40	75.78
0.9	2.62	31.83	72.84
1	2.91	34.26	70.21

Table 6.1 shows that the resonant frequency of the piezoelectric load circuit can be changed over a 1.85:1 range of frequency. The voltage across C_{PZT} for a G_{POT} setting of 0.9 is shown in Figure 6.15, as an example. In this example V_{PZT} was $1V$ peak to peak.

The peak to peak voltage across C_{PZT} is $14V_{pk\text{-}pk}$. The voltage across C_{PZT} was measured instead of the amplifier voltage because the capacitor inherently attenuates the PWM switching voltages across it providing a clear indication of resonance. The simulation showed that the resonant frequency was around $74Hz$. A more precise measurement from the simulation could not easily be achieved, because the simulation takes several hours to reach a steady state due to the high Q.

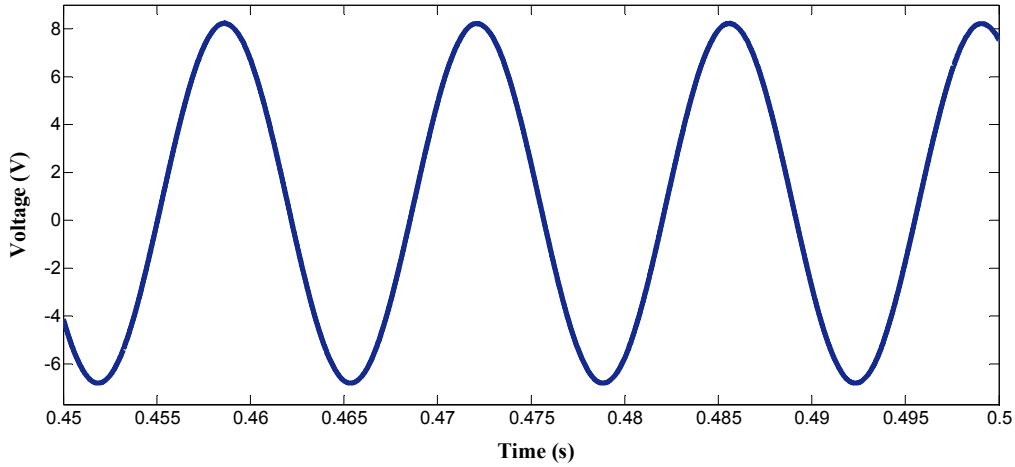

Figure 6.15: Simulated C_{PZT} voltage with $G_{POT} = 0.9$

The simulated circuit showed that the voltage across C_{PZT} is extremely sensitive to the frequency of V_{PZT}. The simulation also showed that by altering the amplifier gain with G_{POT}, the effective inductance and hence the resonance frequency can be changed.

6.7 Experimental Test of Prototype Amplified Inductor Circuit

6.7.1 Laboratory Setup and Initial Measurements

The amplified inductor circuit was tested as shown in Figure 6.16, however instead of using a piezoelectric harvester, a Farnell FG1 function generator in series with a $150nF$ capacitor was used, to prove the concept. The amplified inductor circuit was powered by a $5V$ battery and a $60V_{pk\text{-}pk}$ supply. The effectiveness of the amplified inductor circuit was ascertained by measuring the voltage across the capacitor with a LeCroy 44Xi-A digital oscilloscope.

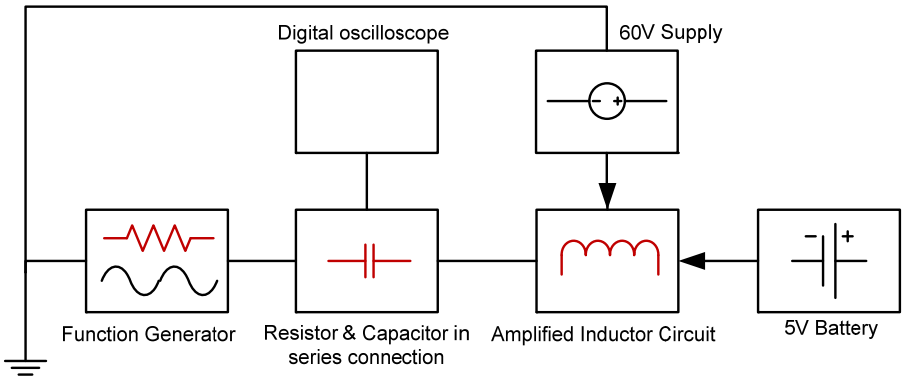

Figure 6.16: Experimental setup for amplified inductor circuit

Figure 6.17 shows measured triangle and square waveform output voltages from A_2 and the PWM output voltage from A_1. It can be seen that these waveforms are similar to the simulated waveforms in Section 6.6. The switching frequency was measured as 26.5kHz, which is lower than the simulated value of 30.5kHz.

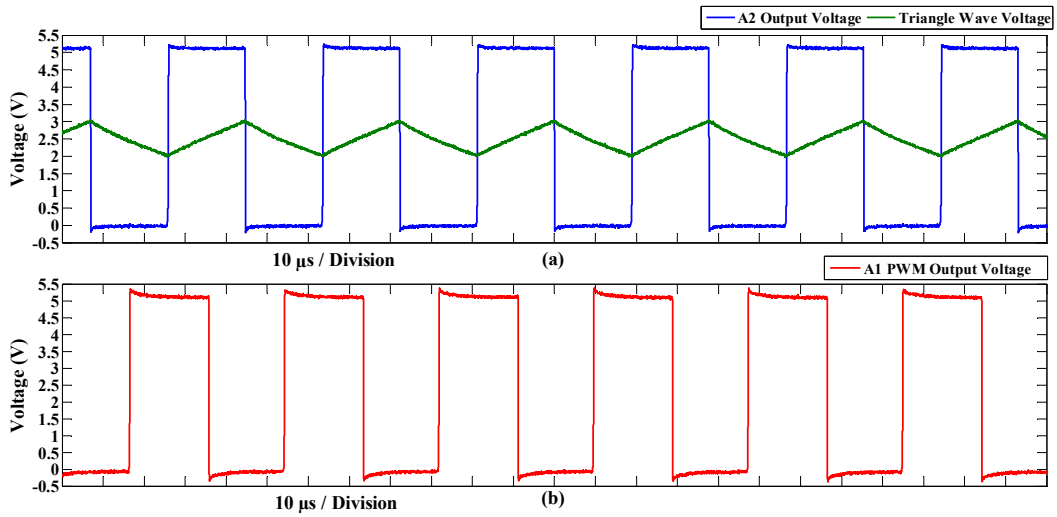

Figure 6.17: Measured waveforms (a) Measured triangle wave and square wave generated by A2 (b) PWM block output voltage

6.7.2 Amplified Inductor Circuit Frequency Tuning Measurements

In this experiment, the resonant frequency of the circuit was found by manually tuning the function generator to find the frequency where the maximum peak to peak voltage occurs, for G_{POT} values from 0 to 0.9. The output from the function generator

was a sinusoidal $1V$ peak to peak signal. The results for G_{POT}=0.2 and 0.9 are shown in this section, as an example, in Figures 6.18 and 6.19. A full set of results for G_{POT}=0 to 0.9 is given in Appendix D.

The first test carried out was to find the resonant frequency of the system with G_{POT} set to zero, so that there is no amplifier gain. This frequency was found to be $124Hz$, and is due to the $150nF$ capacitor resonating with the $10H$ inductor L_1. the value is close to the calculated value of $129.95Hz$.

Figure 6.18 shows the voltage across C_{PZT} when G_{POT}=0.2 and function generator is adjusted to achieve resonance. The frequency is $108Hz$. the frequency has decreased from 124Hz to 108Hz due to the increased amplifier gain A. Thus the effective inductance has increased. The resonant frequency is very close to the calculated value of $106.63Hz$ shown in Table 6.1. The peak to peak value of the voltage across C_{PZT} can be seen to be around $17V$.

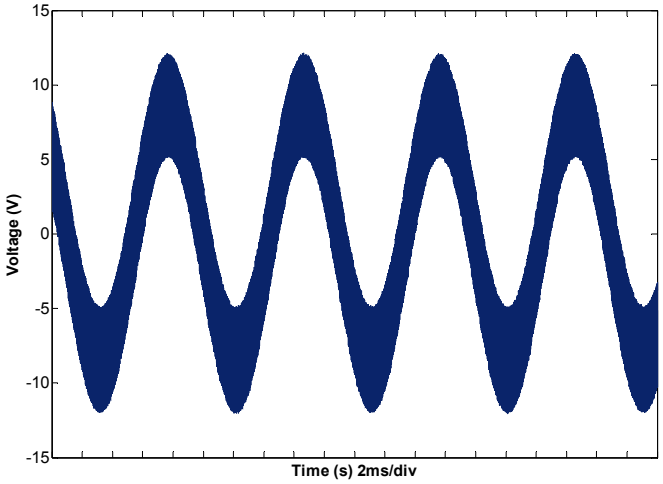

Figure 6.18: Measured C_{PZT} voltage with G_{POT} = 0.2

When G_{POT} is set to 0.9 and the function generator adjusted for resonance, the waveform shown in Figure 6.19 results. The frequency has dropped to 90 Hz and the voltage across C_{PZT} is around $12V$ peak to peak. This frequency is significantly different to the calculated frequency of $72.84Hz$ shown in Table 6.1. The possible reasons for causing this will be discussed in the next section.

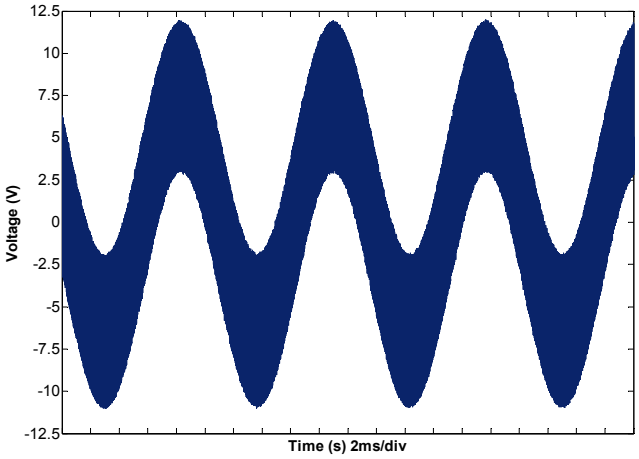

Figure 6.19: Measured C_{PZT} voltage with $G_{POT} = 0.9$

Another method of increasing the effective inductance is to increase the supply voltage. This increases A and thereby effective inductance. The ±30V supply was increased to ±32V, and the result is shown in Figure 6.20. A further frequency drop of approximately 2*Hz* was found to occur so that the circuit resonates at 88*Hz*, however the amplitude of the voltage did not change.

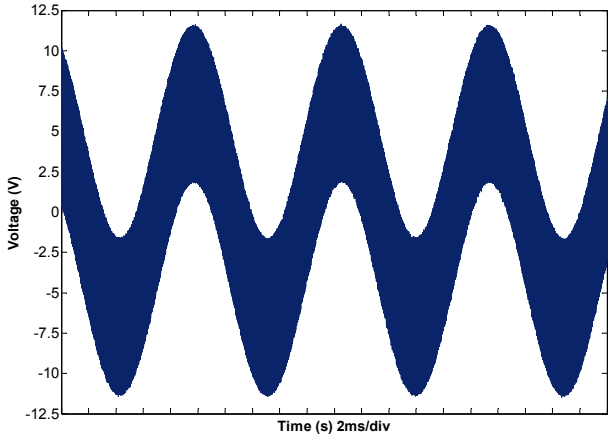

Figure 6.20: Measured C_{PZT} voltage with $G_{POT} = 0.9$ with increased supply voltage

6.8 Results Comparison and Discussion

In this section, using the measured value of resonant frequency from Section 6.7 and Appendix D, the effective resistance, inductance and electrical Q are calculated and compared with the measured results.

6.8.1 Frequency Tuning and Effective Inductance

In Figures 6.21 and 6.22, the effective inductance and resonant frequency are compared.

Figure 6.21 shows that by increasing the value of G_{POT}, the calculated resonant frequency decreases from 129.9Hz to 72.8Hz, whereas the measured values from the test circuit decrease from 124Hz to 90Hz. In both curves the drop in frequency is due to the increased effective inductance in the circuit. The measured and calculated results show a significant disagreement when G_{POT} is greater than 0.3, showing that the amplified inductor circuit becomes less effective when A increases above about 0.87.

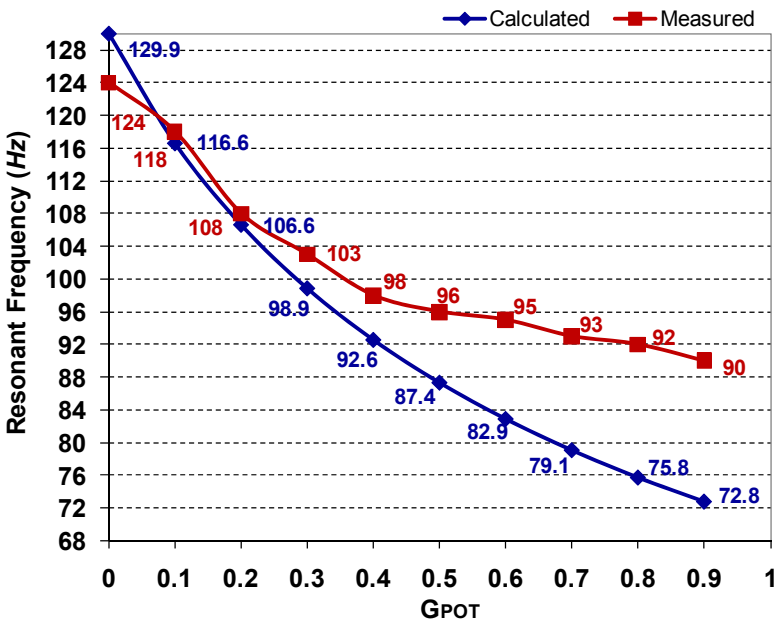

Figure 6.21: Resonance frequency vs. G_{POT} value

The calculated and measured effective inductance L_{TOTAL} of the circuit are compared in Figure 6.22. As G_{POT} increases, the gain A increases resulting in an increased effective inductance of the circuit, for both measured and calculated results.

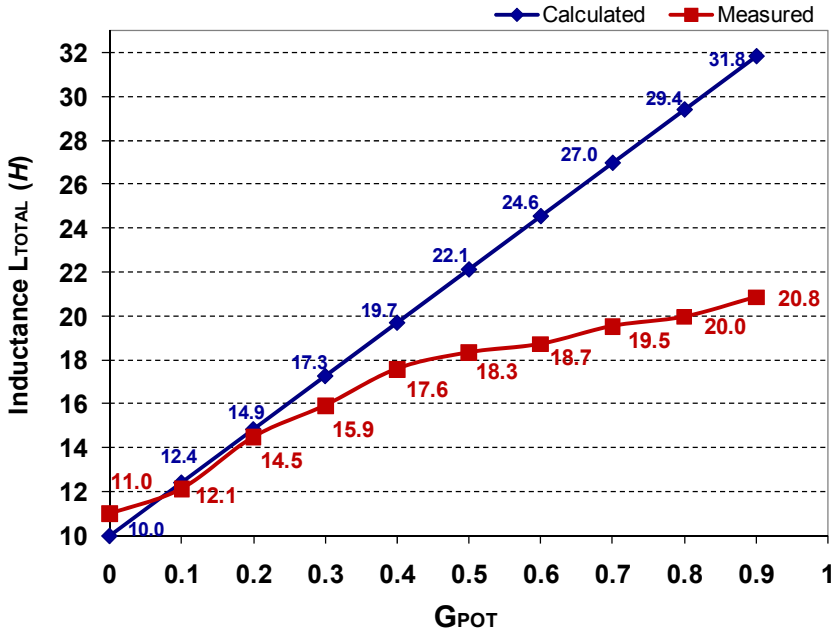

Figure 6.22: Effective inductance L_{TOTAL} vs. G_{POT}

However for the test circuit the calculated inductance is $11H$ when G_{POT} is zero, and the effective inductance does not increase linearly with G_{POT}.

6.8.2 Resistance from Amplifier Lag

The effective resistance of the amplifier can be calculated as follows:

The filter RC time constant is:

$$T = RC = \left(\frac{1M\Omega \times 50k\Omega}{1M\Omega + 50k\Omega}\right) \times 3.3nF = 157\mu s \tag{6.16}$$

The term $\omega^2 T^2$ in Equation (6.11) is small and can be assumed to be zero. Hence the amplifier effective resistance R_{amp} can be simplified from Equation (6.11) as:

$$R_{amp} = \frac{\omega^2 L_1 A N_r T}{1+\omega^2 T^2} \approx \omega^2 L_1 A N_r T \tag{6.17}$$

Figures 6.23 shows how the calculated and measured values of resistance due to the phase lag in the circuit, change with G_{POT} and resonant frequency.

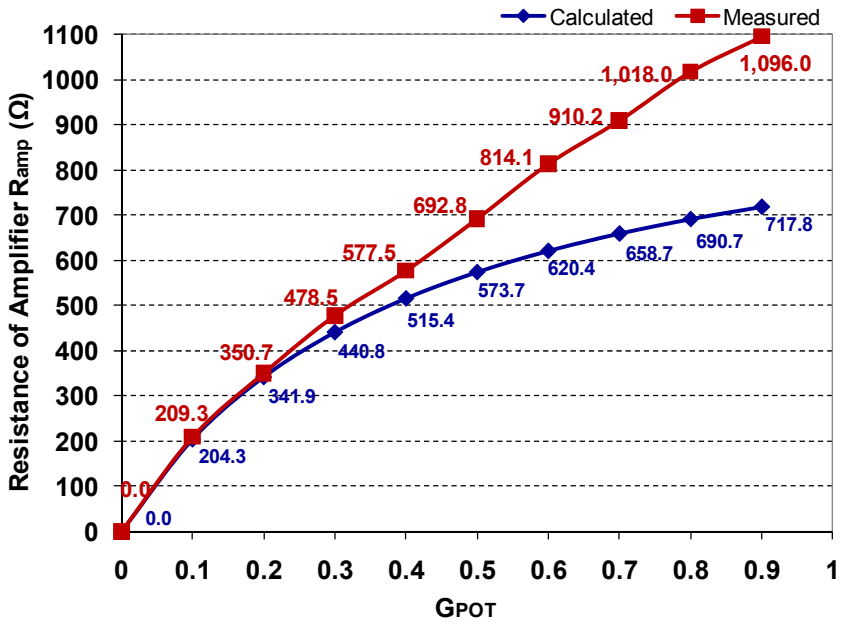

Figure 6.23: Resistance of the circuit R_{amp} vs. G_{POT}

Figure 6.23 shows that the measured resistance associated with the amplified inductance is higher than the calculated value. Both calculated and measured resistance increase with G_{POT} setting, and the curves separate at around a G_{POT} setting of 0.3.

6.8.3 Electrical Quality Factor

The electrical quality factor Q at resonance can be obtained from equation (6.18)

$$Q = \frac{1}{\omega R_{TOTAL} C_{PZT}} = \frac{\omega L_{TOTAL}}{R_{TOTAL}} = \frac{\omega(L_1 + L_1 A N_r)}{R_{PZT} + R_1 + \omega^2 L_1 A N_r T + R_{amp\_output}} \qquad (6.18)$$

In Equation (6.18), R_{PZT} is 60Ω and R_1 is the inductor winding resistance of 87Ω (see Appendix C).

The R_{amp_output} term represents the output resistance of the amplifier. R_{amp_output} was measured by loading the amplifier with various resistors down to 1kΩ and observing the output voltage drop.

By this technique R_{amp_output} was found to be less than 10Ω, and can therefore be ignored. The measured and calculated quality factors derived from Figures 6.22 and 6.23 are shown in Figures 6.24.

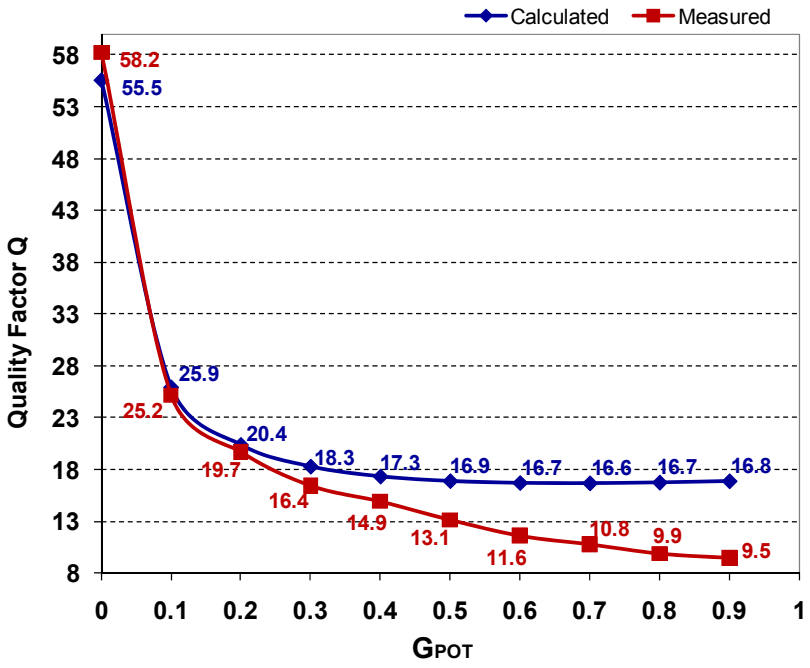

Figure 6.24: Quality factor Q vs. G_{POT}

6.8.4 Summary

From Figures 6.21, 6.22, 6.23 and 6.24, it can be seen that the circuit does not operate as predicted. The effective inductance is low and losses are also much higher than the calculated values. These two effects lead to low quality factor.

In addition it was found that a G_{POT} setting of 1 was not achievable in the experiment. Increasing G_{POT} above 0.9 create an instability in the circuit. In an attempt to determine the reason(s) for these effects, investigations were carried out starting by measuring the losses in the circuit.

6.9 Circuit Stability and Losses

Initial tests involved measuring the MOSFET switching losses and the loss in the circuit connected to the $5V$ battery, with and without the $10H$ inductor being connected. G_{POT} was set to zero for these tests. The measured results are shown in Figures 6.26 and 6.25 respectively.

It can be seen from Figure 6.25 that the $5V$ battery power is low and is not dependent upon whether the inductor is or is not connected. The $5V$ battery is however dependent on the MOSFET supply voltage. This because the gate charge needed to turn on/off the MOSFET is dependent on V_{ds}.

However Figure 6.26 shows that connecting the inductor causes a ten fold increase in power taken from the $\pm 30V$ supplies.

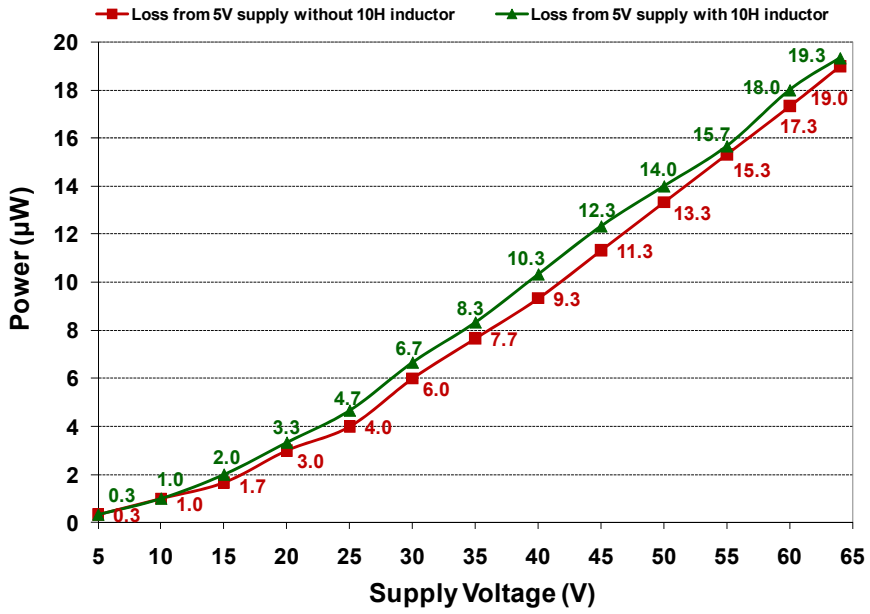

Figure 6.25: Measured 5V supply loss with and without the inductor connected

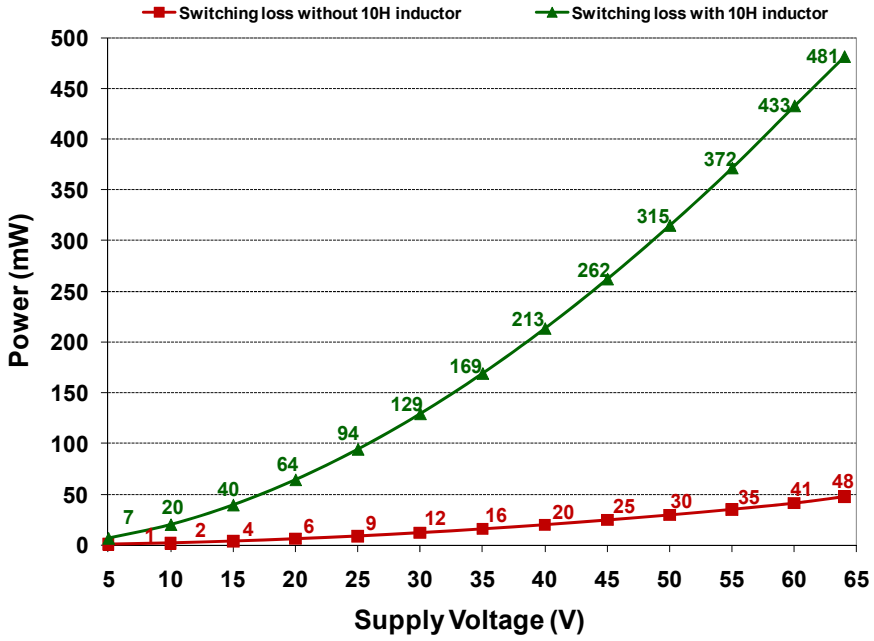

Figure 6.26: Measured MOSFET switching loss with and without the inductor connected

The final test was to find the power taken from the $\pm 30V$ and the $5V$ supply with the inductor and oscillator connected and the PWM block operating as normal. The measured results are shown in Figures 6.27 and 6.28 respectively.

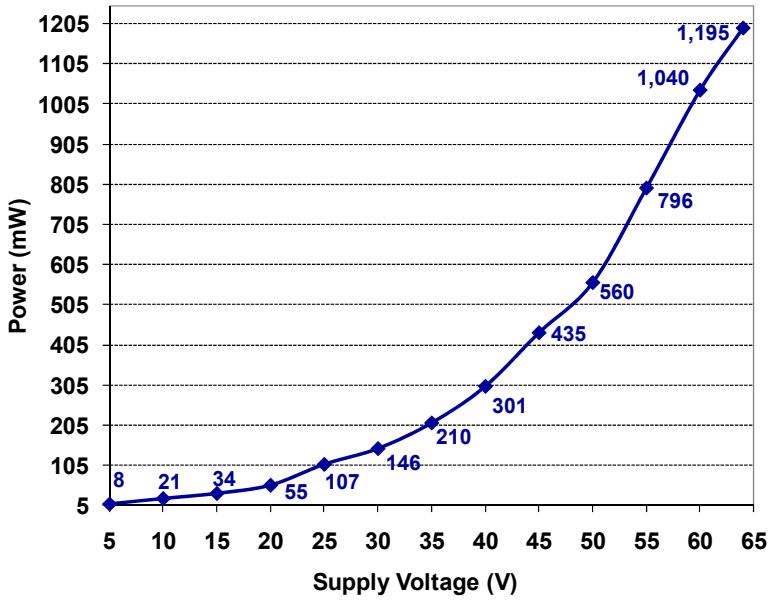

Figure 6.27: Measured switching losses during PWM

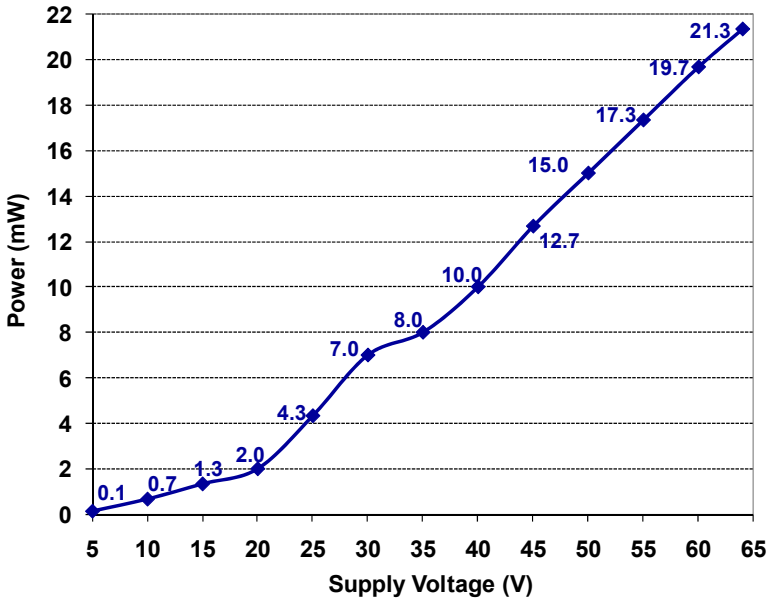

Figure 6.28: Measured losses from the 5V supply during PWM

From the results obtained, it was concluded that the reason for this loss mechanism and the causes of the circuit instability is not clear and cannot be identified. However, Figure 6.26 provides an insight. At $60V$ supply the measured losses were $41mW$, and

connecting the inductor caused an extra 392*mW* loss. To help provide an insight into the cause of this loss, the inductor was tested at various frequencies, see Table 6.2.

Table 6.2: Inductor measurement at various frequencies

Test Frequency (*Hz*)	Inductance L_1 (N_1 turns) (*H*)	Sense winding Inductance L_2 (N_2 turns) (*H*)	Winding Resistance R_1 (N_1 turns) (Ω)	Sense Winding Resistance R_2 (N_1 turns) (Ω)
1k	10.99	7.72	197	155
1.5k	13.11	9.19	518	199
2k	17.98	12.59	1.8k	401
2.5k	34.39	23.72	12.0k	7.9k
2.78k	84.16	57.26	95.7k	61.6k
2.88k	206.27	133.871	649.8k	380.6k
2.98k	- 476.44	-393.36	4.8M	5.2M
25k	-125m	-90m	294	196

Table 6.2 shows that the inductor impedance becomes capacitive at a frequency between 2.88*kHz* and 2.98*kHz*. It is concluded that the inductor forms a parallel resonant *LC* circuit at that frequency. The capacitance must arise from the winding technique in which many closely spaced turns have been used. At 25*kHz*, which is close to the switching frequency, the inductor has a low impedance and will therefore draw a high current, creating a high loss.

6.10 Conclusion

This chapter has introduced, simulated and tested an amplified inductor circuit for piezoelectric energy harvesters. The method proposed is based on the time constant regulator system developed in early 1970s [181, 182], to overcome high winding resistances in micromachines. The method was briefly reviewed in Section 6.2. Sections 6.3, 6.4 and 6.5 explain the theory of the proposed circuit, and explain how it could be implemented with a piezoelectric harvester to overcome its capacitive

output impedance. Sections 6.6 and 6.7 provide simulation results and experimental results of the circuit respectively. Both results show that the circuit proposed should produce an amplified effective inductance. This inductance can be tuned either by potentiometer or by adjusting the supply voltage to the MOSFET output stage, to the exact inductance required so that it can be resonated with the piezoelectric harvester output capacitance. The comparison and discussion of the results are in Section 6.8 and 6.9.

The study and analysis of the amplified inductor circuit was carried out for a single cantilever frequency transverse mode. Because the output capacitance of piezoelectric material varies slightly with different frequencies, the concept introduced here is to have an amplified circuit which can detect the changes in resonant frequency and adjust the effective inductance to provide complex conjugate matching. The circuit would require a control loop to optimise the output power.

The proposed circuit was found to be much more lossy than predicted. A simulation of the amplifier was carried out using OrCad Pspice, to determine the switching losses at 60V supply. The simulation predicted a loss of $10mW$, instead of the $41mW$ measured.

It is concluded that the circuit does not operate as predicted, the most likely reason for this is multiple switching of output turns due to switching signals getting into the modulator input. With multiple switching, a MOSFET turning on injects through capacitive coupling a signal into the PWM block, which then turns themself off. As the MOSFET turns off it injects a further signal into the PWM block which tells the MOSFET to turn on again. The process can be repeated several time. Thus instead of one switching transition, there are several, resulting in an energy loss, therefore is difficult to measure on the circuit because the PWM block is connected to the output terminal of the amplifier.

In Figures 6.18, 6.19 and 6.20, it can be seen that there is high frequency ripple on the voltage across the $150nF$ capacitor. This is due to resonance, at a frequency close to the switching frequency, of the inter winding capacitance and inductance of the

inductor. The inter winding capacitance forms a *LC* resonance with the inductances of the windings at around 27*kHz*, which is very close to the switching frequency of 30*kHz*.

A loss calculation of the inductor was carried out, see Appendix C, the calculation shown that for a switching frequency of 30*kHz* and a sine wave of 100*Hz*. The hysteresis loss of the inductor is around 2.5*mW*. In ideal cases, the circuit should consumes no more than 13*mW*.

Chapter 7 :

Conclusion, Research Outcomes and Future Work

7.1 General Conclusions

The work described in this thesis is aimed at improving piezoelectric cantilever energy harvesting techniques, so that harvesters can obtain energy over a wide bandwidth. In order to achieve this, the task has been investigated from two main directions – the mechanical structure of the harvester and the complex conjugate load matching circuit. For this reason the thesis is in two parts. Chapter 1 describes the project objectives and motivations.

One approach towards achieving a wide bandwidth is to investigate the mechanical vibration model of piezoelectric energy harvesters. A Rayleigh-Ritz analysis of a cantilever structure is described in Chapter 2, this is followed by a summary of the electromechanical behaviour of piezoelectric materials. A literature review of wideband/tunable energy harvesters is also given in Chapter 2, followed by a summary and discussion.

Following the review in Chapter 2, a novel multiresonant structure which may be used for wide band piezoelectric energy harvesting was proposed, in Chapter 3. A Rayleigh-Ritz analysis and simulation for this multiresonant harvester was also carried out. From the analysis and simulation results, it was found that with an

appropriate design configuration, the multiresonant structure is able to harvest energy over a range of frequencies.

In Chapter 3, the experimental results for a cantilever array system and a multiresonant beam are given. The results show that although the multiresonant beam system may need further optimization, the proposed structure is able to harvest energy at several resonant frequencies.

From the analysis of the multiresonant system, it was found that several parameters can be adjusted to alter the beam resonant frequencies, including the dimensions of the side cantilevers and the clamped-clamped beam, also the mass loading and location of the side cantilevers.

Initial tests of the multiresonant beam were carried out by using a much longer beam than the one described in Chapter 4, of around 40*cm*. The locations of the five side cantilevers were close to the centre of the beam at 20*cm*, with 3*cm* spacing in between them. A relatively poor bandwidth was found for the system, since the spacing between the cantilevers was small, compared to the 40*cm* overall length of the beam. It was observed that the five side cantilevers tended to share a similar resonant frequency, with or without the tip masses.

Consider now the structure of the device. It can be categorised as either a symmetrical system or a non-symmetrical system, see Figure 7.1.

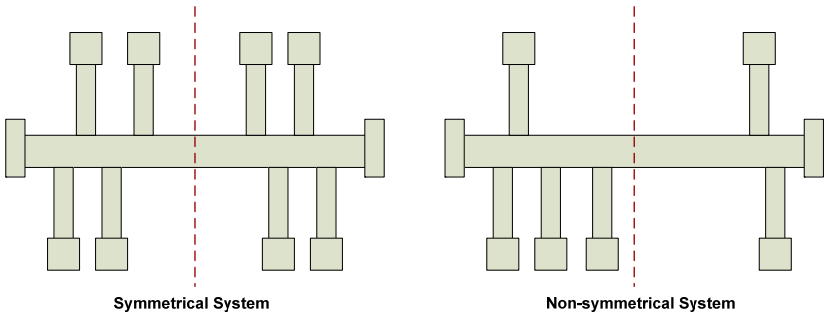

Figure 7.1: Top view of symmetrical and non-symmetrical multiresonant beam

Imagine the clamped-clamped beam is split at a line halfway between the two clamps. If the left hand side is the mirror image of the right hand side, then the beam is symmetrical. If the mirror image is not the same then the beam is non-symmetrical.

For a symmetrical system with identical cantilever tip masses, the strain will be distributed along the beam, with the maximum strain occuring close to the clamp locations. A similar strain distribution will occur for the left hand and right hand side of the beam. The symmetrical system is relatively easy to analyse. For a non-symmetrical system, the location of the maximum beam transmissibility will not necessarily be in the middle. There may be advantages to the non-symmetric system, as it may allow a reduction in piezoelectric transducer length and therefore cost.

When the cantilevers are close together they tend to interact so that their resonant frequencies are nearly the same. If the cantilevers are mounted on different sides of the main beam, it may be possible to minimise the effects of interactions between cantilevers, such that if one cantilever is resonating, its resonant frequency will be modified less by the other cantilevers. Such an approach will need an automatic optimization calculation and is discussed in the next section.

From the simulation and experimental tests, it can be seen that there is a similarity between predicted and measured transmissibility curves without tip masses. Also, the agreement between transmissibility and voltage responses proved that the new energy harvesting design is potentially feasible for harvesting energy from environmental vibrations or variable speed machines. The design also enables possibly higher torsion energy to be produced compared to a single cantilever harvester, since it uses the torsion mode of piezoelectric materials. However the torsion response was not measured in this work as the accelerometers used are only sensitive to heave motion.

Harvesters comprising several individual piezoelectric cantilevers, have electrical outputs which ideally should be summed, in a manner that avoids phase cancellation of the individual voltage outputs produced by each piezoelectric transducer if optimum power is needed. It should be noted that such phase cancellation is due to

the voltage produced some piezoelectric elements being out of phase. The circuits which may be used to overcome phase cancellation of each piezoelectric transducer can be complicated and lossy. The multiresonant design must have the same problem since the PFC occupies nearly all the beam, but the degree to which this occurs cannot be determined at this time. The advantage of the multiresonant beam harvester is that it only uses one PFC, and is cheap to construct in comparison to the cantilever array designs proposed by Shahruz et al [84, 85, 94] and others [9, 114].

The second part of the thesis describes an investigation into piezoelectric harvester load matching. Several electrical loading methods were reviewed and are described in Chapter 5. The trend for optimising piezoelectric harvester output power is to reduce the effect of its output capacitive impedance. SSHI and synchronous charge extraction circuits were proposed by Lefeuvre et al [15, 16, 23], and others [26, 31, 32]. These circuits only partially compensate for capacitive output impedance. The complex conjugate method requires a high inductance to compensate, and this is generally impractical since the inductor size can become excessive.

It was concluded by the author that a load circuit which could simulate an inductor is needed for maximum power extraction. Hence an amplified inductor circuit is proposed in Chapter 6.

In Chapter 6, a prototype amplified inductor circuit is described, simulated and tested. The simulation and measured results show that the proposed circuit can provide an amplified inductance which is variable. Unfortunately, the prototype circuit was found to be lossy and unstable at low switching frequencies.

One way to reduce the excessive loss, is to use a lower switching frequency. The circuit was originally designed to operate at 15*kHz*. However, it was found that when switching at this frequency, the circuit was unstable. Thus the circuit was modified to work at 26*kHz* where it is much more stable, and this latter circuit is the one described in the thesis.

It is believed that, as mentioned in Section 6.9, due to winding capacitance, the inductor forms a parallel LC circuit resonant at around $3kHz$, and this resonance is modifying the feedback loop creating an instability.

There also seems to be a higher switching loss in the amplifier circuit than the simulation predicts – $41mW$ instead of $10mW$. The precise reason for the extra $31mW$ loss is unclear, but it is probably due to poor layout of the circuit, causing multiple switching of the output transistors. Future work will have to concentrate on achieving a circuit layout which avoids spurious feedback and the multiple switching problem.

Reduction of the inductor winding capacitance might be achieved by using a lower inductance value, although the switching frequency will then need to be higher, causing higher circuit energy consumption. A different winding technique could also be considered, or several lower value inductors connected in series could be used, in which each inductor, having a lower number of turns has a lower capacitance. The disadvantage of these two techniques maybe an increased overall size.

The inductor also could be redesigned using a higher permeability ferrite and possibly no air gap. This would reduce the number of required turns and hence winding capacitance. However inductor non linearity may need consideration.

A further problem concerns the transfer of power from the circuit to the electronic load. A bidirectional power supply will be needed to efficiently transfer the power between the $5V$ and $30V$ supply, for instance, and the electronic load could then be powered from the $5V$ supply.

To ensure start up of the circuit, the $5V$ supply would be a rechargeable battery. A vibration sense circuit would then be needed which, when the vibration level was enough, connected the $5V$ and $30V$ supplies to the circuit.

Although the amplified inductor circuit needs further work to make it suitable for energy harvesting, it may already have a practical use in vibration absorption.

Vibration absorption is a technique which uses piezoelectric transducers to damp vibrations in structures. This is frequently achieved by absorbing the electrical energy in an external circuit. The amplified inductor circuit could be useful in this area, despite its losses, because where vibration absorption is needed, energy is usually available from other power sources.

7.2 Research Outcomes

Four publications have resulted from the work described and these are listed here.

Journal paper:

(1) S. Qi, R. Shuttleworth, S. O. Oyadiji, J. Wright, "Design of a Multiresonant beam for broadband piezoelectric energy harvesting" *Jounal of Smart Materials and Structures, Institute of Physics, Vol. 19, No. 9, 2010, Impact factor 1.749*

Conference Papers:

(1) S. Qi, R. Shuttleworth, S. O. Oyadiji, "Multiple resonances piezoelectric energy harvesting generator" *Proceedings of the ASME Conference on Smart Materials, Adaptive Structures and Intelligent Systems*, *Oxnard*, *California*, *USA*, September 21-23, 2009.

Awarded best student paper of the symposium, SMASIS, USA, 2009

(2) S. O. Oyadiji, S. Qi, R. Shuttleworth, "Development of multiple cantilevered piezo fiber composite beams vibration energy harvester for wireless sensors" *World Congress of Engineering Asset Management*, *Athens*, Greece, September, 2009

(3) S. O. Oyadiji, Z. Zhu, R. Sun, R. Pietruszkiewicz, P. Charles, S. Qi, R. Shuttleworth, "Self-powered intelligent wireless disposable micro-sensors"

Wireless Sensing Demonstrator Showcase, National Physical Laboratory, UK, 2009

7.3 Future Work

The suggested future work from the analyses and results described in this thesis are also divided into two parts - the mechanical structure and the electronic circuits.

For the multiresonant beam structure, there are several techniques that can be tried to broaden the frequency response. Firstly, two or more multiresonant beams can be used to cover the frequency dips due to anti-resonances, so that a flatter vibration response can be achieved. This is described in Section 3.8. Secondly, the parameters of the prototype multiresonant beam design have not yet been optimized. Automatic optimization could be achieved by using genetic algorithms to broaden the bandwidth. A genetic algorithm could adjust the beam variables (e.g. number of cantilevers used and clamp locations), to achieve a better frequency response. The challenge is to first define practical boundary conditions. Secondly, the output to be optimised (e.g. gain against bandwidth response), needs to be defined. For example, a gain of 10 in transmissibility from 10*Hz* to 15*Hz*, is not necessarily better than a gain of 5 from 20*Hz* to 30*Hz*, although they have the same gain bandwidth product. Therefore, it is important to optimise a set of specific beam parameters, to suit different applications.

The results from the existing simulation are approximate, and Rayleigh-Ritz analysis does not include the piezoelectric transducer. This was done so that a simple model can be used to enable an understanding of the physical processes behind the functioning of the system [48, 90]. Also, it is assumed that the cantilevers bend from the root, and do not distort the main beam. In practice some flexing of the main beam in sympathy with the cantilevers motion, at the point where the cantilever connects to the main beam, must occur. Further modelling work should take this into account.

The experimental work carried out in Chapter 4 used accelerometers which only measure heave motion. Torsion response is a factor which causes a difference between the measured acceleration and PFC voltage, see Section 4.3.2. A different measurement technique, such as laser vibrometry may be used to measure torsion vibrations of the beam. However, torsional modes tend to occur at much higher frequencies than fundamental bending modes, therefore when the device resonates at low frequencies, less energy can be harvested from torsional response compared to that from bending modes.

Another possibility for a more accurate measurement of the multiresonant beam structure, is to use a beam constructed from Perspex. This will allow strain at any location on the beam to be measured using the photo-elastic effect. Such an approach will provide a more detailed understanding of the structure, allowing the beam responses to be optimised. Ultimately, a multiresonant beam made from a single piezoelectric material could be fabricated to overcome the phase cancellation issues that occur when using multiple piezoelectric beams connected in parallel.

Overall, the active material is restricted to the central clamped-clamped beam. Thus, the ratio of the mass of the active material to the passive material and therefore the power density is low. Consequently, the power density is low. An improvement to power density might be achieved by designing a multiresonant harvester comprising several individual piezoelectric cantilevers in which the entire length of each beam (clamped-clamped and cantilever beams) is covered by active material [48, 90].

PWM needs a high switching frequency. It may be that there are other modulation techniques which can use a lower switching frequency. This should be investigated since a lower switching frequency will produce less switching losses and improve the circuits usefulness.

There is a control technique which can perform automatic tuning. The controller injects a low frequency sine wave into the system and observes how the system responds to this signal. The controller observes the slope of the response and from this can determine if the inductance value needs increasing or decreasing. Such a

system could be implemented in low power CMOS. Thus the harvester could be made self tuning so that optimum power output is achieved.

References

[1] S. Anton, and H. Sodano, "A review of power harvesting using piezoelectric materials (2003–2006)," *Smart Materials and Structures,* vol. 16, pp. R1, 2007.

[2] H. Sodano, D. Inman, and G. Park, "A review of power harvesting from vibration using piezoelectric materials," *Shock and Vibration Digest,* vol. 36, no. 3, pp. 197-206, 2004.

[3] S. J. Roundy, "Energy scavenging for wireless sensor nodes with a focus on vibration to electricity conversion," *PhD Thesis, Berkeley, The University of California*, 2003.

[4] L. Mateu, and F. Moll, "Review of energy harvesting techniques and applications for microelectronics," *Proceeding of SPIE,* vol. 5837, pp. 359-373, 2005.

[5] E. Torres, and G. Rincón-Mora, "Electrostatic energy harvester and Li-Ion charger circuit for micro-scale applications," *49th IEEE International Midwest Symposium on Circuits and Systems, MWSCAS, San Juan,* vol. 1, pp. 65-69, 2006.

[6] S. P. Beeby, R. N. Torah, M. J. Tudor, P. Glynne-Jones, T. O'Donnell, C. R. Saha, and S. Roy, "A micro electromagnetic generator for vibration energy harvesting," *Journal of Micromechanics and Microengineering,* vol. 17, no. 7, pp. 1257-1265, 2007.

[7] T.-H. Cheng, and I.-K. Oh, "A current-flowing electromagnetic shunt damper for multi-mode vibration control of cantilever beams," *Smart Materials and Structures,* vol. 18, no. 9, pp. 095036, 2009.

[8] GlynneJones, and P., "An electromagnetic, vibration-powered generator for intelligent sensor systems," *Sensors and Actuators A: Physical,* vol. 110, no. 1-3, pp. 344-349, 2004.

[9] I. Sari, T. Balkan, and H. Kulah, "An electromagnetic micro power generator for wideband environmental vibrations," *Sensors and Actuators A: Physical,* vol. 145, pp. 405-413, 2007.

[10] Y. Tadesse, Z. Shujun, and S. Priya, "Multimodal energy harvesting system: piezoelectric and electromagnetic," *Journal of Intelligent Material Systems and Structures,* vol. 20, no. 5, pp. 625-632, 2008.

[11] D. Vasic, F. Costa, and E. Sarraute, "Comparing piezoelectric and coreless electromagnetic transformer approaches in IGBT driver," *The European Physical Journal of Applied Physics,* vol. 34, no. 3, pp. 237-242, 2006.

[12] B. Yang, C. Lee, W. Xiang, J. Xie, J. Han He, R. K. Kotlanka, S. P. Low, and H. Feng, "Electromagnetic energy harvesting from vibrations of multiple frequencies," *Journal of Micromechanics and Microengineering,* vol. 19, no. 3, pp. 035001, 2009.

[13] D. Zhu, S. Roberts, M. J. Tudor, and S. P. Beeby, "Design and experimental characterization of a tunable vibration-based electromagnetic micro-generator," *Sensors and Actuators A: Physical,* vol. 158, no. 2, pp. 284-293, 2010.

[14] S. Adhikari, M. I. Friswell, and D. J. Inman, "Piezoelectric energy harvesting from broadband random vibrations," *Smart Materials and Structures,* vol. 18, no. 11, pp. 115005, 2009.

[15] A. Badel, "Efficiency enhancement of a piezoelectric energy harvesting device in pulsed operation by synchronous charge inversion," *Journal of Intelligent Material Systems and Structures,* vol. 16, no. 10, pp. 889-901, 2005.

[16] A. Badel, D. Guyomar, E. Lefeuvre, and C. Richard, "Piezoelectric energy harvesting using a synchronized switch technique," *Journal of Intelligent Material Systems and Structures,* vol. 17, no. 8-9, pp. 831-839, 2006.

[17] J. Brufau-Penella, and M. Puig-Vidal, "Piezoelectric energy harvesting improvement with complex conjugate impedance matching," *Journal of Intelligent Material Systems and Structures,* vol. 20, no. 5, pp. 597-608, 2008.

[18] M. J. Guan, and W. H. Liao, "Characteristics of energy storage devices in piezoelectric energy harvesting systems," *Journal of Intelligent Material Systems and Structures,* vol. 19, no. 6, pp. 671-680, 2007.

[19] M. J. Guan, and W. H. Liao, "On the efficiencies of piezoelectric energy harvesting circuits towards storage device voltages," *Smart Materials and Structures,* vol. 16, no. 2, pp. 498-505, 2007.

[20] S. Kim, "Piezoelectric energy harvesting with a clamped circular plate: analysis," *Journal of Intelligent Material Systems and Structures,* vol. 16, no. 10, pp. 847-854, 2005.

[21] S. Kim, "Piezoelectric energy harvesting with a clamped circular plate: experimental study," *Journal of Intelligent Material Systems and Structures,* vol. 16, no. 10, pp. 855-863, 2005.

[22] N. Kong, D. S. Ha, A. Erturk, and D. J. Inman, "Resistive impedance matching circuit for piezoelectric energy harvesting," *Journal of Intelligent Material Systems and Structures,* vol. 21, no. 13, pp. 1293-1302, 2010.

[23] E. Lefeuvre, "Piezoelectric energy harvesting device optimization by synchronous electric charge extraction," *Journal of Intelligent Material Systems and Structures,* vol. 16, no. 10, pp. 865-876, 2005.

[24] E. Lefeuvre, A. Badel, A. Benayad, L. Lebrun, C. Richard, and D. Guyomar, "A comparison between several approaches of piezoelectric energy harvesting," *Journal de Physique IV (Proceedings),* vol. 128, pp. 177-186, 2005.

[25] J. R. Liang, and W. H. Liao, "Piezoelectric energy harvesting and dissipation on structural damping," *Journal of Intelligent Material Systems and Structures,* vol. 20, no. 5, pp. 515-527, 2008.

[26] J. Qiu, H. Jiang, H. Ji, and K. Zhu, "Comparison between four piezoelectric energy harvesting circuits," *Frontiers of Mechanical Engineering in China,* vol. 4, no. 2, pp. 153-159, 2009.

[27] Y. K. Ramadass, and A. P. Chandrakasan, "An efficient piezoelectric energy harvesting interface circuit using a bias-flip rectifier and shared inductor," *IEEE Journal of Solid-State Circuits,* vol. 45, no. 1, pp. 189-204, 2010.

[28] M. Ramsay, and W. Clark, "Piezoelectric energy harvesting for bio-MEMS applications," *Smart Structures and Materials 2001: Industrial and Commercial Applications of Smart Structures Technologies,* vol. 4332, pp. 429, March 05, 2001.

[29] B. Ren, S. W. Or, Y. Zhang, Q. Zhang, X. Li, J. Jiao, W. Wang, D. a. Liu, X. Zhao, and H. Luo, "Piezoelectric energy harvesting using shear mode 0.71Pb(Mg[sub 1/3]Nb[sub 2/3])O[sub 3]–0.29PbTiO[sub 3] single crystal cantilever," *Applied Physics Letters,* vol. 96, no. 8, pp. 083502, 2010.

[30] Y. C. Shu, and I. C. Lien, "Analysis of power output for piezoelectric energy harvesting systems," *Smart Materials and Structures,* vol. 15, no. 6, pp. 1499-1512, 2006.

[31] Y. C. Shu, I. C. Lien, and W. J. Wu, "An improved analysis of the SSHI interface in piezoelectric energy harvesting," *Smart Materials and Structures,* vol. 16, no. 6, pp. 2253-2264, 2007.

[32] Y. C. Shu, I. C. Lien, W. J. Wu, and S. M. Shiu, "Comparisons between parallel- and series-SSHI interfaces adopted by piezoelectric energy harvesting systems," *Proceedings of SPIE,* vol. 7288, pp. 728808-12, 2009.

[33] H. A. Sodano, "Comparison of piezoelectric energy harvesting devices for recharging batteries," *Journal of Intelligent Material Systems and Structures,* vol. 16, no. 10, pp. 799-807, 2005.

[34] J. W. Sohn, S. B. Choi, and D. Y. Lee, "An investigation on piezoelectric energy harvesting for MEMS power sources," *Proceedings of the Institution of Mechanical Engineers, Part C: Journal of Mechanical Engineering Science,* vol. 219, no. 4, pp. 429-436, 2005.

[35] J. Twiefel, "Model-based design of piezoelectric energy harvesting systems," *Proceedings of SPIE,* vol. 6169, pp. 616909-10, 2006.

[36] J. Twiefel, B. Richter, T. Sattel, and J. Wallaschek, "Power output estimation and experimental validation for piezoelectric energy harvesting systems," *Journal of Electroceramics,* vol. 20, no. 3-4, pp. 203-208, 2007.

[37] D. A. Wang, and H. H. Ko, "Piezoelectric energy harvesting from flow-induced vibration," *Journal of Micromechanics and Microengineering,* vol. 20, no. 2, pp. 025019, 2010.

[38] S. Roundy, "Toward self-tuning adaptive vibration-based microgenerators," *Proceedings of SPIE,* vol. 5649, pp. 373-384, 2005.

[39] S. Roundy, E. Leland, J. Baker, E. Carleton, E. Reilly, E. Lai, B. Otis, J. Rabaey, P. Wright, and V. Sundararajan, "Improving power output for vibration-based energy scavengers," *IEEE Pervasive computing,* vol. 4, no. 1, pp. 28-36, 2005.

[40] S. Roundy, and P. K. Wright, "A piezoelectric vibration based generator for wireless electronics," *Smart Materials and Structures,* vol. 13, no. 5, pp. 1131-1142, 2004.

[41] D. Zhu, M. J. Tudor, and S. P. Beeby, "Strategies for increasing the operating frequency range of vibration energy harvesters: a review," *Measurement Science and Technology,* vol. 21, no. 2, pp. 022001, 2010.

[42] MorganElectroCeramics, "Morgan Electro Ceramics datasheets on piezoelectric materials," *http://www.morganelectroceramics.com/, accessed on 14/05/2009*

[43] A. Bent, and N. Hagood, "Piezoelectric fiber composites with interdigitated electrodes," *Journal of Intelligent Material Systems and Structures,* vol. 8, no. 11, pp. 903, 1997.

[44] N. E. Ghouti, "Hybrid modeling of a traveling wave piezoelectric motor," *PhD Thesis, Department of control engineering, Aalborg University, Denmark*, 2000.

[45] O. Guillon, F. Thiebaud, and D. Perreux, "Tensile fracture of soft and hard PZT," *International Journal of Fracture,* vol. 117, no. 3, pp. 235-246, 2002.

[46] PICeramic, "DuraAct™ piezoelectric patch transducers for industry and research and Piezoelectric materials (PZT) tutorials and datasheets," *PI Ceramic GmbH http://www.piceramic.com, accessed on 07/08/2009*.

[47] V. Carazo, "Novel piezoelectric transducers for high voltage measurements," *PhD Thesis, Universitat Politécnica de Catalunya*, 2000.

[48] S. Qi, R. Shuttleworth, S. Oyadiji, and J. Wright, "Design of a multiresonant beam for broadband piezoelectric energy harvesting," *Smart Materials and Structures,* vol. 19, pp. 094009, 2010.

[49] AdvancedCerametrics, "Piezoelectric Fibre Composite Bimorph (PFCB) material datasheets," *Advanced Cerametrics Inc. (ACI), http://www.advancedcerametrics.com/, accessed on 16/05/2009*.

[50] M. Kettani, "Direct energy conversion," *Book, Addison Wesley Longman Publishing, ISBN: 0201036630*, 1970.

[51] D. Shen, S. Choe, and D. Kim, "Analysis of piezoelectric materials for energy harvesting devices under high-g vibrations," *Japanese Journal of Applied Physics,* vol. 46, no. 10A, pp. 6755-6760, 2007.

[52] C. Williams, and R. Yates, "Analysis of a micro-electric generator for microsystems," *Sensors and Actuators A: Physical,* vol. 52, no. 1-3, pp. 8-11, 1996.

[53] N. Elvin, A. Elvin, and D. Choi, "A self-powered damage detection sensor," *The Journal of Strain Analysis for Engineering Design,* vol. 38, no. 2, pp. 115-124, 2003.

[54] N. Elvin, A. Elvin, and M. Spector, "A self-powered mechanical strain energy sensor," *Smart Materials and Structures,* vol. 10, pp. 293, 2001.

[55] T. Ng, and W. Liao, "Sensitivity analysis and energy harvesting for a self-powered piezoelectric sensor," *Journal of Intelligent Material Systems and Structures,* vol. 16, no. 10, pp. 785, 2005.

[56] A. Techet, J. Allen, and A. Smits, "Piezoelectric eels for energy harvesting in the ocean," *Proceedings of the 12th International Offshore and Polar Engineering Conference Kitakyushu, Japan*, May 26-31, 2002.

[57] S. Priya, C. Chen, D. Fye, and J. Zahnd, "Piezoelectric windmill: a novel solution to remote sensing," *Japanese Journal of Applied Physics,* vol. 44, no. 3, pp. 104-107, 2005.

[58] S. Priya, "Modeling of electric energy harvesting using piezoelectric windmill," *Applied Physics Letters,* vol. 87, pp. 184101, 2005.

[59] T. Starner, "Human-powered wearable computing," *IBM systems Journal,* vol. 35, no. 3.4, pp. 618-629, 1996.

[60] J. Kymissis, C. Kendall, J. Paradiso, and N. Gershenfeld, "Parasitic power harvesting in shoes," *Second International Conference on Wearable Computers, Pittsburgh, PA, USA*, pp. 132-139, Oct 19-20, 1998.

[61] N. Shenck, "A demonstration of useful electric energy generation from piezoceramics in a shoe," *Msc Thesis, Massachusetts Institute of Technology, United states*, 1999.

[62] C. D. Richards, M. J. Anderson, D. F. Bahr, and R. F. Richards, "Efficiency of energy conversion for devices containing a piezoelectric component," *Journal of Micromechanics and Microengineering,* vol. 14, no. 5, pp. 717-721, 2004.

[63] J. D. Adams, B. Rogers, L. Manning, Z. Hu, T. Thundat, H. Cavazos, and S. C. Minne, "Piezoelectric self-sensing of adsorption-induced microcantilever bending," *Sensors and Actuators A: Physical,* vol. 121, no. 2, pp. 457-461, 2005.

[64] J. Ajitsaria, S. Y. Choe, D. Shen, and D. J. Kim, "Modeling and analysis of a bimorph piezoelectric cantilever beam for voltage generation," *Smart Materials and Structures,* vol. 16, no. 2, pp. 447-454, 2007.

[65] K. Alhazza, A. Nayfeh, and M. Daqaq, "On utilizing delayed feedback for active-multimode vibration control of cantilever beams," *Journal of Sound and Vibration,* vol. 319, no. 3-5, pp. 735-752, 2009.

[66] W. J. Choi, Y. Jeon, J. H. Jeong, R. Sood, and S. G. Kim, "Energy harvesting MEMS device based on thin film piezoelectric cantilevers," *Journal of Electroceramics,* vol. 17, no. 2-4, pp. 543-548, 2006.

[67] T. Cui, D. Markus, S. Zurn, and D. L. Polla, "Piezoelectric thin films formed by MOD on cantilever beams for micro sensors and actuators," *Microsystem Technologies,* vol. 10, no. 2, pp. 137-141, 2004.

[68] C. Eichhorn, F. Goldschmidtboeing, and P. Woias, "Bidirectional frequency tuning of a piezoelectric energy converter based on a cantilever beam," *Journal of Micromechanics and Microengineering,* vol. 19, no. 9, pp. 094006, 2009.

[69] Eissa, and M., "Vibration control of a cantilever beam subject to both external and parametric excitation," *Applied Mathematics and Computation,* vol. 152, no. 3, pp. 611-619, 2004.

[70] A. Erturk, and D. J. Inman, "On mechanical modeling of cantilevered piezoelectric vibration energy harvesters," *Journal of Intelligent Material Systems and Structures,* vol. 19, no. 11, pp. 1311-1325, 2008.

[71] L. A. Flores-Herrera, E. A. Merchán-Cruz, A. T. Velázquez-Sánchez, and R. Rivera-Blas, "Algorithm for estimating natural frequencies and mode shapes of cantilever MEMS microbeams," *Applied Mechanics and Materials,* vol. 15, pp. 95-100, 2009.

[72] C. P. Green, and J. E. Sader, "Torsional frequency response of cantilever beams immersed in viscous fluids with applications to the atomic force microscope," *Journal of Applied Physics,* vol. 92, no. 10, pp. 6262, 2002.

[73] M. Gurgoze, "On the representation of a cantilevered beam carrying a tip mass by an equivalent spring mass system," *Journal of Sound and Vibration,* vol. 282, no. 1-2, pp. 538-542, 2005.

[74] T. J. Johnson, "Energy harvesting from mechanical vibrations using piezoelectric cantilever beams," *Proceedings of SPIE,* vol. 6169, pp. 61690D-12, 2006.

[75] J. Lin, B. Lee, and B. Alphenaar, "The magnetic coupling of a piezoelectric cantilever for enhanced energy harvesting efficiency," *Smart Materials and Structures,* vol. 19, no. 4, pp. 045012, 2010.

[76] A. Maccari, "Vibration control for the primary resonance of a cantilever beam by a time delay state feedback," *Journal of Sound and Vibration,* vol. 259, no. 2, pp. 241-251, 2003.

[77] S. E. Moon, "Sustainable vibration energy harvesting based on Zr-doped PMN-PT piezoelectric single crystal cantilevers," *ETRI Journal,* vol. 31, no. 6, pp. 688-694, 2009.

[78] C. Pany, "Calculation of non-linear fundamental frequency of a cantilever beam using non-linear stiffness," *Journal of Sound and Vibration,* vol. 256, no. 4, pp. 787-790, 2002.

[79] H. A. Sodano, "Generation and storage of electricity from power harvesting devices," *Journal of Intelligent Material Systems and Structures,* vol. 16, no. 1, pp. 67-75, 2005.

[80] C. Spier, "Study of optimal locations of piezo-patch actuators and sensors on a cantilever beam for maximum frequency gaps," *Proceedings of SPIE,* vol. 6166, pp. 616606-12, 2006.

[81] J. W. Yi, W. Y. Shih, and W.-H. Shih, "Effect of length, width, and mode on the mass detection sensitivity of piezoelectric unimorph cantilevers," *Journal of Applied Physics,* vol. 91, no. 3, pp. 1680, 2002.

[82] C. Zehetner, and H. Irschik, "Dynamic shape control of a flying cantilever by piezoelectric actuation," *Pamm,* vol. 3, no. 1, pp. 132-133, 2003.

[83] Q. Zheng, Z. Wang, and Y. Xu, "Symmetric air-spaced cantilevers for strain sensing," *Sensors and Actuators A: Physical,* vol. 147, no. 1, pp. 142-149, 2008.

[84] S. Shahruz, "Design of mechanical band-pass filters with large frequency bands for energy scavenging," *Mechatronics,* vol. 16, no. 9, pp. 523-531, 2006.

[85] S. Shahruz, "Design of mechanical band-pass filters for energy scavenging: multi-degree-of-freedom models," *Journal of Vibration and Control,* vol. 14, no. 5, pp. 753, 2008.

[86] E. Lefeuvre, A. Badel, C. Richard, and D. Guyomar, "Energy harvesting using piezoelectric materials: case of random vibrations," *Journal of Electroceramics,* vol. 19, no. 4, pp. 349-355, 2007.

[87] S. Sherrit, H. Wiederick, B. Mukherjee, and M. Sayer, "An accurate equivalent circuit for the unloaded piezoelectric vibrator in the thickness mode," *Journal of Physics d: applied physics,* vol. 30, pp. 2354, 1997.

[88] G. Warburton, "The dynamical behaviour of structures," *Book, Pergamon Press, ISBN: 0080203639*, 1964.

[89] R. Blevins, "Formulas for natural frequency and mode shape," *Book, Litton Educational Publishing, ISBN: 0442207107*, 1979.

[90] S. Qi, R. Shuttleworth, and S. Oyadiji, "Multiple resonances piezoelectric energy harvesting generator," *Proceedings of the ASME Conference on Smart Materials, Adaptive Structures and Intelligent Systems, Oxnard, California, USA*, September 21-23, 2009.

[91] S. Oyadiji, Z. Zhu, R. Sun, R. Pietruszkiewicz, P. Charles, S. Qi, and R. Shuttleworth, "Self-powered intelligent wireless disposable micro-sensors," *Wireless Sensing Demonstrator Showcase, National Physical Laboratory*, 2009.

[92] S. Oyadiji, S. Qi, and R. Shuttleworth, "Development of multiple cantilevered piezo fiber composite beams vibration energy harvester for wireless sensors," *World Congress of Engineering Asset Management, Athens, Greece*, September, 2009.

[93] S. Shahruz, "Limits of performance of mechanical band-pass filters used in energy scavenging," *Journal of Sound and Vibration,* vol. 293, no. 1-2, pp. 449-461, 2006.

[94] S. Shahruz, "Performance of mechanical bandpass filters used in energy scavenging in the presence of fabrication errors and coupling," *Journal of Vibration and Acoustics,* vol. 130, no. 5, pp. 054505, 2008.

[95] J. Wright, *Personal Communication, University of Manchester, UK*, 2008.

[96] N. Dutoit, and B. Wardle, "Performance of microfabricated piezoelectric vibration energy harvesters," *Integrated Ferroelectrics,* vol. 83, no. 1, pp. 13-32, 2006.

[97] N. Dutoit, B. Wardle, and S. Kim, "Design considerations for MEMS-scale piezoelectric mechanical vibration energy harvesters," *Integrated Ferroelectrics,* vol. 71, no. 1, pp. 121-160, 2005.

[98] P. Mitcheson, T. Green, E. Yeatman, and A. Holmes, "Architectures for vibration-driven micropower generators," *Microelectromechanical Systems, Journal of,* vol. 13, no. 3, pp. 429-440, 2004.

[99] F. Tse, I. Morse, and R. Hinkle, "Mechanical Vibrations," *Book, Allyn and Bacon Inc, ISBN: 0205059406*, 1963.

[100] R. Harker, "Generalized methods of vibration analysis," *Book, Wiley New York, ISBN: 0471867357*, 1983.

[101] D. Hartog, "Mechanical vibrations," *Book, New York and London: McGraw-Hill Book Co. Inc, ISBN: 9781406734812*, 1940.

[102] P. Laura, J. Pombo, and E. Susemihl, "A note on the vibrations of a clamped-free beam with a mass at the free end," *Journal of Sound and Vibration,* vol. 37, no. 2, pp. 161-168, 1974.

[103] Y. Ryu, J. Kim, and C. Cheong, "Piezoelectric shunting parameter estimation using electrical impedance models," *Proceedings of SPIE,* vol. 3989, pp. 39, 2000.

[104] T. Tsuchiya, and Y. Kagawa, "On the Passive Vibration Damping by Piezoelectric Transducers with Inductive Loading," *Systems Modeling and Simulation: Theory and Applications*, pp. 197-204, 2005.

[105] S. Fung, and M. Pong, "An improved model for Rosen type piezoelectric transformer for power converter," *35th Annual IEEE Power Elecrronics Specialisrs Conference,* vol. 1, pp. 731-735, 2004.

[106] A. Flynn, and S. Sanders, "Fundamental limits on energy transfer and circuit considerations for piezoelectric transformers," *IEEE Transactions on Power Electronics,* vol. 17, no. 1, pp. 8-14, 2002.

[107] N. G. Elvin, and A. A. Elvin, "A general equivalent circuit model for piezoelectric generators," *Journal of Intelligent Material Systems and Structures,* vol. 20, no. 1, pp. 3-9, 2008.

[108] R. A. Islam, H. Kim, S. Priya, and H. Stephanou, "Piezoelectric transformer based ultrahigh sensitivity magnetic field sensor," *Applied Physics Letters,* vol. 89, no. 15, pp. 152908, 2006.

[109] M. Saghafi, and A. Meghdari, "Electrical equivalent circuit of multi-mode flexible beams with piezoelectric elements," *Journal of Intelligent Material Systems and Structures,* vol. 19, no. 5, pp. 621-627, 2007.

[110] F. Viana, and J. Steffen, V, "Multimodal vibration damping through piezoelectric patches and optimal resonant shunt circuits," *Journal of the Brazilian Society of Mechanical Sciences and Engineering,* vol. 28, pp. 293-310, 2006.

[111] N. El Ghouti, "Hybrid modeling of a traveling wave piezoelectric motor," *PhD Thesis, Aalborg University, Denmark*, 2000.

[112] F. Mohammadi, A. Khan, and R. B. Cass, "Power generation from piezoelectric lead zirconate titanate fiber composites," *Materials Research Society,* vol. 736, pp. 263-270, 2003.

[113] J. Snowdon, "Vibration and shock in damped mechanical systems," *Book, John Wiley & Sons Inc, New York, ISBN: 0471810002*, 1968.

[114] M. Ferrari, V. Ferrari, M. Guizzetti, D. Marioli, and A. Taroni, "Piezoelectric multifrequency energy converter for power harvesting in autonomous microsystems," *Sensors and Actuators A: Physical,* vol. 142, no. 1, pp. 329-335, 2008.

[115] C. Zhang, and W. Chen, "A wideband magnetic energy harvester," *Applied Physics Letters,* vol. 96, no. 12, pp. 123507, 2010.

[116] J. Liu, H. Fang, Z. Xu, X. Mao, X. Shen, D. Chen, H. Liao, and B. Cai, "A MEMS-based piezoelectric power generator array for vibration energy harvesting," *Microelectronics Journal,* vol. 39, no. 5, pp. 802-806, 2008.

[117] Z. Chew, and L. Li, "Design and characterisation of a piezoelectric scavenging device with multiple resonant frequencies," *Sensors and Actuators A: Physical*, 2010.

[118] S. Jung, and K. Yun, "A wideband energy harvesting device using snap-through buckling for mechanical frequency-up conversion," *2010 IEEE 23rd International Conference on Micro Electro Mechanical Systems (MEMS), Wanchai, Hong Kong*, pp. 1207-1210, 2010.

[119] S. Jung, and K. Yun, "Energy-harvesting device with mechanical frequency-up conversion mechanism for increased power efficiency and wideband operation," *Applied Physics Letters,* vol. 96, pp. 111906, 2010.

[120] B. Marinkovic, and H. Koser, "Smart Sand - a wide bandwidth vibration energy harvesting platform," *Applied Physics Letters,* vol. 94, pp. 103505, 2009.

[121] D. A. W. Barton, S. G. Burrow, and L. R. Clare, "Energy harvesting from vibrations with a nonlinear oscillator," *Journal of Vibration and Acoustics,* vol. 132, no. 2, pp. 021009, 2010.

[122] S. G. Burrow, L. R. Clare, A. Carrella, and D. Barton, "Vibration energy harvesters with non-linear compliance," *Proceedings of SPIE,* vol. 6928, pp. 692807-10, 2008.

[123] S. G. Burrow, and L. R. Clare, "Open-loop power conditioning for vibration energy harvesters," *Electronics Letters,* vol. 45, no. 19, pp. 999, 2009.

[124] M. Mansour, M. Arafa, and S. Megahed, "Resonator with magnetically adjustable natural frequency for Vibration Energy Harvesting," *Sensors and Actuators A: Physical,* vol. 163, no. 1, pp. 297-303, 2010.

[125] X. Wu, J. Lin, S. Kato, K. Zhang, T. Ren, and L. Liu, "A frequency adjustable vibration energy harvester," *Proceedings of PowerMEMS 2008 and microEMS2008, Sendai, Japan*, November 9-12, 2008.

[126] D. Morris, J. Youngsman, M. Anderson, and D. Bahr, "A resonant frequency tunable, extensional mode piezoelectric vibration harvesting mechanism," *Smart Materials and Structures,* vol. 17, pp. 065021, 2008.

[127] M. Soliman, E. Abdel-Rahman, E. El-Saadany, and R. Mansour, "A wideband vibration-based energy harvester," *Journal of Micromechanics and Microengineering,* vol. 18, pp. 115021, 2008.

[128] D. Zhu, S. Roberts, J. Tudor, and S. Beeby, "Closed loop frequency tuning of a vibration-based micro-generator," *Proceedings of PowerMEMS and microEMS, Sendai, Japan*, 2008.

[129] W. Wu, Y. Chen, Y. Chen, C. Wang, and Y. Chen, "Smart wireless sensor network powered by random ambient vibrations," *IEEE International Conference on System, Man and Cybernetics,* vol. 4, pp. 2701-2708, 2006.

[130] M. Ferrari, V. Ferrari, M. Guizzetti, B. Andò, S. Baglio, and C. Trigona, "Improved energy harvesting from wideband vibrations by nonlinear piezoelectric converters," *Procedia Chemistry,* vol. 1, no. 1, pp. 1203-1206, 2009.

[131] S. Shahruz, "Elimination of vibration localization in mistuned periodic structures," *Journal of Sound and Vibration,* vol. 281, no. 1-2, pp. 452-462, 2005.

[132] LinearTechnology, *http://www.linear.com/*, accessed on 08/01/2011.

[133] M. Lallart, S. R. Anton, and D. J. Inman, "Frequency self-tuning scheme for broadband vibration energy harvesting," *Journal of Intelligent Material Systems and Structures,* vol. 21, no. 9, pp. 897-906, 2010.

[134] A. Cammarano, S. G. Burrow, D. A. W. Barton, A. Carrella, and L. R. Clare, "Tuning a resonant energy harvester using a generalized electrical load," *Smart Materials and Structures,* vol. 19, no. 5, pp. 055003, 2010.

[135] Davis, and C., "An Actively Tuned Solid-State Vibration Absorber Using Capacitive Shunting of Piezoelectric Stiffness," *Journal of Sound and Vibration,* vol. 232, no. 3, pp. 601-617, 2000.

[136] J. Schoeftner, and H. Irschik, "Passive damping and exact annihilation of vibrations of beams using shaped piezoelectric layers and tuned inductive networks," *Smart Materials and Structures,* vol. 18, no. 12, pp. 125008, 2009.

[137] S. Wu, "Piezoelectric shunts with a parallel RL circuit for structural damping and vibration control," *Proceedings of SPIE,* vol. 2720, pp. 259, 1996.

[138] S. Y. Wu, "Method for multiple mode piezoelectric shunting with single PZT transducer for vibration control," *Journal of Intelligent Material Systems and Structures,* vol. 9, no. 12, pp. 991-998, 1998.

[139] K. Yamada, H. Matsuhisa, H. Utsuno, and K. Sawada, "Optimum tuning of series and parallel LR circuits for passive vibration suppression using piezoelectric elements," *Journal of Sound and Vibration,* vol. 329, no. 24, pp. 5036-5057, 2010.

[140] U. Andreaus, and M. Porfiri, "Effect of electrical uncertainties on resonant piezoelectric shunting," *Journal of Intelligent Material Systems and Structures,* vol. 18, no. 5, pp. 477-485, 2006.

[141] A. Belloli, D. Niederberger, S. Pietrzko, M. Morari, and P. Ermanni, "Structural vibration control via R-L shunted active fiber composites," *Journal of Intelligent Material Systems and Structures,* vol. 18, no. 3, pp. 275-287, 2006.

[142] G. Lesieutre, "Vibration damping and control using shunted piezoelectric materials," *The Shock and Vibration Digest,* vol. 30, no. 3, pp. 187-195, 1998.

[143] D. Niederberger, A. Fleming, S. O. R. Moheimani, and M. Morari, "Adaptive multi-mode resonant piezoelectric shunt damping," *Smart Materials and Structures,* vol. 13, no. 5, pp. 1025-1035, 2004.

[144] D. Niederberger, and M. Morari, "An autonomous shunt circuit for vibration damping," *Smart Materials and Structures,* vol. 15, no. 2, pp. 359-364, 2006.

[145] C. Park, and D. Inman, "Uniform model for series RL and parallel RL shunt circuits and power consumption," *SPIE Conference on Smart Structures and Integrated Systems,* vol. 3668, pp. 797, 1999.

[146] C. Park, and D. Inman, "Enhanced piezoelectric shunt design," *Shock and Vibration,* vol. 10, no. 2, pp. 127-133, 2003.

[147] A. Leissa, and M. Sonalla, "Vibrations of cantilever beams with various initial conditions," *Journal of Sound and Vibration,* vol. 150, no. 1, pp. 83-99, 1991.

[148] D. Jenkins, M. Cunningham, W. Clegg, and M. Bakush, "Measurement of the modal shapes of inhomogeneous cantilevers using optical beam deflection," *Measurement Science and Technology,* vol. 6, pp. 160, 1995.

[149] H. A. B. Mustafa, and M. T. E. Khan, "Microstructure cantilever beam for current measurement," *South Africa Journal of Science,* vol. 105, pp. 264-269, 2009.

[150] S. Whitney, "Vibrations of Cantilever Beams: Deflection, Frequency, and Research Uses " *Web link: http://emweb.unl.edu/Mechanics-Pages/Scott-Whitney/325hweb/Beams.htm, accessed on 05/03/2011*, April 23, 1999.

[151] S. O. Oyadiji, *Personal communication, University of Manchester, UK*, 05/03/2011.

[152] L. M. Swallow, J. K. Luo, E. Siores, I. Patel, and D. Dodds, "A piezoelectric fibre composite based energy harvesting device for potential wearable

applications," *Smart Materials and Structures,* vol. 17, no. 2, pp. 025017, 2008.

[153] K. Van Dyke, "The Piezo-electric Resonator and its Equivalent Network," *Proc. Inst. Radio Engrs., NY,* vol. 16, pp. 742, 1928.

[154] C. Park, "On the circuit model of piezoceramics," *Journal of Intelligent Material Systems and Structures,* vol. 12, no. 7, pp. 515, 2001.

[155] Y. Yang, and L. Tang, "Equivalent circuit modeling of piezoelectric energy harvesters," *Journal of Intelligent Material Systems and Structures,* vol. 20, no. 18, pp. 2223-2235, 2009.

[156] C. Niezrecki, and H. H. Cudney, "Improving the power consumption characteristics of piezoelectric actuators," *Journal of Intelligent Material Systems and Structures,* vol. 5, no. 4, pp. 522-529, 1994.

[157] A. Guisado, J. L. Torres, and A. M. Gonzalez, "Study of equivalent circuits of piezoceramics to use in simulations with Pspice," *Ferroelectrics,* vol. 293, no. 1, pp. 307-319, 2003.

[158] S. Lin, "Electro-mechanical equivalent circuit of a piezoelectric ceramic thin circular ring in radial vibration," *Sensors and Actuators A: Physical,* vol. 134, no. 2, pp. 505-512, 2007.

[159] F. Feng, J. Shen, and J. Deng, "A 2D equivalent circuit of piezoelectric ceramic ring for transducer design," *Ultrasonics,* vol. 44, pp. e723-e726, 2006.

[160] E. Anderson, and N. Hagood, "Simultaneous piezoelectric sensing/actuation: analysis and application to controlled structures," *Journal of Sound and Vibration,* vol. 174, no. 5, pp. 617-639, 1994.

[161] D. Campolo, M. Sitti, and R. Fearing, "Efficient charge recovery method for driving piezoelectric actuators with quasi-square waves," *Ultrasonics, Ferroelectrics and Frequency Control, IEEE Transactions on,* vol. 50, no. 3, pp. 237-244, 2003.

[162] J. Gittings, C. Bowen, I. Turner, F. Baxter, and J. Chaudhuri, "Characterisation of ferroelectric-calcium phosphate composites and ceramics," *Journal of the European Ceramic Society,* vol. 27, no. 13-15, pp. 4187-4190, 2007.

[163] D. Guyomar, A. Badel, E. Lefeuvre, and C. Richard, "Toward energy harvesting using active materials and conversion improvement by nonlinear processing," *IEEE Transactions on Ultrasonics, Ferroelectrics and Frequency Control,* vol. 52, no. 4, pp. 584-595, 2005.

[164] D. Guyomar, C. Magnet, E. Lefeuvre, and C. Richard, "Power capability enhancement of a piezoelectric transformer," *Smart Materials and Structures,* vol. 15, no. 2, pp. 571-580, 2006.

[165] E. Lefeuvre, A. Badel, C. Richard, L. Petit, and D. Guyomar, "A comparison between several vibration-powered piezoelectric generators for standalone systems," *Sensors and Actuators A: Physical,* vol. 126, no. 2, pp. 405-416, 2006.

[166] G. Ivensky, S. Bronstein, and S. Ben-Yaakov, "A comparison of piezoelectric transformer AC/DC converters with current doubler and voltage doubler rectifiers," *IEEE Transactions on Power Electronics,* vol. 19, no. 6, pp. 1446-1453, 2004.

[167] G. Ivensky, M. Shvartsas, and S. Ben-Yaakov, "Analysis and modeling of a voltage doubler rectifier fed by a piezoelectric transformer," *IEEE Transactions on Power Electronics,* vol. 19, no. 2, pp. 542-549, 2004.

[168] T. Le, J. Han, A. von Jouanne, K. Mayaram, and T. Fiez, "Piezoelectric micro-power generation interface circuits," *IEEE Journal of Solid-State Circuits,* vol. 41, no. 6, pp. 1411-1420, 2006.

[169] C. Richard, D. Guyomar, D. Audigier, and G. Ching, "Semi-passive damping using continuous switching of a piezoelectric device," *Proceedings of SPIE,* vol. 3672, pp. 104, 1999.

[170] S. Ben-Yaakov, and N. Krihely, "Resonant rectifier for piezoelectric sources," *IEEE Twentieth Applied Power Electronics Conference and Exposition, APEC,* vol. 1, pp. 249-253, 2005.

[171] H. W. Jackson, "Introduction to Electronic Circuits," *Book, Prentice-Hall, Englewood Cliffs, New Jersey, ISBN: 0195423100*, 1959.

[172] P. Horowitz, and W. Hill, "The art of electronics," *Book, Cambridge university press, ISBN: 0521370957*, 1989.

[173] A. Antoniou, "Realisation of gyrators using operational amplifiers and their use in RC-active-network synthesis," *Proceeding of IEEE,* vol. 116, no. 11, pp. 1838-1850, 1969.

[174] R. Riordan, "Simulated inductors using differential amplifiers," *Electronics Letters,* vol. 3, no. 2, pp. 50-51, 1967.

[175] C. Luo, M. Whitehead, and H. Hofmann, "Design and testing of a power electronic synthetic inductor," *International Journal of Electronics,* vol. 96, no. 12, pp. 1249-1264, 2009.

[176] L. Torres, "Inductorless Chua's circuit," *Electronics Letters,* vol. 36, no. 23, pp. 1915-1916, 2000.

[177] B. Muthuswamy, T. Blain, and K. Sundqvist, "A Synthetic Inductor Implementation of Chua's Circuit," *Technical Report, University of California at Berkeley, No. UCB/EECS-2009-2*, 2009.

[178] L. Chua, "Chua's circuit: An overview ten years later," *J. Circuits Syst. Comput,* vol. 4, no. 2, pp. 117–159, 1994.

[179] A. Antoniou, "Gyrators using operational amplifiers," *Electronics Letters,* vol. 3, no. 8, pp. 350-352, 1967.

[180] A. Antoniou, and K. Naidu, "Modeling of a gyrator circuit," *IEEE Transactions on Circuit Theory,* vol. 20, no. 5, pp. 533-540, 1973.

[181] T. Hammons, and A. Parsons, "Design of Micro alternator for Power System Stability Investigations," *Proceedings of the IEE,* vol. 118, no. 10, pp. 1421-1441, 1971.

[182] M. Newton, and B. Hogg, "Optimal control of a micro-alternator system," *IEEE Transactions on Power Apparatus and Systems,* vol. 95, no. 6, pp. 1822-1833, 1976.

[183] S. Kabir, and R. Shuttleworth, "Brushless exciter model," *IEE Proceedings of Generation, Transmission and Distribution,* vol. 141, pp. 61-67, 1994.

[184] D. Auckland, and R. Shuttleworth, "Compensation systems for a micromachine model," *IEE Proceedings of Generation, Transmission and Distribution,* vol. 128, no. 1, pp. 12-17, 1981.

[185] J. B. X. Devotta, and V. Srinivasan, "Digital time-constant regulator for micromachines," *International Journal of Electronics,* vol. 55, no. 2, pp. 253-258, 1983.

[186] D. Slomovitz, "Electronic compensation of inductive voltage dividers and standard voltage transformers," *IEEE Transactions on Instrumentation and Measurement,* vol. 47, no. 2, pp. 465-468, 1999.

[187] D. Slomovitz, "Electronic compensation of voltage transformers," *IEEE Transactions on Instrumentation and Measurement,* vol. 37, no. 4, pp. 652-654, 1988.

[188] P. Daponte, "Electronically compensated current transformer modelling," *Measurement,* vol. 15, no. 4, pp. 213-222, 1995.

[189] A. Baccigalupi, and A. Liccardo, "A Low Cost Device for the Compensation of Voltage Transformers," *IEEE Instrumentation and Measurement Technology Conference Proceedings, IMTC, Victoria, BC*, pp. 1282-1287, 2008.

[190] F. Fallside, "Ripple instability in closed-loop pulse-modulation systems including invertor drives," *Proceedings of the Institution of Electrical Engineers,* vol. 115, no. 1, pp. 218-228, 1968.

[191] R. Shuttleworth, "On the modeling of a large alternator using a micromachine," *PhD Thesis, University of Manchester, UK*, 1976.

[192] T. Ikeda, "Fundamentals of piezoelectricity," *Book, Oxford University Press Oxford, ISBN:0198563396*, 1990.

[193] R. Luck, and E. Agba, "On the design of piezoelectric sensors and actuators," *ISA transactions,* vol. 37, no. 1, pp. 65-72, 1998.

[194] TexasInstruments, "Texas Instruments datasheets and design notes: Section 2 magnettic core characteristics, Section 4, Power transformer design, Section 5: Inductor and flyback transformer design, ," *Texas Instruments Incorporated*, 2001.

Appendix A:

Parameters of Piezoelectric Material

The piezoelectric relations describe the interactions between the electrical and mechanical behaviour of the material and are assumed here to be linear. Ignoring spatial coordinates, the linear equations for piezoelectricity are shown in Table A.1 [45, 47, 111, 192].

Table A.1: Different piezoelectric relationships in matrix notation [47, 111]

Independent Variable	Type	Piezoelectric relation	Form
$\tilde{T}, \tilde{E}$	Intensive	$\left\{\begin{matrix}\tilde{S} = s^E \tilde{T} + d^t \tilde{E} \\ \tilde{D} = d\tilde{T} + \varepsilon^T \tilde{E}\end{matrix}\right\}$	*d*-form
$\tilde{S}, \tilde{D}$	Extensive	$\left\{\begin{matrix}\tilde{T} = c^D \tilde{S} - h^t \tilde{D} \\ \tilde{E} = -h\tilde{S} + \beta^S \tilde{D}\end{matrix}\right\}$	*h*-form
$\tilde{T}, \tilde{D}$	Mixed	$\left\{\begin{matrix}\tilde{S} = s^D \tilde{T} + g^t \tilde{D} \\ \tilde{E} = -g\tilde{T} + \beta^T \tilde{D}\end{matrix}\right\}$	*g*-form
$\tilde{S}, \tilde{E}$	Mixed	$\left\{\begin{matrix}\tilde{T} = c^E \tilde{S} - e^t \tilde{E} \\ \tilde{D} = e\tilde{S} + \varepsilon^S \tilde{E}\end{matrix}\right\}$	*e*-form

As shown in Table A.1, the two mechanical variables and the two electrical variables can be used to provide 4 sets of piezoelectric relationships, to model the coupling between mechanical and electrical effects. In these relationships s^E and s^D are the compliances at constant electrical field strength and displacement respectively, ε^T and ε^S are the electrical permittivities at constant stress and constant strain respectively. c^D is the stiffness at constant electrical field displacement and c^E is the stiffness at constant electrical field, and β^S and β^T are the impermeability constants. The *d*-form and *e*-form relationships show piezoelectric coefficients for strain-

charge relationships, and *g*- and *h*-forms give the piezoelectric coefficients for strain-voltage relationships. Detailed analysis of such forms can be found in [192, 193]. The terms d and d^t are the piezoelectric charge constants, h, h^t are the piezoelectric deformation constants, g and g^t are the piezoelectric voltage constants, and e and e^t are the piezoelectric stress constants.

Consider first the intensive piezoelectric relationships (*d*-form) in which electric field and stress are chosen to be independent field variables and d is the piezoelectric strain constant [47, 111, 192].

The relationship between variables in the *d*-form piezoelectric system is:

$$\begin{Bmatrix} \tilde{S} = s^E \tilde{T} + d^t \tilde{E} \\ \tilde{D} = d\tilde{T} + \varepsilon^T \tilde{E} \end{Bmatrix}$$

In a piezoelectric device, there are three coordinates and the values of the variables in *d*-form may be different in each coordinate. Details of these can be found in Figure 1.3 in Chapter 1. Hence:

$$\tilde{D} = \begin{bmatrix} D_1 \\ D_2 \\ D_3 \end{bmatrix};\ \tilde{E} = \begin{bmatrix} E_1 \\ E_2 \\ E_3 \end{bmatrix};\ \varepsilon = \begin{bmatrix} \varepsilon_{11} & \varepsilon_{12} & \varepsilon_{13} \\ \varepsilon_{21} & \varepsilon_{22} & \varepsilon_{23} \\ \varepsilon_{31} & \varepsilon_{32} & \varepsilon_{33} \end{bmatrix};\ \tilde{S} = \begin{bmatrix} S_1 \\ S_2 \\ S_3 \\ S_4 \\ S_5 \\ S_6 \end{bmatrix};\ \tilde{T} = \begin{bmatrix} T_1 \\ T_2 \\ T_3 \\ T_4 \\ T_5 \\ T_6 \end{bmatrix}$$

therefore:

$$d = \begin{bmatrix} d_{11} & d_{12} & d_{13} & d_{14} & d_{15} & d_{16} \\ d_{21} & d_{22} & d_{23} & d_{24} & d_{25} & d_{26} \\ d_{31} & d_{32} & d_{33} & d_{34} & d_{35} & d_{36} \end{bmatrix};\ s = \begin{bmatrix} s_{11} & s_{12} & s_{13} & s_{14} & s_{15} & s_{16} \\ s_{21} & s_{22} & s_{23} & s_{24} & s_{25} & s_{26} \\ s_{31} & s_{32} & s_{33} & s_{34} & s_{35} & s_{36} \\ s_{41} & s_{42} & s_{43} & s_{44} & s_{45} & s_{46} \\ s_{51} & s_{52} & s_{53} & s_{54} & s_{55} & s_{56} \\ s_{61} & s_{62} & s_{63} & s_{64} & s_{65} & s_{66} \end{bmatrix}$$

where the subscripts refer to the coordinate system shown in Figure 1.3. It is usual to choose the coordinate system so that the electrode plates of the piezoelectric ceramic are perpendicular to axis 3. Then the electric field $\tilde{E}$ and electric displacement $\tilde{D}$ are also in the direction of axis 3, and the equations for $\tilde{D}$ and $\tilde{E}$ can be simplified to:

$$\tilde{D} = \begin{bmatrix} 0 \\ 0 \\ D_3 \end{bmatrix}; \quad \tilde{E} = \begin{bmatrix} 0 \\ 0 \\ E_3 \end{bmatrix}$$

Thus, the non-zero components of electric field $\tilde{E}$ and electric displacement $\tilde{D}$ are D_3 and E_3 respectively. Also particularly for PZT ceramic material belonging to the crystal class "6*mm*" of the hexagonal system described by [111, 192], the matrix function *d* can be further reduced due to the symmetry involved in the interaction process.

$$d = \begin{bmatrix} 0 & 0 & 0 & 0 & d_{15} & 0 \\ 0 & 0 & 0 & d_{15} & 0 & 0 \\ d_{31} & d_{31} & d_{33} & 0 & 0 & 0 \end{bmatrix}$$

Since the components of the matrix *d* are reduced to only three, non-zero elements d_{31}, d_{33} and d_{15}, so the electromechanical coupling in piezoelectric ceramics is achieved through three principal modes of vibration. These modes are the longitudinal mode (d_{33}), the transverse mode (d_{31}) and shear mode (d_{15}). The piezoelectric coefficient d_{ij} is used for both piezoelectric direct and converse effect as in [47]:

$$d_{ij}^{\theta} = \begin{cases} = \left[\dfrac{\partial S_j}{\partial E_i}\right]_{\tilde{D},\theta} = \left(\dfrac{m}{V}\right) & \text{Converse Effect (Actuator)} \\ = \left[\dfrac{\partial D_i}{\partial T_j}\right]_{\tilde{S},\theta} = \left(\dfrac{C}{N}\right) & \text{Direct Effect (Generator)} \end{cases}$$

Table A.2 [46, 49] gives the parameters of the piezoelectric material in "direct effect". For "reverse effect", the material are used as piezoelectric actuators, thus d_{33} will have the unit of *m/V*.

Table A.2: Parameters of the PZT5A(used in PFC) and PIC252(used in P876.A11)

Parameters	Symbol	Unit	PZT5A	PIC252/PIC255
Density	ρ	g/cm^3	7.5	7.80
Curie temperature	Tc	$°C$	350	350
Mechanical quality factor	Q_m	-	100	80
Coupling factor	k_p	-	0.62	0.62
	k_{31}		0.36	0.35
	k_{33}		0.72	0.69
	k_{15}		0.69	0.66
Piezoelectric charge constant	d_{31}	10^{-12} C/N	-173	-180
	d_{33}		380	400
	d_{15}		582	550
Piezoelectric voltage constant	g_{31}	$10^{-3}Vm/N$	-11.5	-11.3
	g_{33}		25	25
Elastic constant	S_{11}^E	$10^{-12}m^2/N$	15.2	16.1
	S_{33}^E		18.3	20.7

The optimal tuning ratio δ and optimal damping factor ξ in series connection are given by [110, 145]:

$$\delta_{OPT} = \sqrt{1 + K_{ij}^{\ 2}}$$

$$\xi_{OPT} = \frac{\sqrt{2}K_{ij}}{(1 + K_{ij}^2)}$$

Hence, the resistance and optimal required inductance to resonate with the piezoelectric output capacitance is [110]:

$$L_{OPT} = \frac{1}{C_{PZT}\omega_e^{\,2}} = \frac{1}{C_{PZT}(\omega_m \delta_{OPT})^2} = \frac{1}{C_{PZT}(1+K_{ij}^{\,2})\omega_m^{\,2}}$$

$$R_{OPT} = \frac{\xi_{OPT}}{C_{PZT}\omega_m} = \frac{\sqrt{2}K_{ij}}{C_{PZT}\omega_m(1+K_{ij}^{\,2})}$$

where ω_e and ω_m are the electrical and mechanical resonant frequencies respectively. The equations shown that the coupling factor will affect the damping in the electrical system, hence the optimal inductance and resistance are also affected.

Appendix B:

Matrices of Multiresonant Beam Mass

$\tilde{M}_{11}(11)$ is:

$$\begin{bmatrix} \int_0^{l_{cc}} M\phi_1^2(x)dx + m_1\phi_1^2(c_1) + m_2\phi_1^2(c_2) & \int_0^{l_{cc}} M\phi_1(x)\phi_2(x)dx + m_1\phi_1(c_1)\phi_2(c_1) + m_2\phi_1(c_2)\phi_2(c_2) \\ \int_0^{l_{cc}} M\phi_1(x)\phi_2(x)dx + m_1\phi_1(c_1)\phi_2(c_1) + m_2\phi_1(c_2)\phi_2(c_2) & \int_0^{l_{cc}} M\phi_2^2(x)dx + m_1\phi_2^2(c_1) + m_2\phi_2^2(c_2) \end{bmatrix}$$

$\tilde{M}_{11}(12)$ is:

$$\begin{bmatrix} m_1l_1\phi_1(c_1)\psi_1(c_1) - m_2l_2\phi_1(c_2)\psi_1(c_2) & m_1l_1\phi_1(c_1)\psi_2(c_1) - m_2l_2\phi_1(c_2)\psi_2(c_2) \\ m_1l_1\phi_2(c_1)\psi_1(c_1) - m_2l_2\phi_2(c_2)\psi_1(c_2) & m_1l_1\phi_2(c_1)\psi_2(c_1) - m_2l_2\phi_2(c_2)\psi_2(c_2) \end{bmatrix}$$

$\tilde{M}_{11}(13)$ is:

$$\begin{bmatrix} m_1\phi_1(c_1) & m_1\phi_2(c_1) \\ m_2\phi_1(c_2) & m_2\phi_2(c_2) \end{bmatrix}$$

$\tilde{M}_{11}(21)$ is:

$$\begin{bmatrix} m_1l_1\phi_1(c_1)\psi_1(c_1) - m_2l_2\phi_1(c_2)\psi_1(c_2) & m_1l_1\phi_1(c_1)\psi_2(c_1) - m_2l_2\phi_1(c_2)\psi_2(c_2) \\ m_1l_1\phi_2(c_1)\psi_1(c_1) - m_2l_2\phi_2(c_2)\psi_1(c_2) & m_1l_1\phi_2(c_1)\psi_2(c_1) - m_2l_2\phi_2(c_2)\psi_2(c_2) \end{bmatrix}^T$$

$\tilde{M}_{11}(22)$ is:

$$\begin{bmatrix} \int_0^{l_{cc}} \chi\psi_1^2(x)dx + m_1 l_1^2 \psi_1^2(c_1) + m_2 l_2^2 \psi_1^2(c_2) & \int_0^{l_{cc}} \chi\psi_1(x)\psi_2(x)dx + m_1 l_1^2 \psi_1(c_1)\psi_2(c_1) - m_2 l_2^2 \psi_1(c_2)\psi_2(c_2) \\ \int_0^{l_{cc}} \chi\psi_1(x)\psi_2(x)dx + m_1 l_1^2 \psi_1(c_1)\psi_2(c_1) - m_2 l_2^2 \psi_1(c_2)\psi_2(c_2) & \int_0^{l_{cc}} \chi\psi_1^2(x)dx + m_1 l_1^2 \psi_1^2(c_1) + m_2 l_2^2 \psi_1^2(c_2) \end{bmatrix}$$

$\tilde{M}_{11}(23)$ is:

$$\begin{bmatrix} m_1 l_1 \psi_1(c_1) & -m_2 l_2 \psi_1(c_2) \\ m_1 l_1 \psi_2(c_1) & -m_2 l_2 \psi_2(c_2) \end{bmatrix}$$

$\tilde{M}_{11}(31)$ is:

$$\begin{bmatrix} m_1 \phi_1(c_1) & m_1 \phi_2(c_1) \\ m_2 \phi_1(c_2) & m_2 \phi_2(c_2) \end{bmatrix}^T$$

$\tilde{M}_{11}(32)$ is:

$$\begin{bmatrix} m_1 l_1 \psi_1(c_1) & -m_2 l_2 \psi_1(c_2) \\ m_1 l_1 \psi_2(c_1) & -m_2 l_2 \psi_2(c_2) \end{bmatrix}^T$$

$\tilde{M}_{11}(33)$ is:

$$\begin{bmatrix} m_1 & 0 \\ 0 & m_2 \end{bmatrix}$$

Appendix C:

Design of an Inductor for Amplified Inductor Circuit

To design the 10*H* inductor, an EPCOS ETD59 ferrite core was used, material type is N97. The permittivity of free space μ is $4\pi 10^{-7}(WbA^{-1}m^{-1})$, cross sectional area of the core A_e is $368mm^2$ and the diameter of the copper wire is 0.2*mm*. The formula and equations used in this Appendix can be found in [194].

For a 10*H* inductor:

$$N = \sqrt{\frac{Ll}{\mu A_e}} = \sqrt{\frac{10 \times 0.2 \times 10^{-3}}{4\pi \times 10^{-7} \times 368 \times 10^{-6}}} = 2080 turns$$

The estimated winding resistance of R_1 is $228m \times 0.337\Omega = 77.8\Omega$. The measured inductor details are given in Table C.1.

Table C.1: Inductance and resistance measurement

Tested Frequency (*Hz*)	Inductance L_1 (N_1 turns) (*H*)	Sense winding Inductance L_2 (N_2 turns) (*H*)	Winding Resistance R_1 (N_1 turns) (Ω)	Sense Winding Resistance R_2 (N_1 turns) (Ω)
80	10.04	7.11	87.74	83.56

Leakage inductance was measured to be between 31*mH* and 48*mH*. The measured inductance value of 7.11*H* is close to the estimation as:

$$L_2 = (\frac{N_2}{N_1})^2 L_1 = (\frac{1750}{2100})^2 \times 10.04H = 6.97H$$

The losses of this inductor are calculated as follows:

For a switching frequency of 30*kHz*,

$$dt = \frac{(\frac{1}{f_s})}{4} = \frac{33.33\mu s}{4} = 8.33\mu s$$

rearranging $E = NA_e \frac{dB}{dt}$ yields:

$$dB = \frac{Edt}{NA_e} = \frac{30 \times 8.33 \times 10^{-6}}{2100 \times 368 \times 10^{-6}} = 0.323mT$$

Assume the core loss is around $8kW/m^3$ at 30*mT* and 100*kHz*, for a N97 ferrite material. The hysteresis loss of the ferrites varies with the flux density swing ΔB^n, where *n* is generally between 2.5 and 3. V_e for ETD59 is $51200mm^3$.

There are two frequencies in the circuit, 30*kHz* switching frequency and a sinusoidal input frequency around 100*Hz*.

For the loss due to 30*kHz* switching, is:

$$8000 {}^{kW}\!/_{m^3} \times (\frac{0.323mT}{30mT})^{2.5} \times (\frac{30kHz}{100kHz}) \times 51200 \times 10^{-9} m^3 = 1.47\mu W$$

For 100*Hz* sinusoidal input frequency:

$$E_{RMS} = 4.44 \times \hat{B} \times A_e \times N_1 \times f$$

Therefore:

$$\begin{aligned}\hat{B} &= \frac{E_{RMS}}{4.44 \times \times A_e \times N_1 \times f} \\ &= \frac{30}{\sqrt{2} \times 4.44 \times 368 \times 10^{-6} \times 2100 \times 100} \\ &= 61.8mT\end{aligned}$$

Using $8kW/m^3$ at $30mT$ for the N97 material, the loss due to the $100Hz$ is:

$$8000 {kW}/{m^3} \times (\frac{61.8mT}{30mT})^{2.5} \times (\frac{100Hz}{100kHz}) \times 51200 \times 10^{-9} m^3 = 2.49mW$$

Therefore the total loss due to the inductor is around $2.5mW$.

Appendix D:

Measured Results of Amplified Inductor Circuit Frequency Tuning

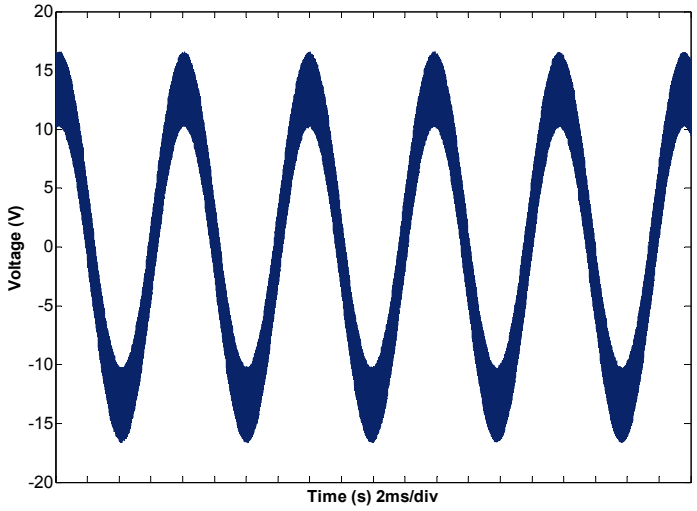

Figure D.1: Measured C_{PZT} voltage with $G_{POT} = 0$

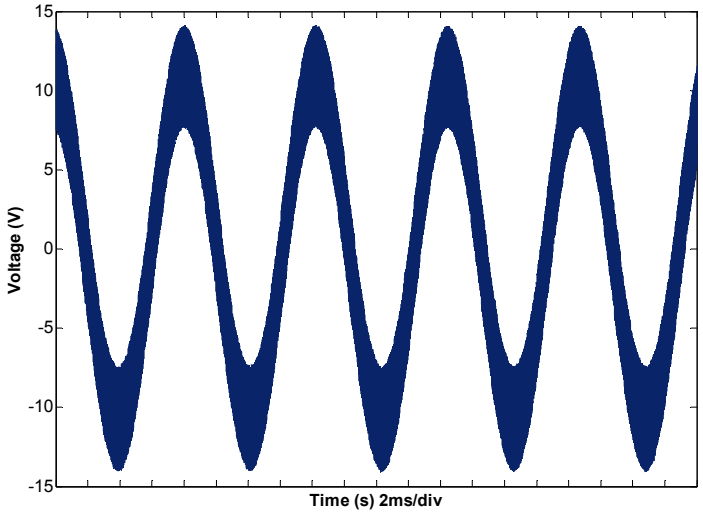

Figure D.2: Measured C_{PZT} voltage with $G_{POT} = 0.1$

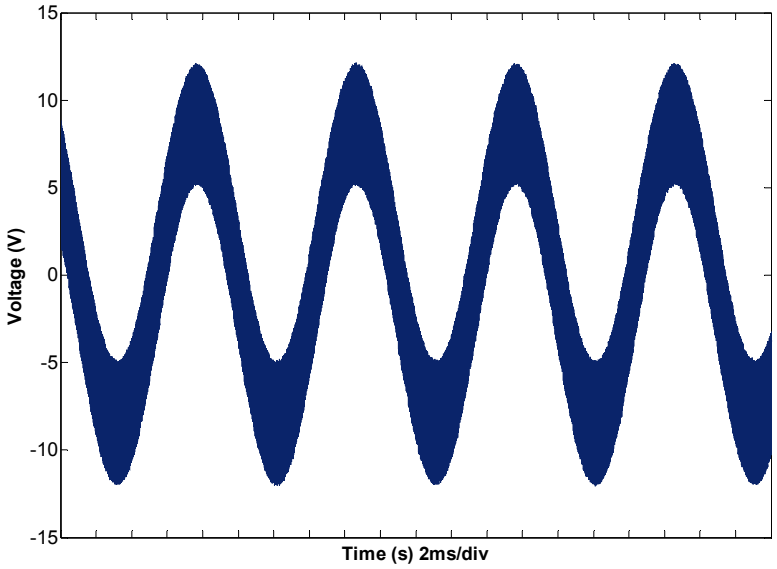

Figure D.3: Measured C_{PZT} voltage with $G_{POT} = 0.2$

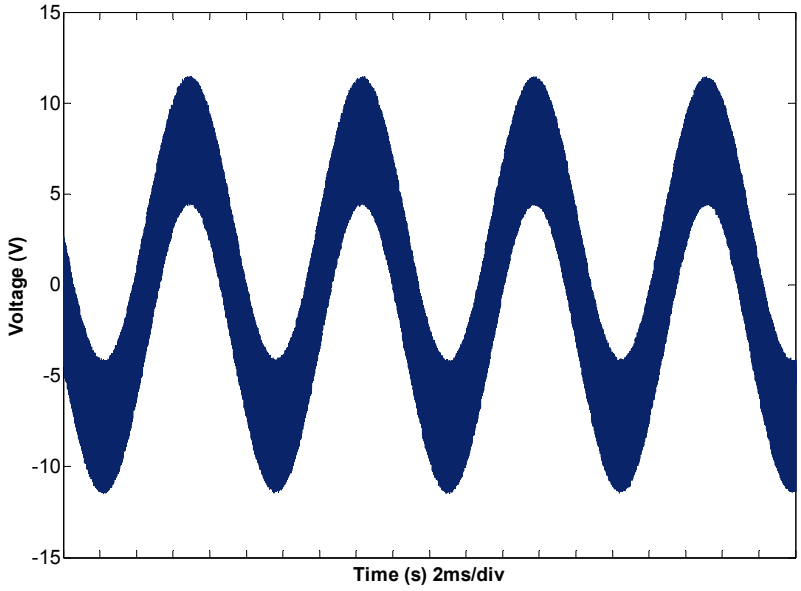

Figure D.4: Measured C_{PZT} voltage with $G_{POT} = 0.3$

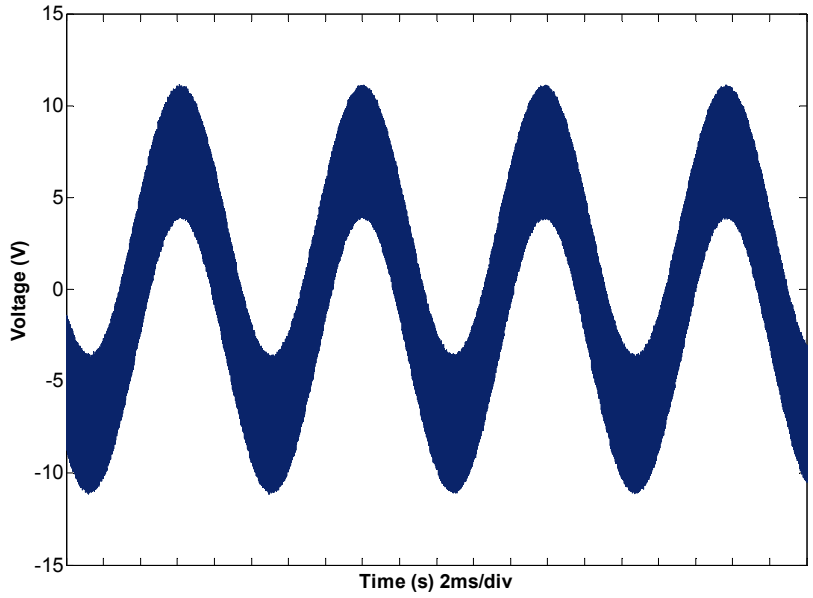

Figure D.5: Measured C_{PZT} voltage with $G_{POT} = 0.4$

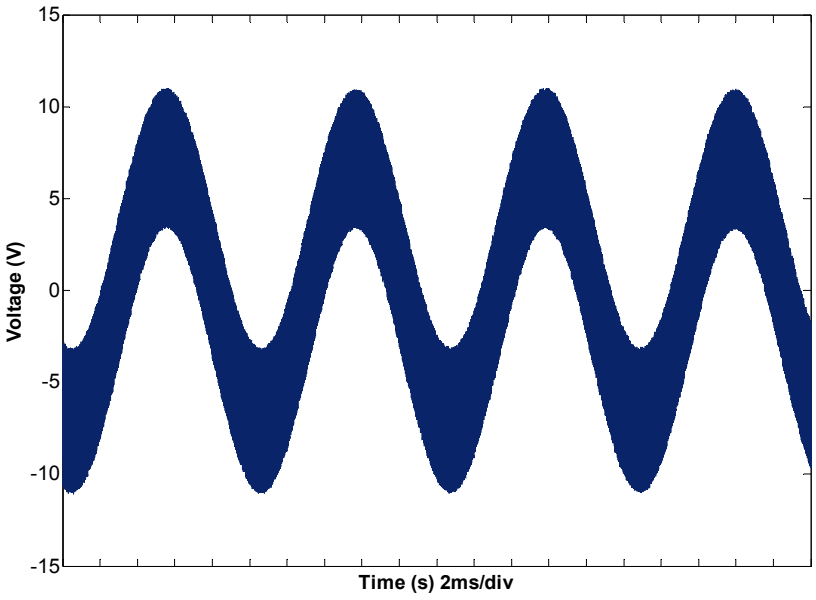

Figure D.6: Measured C_{PZT} voltage with $G_{POT} = 0.5$

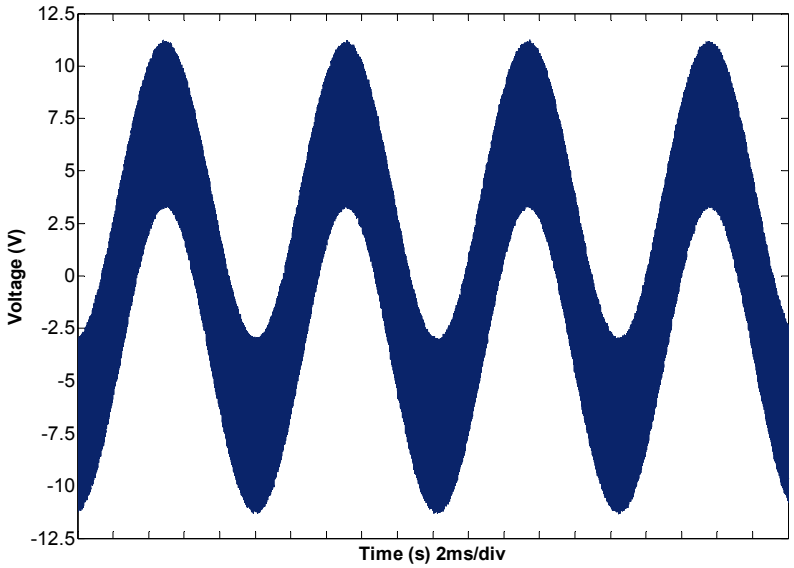

Figure D.7: Measured C_{PZT} voltage with $G_{POT} = 0.6$

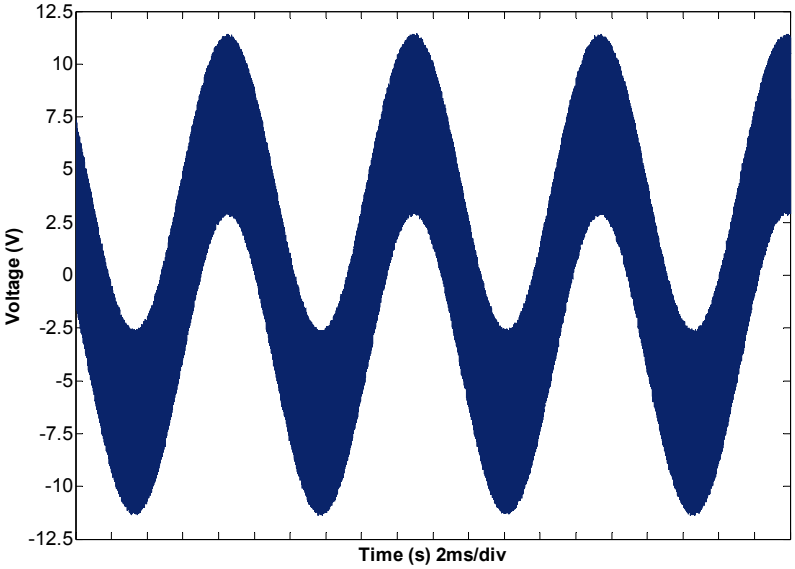

Figure D.8: Measured C_{PZT} voltage with $G_{POT} = 0.7$

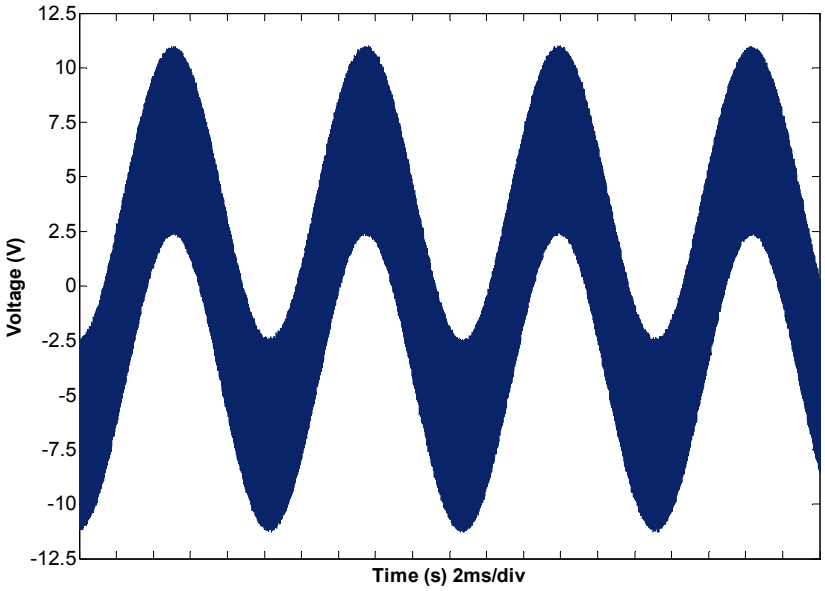

Figure D.9: Measured C_{PZT} voltage with $G_{POT} = 0.8$

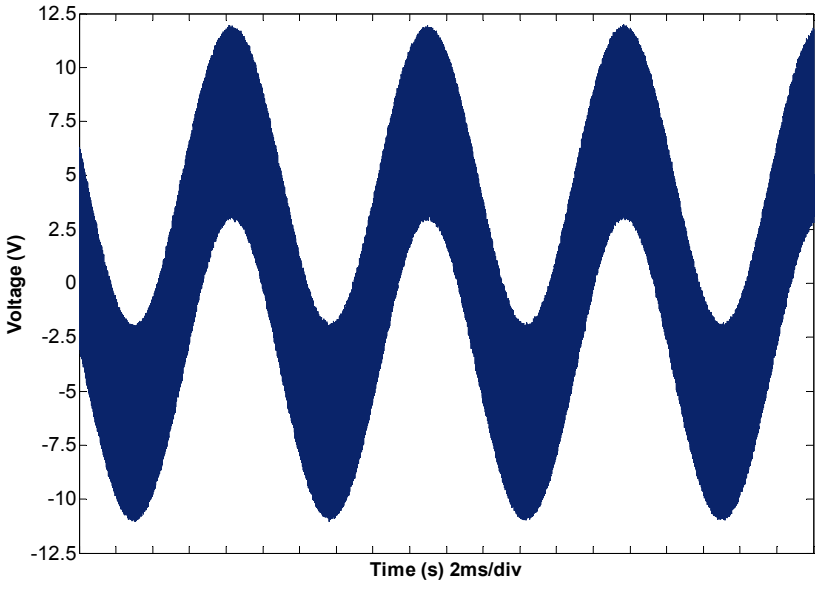

Figure D.10: Measured C_{PZT} voltage with $G_{POT} = 0.9$

Appendix E:

Reprint -

Design of a Multiresonant Beam for Broadband Piezoelectric Energy Harvesting

Author:

S. Qi, R. Shuttleworth, S. O. Oyadiji, J. Wright,

Publisher:

Jounal of Smart Materials and Structures, Institute of Physics, Vol. 19, No. 9, 2010, Impact factor 1.749

IOP Publishing Smart Materials and Structures
Smart Mater. Struct. **19** (2010) 094009 (10pp) doi:10.1088/0964-1726/19/9/094009

Design of a multiresonant beam for broadband piezoelectric energy harvesting

Shaofan Qi[1], **Roger Shuttleworth**[1], **S Olutunde Oyadiji**[2] **and Jan Wright**[2]

[1] School of Electrical and Electronic Engineering, University of Manchester, UK
[2] School of Mechanical, Aerospace and Civil Engineering, University of Manchester, UK

Received 1 February 2010, in final form 28 May 2010
Published 5 August 2010
Online at stacks.iop.org/SMS/19/094009

Abstract
This paper describes initial investigations into the behavior of a mechanical system for a proposed novel energy harvesting device. The device comprises a clamped–clamped beam piezoelectric fiber composite generator with side mounted cantilevers. These side mounted cantilevers are tuned by added masses to be resonant at different frequencies. A Rayleigh–Ritz model has been developed to predict the vibration response of the device and results from this model and from the real system are compared. The mechanical aspects of the device show a wide band energy harvesting characteristic in comparison to a single cantilever piezoelectric harvester.

(Some figures in this article are in colour only in the electronic version)

1. Introduction

Condition monitoring, CM, of industrial plants is of great interest to manufacturers as it can give warning of impending machine failure or system deterioration and permit timely repairs thus saving manufacturing costs. The recent availability of low cost sensors and low power signal processing devices makes CM a viable and necessary proposition if industrial competitiveness is to be maintained. However, where the manufacturing plant is spread over a wide area or large volume, the cost of wiring a multiplicity of sensors can be excessive, preventing adequate CM implementation.

In recent years a possible solution to the problem of high wiring cost has been investigated—wireless sensors, powered by batteries. However, batteries need frequent replacement and can be expensive to replace, so a further development is energy harvesting, whereby ambient energy, e.g. thermal, light, vibration, electromagnetic or other, is captured and converted to electricity, to supply the CM sensors and the low power radio transmitters (and in some cases receivers). The transmitters send the processed CM information to a distant monitoring system, completely eliminating the need for any wire connections. Typical wireless systems include ZigBee, Bluetooth etc, as shown in figure 1.

Although sensing, processing and transmitting technologies are becoming well developed and highly efficient, nevertheless there exists scope for improvement in energy harvesting systems.

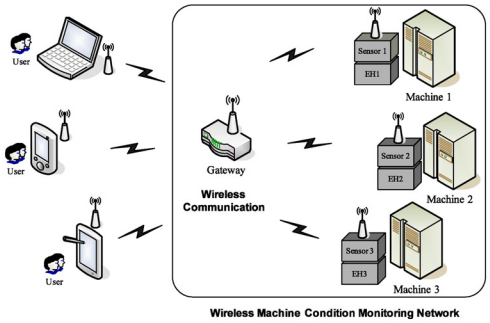

Figure 1. Wireless condition monitoring system.

Energy harvesters only need to produce low electrical powers, typically between 1 and 10 mW to power CM sensors, and can achieve this by several means. Of great interest at present is the improvement of energy harvesters collecting vibration energy. In these devices ambient vibrations are converted into electricity by means of a cantilever, which provides resonant mechanical amplification, and upon which is attached a piezoelectric [1–8] or electromagnetic generator [9]. These harvesters are often clamped to a machine bed plate and use the vibrations of the machine being monitored as the energy source.

The ambient vibration frequencies that the harvesters are subjected to, have to be within a narrow frequency

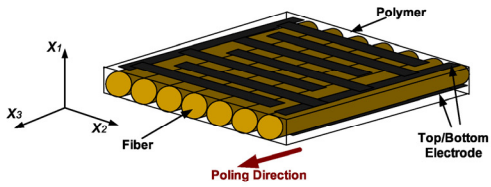

Figure 2. Geometry and mode operation for PFC.

range situated around the cantilever's natural frequency for amplification to occur. Should the machine's vibration frequency be too far away from the natural frequency (typically a few Hz), then a significant drop in output power results [5, 6, 10].

Often a machine will produce vibrations encompassing a range of frequencies, varying in frequency and amplitude as the machine load and speed change. In these situations a single cantilever harvester is less effective, and instead a harvester is needed which can work efficiently over a range of frequencies. Adding mechanical damping is one means of broadening the response of a vibrating cantilever [11]. However, for a vibration energy harvesting device, the consequent loss of efficiency is undesirable, and for this reason the technique is hardly ever used.

Shahruz [7, 8] was one of the first to describe a wide band energy harvester. In this device an array of cantilevers, each of slightly different natural frequency, and each having a piezo device mounted upon it, was excited by vibrations. The device had a band of closely spaced mechanical resonance peaks. His theoretical predictions suggest that the device could harvest vibration energy over a wider range of frequencies than a single cantilever. Sari *et al* [9] produced a micro-harvester with a multiplicity of different length cantilevers, using electromagnetic generators (one coil per cantilever, all coils electrically in parallel) and a shared magnet. This showed a flat wide band response, but it was considered that the output power density of 0.35 μW cm^{-3} was low due to destructive interference between the signals generated by the individual resonators [9].

Soliman *et al* [12] investigated a cantilever with a stopper to limit the amplitude of vibration, and showed that a 240% increase in bandwidth resulted from their device. However, the system's bandwidth is inevitably a complex function of amplitude and in a practical device the stopper would need to be moved in an automatic manner to compensate. It is difficult to envisage a practical system that could achieve this compensation.

Morris *et al* [13] describe a tunable prototype harvester using PVDF sheet in a clamped–clamped structure. This is manually tunable over a wide range by an adjustable screw but has no method of automatic tuning. Zhu *et al* [14] produced a tunable harvester using magnetic tensioning of a cantilever. The generator is electromagnetic and tunable over a range of approximately 70–95 Hz. They estimate the duty cycle for automatic tuning to be 230 s, this limit being imposed by the energy consumption of the tuning device. It is debatable whether the response time of this harvester is short enough to allow frequency tracking in practice.

Figure 3. Piezoelectric fiber composite bimorph (PFCB).

To summarize, most researchers have concentrated on varying the stiffness to achieve cantilever tuning. Other techniques such as capacitive loading have also been described [15]. This paper describes preliminary work in the development of a broadband energy harvester using multiresonant beams. The configuration comprises a clamped–clamped main beam with small cantilevers attached to one side. The multiresonant responses of the small cantilevers induce a wide band strain distribution in the main beam on which a piezoelectric fiber composite strip is attached.

The paper consists of six sections. Section 1 is the introduction. Section 2 summarizes existing piezoelectric energy harvester technology. Section 3 presents the proposed piezoelectric multiple cantilever energy harvester, and gives a Rayleigh–Ritz mathematical evaluation. Section 4 shows software simulation results of the structure. Section 5 describes experimental work with studies of different multiple cantilever design alternatives. Section 7 provides the conclusion and suggests future work.

2. Piezoelectric materials for energy harvesting

In order to convert ambient vibration energy into electricity, piezoelectric films are now commonly incorporated into energy harvesting devices. Piezoelectric fiber composite (PFC) is one of the most commonly used piezoelectric films [16]. PFC uses an interdigitated electrode pattern to increase the effective ceramic volume, as shown in figure 2, allowing the piezoelectric primary axis to align with the fiber direction, permitting higher strain levels.

Figure 2 illustrates the geometry of the interdigitated electrode piezoelectric fiber composite device. Electrode patterns have fingers of alternating polarity, and are exact mirror images on the top and bottom faces. Poling is predominantly along the X_3 axis [16]. Application of an electric field produces primary actuation along the fibers, and transverse actuation perpendicular to the fibers.

A PFC Bimorph, PFCB, contains two layers of PFC material, mounted above and below a stainless steel shim, as shown in figure 3.

Most applications for piezoelectric materials are based on their direct effect [5], see figure 4.

In figure 4, if the material is vibrated by an external force, a voltage will appear between the electrodes. The PFCB used was manufactured by Advanced Cerametrics (ACI), and when operated at its resonant frequency, can generate voltages of over 400 V_{pk-pk}. Flexible piezoelectric devices such as PFCBs are attractive for energy harvesting applications, because of their ability to withstand high strain.

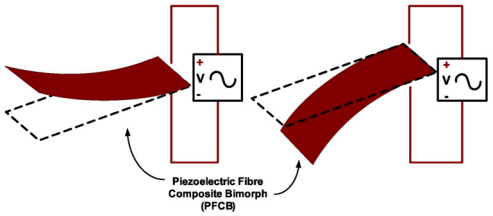

Figure 4. Direct effect of piezoelectric ceramic.

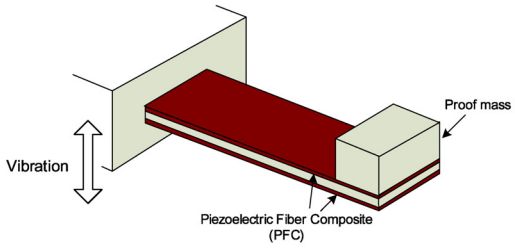

Figure 5. Single piezoelectric cantilever generator model.

Unfortunately PFC has a lower coupling coefficient than 'hard' PZT5A material, however its greater flexibility makes it more suitable for energy harvesting applications, where applications typically have resonant frequencies below 100 Hz.

3. Piezoelectric cantilever energy harvester

Figure 5 shows the piezoelectric cantilever generator model developed by Roundy [5]. It comprises a cantilever beam on which are mounted piezoelectric fibers (top and bottom layers) and a proof mass. By applying vibration to the cantilever's support, mechanical vibration energy is converted into electricity by the piezoelectric fiber composite (PFC) material.

Several researchers have described similar devices [1–6] and the system is generally analyzed as a mass–spring–damper system as shown in figure 6.

From [5], the equation representing dynamic motion of the piezoelectric device is:

$$m\ddot{z} + (c_e + c_m)\dot{z} + kz = -m\ddot{y} \quad (1)$$

where z is the spring deflection, y is the input displacement, m is the mass, c_e and c_m are the electrical and mechanical damping coefficients and k is the spring constant.

When the ambient vibration frequency matches the resonant frequency of the cantilever, energy conversion is at its most efficient, otherwise the efficiency is low. The device has a high Q, around 100 [17], and is not suited to variable frequency vibrations due to its narrow operating bandwidth.

Figure 7 shows the form of system output for a multiple degree of freedom system which is typical for a piezoelectric energy harvester, the system working most effectively at its first resonant frequency of perhaps around one hundred Hz,

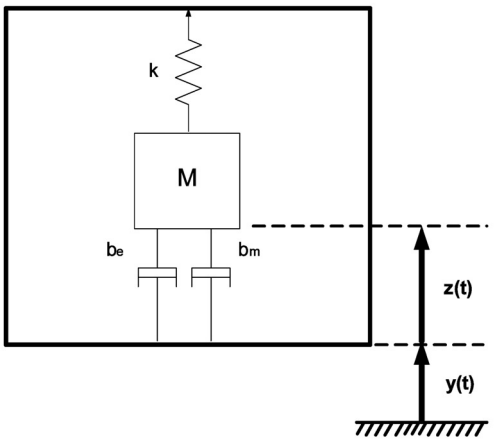

Figure 6. Mechanical model of typical cantilever energy harvester.

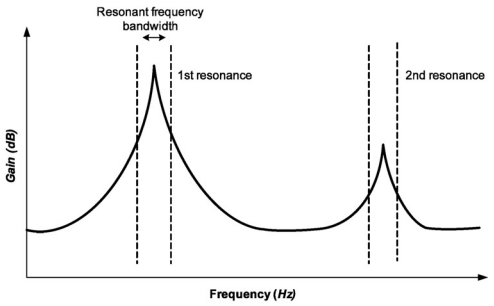

Figure 7. Estimated piezoelectric cantilever generator output.

depending on stiffness k and proof mass m. The damping produced in mechanical systems by electrical networks has been discussed in [18].

In [1, 6, 19], resonant frequencies of piezoelectric generators were designed to match an environmental vibration frequency, to achieve maximum output power. Although it is possible to design an energy harvester in which the resonant frequency matches the vibration frequency, for a variable speed industrial plant, vibrations occur over a range of frequencies, making the cantilever generator device with one resonant peak less effective. Consequently interest has arisen in the design of an energy harvesting device which can operate over a wider frequency band.

To achieve this wider bandwidth a multiple cantilever beam structure is proposed, as shown in figure 8. The structure comprises a clamped–clamped beam which is accelerated equally at its clamped ends due to the ambient vibration. The beam supports several small cantilevers.

The system has many resonant frequencies due to the several different cantilevers. The strains produced by the cantilevers when excited at their resonant frequencies by the ambient vibration are summated within the clamped–clamped beam, and converted to an electrical form by the PFCB. The resonant frequency of a cantilever depends primarily upon its

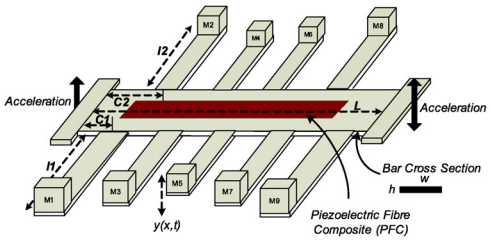

Figure 8. Proposed multiple cantilever structure.

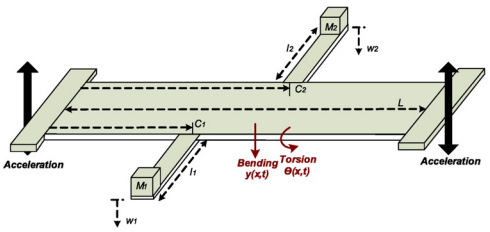

Figure 9. Clamped–clamped beam with two cantilevers.

stiffness and proof mass; therefore by adjusting one or both of these the cantilevers' resonant frequencies can be altered. The response of the PFCB to the vibration acceleration at the end supports should thus have a multitude of resonance peaks, if the parameters are chosen appropriately. Whereas a single cantilever system, as used for energy harvesting by previous researchers, has only one resonance peak, the proposed design should work over a wider bandwidth, enabling energy to be harvested over a wider spectrum. The design has only one PFC device, mounted on the clamped–clamped beam. This eliminates the need for electrical connections, as would be required in harvesters comprising a multiplicity of individual cantilevers.

4. Mathematical evaluation of multiple cantilever structure

To determine if the concept is valid a Rayleigh–Ritz mechanical analysis of the proposed system was carried out. Since the cantilever beams can be mounted on either side of the main beam, the analysis started with a clamped–clamped beam having two cantilevers, one on each side, as shown in figure 9. The clamped–clamped ends are subjected to the same vertical vibration.

Figure 9 shows two cantilevers attached to the main beam at positions c_1 and c_2. M_1 and M_2 are the cantilever proof masses, l_1 and l_2 are the cantilever lengths, and L is the clamped–clamped beam length. We assume two mode shapes for bending $y(x,t)$ and torsion $\theta(x,t)$, as given in equations (2) and (3). Further to the analysis of the standard cantilever model from the previous section, torsional vibration of the beam is also considered.

$$y(x,t) = q_0(t)\phi_0(x) + q_1(t)\phi_1(x) + q_2(t)\phi_2(x)\cdots \quad (2)$$

$$\theta(x,t) = b_1(t)\psi_1(x) + b_2(t)\psi_2(x)\cdots. \quad (3)$$

In equations (2) and (3) $\phi_i(x)$ and $\psi_i(x)$ are the known shape functions, $q_i(t)$ and $b_i(t)$ are the unknown functions or generalized coordinates. For a clamped–clamped beam, the mode shapes are given by [20]

$$\phi_i(x) = \cosh\frac{\lambda_i x}{L} - \cos\frac{\lambda_i x}{L} - \frac{\cosh\lambda_i - \cos\lambda_i}{\sinh\lambda_i - \sin\lambda_i} \times \left(\sinh\frac{\lambda_i x}{L} - \sin\frac{\lambda_i x}{L}\right) \quad (4)$$

$$\psi_i(x) = \sin\frac{\mathrm{i}\pi x}{L}. \quad (5)$$

The strain energy U for the system is given by

$$U(t) = \tfrac{1}{2}\int_0^L EIy''^2(x,t)\,\mathrm{d}x + \tfrac{1}{2}\int_0^L GJ\theta'^2(x,t)\,\mathrm{d}x + \tfrac{1}{2}\sum_{j=1}^{2} k_j y_j^2 \quad (6)$$

where k_j is the stiffness of a cantilever, E is the material's Young's modulus, I is the second moment of inertia and the product EI is flexural rigidity. G is the material shear modulus, J is the section torsion constant and the product GJ is the torsional rigidity. The first term on the right-hand side of (6) represents the strain energy of bending, the second term is the torsional strain energy and the third term is the cantilever strain energy.

The kinetic energy of the model is given by (7),

$$T(t) = \tfrac{1}{2}\int_0^L m\dot{y}^2(x,t)\,\mathrm{d}x + \tfrac{1}{2}\int_0^L \gamma\dot{\theta}^2(x,t)\,\mathrm{d}x + \tfrac{1}{2}\sum_{j=1,3,5}^{n} M_j(\dot{y}_j + \dot{y}(c_j) + l_j\dot{\theta}(c_j))^2 + \tfrac{1}{2}\sum_{j=2,4,6}^{n} M_j(\dot{y}_j + \dot{y}(c_j) - l_j\dot{\theta}(c_j))^2 \quad (7)$$

where n is the total number of cantilevers, m is the mass per unit length, γ is the mass moment of inertia, in twist, per unit length and c_j is the cantilever location along the main beam. Thus on the right-hand side of equation (7), the first term corresponds to the kinetic energy of bending, the second term is the kinetic energy due to beam torsion, the third term corresponds to the kinetic energy of odd numbered cantilevers and the fourth term corresponds to the kinetic energy of even numbered cantilevers, odd and even numbered cantilevers being mounted on opposite sides of the beam.

Substituting the equations representing the terms $y''(x,t)$ and $\theta'(x,t)$,

$$y''(x,t) = q_0\phi_0''(x) + q_1\phi_1''(x) + q_2\phi_2''(x) \quad (8)$$

$$\theta'(x,t) = b_1\psi_1'(x) + b_2\psi_2'(x) \quad (9)$$

into (6), the system strain energy equation becomes:

$$U = \tfrac{1}{2}\int_0^L EI(q_0\phi_0''(x) + q_1\phi_1''(x) + q_2\phi_2''(x))^2\,\mathrm{d}x + \tfrac{1}{2}\int_0^L GJ(b_1\psi_1'(x) + b_2\psi_2'(x))^2\,\mathrm{d}x + \tfrac{1}{2}\sum_{j=1}^{2} k_j y_j^2. \quad (10)$$

Similarly for the kinetic energy equation, substituting the terms representing $\dot{y}(x,t)$ and $\dot{\theta}(x,t)$,

$$\dot{y}(x,t) = \dot{q}_0(t)\phi_0 + \dot{q}_1(t)\phi_1 + \dot{q}_2(t)\phi_2 \tag{11}$$

$$\dot{\theta}(x,t) = \dot{b}_1(t)\psi_1 + \dot{b}_2(t)\psi_2 \tag{12}$$

into (7), yields the kinetic energy equation as

$$\begin{aligned} T = {} & \tfrac{1}{2}\int_0^L m(\dot{q}_0(t)\phi_0 + \dot{q}_1(t)\phi_1 + \dot{q}_2(t)\phi_2)^2\,\mathrm{d}x \\ & + \tfrac{1}{2}\int_0^L \gamma(\dot{b}_1(t)\psi_1' + \dot{b}_2(t)\psi_2)^2\,\mathrm{d}x \\ & + \tfrac{1}{2}M_1(\dot{y}_1 + \dot{q}_0(t)\phi_0(c_1) + \dot{q}_1(t)\phi_1(c_1) \\ & + \dot{q}_2(t)\phi_2(c_1) + l_1\dot{b}_1(t)\psi_1(c_1) + l_1\dot{b}_2(t)\psi_2(c_1))^2 \\ & + \tfrac{1}{2}M_2(\dot{y}_2 + \dot{q}_0(t)\phi_0(c_2) + \dot{q}_1(t)\phi_1(c_2) + \dot{q}_2(t)\phi_2(c_2) \\ & - l_2\dot{b}_1(t)\psi_1(c_1) - l_2\dot{b}_2(t)\psi_2(c_2))^2. \end{aligned} \tag{13}$$

To provide the equation of motion using strain energy U and kinetic energy T, the Lagrange equation given by [20]

$$\begin{aligned} & \frac{\mathrm{d}}{\mathrm{d}t}\left(\frac{\partial T}{\partial \dot{q}_j}\right) - \frac{\partial T}{\partial q_j} + \frac{\partial \xi}{\partial \dot{q}_j} + \frac{\partial U}{\partial q_j} = Q_j \\ & = \frac{\partial(\delta W)}{\partial(\delta q_j)} \qquad \text{for } j = 1, 2, \ldots, N \end{aligned} \tag{14}$$

is used in terms of the generalized coordinate q_j, where ξ is the dissipative function or damper contribution, Q_j is the generalized force, δW is the incremental work done, and δq_j is the virtual displacement.

Assume the system is under free vibration, therefore the incremental work done term δW in (14) is zero, and derivations for the other terms in the equation are required. After determining each term in (14) by substituting from (10) and (13), the Lagrange equation gives the equations of motion in matrix form as:

$$\tilde{M} \times \begin{bmatrix} \ddot{q}_0 \\ \ddot{q}_1 \\ \ddot{q}_2 \\ \ddot{b}_1 \\ \ddot{b}_2 \\ \ddot{y}_1 \\ \ddot{y}_2 \end{bmatrix} + \tilde{C} \times \begin{bmatrix} \dot{q}_0 \\ \dot{q}_1 \\ \dot{q}_2 \\ \dot{b}_1 \\ \dot{b}_2 \\ \dot{y}_1 \\ \dot{y}_2 \end{bmatrix} + \tilde{K} \times \begin{bmatrix} q_0 \\ q_1 \\ q_2 \\ b_1 \\ b_2 \\ y_1 \\ y_2 \end{bmatrix} = 0 \tag{15}$$

where $\tilde{M}$, $\tilde{K}$ and $\tilde{C}$ are the 7×7 matrices of effective beam mass, stiffness and damping. Assuming constant damping, each row and column of matrices $\tilde{M}$, $\tilde{K}$ can be filled, where q_0, q_1, q_2, b_1, b_2 are the variables in the strain energy and kinetic energy equations (8) and (11).

Therefore, the multiple cantilever system transmissibility can be predicted using the mass and stiffness matrices derived. The analysis can also be applied to the clamped–clamped beam structure shown in figure 9 where there are more than two added cantilevers, however as a consequence there is an expanded mass matrix $\tilde{M}$ and stiffness matrix $\tilde{K}$.

Equation (15) can be rewritten as (16)

$$\begin{bmatrix} \tilde{M}_{00} & \tilde{M}_{01} \\ \tilde{M}_{10} & \tilde{M}_{11} \end{bmatrix} \times \begin{bmatrix} \ddot{q}_0 \\ \ddot{q}_1 \\ \ddot{q}_2 \\ \ddot{b}_1 \\ \ddot{b}_2 \\ \ddot{y}_1 \\ \ddot{y}_2 \end{bmatrix} + \begin{bmatrix} 0 & 0 \\ 0 & \tilde{K}_{11} \end{bmatrix} \times \begin{bmatrix} q_0 \\ q_1 \\ q_2 \\ b_1 \\ b_2 \\ y_1 \\ y_2 \end{bmatrix} = 0. \tag{16}$$

Matrices $\tilde{M}_{00}$, $\tilde{M}_{01}$ and $\tilde{M}_{10}$ are related to the excitation $\ddot{q}_0$, that is the first row and first column of matrix $\tilde{M}$. Thus $\tilde{M}_{00}$ is a 1×1 matrix, $\tilde{M}_{01}$ is a 6×1 matrix, $\tilde{M}_{10}$ is a 1×6 matrix and $\tilde{M}_{11}$ is a 6×6 matrix. There are no corresponding terms in the stiffness matrix $\tilde{K}$ relating to the excitation $\ddot{q}_0$, therefore, the first row and column of $\tilde{K}$ are zero vectors.

Equation (16) is rewritten as

$$M_{00}\ddot{\underline{q}}_0 + M_{01}\ddot{\underline{q}}_{00} = F \tag{17}$$

$$M_{10}\ddot{\underline{q}}_0 + M_{11}\ddot{\underline{q}}_{00} + K_{11}\underline{q}_{00} = 0 \tag{18}$$

where F is the input force on the structure. Since $\ddot{\underline{q}}_0$ is the excitation, therefore equation (17) is a force equation which generates $\ddot{\underline{q}}_0$, and equation (18) finds $\underline{q}_{00}$ representing the response due to excitation $\ddot{\underline{q}}_0$, that is $\underline{q}_{00}$ is equivalent to the response vector $[\,q_1 \quad q_2 \quad b_1 \quad b_2 \quad y_1 \quad y_2\,]^{\mathrm{T}}$ shown in (17). Assuming harmonic excitation for $\ddot{\underline{q}}_0$ and $\underline{q}_{00}$, that is

$$\ddot{\underline{q}}_0 = \ddot{A}_0 \mathrm{e}^{\mathrm{i}\omega t} \tag{19}$$

$$\underline{q}_{00} = \underline{A}_{00}\mathrm{e}^{\mathrm{i}\omega t}. \tag{20}$$

Substituting (19) and (20) into (17) and (18), yields

$$\underline{A}_{00} = -[K_{11} - \omega^2 M_{11}]^{-1} M_{10}\ddot{A}_0. \tag{21}$$

Thus:

$$\ddot{\underline{A}}_{00} = \omega^2[K_{11} - \omega^2 M_{11}]^{-1} M_{10}\ddot{A}_0. \tag{22}$$

Assuming the overall system output is represented by $\ddot{w}$ and letting $\ddot{w}(d_j) = \ddot{W}_j \mathrm{e}^{\mathrm{i}\omega t}$, the expression for $\ddot{w}(d_j)$ is:

$$\begin{aligned} \ddot{w}(d_j) = {} & \ddot{q}_0\phi_0(d_j) + \ddot{q}_1\phi_1(d_j) + \ddot{q}_2\phi_2(d_j) \\ & + b_1\psi_1(d_j) + b_2\psi_2(d_j)\cdots \qquad \text{for } j = 1, 2, \ldots \end{aligned} \tag{23}$$

where d_j is the measurement location on the beam. On the right-hand side of (23) the first term corresponds to the input excitation, and the second and third terms correspond to the bending responses due to the first and second mode shapes. The fourth and fifth terms correspond to torsion responses due to the first and second mode shapes.

Assuming the two mode shapes $\tilde{\phi}$ along the beam, using equation (23), yields

$$\ddot{\underline{W}} = \begin{bmatrix} \phi_0(d_1) \\ \phi_0(d_2) \end{bmatrix} \cdot \ddot{A}_0 + \tilde{\phi} \cdot \ddot{\underline{A}}_{00}. \tag{24}$$

Thus,

$$\begin{Bmatrix} \ddot{W}_1 \\ \ddot{W}_2 \end{Bmatrix} = \begin{bmatrix} \phi_0(d_1) \\ \phi_0(d_2) \end{bmatrix} \ddot{A}_0 + \begin{bmatrix} \phi_1(d_1) & \phi_2(d_2) & 0 & 0 & 0 & 0 \\ \phi_1(d_1) & \phi_2(d_2) & 0 & 0 & 0 & 0 \end{bmatrix} \times \begin{bmatrix} \ddot{A}_1 \\ \ddot{A}_2 \\ \ddot{B}_1 \\ \ddot{B}_2 \\ \ddot{Y}_1 \\ \ddot{Y}_2 \end{bmatrix} \tag{25}$$

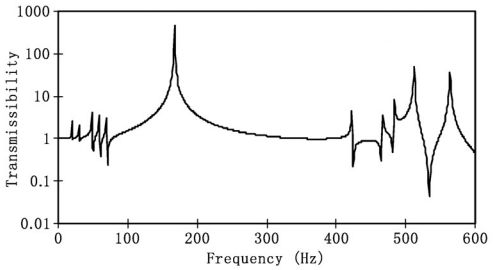

Figure 10. Transmissibility calculated at the center of the multiple cantilever beam.

Table 1. Geometric and material properties of multiple cantilever beam.

	L (mm)	W (mm)	T (mm)	ρ (kg m^{-3})	E (GPa)
Main beam	170	20	1.0	7850	205
Cantilever 1	80	10	1.0	7850	205
Cantilever 2	80	10	1.0	7850	205
Cantilever 3	80	10	1.0	7850	205
Cantilever 4	80	10	1.0	7850	205
Cantilever 5	80	10	1.0	7850	205

where $\begin{bmatrix}\phi_0(d_1)\\ \phi_0(d_2)\end{bmatrix}$ is the excitation force matrix at the main beam clamped ends. By substituting equation (22) for $\underline{\ddot{A}}_{00}$, equation (24) for the output response $\underline{\ddot{W}}$ becomes:

$$\underline{\ddot{W}} = \left\{ \begin{bmatrix}\phi_0(d_1)\\ \phi_0(d_2)\end{bmatrix} + \omega^2 \tilde{\phi} \left[K_{11} - \omega^2 M_{11}\right]^{-1} M_{10} \right\} \ddot{A}_0. \quad (26)$$

Therefore, the transmissibility of the multiple cantilever system is as shown in (27):

$$\underline{T} = \frac{\ddot{W}}{\ddot{A}_0} = \frac{\text{Output}}{\text{Input}} = \begin{bmatrix}\phi_0(d_1)\\ \phi_0(d_2)\end{bmatrix} + \omega^2 \tilde{\phi} \left[K_{11} - \omega^2 M_{11}\right]^{-1} \cdot M_{10}. \quad (27)$$

The analysis can also be applied to the clamped–clamped beam structure shown in figure 6 where there are more than two added cantilevers, however as a consequence there is an expanded mass matrix $\tilde{M}$ and stiffness matrix $\tilde{K}$.

The electromechanical behavior of the piezoelectric device has not been included in the model. The piezoelectric device will add damping and stiffness to the structure [18, 21].

5. Simulation results and discussion

The simulation only considers the first degree of freedom of the cantilever beam, where it is most effective. The transmissibility equation was programmed in Matlab, to predict beam vibration behavior, and a prototype harvester system was investigated, the parameters of which are shown in table 1.

The cantilevers are of the same material, stainless steel, and are mounted at 25 mm, 55 mm, 85 mm, 115 mm and 145 mm respectively along the beam. The predicted transmissibility curve for the beam without tip masses is shown in figure 10.

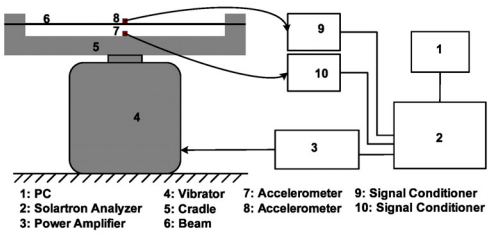

Figure 11. Laboratory measurement setup.

Figure 10 shows resonance peaks occurring over a frequency range of approximately 50–80 Hz and 400–600 Hz respectively, due to the first and second modes of the five cantilevers. The peak at 170 Hz is due to the clamped–clamped beam first bending mode. The model assumes 1% damping ratio in the bending and torsion fields. The transmissibility was simulated at several different locations on the beam. The highest predicted waveform is at the center position of the beam, where the highest deflections occur. However anti-resonances occur in the system due to pole-zero cancelation. These anti-resonances decrease the transmissibility of the system, and reduce the PFCB output.

6. Laboratory test verification and discussion

In order to further verify the proposed design, the cantilever and multiresonant energy harvester were tested in the laboratory. Figure 11 shows the laboratory measurement setup. The transmissibility at the center of the beam was measured using an experimental setup comprising an electromagnetic exciter, a power amplifier, two accelerometers, two signal conditioners and a Solartron Instruments SI1260 Impedance/Gain-phase analyzer.

The cantilever beam was first mounted onto a base or cradle, which was then attached onto a vibration shaker fed by a power amplifier. Two accelerometers were used, with one to measure the response and the other attached on the base as a reference input. The outputs of the accelerometers were connected to a signal conditioner. Both power amplifier and signal conditioner were connected to a Solartron Instruments SI1260 Impedance/Gain-phase analyzer, which was controlled from a PC.

6.1. Single cantilever array test

Initial work involved determining the resonant frequencies of single cantilevers with different tip masses. The approximate values of the required tip masses and their mounting locations were calculated using the standard mass–spring–damper system equation (28) [22]

$$f_i = \frac{1}{2\pi}\left(\frac{\lambda_i}{L}\right)^2 \sqrt{\frac{EI}{\rho A}} \quad (28)$$

where λ_i is the coefficient of mass loading, E is Young's modulus, I is the moment of inertia, ρ is the density of the

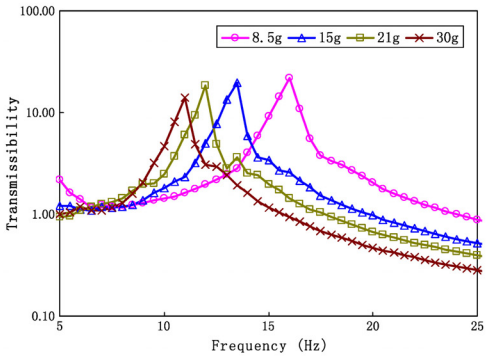

Figure 12. Measured cantilever transmissibility curve with different tip masses at the first resonant peaks.

Table 2. Piezoelectric fiber composite bimorph (PFCB) single cantilever dimensions.

L_{PFCB} (mm)	W_{PFCB} (mm)	T_{SS} (mm)	T_{PFC} (mm)	T_{PFCB} (mm)	ρ_{SS} (kg m^{-3})	E_{SS} (GPa)	M_{PFCB} (g)
80	10	0.4	0.3	1.0	7850	205	7.5

material, A is the cross-sectional area, and L is the length. The parameters of the PFCB are shown in table 2, where T_{SS} is the thickness of the stainless steel shim, and T_{PFC} is the thickness of each PFC layer mounted on the top and the bottom of the PFCB.

A set of tip masses weighing 8.5, 15, 21 and 30 g were used. According to [22], for the first mode of a beam vibration, with a 8.5 g mass loading, λ_i is 1.202 065 78. For a 15 g tip mass, λ_i is 1.076 195 66. For 21 g and 30 g tip masses, λ_i is 0.997 002 23 and 0.917 358 14 respectively.

The curves in figure 12 shows the measured transmissibility curves of four single cantilever systems tuned with different tip masses. The system transmissibility curves overlap to give a broadband response between 10 and 20 Hz where the first resonances occur. In practice the proposed broadened bandwidth concept can be applied to either the first or second (or higher) resonance region. Note that, due to low frequency instrumental noise, the results obtained below 5 Hz are ignored.

As shown in figure 12, the four resonant frequency peaks are approximately between 10 and 20 Hz. This range can be shifted higher or lower with different tip mass selections. Thus the concept outlined in figure 12 should be applicable to a harvester formed from a multiplicity of single cantilevers. Figure 13 shows the multiple cantilever system built and tested in the laboratory.

6.2. Multiple cantilever structure test

A clamped–clamped beam was tested in the laboratory. The measured results are shown in figures 14 and 15. The multiple resonance peaks seen in figure 14 are due to the resonant characteristics of the five cantilevers without tip masses, the dimensions of which are shown in table 1.

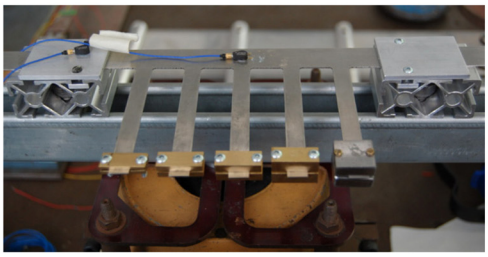

Figure 13. Experimental model of multiple cantilever structure.

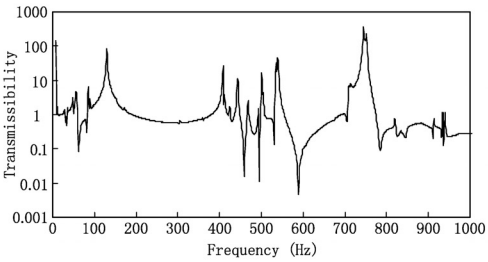

Figure 14. Measured transmissibility of multiple cantilevered beams without tip masses.

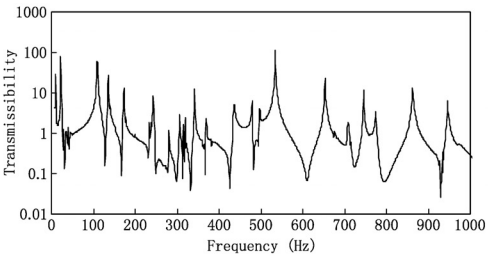

Figure 15. Measured transmissibility of multiple cantilevered beams with tip masses.

Unlike the case shown in figure 15, using tip masses of 8.5 g, 15 g, 21 g, 30 g and 40 g respectively for each cantilever, figure 14 shows that when there are no tip masses, there are no resonances between 150 and 400 Hz. The second mode resonance peaks are at higher frequencies because of the reduced mass loading of the cantilevers, and appear between about 400 and 600 Hz, as can be seen when figures 14 and 15 are compared. The relatively high resonant frequency behavior of the structure is mainly due to the length and thickness of the tested beam, and is in general agreement with the previous predicted transmissibility response shown in figure 10.

The resonance frequency bands can be altered by changing the dimensions of the beam as well as the tip masses. The results show that the beam structure, with multiple cantilevers attached, will cause a multiple resonant frequency effect. Hence, with appropriate tuning of the tip masses according to the beam dimensions, amplification can be made to occur at various frequencies.

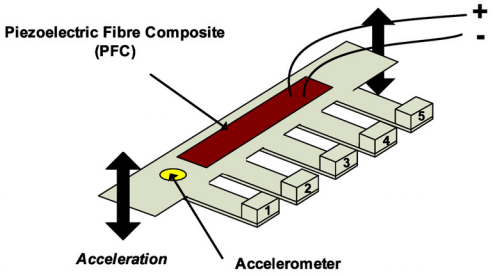

Figure 16. Experimental model of multiple cantilever structure.

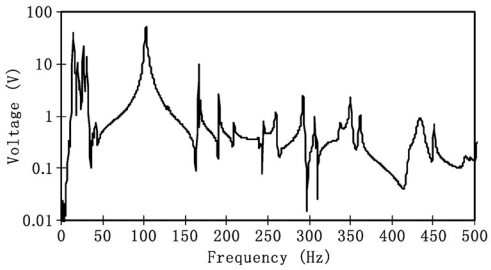

Figure 17. Multiple cantilever PFC voltage output.

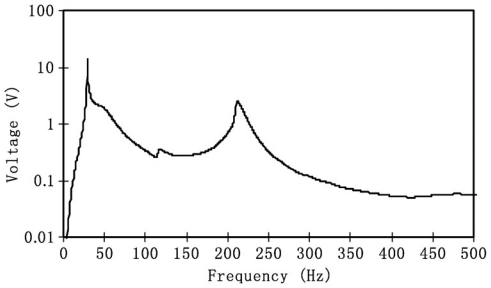

Figure 18. Single cantilever PFC voltage output.

The behavior of two PFCs electrically in parallel was tested on a multiple cantilever beam, as shown in figure 16.

The PFCs are now bent and twisted by the five cantilevers, each of which resonates at a different frequency.

Figure 17 shows the measured voltage output from two PFCs connected in parallel, mounted on the clamped–clamped beam. A multitude of resonance peaks now occur from 15 to 34 Hz. The dips between the peaks are caused by anti-resonances. To further investigate this, a single cantilever model having the same dimensions as a small cantilever on the main beam was tested. The dimensions are shown in table 2 and the measured PFC response is shown in figure 18.

Figure 18 shows the voltage output from the two electrically parallel PFCs mounted on a single cantilever structure, top and bottom respectively.

A detailed comparison between the single and multiple cantilever structure is shown in figure 19. By using the standard

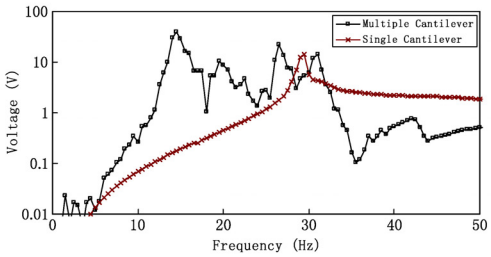

Figure 19. Voltage output comparison between single and multiple cantilevers.

Table 3. Calculated single cantilever resonant frequencies.

	Tip mass (g)	Resonant frequency (Hz)
Cantilever 1	40	19.2281
Cantilever 2	30	21.7281
Cantilever 3	21	25.7285
Cantilever 4	15	29.9782
Cantilever 5	8.5	37.4007

Table 4. Measured multiple cantilever resonant frequencies.

	Resonant frequency (Hz)
Mode 1	14.5
Mode 2	19.5
Mode 3	22.5
Mode 4	26.5
Mode 5	31.0

mass–spring–damper system equations (28) in section 6.1 [22], the resonant frequencies of each side cantilever with different tip masses were calculated. These are shown in table 3.

As shown in tables 3 and 4, the resonant frequencies contributed by each cantilever can be identified in figure 19. There is disagreement between the predicted and measured frequency magnitudes. This is probably because the predicted frequencies are based on the assumption that the clamped end is fixed to a rigid body.

According to table 4, the first mode resonance in figure 19 is due to cantilever 1, while the second, third, fourth and fifth mode resonances are due to the cantilevers 2, 3, 4 and 5 respectively.

The open circuit voltage and short circuit current are around 18 V pk–pk and 0.01 mA pk–pk respectively when the support is subject to an excitation level of 10.47 m s^{-2} pk–pk. This is in good agreement with results achieved by other researchers on similar PFCs [23]. Note that in figures 17–19 the device was driven at an excitation level that is generally higher than would be met in practice in order to produce maximum device output.

The measured results show that the multiple cantilever structure has multiple resonant peaks, as opposed to the single cantilever model, which has only a single resonance around 28 Hz. Hence the multiple cantilever model is more suitable for harvesting variable frequency vibrations.

7. Conclusions

A novel multiple cantilever structure has been proposed in this paper. Mass loading effects on the clamped–clamped beam vibration response have been investigated theoretically using a Rayleigh–Ritz method. From the simulation results, it was found that the cantilever mounting location affects the system response. For different mode shapes, the beam system has different deflections. Therefore, the beam dimensions and cantilever locations have to be chosen appropriately. Predictions show that the new energy harvesting design is feasible for harvesting energy from ambient environmental vibrations as it works over a wide frequency spectrum. It has been shown that there is a fairly close agreement between the predicted and measured transmissibility curves of the proposed design for the case of no tip mass.

The transmissibility of the multiresonant system was calculated for heave motion only. In practice the PFC will respond to torsion as well as heave motion of the clamped–clamped beam. Thus a proper prediction of the PFC output voltage will require torsion to be accounted for.

Further work will concentrate on increasing the number of cantilevers to broaden the spectral response, and determining the design rules for adapting the technology to other frequency ranges whilst providing a broad response. This will be achieved by:

(1) Implementing two (or more) multiple cantilever systems to fill in response dips due to anti-resonances and achieve a flatter vibration response.
(2) Further investigations into methods of adding the responses from several beams to optimize the output.
(3) Finding a suitable high efficiency rectification circuit.
(4) Optimizing the efficiency of the power electronic circuits attached to the output(s) of the beams.
(5) Modeling the effect of clamped–clamped beam torsion on the PFC.

The proposed new design of a piezoelectric cantilever harvester should be suitable for use by remote instruments, such as wireless sensor nodes, in environments where replacement of batteries is difficult, but where there is a plentiful supply of vibration energy.

For this initial investigation, the Rayleigh–Ritz procedure was adopted because it is more flexible, easier to change the configurations of the side cantilevers, and also enables a very quick analysis of the system response. A finite element procedure, on the other hand, will require a much longer time to change the configurations for optimization and to perform the steady state analysis required.

However this initial study did not include the electrical characteristics in the Rayleigh–Ritz modeling, because the desire was to keep the modeling simple in order to enable understanding of the physical processes behind the functioning of the multiresonant harvester design.

Also, it should be noted that in the current design, the active material is restricted to the central clamped–clamped beam. Thus, the ratio of the mass of the active material to the passive material is rather low. Consequently, the power density will be relatively low in comparison to a resonator comprising several individual piezo cantilevers in which the entire length of each beam is covered by active material.

However, the multiresonant beam has the advantage that the different modal strains, developed by the side beams at their individual resonances, are automatically summed up as a total strain in the main clamped–clamped beam, thus making the output electrical power generated truly broadband.

In the case of a resonator comprising several individual piezo cantilevers, on the other hand, the electrical power generated by each beam will have to be summed up using an electric circuit, if phase cancelation of the individual sinusoidal voltages produced by each resonant piezo is to be avoided. It should be noted that such phase cancelation is due to the voltage produced by each piezo being out of phase. Hence, simply connecting the piezos in series or parallel will not produce maximum output power. In fact, in some instances, no power output may occur. In addition, electric circuits that may be used to overcome phase cancelation are rather complicated and lossy.

Furthermore, the multiresonant beam is relatively cheaper than a resonator comprising several individual piezo cantilevers, as the former uses only a fraction of the active material required by the latter. In the multiresonant beam concept presented in this paper, 4–5 dominant modes were produced (see figure 19), to give a broadband effect over the range of their natural frequencies. To obtain a similar effect using a resonator comprising several individual piezo cantilevers will require about 4–5 times as much active material. The cost of the active material being more than 100 times greater than that of the passive material makes a device comprising individual piezo cantilevers much more expensive than the multiresonant beam concept presented here.

Acknowledgments

The authors would like to thank the School of Electrical and Electronic Engineering for the partial scholarship to S Qi, and for funding received for part of this work from the EU FP6 DYNAMITE research project.

References

[1] Shen D, Choe S and Kim D 2007 Analysis of piezoelectric materials for energy harvesting devices under high-*g* vibrations *Japan. J. Appl. Phys.* **46** 6755–60
[2] Anton S R and Sodano H A 2007 A review of power harvesting using piezoelectric materials (2003–2006) *Smart Mater. Struct.* **16** R1–21
[3] Beeby S P, Tudor M J and White N M 2006 Energy harvesting vibration sources for microsystems applications *Meas. Sci. Technol.* **17** R175–95
[4] Sodano H A, Inman D J and Park G 2004 A review of power harvesting from vibration using piezoelectric materials *Shock Vib. Dig.* **36** 197–205
[5] Roundy S J 2003 Energy scavenging for wireless sensor nodes with a focus on vibration to electricity conversion *PhD Thesis* The University of California, Berkeley
[6] Roundy S, Leland E S, Baker J, Carleton E, Reilly E, Lai E, Otis B, Rabaey J M, Wright P K and Sundararajan V 2005

Improving power output for vibration-based energy scavengers *IEEE Pervasive Comput.* **4** 28

[7] Shahruz S M 2006 Design of mechanical band-pass filters with large frequency bands for energy scavenging *Mechatronics* **16** 523–31

[8] Shahruz S M 2008 Design of mechanical band-pass filters for energy scavenging: multi-degree-of-freedom models *J. Vib. Control* **14** 753–68

[9] Sari I, Balkan T and Kulah H 2007 An electromagnetic micro power generator for wideband environmental vibrations *Sensors Actuators* A **145/146** 405–13

[10] Leland E S and Wright P K 2006 Resonance tuning of piezoelectric vibration energy scavenging generators using compressive axial preload *Smart Mater. Struct.* **15** 1413–20

[11] Rao S S 2004 *Mechanical Vibrations* 4th edn (Englewood Cliffs, NJ: Prentice-Hall) ISBN: 9780130489876

[12] Soliman M S M, Abdel-Rahman E M, El-Saadany E F and Mansour R R 2008 A wideband vibration-based energy harvester *J. Micromech. Microeng.* **18** 115021

[13] Morris D J, Youngsman J M, Anderson M J and Bahr D F 2008 A resonant frequency tunable, extensional mode piezoelectric vibration harvesting mechanism *Smart Mater. Struct.* **17** 065021

[14] Zhu D, Roberts S, Tudor M J and Beeby S P 2008 Closed loop frequency tuning of a vibration-based micro-generator *Proc. PowerMEMS and microEMS (Sendai)*

[15] Wu W, Chen Y, Chen Y, Wang C and Chen Y 2006 Smart wireless sensor network powered by random ambient vibrations *IEEE Int. Conf. on System, Man and Cybernetics* vol 4, pp 2701–8

[16] Bent A 1997 Piezoelectric fiber composites with interdigitated electrodes *J. Intell. Mater. Syst. Struct.* **8** 903

[17] Sherrity S, Wiedericky H D, Mukherjeey B K and Sayerz M 1997 An accurate equivalent circuit for the unloaded piezoelectric vibrator in the thickness mode *J. Phys. D: Appl. Phys.* **30** 2354–63

[18] Hagood N W and von Flotow A 1991 Damping of structural vibrations with piezoelectric materials and passive electrical networks *J. Sound Vib.* **146** 243–68

[19] Lefeuvre E, Badel A, Richard C and Guyomar D 2007 Energy harvesting using piezoelectric materials: case of random vibrations *J. Electroceram.* **19** 349–55

[20] Blevins R D 1979 *Formulas for Natural Frequency and Mode Shape* (New York: Litton Educational) ISBN: 0-442-20710-7

[21] Aldraihem O J, Singh T and Wetherhold R C 1997 Realistic determination of the optimal size and location of piezoelectric actuators/sensors *Proc. 1997 IEEE Int. Conf. on Control Applications* pp 435–40

[22] Laura P A A, Pombo J L and Susemihl E A 1974 A note on the vibrations of a clamped-free beam with a mass at the free end *J. Sound Vib.* **37** 161–8

[23] Swallow L M, Luo J K, Siores E, Patel I and Dodds D 2008 A piezoelectric fibre composite based energy harvesting device for potential wearable applications *Smart Mater. Struct.* **17** 7

Appendix F:

Reprint -

Multiple Resonances Piezoelectric Energy Harvesting Generator

Author:

S. Qi, R. Shuttleworth, S. O. Oyadiji

Publisher:

Proceedings of the ASME Conference on Smart Materials, Adaptive Structures and Intelligent Systems, *Oxnard*, *California*, *USA*, September 21-23, 2009.

Proceedings of the ASME 2009 Conference on Smart Materials, Adaptive Structures and Intelligent Systems
SMASIS2009
September 20-24, 2009, Oxnard, California, USA

SMASIS2009-1455

MULTIPLE RESONANCES PIEZOELECTRIC ENERGY HARVESTING GENERATOR

Shaofan Qi[1] Roger Shuttleworth[2] S. Olutunde Oyadiji[3]

[1,2]School of Electrical and Electronic Engineering, University of Manchester, UK
[3]School of Mechanical, Aerospace and Civil Engineering, University of Manchester, UK

ABSTRACT

Energy harvesting is the process of converting low level ambient energy into usable electrical energy, so that remote electronic instruments can be powered without the need for batteries or other supplies. Piezoelectric material has the ability to convert mechanical energy into electrical energy, and cantilever type harvesters using this material are being intensely investigated. The typical single cantilever energy harvester design has a limited bandwidth, and is restricted in ability for converting environmental vibration occurring over a wide range of frequencies. A multiple cantilever piezoelectric generator that works over a range of frequencies, yet has only one Piezo element, is being investigated. The design and testing of this novel harvester is described.

INTRODUCTION

Frequently situations arise where it is desirable to condition-monitor industrial plant distributed over wide areas (e.g. factory floors) using low-power sensors and associated processing equipment, and to relay the information acquired to a central monitoring facility. The cost of wiring is often prohibitive in these cases. Thus there has grown an interest in using RF transfer of information gathered and using energy harvesting techniques to power the distributed sensors and processing devices. Piezoelectric material has been widely investigated for such energy harvesting purposes and various researchers have constructed harvester devices [1-8]. Research into piezoelectric harvesters has grown and the techniques used to obtain energy from ambient vibrations have received attention. Roundy has investigated a single cantilever energy harvester [5], and Sodano et al also reviewed several harvesting devices [2-4].

Previous researchers have shown piezoelectric devices to have a narrow frequency bandwidth, and a low efficiency when operated off resonance, which has limited the use of such devices. In an attempt to overcome the problem, Shahruz investigated methods of harvesting energy from a range of frequencies, by interconnecting several cantilever models [7-8]. This paper discusses a structure that uses several cantilevers mounted together, to form a device working over a wider frequency range than that of a single cantilever, enabling more energy to be harvested.

NOMENCLATURE

l	Cantilever beam length
w	Cantilever beam width
h	Cantilever beam thickness
ρ	Material density
E	Modulus of elasticity (young's modulus)
M	Proof mass
m	Mass per unit length
n	Number of cantilevers mounted
$\ddot{u}(t)$	Acceleration
$\phi(x)$	Mode shape function
$q(t)$	Generalized coordinate
α	Ratio of proof mass to the beam mass
I	Second moment of beam cross section area
$T(t)$	Kinetic energy
c_e	Electrical damping coefficients
c_m	Mechanical damping coefficients
$\tilde{C}$	Damping matrix
$\tilde{M}$	Mass matrix
$\tilde{K}$	Stiffness matrix
R	Resistance
C	Capacitance
L	Inductance

c_1, c_2	Mounted positions of cantilevers
M_1, M_2	Proof masses of cantilever
l_1, l_2	Lengths of cantilevers
L	Length of clamped-clamped beam
$y(x,t)$	Beam bending shape function
$\theta(x,t)$	Beam torsion shape function
U	Strain energy
k_j	Stiffness
EI	Flexural rigidity
G	Material shear modulus
J	Section torsion constant
GJ	Torsional rigidity
Q_j	Generalized coordinate
W	Incremental work done
$\ddot{w}$	Overall system output for transmissibility calculation
$\underline{T}$	Transmissibility
f_n	Natural frequency
χ	Shape function for kinetic energy equation
ψ	Shape function for strain energy equation
γ	Moment of inertia in twist, per unit length
d_j	Measurement location on the beam
C_L	Output capacitance
N	Mechanical to electrical coupling factor

PIEZOELECTRIC DEVICE MODEL

In order to convert ambient vibration energy into electricity, piezoelectric films are now commonly incorporated into energy harvesting devices. Piezoelectric fiber composite (PFC) is one of the most commonly used piezoelectric films [9]. PFC uses an interdigitated electrode pattern to increase the effective ceramic volume, allowing the piezoelectric primary axis to align with the fibre direction, permitting higher strain levels.

The piezoelectric device used, is a piezoelectric fibre composite bimorph, PFCB, manufactured by ACI Ceramics, which when operated at its resonant frequency, can generate voltages of over $400\,V_{pk-pk}$. Flexible piezoelectric materials such as PFCB are attractive for power harvesting applications, because of their ability to withstand high strain, and thus convert more vibration energy to electricity.

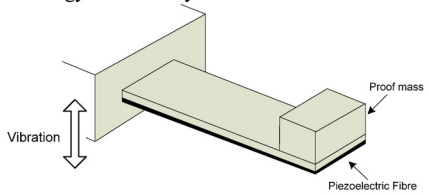

Figure 1: Single piezoelectric cantilever generator model

Figure 1 shows the piezoelectric cantilever generator model developed by Roundy [5]. It comprises a cantilever beam on which are mounted a piezoelectric fiber and proof mass. By applying vibration to the cantilever's support, mechanical vibration energy is converted into electricity by the piezoelectric material. When the ambient vibration frequency matches the resonant frequency of the cantilever, energy conversion is at its most efficient, otherwise the efficiency is low. The device has a high Q, around 100 [10], and is not suited to variable frequency vibrations due to its narrow operating bandwidth. Several other researchers have described similar devices [1,6], and the system is generally analyzed as a mass-spring-damper system as shown in Figure 2.

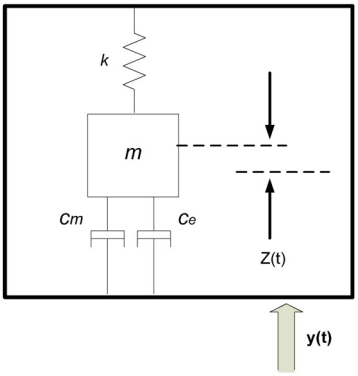

Figure 2: Mechanical model of typical cantilever energy harvester

From [5], the equation representing dynamic motion of the piezoelectric device is:

$$m\ddot{z} + (c_e + c_m)\dot{z} + kz = -m\ddot{y} \tag{1}$$

Where z is the spring deflection, y is the input displacement, m is the mass, c_e and c_m are the electrical and mechanical damping coefficients and k is the spring constant.

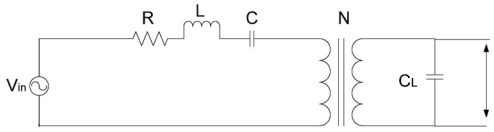

Figure 3: Electrical equivalent circuit of piezoelectric generator

Using standard mechanical to electrical equivalences [11], the piezoelectric cantilever beam system can be converted into the electrical equivalent circuit shown in Figure 3, where the resistance *R* is equivalent to the damping coefficients c_e and

c_m, inductance L is equivalent to mass m, capacitance C is equivalent to $1/k$, C_L is output capacitance and N is the mechanical to electrical coupling factor.

This equivalent circuit provides easier evaluation of the system. The generator is thus simply treated as an AC voltage source with an electrical circuit in series. However the circuit is only correct for one vibration mode, in practice there is more than one mode as shown in Figure 4.

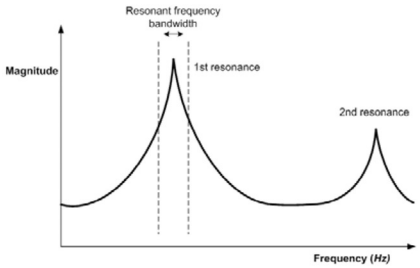

Figure 4: Estimated piezoelectric cantilever generator output

Figure 4 shows the form of system output, the system working most effectively at its resonant frequency of perhaps around one hundred *Hz* depending on stiffness k and proof mass m, around which frequency the electrical model is accurate.

In [1,6,12], resonant frequencies of piezoelectric generators were designed to match an environmental vibration frequency, to achieve maximum output power. Although it is possible to design an energy harvester in which the resonant frequency matches the frequency of the vibration source, for variable speed industrial plant, vibrations occur over a range of frequencies, making the cantilever generator device with one resonant peak less effective. Consequently an interest has arisen in the design of an energy harvesting device which can operate over a wider frequency band.

PROPOSED MULTIPLE CANTILEVER HARVESTER

To achieve this wider bandwidth a multiple cantilever beam structure is proposed, as shown in Figure 5. The structure comprises a clamped-clamped beam which is accelerated equally at its clamped ends due to the ambient vibration. The beam supports several small cantilevers.

The system has many resonant frequencies due to the several different cantilevers. The strains produced by the cantilevers when excited at their resonant frequencies by the ambient vibration are summated within the clamped-clamped beam, and converted to electrical form by the PFCB. The resonant frequency of a cantilever depends primarily upon its stiffness and proof mass, therefore by adjusting one or both of these the cantilevers' resonant frequencies can be altered. The response of the PFCB to the vibration acceleration at the end supports should thus have a multitude of resonance peaks, if the parameters are chosen appropriately. Whereas a single cantilever system, as used for energy harvesting by previous researchers, has only one resonance peak, the proposed design should work over a wider bandwidth, enabling energy to be harvested over a wider spectrum.

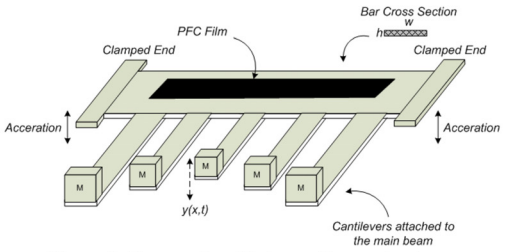

Figure 5: Proposed multiple cantilever structure

To determine if the concept is valid a Rayleigh-Ritz mechanical analysis of the proposed system was carried out. Since the cantilever beams can be mounted on either side of the main beam, the analysis started with a clamped-clamped beam having two cantilevers, one on each side as shown in Figure 6.

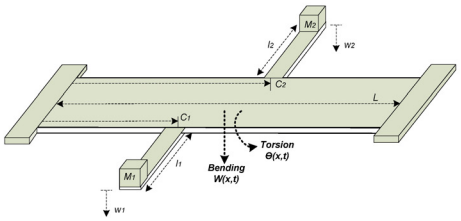

Figure 6: Clamped-clamped beam with two cantilevers

Figure 6 shows two cantilevers attached to the main beam at positions c_1 and c_2. M_1 and M_2 are the proof masses of the cantilevers, l_1 and l_2 are the lengths of the cantilevers, and L is the length of the clamped-clamped beam. We assume two mode shapes for bending $y(x,t)$ and torsion $\theta(x,t)$ as given in equations (2) and (3). Further to the analysis of the standard cantilever model from the previous section, torsional vibration of the beam is also considered. Figure 7 shows the different mode shape forms for the clamped-clamped beam for bending only, as an example.

$$y(x,t) = q_0(t)\phi_0(x) + q_1(t)\phi_1(x) + q_2(t)\phi_2(x)\cdots \quad (2)$$

$$\theta(x,t) = b_1(t)\psi_1(x) + b_2(t)\psi_2(x)\cdots \quad (3)$$

In equations (2) and (3) $\phi(x)$ and $\psi(x)$ are the known shape functions, $q(t)$ and $b(t)$ are the unknown functions

or generalized coordinates. For a clamped-clamped beam, the mode shapes are given by [13]

$$\phi_i(x) = \cosh\frac{\lambda_i x}{L} - \cos\frac{\lambda_i x}{L} - \frac{\cosh\lambda_i - \cos\lambda_i}{\sinh\lambda_i - \sin\lambda_i}\cdot(\sinh\frac{\lambda_i x}{L} - \sin\frac{\lambda_i x}{L}) \tag{4}$$

$$\psi_i(x) = \sin\frac{i\pi x}{L} \tag{5}$$

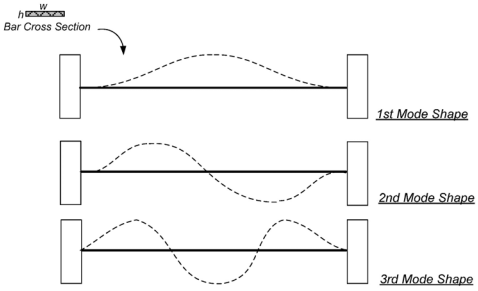

Figure 7: Clamped-clamped beam mode shapes

The strain energy *U* for the system is given by

$$U(t) = \frac{1}{2}\int_0^L EIy''^2(x,t)dx + \frac{1}{2}\int_0^L GJ\theta'^2(x,t)dx + \frac{1}{2}\sum_{j=1}^{2} k_j y_j^{\,2} \tag{6}$$

where k_j is the stiffness of a cantilever, *E* is the material's Young's modulus, I is the second moment of inertia and the product EI is the flexural rigidity. *G* is the material shear modulus, *J* is the section torsion constant and the product *GJ* is the torsional rigidity. The first term on the right hand side of (6) represents the strain energy of bending, the second term is the strain energy of torsion and the third term is the strain energy of the cantilevers.

The kinetic energy of the model is given by (7),

$$\begin{aligned} T(t) &= \frac{1}{2}\int_0^L m\dot{y}^2(x,t)dx + \frac{1}{2}\int_0^L \gamma\dot{\theta}^2(x,t)dx \\ &+ \frac{1}{2}\sum_{j=1,3,5}^{n} M_j(\dot{y}_j + \dot{y}(c_j) + l_j\dot{\theta}(c_j))^2 \\ &+ \frac{1}{2}\sum_{j=2,4,6}^{n} M_j(\dot{y}_j + \dot{y}(c_j) - l_j\dot{\theta}(c_j))^2 \end{aligned} \tag{7}$$

where *n* is the total number of cantilevers, *m* is mass per unit length, γ is the mass moment of inertia, in twist, per unit length and c_j is the cantilever location along the main beam. Thus on the right hand side of equation (7), the first term corresponds to the kinetic energy of bending, the second term is the kinetic energy due to beam torsion, the third term corresponds to the kinetic energy of odd numbered cantilevers and the fourth term corresponds to the kinetic energy of even numbered cantilevers, odd and even numbered cantilevers being mounted on opposite sides of the beam.

Substituting the equations representing the term $y''(x,t)$ and $\theta'(x,t)$, (8) and (9), into (6)

$$y''(x,t) = q_0\phi_0''(x) + q_1\phi_1''(x) + q_2\phi_2''(x) \tag{8}$$

$$\theta'(x,t) = b_1\psi_1'(x) + b_2\psi_2'(x) \tag{9}$$

the system strain energy equation becomes:-

$$\begin{aligned} U = &\frac{1}{2}\int_0^L EI(q_0\phi_0''(x) + q_1\phi_1''(x) + q_2\phi_2''(x))^2 dx \\ &+ \frac{1}{2}\int_0^L GJ(b_1\psi_1'(x) + b_2\psi_2'(x))^2 dx + \frac{1}{2}\sum_{j=1}^{2} k_j y_j^{\,2} \end{aligned} \tag{10}$$

Similarly for the kinetic energy equation, substituting equations (11) and (12), representing the term $\dot{y}(x,t)$ and $\dot{\theta}(x,t)$, into (7) gives,

$$\dot{y}(x,t) = \dot{q}_0(t)\phi_0 + \dot{q}_1(t)\phi_1 + \dot{q}_2(t)\phi_2 \tag{11}$$

$$\dot{\theta}(x,t) = \dot{b}_1(t)\psi_1 + \dot{b}_2(t)\psi_2 \tag{12}$$

yields the kinetic energy equation as,

$$\begin{aligned} T = &\frac{1}{2}\int_0^L m(\dot{q}_0(t)\phi_0 + \dot{q}_1(t)\phi_1 + \dot{q}_2(t)\phi_2)^2 dx \\ &+ \frac{1}{2}\int_0^L \gamma(\dot{b}_1(t)\psi_1' + \dot{b}_2(t)\psi_2)^2 dx \\ &+ \frac{1}{2}M_1(\dot{y}_1 + \dot{q}_0(t)\phi_0(c_1) + \dot{q}_1(t)\phi_1(c_1) \\ &+ \dot{q}_2(t)\phi_2(c_1) + l_1\dot{b}_1(t)\psi_1(c_1) + l_1\dot{b}_2(t)\psi_2(c_1))^2 \\ &+ \frac{1}{2}M_2(\dot{y}_2 + \dot{q}_0(t)\phi_0(c_2) + \dot{q}_1(t)\phi_1(c_2) + \dot{q}_2(t)\phi_2(c_2) \\ &- l_2\dot{b}_1(t)\psi_1(c_1) - l_2\dot{b}_2(t)\psi_2(c_2))^2 \end{aligned} \tag{13}$$

To provide the equation of motion using strain energy *U* and kinetic energy *T*, the Lagrange equation given by [13-14]

$$\frac{d}{dt}(\frac{\partial T}{\partial\dot{q}_j}) - \frac{\partial T}{\partial q_j} + \frac{\partial\xi}{\partial\dot{q}_j} + \frac{\partial U}{\partial q_j} = Q_j = \frac{\partial(\delta W)}{\partial(\delta q_j)} \quad \text{for} \quad j = 1,2...N \tag{14}$$

is used in terms of the generalized coordinate q_j, where ξ is the dissipative function or damper contribution, Q_j is the generalized force, δW is the incremental work done, and δq_j is virtual displacement.

Assume the system is under free vibration, therefore the incremental work done term δW in (14) is zero, and derivations for the other terms in the equation are required. After determining each term in (14) by substituting from (10) and (13), the Lagrange equation gives the equations of motion in matrix form as:-

$$\widetilde{M}\times\begin{bmatrix}\ddot{q}_0\\ \ddot{q}_1\\ \ddot{q}_2\\ \ddot{b}_1\\ \ddot{b}_2\\ \ddot{y}_1\\ \ddot{y}_2\end{bmatrix}+\widetilde{C}\times\begin{bmatrix}\dot{q}_0\\ \dot{q}_1\\ \dot{q}_2\\ \dot{b}_1\\ \dot{b}_2\\ \dot{y}_1\\ \dot{y}_2\end{bmatrix}+\widetilde{K}\times\begin{bmatrix}q_0\\ q_1\\ q_2\\ b_1\\ b_2\\ y_1\\ y_2\end{bmatrix}=0 \tag{15}$$

where $\widetilde{M}$, $\widetilde{K}$ and $\widetilde{C}$ are the *7x7* matrices of effective beam mass, stiffness and damping. Assuming constant damping, each row and column of matrices $\widetilde{M}$, $\widetilde{K}$ can be filled, where q_0, q_1, q_2, b_1, b_2 are the variables in the strain energy and kinetic energy equations (8) and (11).

After matrices $\tilde{M}$, $\tilde{K}$ and $\tilde{C}$ are obtained, the transmissibility *T* (also described as the ratio of system output to input) of the system is needed. When the transmissibility is greater than 1, then amplification occurs. Damping is assumed to be constant throughout the analysis, however it will often be found that the damping value varies with vibration frequency.

Equation (15) can be rewritten as (16)

$$\begin{bmatrix}\widetilde{M}_{00} & \widetilde{M}_{01}\\ \widetilde{M}_{10} & \widetilde{M}_{11}\end{bmatrix}\times\begin{bmatrix}\ddot{q}_0\\ \ddot{q}_1\\ \ddot{q}_2\\ \ddot{b}_1\\ \ddot{b}_2\\ \ddot{y}_1\\ \ddot{y}_2\end{bmatrix}+\begin{bmatrix}0 & 0\\ 0 & \widetilde{K}_{11}\end{bmatrix}\times\begin{bmatrix}q_0\\ q_1\\ q_2\\ b_1\\ b_2\\ y_1\\ y_2\end{bmatrix}=0 \tag{16}$$

Matrices $\widetilde{M}_{00}$, $\widetilde{M}_{01}$ and $\widetilde{M}_{10}$ are related to the excitation $\ddot{q}_0$, that is the first row and first column of matrix $\widetilde{M}$. Thus $\widetilde{M}_{00}$ is a *1x1* matrix, $\widetilde{M}_{01}$ is a *6x1* matrix, $\widetilde{M}_{10}$ is a *1x6* matrix and $\widetilde{M}_{11}$ is a *6x6* matrix. There are no corresponding terms in the stiffness matrix $\widetilde{K}$ relating to the excitation $\ddot{q}_0$, therefore, the first row and column of $\widetilde{K}$ are zero vectors.

Equation (16) is rewritten as

$$M_{00}\ddot{\underline{q}}_0+M_{01}\ddot{\underline{q}}_{00}=F \tag{17}$$

$$M_{10}\ddot{\underline{q}}_0+M_{11}\ddot{\underline{q}}_{00}+K_{11}\underline{q}_{00}=0 \tag{18}$$

where *F* is input force on the structure. Since $\ddot{\underline{q}}_0$ is the excitation, therefore equation (17) is a force equation which generates $\ddot{\underline{q}}_0$, and equation (18) finds $\underline{q}_{00}$ representing the response due to excitation $\ddot{\underline{q}}_0$, that is $\underline{q}_{00}$ is equivalent to the response vector $\begin{bmatrix}q_1 & q_2 & b_1 & b_2 & y_1 & y_2\end{bmatrix}^T$ shown in (17). Assuming harmonic excitation for $\ddot{\underline{q}}_0$ and $\underline{q}_{00}$, that is

$$\ddot{\underline{q}}_0=\ddot{\underline{A}}_0e^{i\omega t} \tag{19}$$

$$\underline{q}_{00}=\underline{A}_{00}e^{i\omega t} \tag{20}$$

Substituting (19) and (20) into (17) and (18), yields

$$\underline{A}_{00}=-\left[K_{11}-\omega^2M_{11}\right]^{-1}M_{10}\ddot{\underline{A}}_0 \tag{21}$$

Thus:

$$\ddot{\underline{A}}_{00}=\omega^2\left[K_{11}-\omega^2M_{11}\right]^{-1}M_{10}\ddot{\underline{A}}_0 \tag{22}$$

Assuming overall system output is represented by $\ddot{w}$ and let $\ddot{w}(dj)=\ddot{W}_je^{i\omega t}$, the expression for $\ddot{w}(dj)$ is:

$$\begin{aligned}\ddot{w}(d_j)&=\ddot{q}_0\phi_0(d_j)+\ddot{q}_1\phi_1(d_j)+\ddot{q}_2\phi_2(d_j)\\&+b_1\psi_1(d_j)+b_2\psi_2(d_j)...\end{aligned}\quad for\ j=1,2... \tag{23}$$

where d_j is the measurement location on the beam. On the right hand side of (23) the first term corresponds to the input excitation, and the second and third terms correspond to the bending responses due to the first and second mode shapes. The fourth and fifth terms correspond to torsion responses due to the first and second mode shapes.

Assuming two mode shapes $\tilde{\phi}$ along the beam, using equation (23), yields

$$\underline{\ddot{W}}=\begin{bmatrix}\phi_0(d_1)\\ \phi_0(d_2)\end{bmatrix}\cdot\ddot{\underline{A}}_0+\tilde{\phi}\cdot\ddot{\underline{A}}_{00} \tag{24}$$

Thus,

$$\begin{Bmatrix} \ddot{W}_1 \\ \ddot{W}_2 \end{Bmatrix} = \begin{bmatrix} \phi_0(d_1) \\ \phi_0(d_2) \end{bmatrix} \ddot{A}_0 + \begin{bmatrix} \phi_1(d_1) & \phi_2(d_2) & 0 & 0 & 0 & 0 \\ \phi_1(d_1) & \phi_2(d_2) & 0 & 0 & 0 & 0 \end{bmatrix} \begin{bmatrix} \ddot{A}_1 \\ \ddot{A}_2 \\ \ddot{B}_1 \\ \ddot{B}_2 \\ \ddot{Y}_1 \\ \ddot{Y}_2 \end{bmatrix} \quad (25)$$

where $\begin{bmatrix} \phi_0(d_1) \\ \phi_0(d_2) \end{bmatrix}$ is the excitation force matrix at the main beam clamped ends. By substituting equation (22) for $\underline{\ddot{A}}_{00}$, equation (24) for the output response $\underline{\ddot{W}}$ becomes:-

$$\underline{\ddot{W}} = \left\{ \begin{bmatrix} \phi_0(d_1) \\ \phi_0(d_2) \end{bmatrix} + \omega^2 \tilde{\phi} \left[K_{11} - \omega^2 M_{11} \right]^{-1} M_{10} \right\} \ddot{A}_0 \quad (26)$$

Therefore, the transmissibility of the multiple cantilever system is as shown in (27):

$$\underline{T} = \frac{\underline{\ddot{W}}}{\ddot{A}_0} = \frac{Output}{Input} = \begin{bmatrix} \phi_0(d_1) \\ \phi_0(d_2) \end{bmatrix} + \omega^2 \tilde{\phi} \left[K_{11} - \omega^2 M_{11} \right]^{-1} \cdot M_{10} \quad (27)$$

The analysis can also be applied to the clamped-clamped beam structure shown in Figure 6 where there are more than two added cantilevers, however as a consequence there is an expanded mass matrix $\tilde{M}$ and stiffness matrix $\tilde{K}$.

SIMULATION RESULTS AND DISCUSSION

The transmissibility equation was programmed in Matlab, to predict beam vibration behavior. A prototype harvester system was investigated, consisting of a stainless-steel (Young's modulus = $205x10^9 Nm^{-2}$), clamped-clamped beam with dimensions 170 x 20 x 1 mm. The cantilevers are of the same material and are mounted at 25mm, 55mm, 85mm, 115mm and 145mm respectively along the beam. The predicted transmissibility curve for the beam without tip masses is shown in Figure 9.

Figure 8 shows resonance peaks occurring over a frequency range of approximately 50*Hz* to 80*Hz* and 400*Hz* to 600*Hz* respectively, due to the first and second modes of the five cantilevers. The peak at 170Hz is due to the clamped-clamped beams first bending mode. The model assumes 1% damping ratio in the bending and torsion fields. The transmissibility was simulated at several different locations on the beam. The highest predicted waveform is at the centre position of the beam, where the highest deflections occur, and this is in agreement with the first system bending mode shape shown in Figure 7. However anti-resonances occur in the system due to pole-zero cancellation. These anti-resonances decrease the transmissibility of the system, and reduce the piezoelectric output.

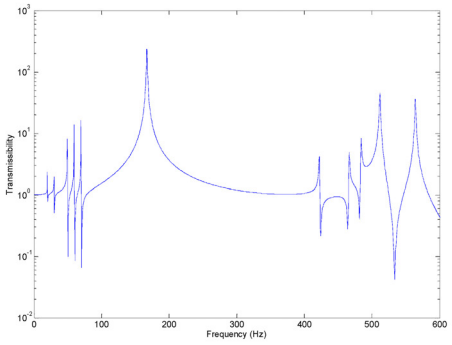

Figure 8: Transmissibility calculated at the centre of the multiple cantilever beam

Anti-resonances occur in every resonant system, and therefore it is impossible to remove these by varying the beam parameters. A possible means of reducing the effects of anti-resonances is to have two separate clamped-clamped beams, one on top of the other, perhaps, so that both are subject to the same vibration source, each having a number of cantilevers mounted upon it. With appropriate beam parameters, the transmissibility of, say, the lower beam can be frequency shifted slightly with respect to the upper beam to produce a combined transmissibility, see Figure 9.

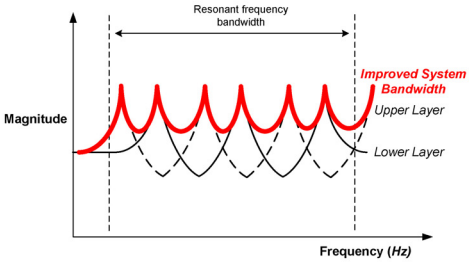

Figure 9: Output of two beam multiple-cantilever design

In Figure 9 the lower and the upper beam transmissibilities are shown in thin and dashed lines. The peaks in the upper beam's transmissibility are placed so as to be at the same frequency as the anti-resonances of the lower beam and vice versa. By doing so the transmissibility of the system is improved to that of the upper curve shown in bold.

LAB TEST VERIFICATION AND DISCUSSION

Initial work involved determining the resonant frequencies of single cantilevers with different tip masses. The approximate required tip masses and mounting location versus resonant frequency relationship was calculated using standard mass-spring-damper system equations [13-15].

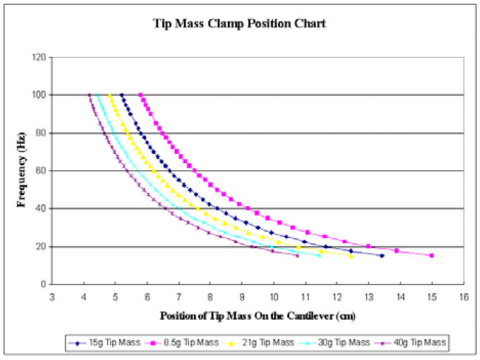

Figure 10: Multiple cantilever tip mass selection chart

Figure 10 shows how the calculated resonant frequency of the single cantilevers changes as the position of the mass on the cantilever is varied, for several different tip masses. Using this chart, a series of cantilever resonant frequencies can be easily set up. This is shown in Figure 11.

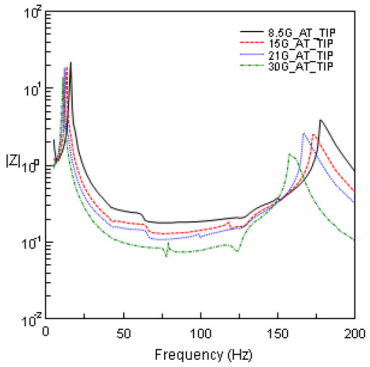

Figure 11: Measured cantilever transmissibility curve with different tip masses

The curves in Figure 11 show the measured transmissibility curves of four single cantilevers system tuned with different tip masses. The system transmissibility curves overlap between 7*Hz* and 14*Hz* and also between 150*Hz* and 175*Hz* where the first and second resonances occur. Therefore the proposed broadened bandwidth concept can be applied to either the first or second resonance region. A detailed frequency curve for the first mode is shown in Figure 12. Note that due to low frequency instrument noise, the results obtained below 5*Hz* are ignored.

As shown in Figure 12, the four resonant frequency peaks are approximately between 7*Hz* and 20*Hz*. This bandwidth can also be shifted higher or lower with different tip mass selections. Thus the concept outlined in Figure 9 should be applicable to a harvester formed from a multiplicity of single cantilevers. Figure 14 shows the multiple cantilever system built and tested in the lab.

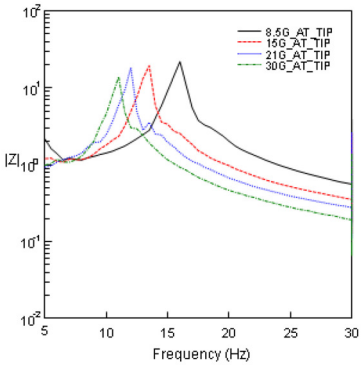

Figure 12: Measured cantilever transmissibility curve with different tip masses at first resonant peaks

A 170mm x 20mm x 1mm clamped-clamped beam was tested in the lab as shown in Figure 13. The five cantilevers are of size 80mm x 10mm x 1mm. Five different tip masses of 10, 15, 20, 30 and 40 grams were used. The transmissibility at the centre of the beam was measured using an experimental setup comprising an electromagnetic exciter, a power amplifier, two accelerometers, two signal conditioners and a Solartron Instruments SI1260 Impedance/Gain-phase analyzer. The measured result is shown in Figure 14. The multiple resonance peaks seen in Figure 14 are due to the resonant characteristics of the five cantilevers.

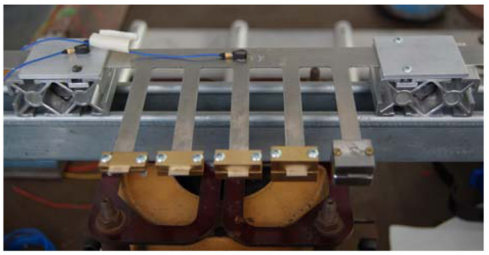

Figure 13: Experimental model of multiple cantilever structure

Unlike the case with tip masses shown in Figure 14, Figure 15 shows that when there are no tip masses, the resonances between 150*Hz* and 370*Hz* disappear. Actually, the resonance peaks have shifted to higher frequencies because of the reduced mass loading of the cantilevers, and now appear between about 400*Hz* and 500*Hz* as can be seen when Figures 14 and 15 are compared. The relatively high resonant frequency behaviour of the structure is mainly due to the length and thickness of the

tested beam, and is in general agreement with the previous predicted transmissibility response shown in Figure 8.

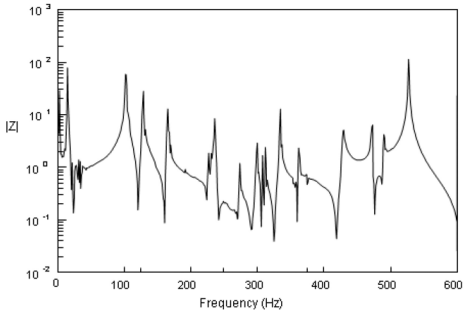

Figure 14: Measured transmissibility of multiple cantilevered beams with different tip masses

The measured transmissibility curve of the beam without the tip masses is shown in Figure 15.

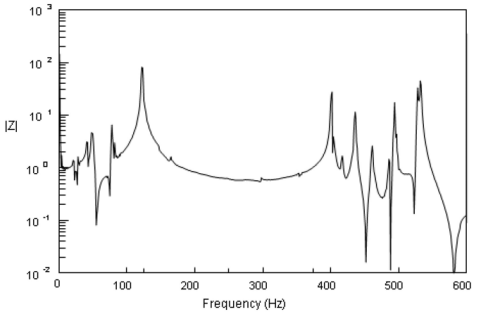

Figure 15: Measured transmissibility of multiple cantilever beam without tip masses

The resonance frequency bands can be altered by changing the dimension of the beam as well as the tip masses. The results show that the beam structure, with multiple cantilevers attached, will cause a multiple resonant frequency effect. Hence, with appropriate tuning of the tip masses according to the beam dimensions, amplification can be made to occur at various frequencies.

CONCLUSIONS

A novel multiple cantilever structure has been proposed in this paper. Mass loading and the effect of different beam dimensions have been investigated theoretically using a Rayleigh-Ritz method. From the predictions and simulation results, it was found that the cantilever mounted locations affect the whole system frequency and sensitivity. For different mode shapes, the beam system will also have different deflections. Therefore, beam dimensions and cantilever locations have to be chosen appropriately. The predictions show that the new energy harvesting design is feasible for harvesting energy from ambient environmental vibrations, as it works over a wide frequency spectrum. It has been shown that there is a fairly close agreement between the predicted and measured transmissibility curves of the proposed design for the case of no tip mass.

Further work will concentrate on increasing the number of cantilevers to broaden the spectral response, and determining the design rules for adapting the technology to other frequency ranges whilst providing a broad response. This will be achieved by:

1. Implementing two (or more) multiple cantilever systems to fill in response dips due to anti-resonances and achieve a flatter vibration response.
2. Further investigations into methods of adding the responses from several beams to optimise the output.
3. Finding a suitable high efficiency rectification circuit
4. Optimising the efficiency of the power electronic circuits attached to the output(s) of the beams

The proposed new design of piezoelectric cantilever harvester should be suitable for use by remote instruments, such as wireless sensor nodes, in remote environments where replacement of batteries is difficult, but there is a plentiful supply of vibration energy.

ACKNOWLEDGEMENT

The authors would like to thank Prof. Jan Wright for his contribution to the theoretical development and the experimental test program. They also thank the School of Electrical and Electronic Engineering for partial scholarship to S. Qi, and for funding received for part of this work from the EU FP6 DYNAMITE research project.

REFERENCES

[1] Shen, D., Choe, S. and Kim, D., 2007, “Analysis of piezoelectric materials for energy harvesting devices under high-g vibrations” *Japanese Journal of Applied Physics,* Vol. 46, No. 10A, pp. 6755-6760

[2] Anton, S., R., Sodano, H., A., 2007, “A review of power harvesting using piezoelectric materials (2003-2006)”, *Smart Material and Structures*, 16, pp. R1-R21

[3] Beeby, S., P., Tudor, M., J., and White, N., M., 2006, “Energy harvesting vibration sources for microsystems applications” *Measurement Science and Technology*, pp.R175-R195

[4] Sodano, H., A., Inman, D., J. and Park, G., 2004, “A review of power harvesting from vibration using piezoelectric materials”, *The Shock and Vibration Digest*, Vol. 36, No. 3, pp. 197-205.

[5] Roundy, S., J., 2003, “Energy scavenging for wireless sensor nodes with a focus on vibration to electricity

conversion", *PhD. Thesis*, *Berkeley*, *The University of California*
[6] Roundy, S., Leland, E., S., Baker, J., Carleton, E., Reilly, E., Lai, E., Otis, B., Rabaey, J., M., Wright, P., K. and Sundararajan, V., 2005, "Improving power output for vibration-based energy scavengers" *IEEE Pervasive Comput*. 4 no.1, 28.
[7] Shahruz, S., M., 2006, "Design of mechanical band-pass filters with large frequency bands for energy scavenging" *Mechatronics* 16, pp. 523-531
[8] Shahruz, S., M., 2008, "Design of mechanical band-Pass Filters for energy scavenging: multi-degree-of-freedom models" *Journal of Vibration and Control,* 14(5), pp. 753-768
[9] Bent, A., 1997, "Piezoelectric fiber composites with interdigitated electrodes" *Journal of Intelligent Material Systems and Structures* 8, 903
[10] Sherrity, S., Wiedericky, H., D., Mukherjeey, B., K. and Sayerz, M., 1997, "An accurate equivalent circuit for the unloaded piezoelectric vibrator in the thickness mode" *J. Phys. D: Appl. Phys.* 30 2354–2363.
[11] Cheever, E., 2005, "Analogous electrical and mechanical systems", Swarthmore college website: http://www.swarthmore.edu/NatSci/echeeve1/Ref/Analogs/ElectricalMechanicalAnalogs.html
[12] Lefeuvre, E., Badel, A., Richard, C., Guyomar, D., 2007, "Energy harvesting using piezoelectric materials: case of random vibrations" *Journal of Electroceram*, 19, pp. 349-355
[13] Blevins, R., D., 1979, "Formulas for natural frequency and mode shape" *Litton Educational Publishing, ISBN: 0-442-20710-7*
[14] Snowdon, J., C., 1968, "Vibration and shock in damped mechanical systems" *John Wiley & Sons, Inc. Library of Congress Catalog Card Number 68-18630, GB 471 81001X*
[15] Laura, P., A., A., Pombo, J., L. and Susemihl, E., A., 1974, "A note on the vibrations of a clamped-free beam with a mass at the free end" *Journal of Sound and Vibration* 37(2), 161-168

Appendix G:

Reprint -

Development of Multiple Cantilevered Piezo Fibre Composite Beams Vibration Energy Harvester for Wireless Sensors

Author:

S. O. Oyadiji, S. Qi, R. Shuttleworth

Publisher:

World Congress of Engineering Asset Management, *Athens*, Greece, September, 2009

DEVELOPMENT OF MULTIPLE CANTILEVERED PIEZO FIBRE COMPOSITE BEAMS VIBRATION ENERGY HARVESTER FOR WIRELESS SENSORS

S. Olutunde Oyadiji[a], Shaofan Qi[b] and Roger Shuttleworth[b]

[a] *School of Mechanical, Aerospace and Civil Engineering, University of Manchester, Manchester M60 1QD, UK.*

[b] *School of Electrical and Electronic Engineering, University of Manchester, Manchester M60 1QD, UK.*

Abstract: There is considerable interest in the development of battery-free mobile electronics systems such as wireless sensors which are used for the conditioning monitoring of engineering assets some of which are located in hostile environments. The main focus has been on the development of techniques for the harvesting of energy from ambient sources. One of the main sources of ambient energy is mechanical vibration. A number of vibration energy harvesting devices have been developed using electromagnetic, electrostatic or piezoelectric principles. A currently favoured approach is the use of piezoelectric fibre composite (PFC) materials in the form of a cantilevered beam with a tip mass. This enables significant energy to be harvested at the resonance peak of the PFC-mass vibration system. However, off the resonance peak, the harvested vibration energy is relatively too small and, consequently, the bandwidth of reasonable energy harvesting is too small. To overcome this problem, this paper presents the use of a vibration energy harvesting device consisting of four PFC beams with tip masses. Each beam is tuned to a slightly different resonance frequency. Thus, the bandwidth of significant vibration energy harvesting is considerably extended. It is shown that the multiple cantilevered PFC beams vibration energy harvester can harvest energy from ambient vibrations more effectively than a single cantilevered PFC beam vibration energy harvester.

Key Words: Vibration Energy Harvesting, Wireless Sensor, Cantilevered Beam, Piezoelectric Fibre Composite.

1 INTRODUCTION

Currently, most wireless sensor nodes are battery-powered and, therefore, require regular checks of the charge level of the batteries and of replacements of the batteries when they are no longer adequate. This considerably limits the autonomy of the sensor nodes and adds costs to any condition maintenance programme. Ideally, the sensor nodes should be self-powered and battery-less. This has led to an interest in designing electronics systems with the capability of deriving their electrical power needs from surroundings. The technique for doing this has come to be known as energy or power harvesting. It is essentially the conversion of low level ambient energy, such as vibration, heat or light energy, into usable but small amount of electrical power [1-5].

Mechanical vibration is one of the main sources of ambient energy. The harvesting of mechanical vibration energy has been achieved using electromagnetic [6-8], electrostatic [9-11] and piezoelectric [12-14] devices. But the development of piezoelectric vibration energy harvesters has dominated research effort in the last 5 to 10 years. In order to convert the ambient kinetic or vibration energy into electric power, piezoelectric materials are commonly incorporated in energy harvesting devices. A typical piezoelectric vibration energy harvesting device is a cantilevered beam consisting of one or two piezoelectric material layers bonded to the top and bottom surfaces of usually a metallic base structure. The configuration consisting of one piezoelectric layer is known as a unimorph while the configuration consisting of two piezoelectric layers is known as a bimorph. The vibration energy harvesting cantilevered beam is fixed to a vibrating structure from which vibration energy is to be extracted. The dynamic strain induced in the piezoelectric layers generates electric power across the electrodes of the piezoelectric layers.

One of the most commonly used piezoelectric materials is piezoelectric fibre composite (PFC). It enables realistic applications which require highly distributed actuation and sensing, maintains the majority of the stiffness and bandwidth of monolithic piezoelectric ceramics. A popular mode of application of PFC for vibration energy harvesting is as a cantilevered

beam with a tip mass. The magnitude of the tip mass and its location along the length of the beam can be adjusted in order to obtain a resonance frequency which coincides with the dominant frequency of the ambient vibration energy. This enables significant amounts of energy to be harvested at the resonance peak of the PFC-mass vibration system. However, off the resonance peak, the harvested vibration energy is relatively too small and, consequently, the bandwidth of reasonable energy harvesting is too small. To overcome this problem, this paper presents the use of a vibration energy harvesting device consisting of four PFC beams with tip masses. Each beam is tuned to a slightly different resonance frequency. Thus, the bandwidth of significant vibration energy harvesting is considerably extended. The results of these investigations show that the multiple cantilevered PFC beams vibration energy harvester has the potential to harvest energy from ambient vibrations more effectively and efficiently and over a wider frequency band than a single cantilevered PFC beam vibration energy harvester.

2 THEORY

A cantilevered PFC beam is excited at the base. This induces dynamic strain in the beam which, therefore, produces a voltage across its electrodes. The theoretical simulation of the induced strain can be achieved by analysis of the beam as a continuous vibrating system with distributed parameters using the classical Bernoulli-Euler beam theory. The result of this analysis will give a multi-modal behaviour. Alternatively, a cantilevered PFC beam can be represented by an equivalent lumped-parameter, single degree-of-freedom (SDOF) system. This latter approach will yield an unimodal behaviour but it is much simpler to employ in studying the voltage generating behaviour of the beam.

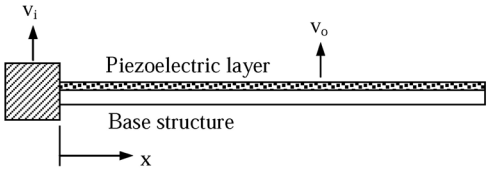

Figure 1. Cantilevered piezoelectric unimoph beam subjected to base excitation

2.1 Transverse Vibration of Cantilevered Beam

Figure 1 shows a cantilevered piezoelectric unimorph beam which is subjected to base excitation. The absolute transverse displacement of any point on the beam is given by,

$$v(x,t) = v_i(x,t) + v_o(x,t) \tag{1}$$

where $v_o(x,t)$ is the transverse displacement of any point on the beam relative to the clamped base of the beam, and $v_i(x,t)$ is the base excitation of the beam. Assuming that the beam is undamped, the equation of motion for free transverse vibrations in terms of the absolute displacement $v(x,t)$ is given by the Bernoulli-Euler beam equation as,

$$EI\frac{\partial^4 v}{\partial x^4} + \rho A\frac{\partial^2 v}{\partial t^2} = 0 \tag{2}$$

in which $v=v(x,t)$, E is Young's modulus of elasticity, I is second moment of area, ρ is mass density and A is cross-sectional area.

PFC beams are usually quite thin and flexible such that their motion will be affected by air damping. Also, they have got some internal structural damping. Including these damping effects, the equation of motion becomes [15,16],

$$EI\frac{\partial^4 v}{\partial x^4} + c_s I\frac{\partial^5 v}{\partial x^4 \partial t} + c_a\frac{\partial v}{\partial t} + \rho A\frac{\partial^2 v}{\partial t^2} = 0 \tag{3}$$

where c_s denotes structural damping coefficient and c_a denotes air damping coefficient. Substituting Equation (1) in Equation (3) gives,

$$EI\frac{\partial^4 v_o}{\partial x^4} + c_s I\frac{\partial^5 v_o}{\partial x^4 \partial t} + c_a\frac{\partial v_o}{\partial t} + \rho A\frac{\partial^2 v_o}{\partial t^2} = -\rho A\frac{\partial^2 v_i}{\partial t^2} - c_a\frac{\partial v_i}{\partial t} \tag{4}$$

Equation (4) can be solved to obtain the transmissibility expression which relates the output transverse displacement response at the tip of the beam to the base excitation of the beam. In [15,16], Equation (4) has been solved to obtain the relative displacement transmissibility of the tip of the beam in the absence [15] or presence [16] of a tip mass. However, the focus in this paper is to use an equivalent single degree of freedom model to analyse the response of the beam in order to obtain the absolute displacement transmissibility of the tip of the beam.

2.2 Equivalent Single Degree of Freedom Model of Cantilevered Beam

Figure 2 shows the equivalent single degree-of-freedom (SDOF) model of the cantilevered piezoelectric unimoph beam subjected to base excitation. The absolute transverse displacement of the tip of the beam is given by $v_o(t)$ while $v_i(t)$ is the base excitation of the beam.

The equivalent mass of the cantilevered beam is denoted by m_e while m denotes the added tip mass of the beam. Also, k_e and c_e are the equivalent stiffness and damping coefficient of the beam. The equivalent mass, equivalent stiffness and equivalent damping coefficient are related to the mass density ρ, Young's modulus E, second moment of area I, cross-sectional area A and length L of the beam as follows [17],

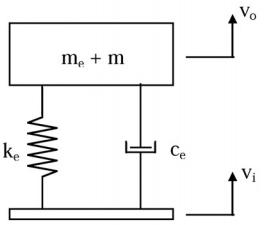

Figure 2. SDOF model of cantilevered piezoelectric unimoph beam subjected to base excitation

$$m_e = 0.24\rho AL; \qquad k_e = \frac{3EI}{L^3}; \qquad c_e = 2\zeta\sqrt{k_e(m_e+m)} \tag{5}$$

where the damping ratio ζ includes the internal structural damping of the beam as well as the external air damping. Using Newton's laws, the equation of motion of the SDOF system can be derived as,

$$M\frac{d^2v_o}{dt^2} + c_e\frac{d(v_o - v_i)}{dt} + k_e(v_o - v_i) = 0 \tag{6}$$

where $M = m_e + m$. If the base excitation is of the form,

$$v_i = V_i e^{j\omega t} \tag{7}$$

then, the tip response will be of the form,

$$v_o = \overline{V}_o e^{j\omega t} \tag{8}$$

where V_i is the amplitude of the excitation, $\overline{V}_o$ is the complex amplitude of the response and $j = \sqrt{-1}$. Substituting Equations (7) and (8) in Equation (6) gives,

$$(-M\omega^2 + j\omega c_e + k_e)\overline{V}_o = (j\omega c_e + k_e)V_i \tag{9}$$

which gives the complex transmissibility as,

$$\overline{T} = \frac{\overline{V}_o}{V_i} = \frac{j\omega c_e + k_e}{-M\omega^2 + j\omega c_e + k_e} \tag{10}$$

Dividing the top and bottom of the right side of Equation (9) gives,

$$\overline{T} = \frac{1 + j\dfrac{\omega c_e}{k_e}}{1 - \dfrac{M\omega^2}{k_e} + j\dfrac{\omega c_e}{k_e}} \tag{11}$$

Defining the undamped angular natural frequency and the viscous damping ratio, respectively, as:

$$\omega_n = \sqrt{\frac{k_e}{M}} \quad \text{and} \quad \zeta = \frac{c_e}{2\sqrt{k_e M}} \tag{12}$$

Then, Equation (11) becomes,

$$\overline{T} = \frac{1 + j2\zeta\beta}{1 - \beta^2 + j2\zeta\beta} \tag{13}$$

where the frequency ratio, $\beta = \omega / \omega_n = f / f_n$ and ω, ω_n are measured in rad/s while f, f_n are measured in Hz.. Thus, the amplitude of the complex transmissibility is given by,

$$T = |\overline{T}| = \left[\frac{1 + (2\zeta\beta)^2}{\left(1 - \beta^2\right)^2 + (2\zeta\beta)^2} \right]^{1/2} \tag{14}$$

3 DISCUSSION OF PREDICTED RESPONSES

The transmissibility amplitudes for four cantilevered beams are predicted using Equation (14). Four cases, which involve different fundamental natural frequencies of the beams as shown in Table 1, are studied. For Case 1, the fundamental natural frequencies are 10, 11, 12 and 13 Hz, and for Case 2 they are 10, 12, 14 and 16 Hz. Similarly, for Case 3 the fundamental natural frequencies are 10, 15, 20 and 25 Hz, and for Case 4 they are 10, 20, 30 and 40 Hz. In all cases, equivalent viscous damping ratios of the beams of 0.01 and 0.02 are used in the predictions. The results are shown in Figures 3 to 6.

Table 1

Fundamental natural frequencies of the four cantilevered beams

Case ID	Fundamental natural frequency (Hz)			
	Beam 1	Beam 2	Beam 3	Beam 4
Case 1	10	11	12	13
Case 2	10	12	14	16
Case 3	10	15	20	25
Case 4	10	20	30	40

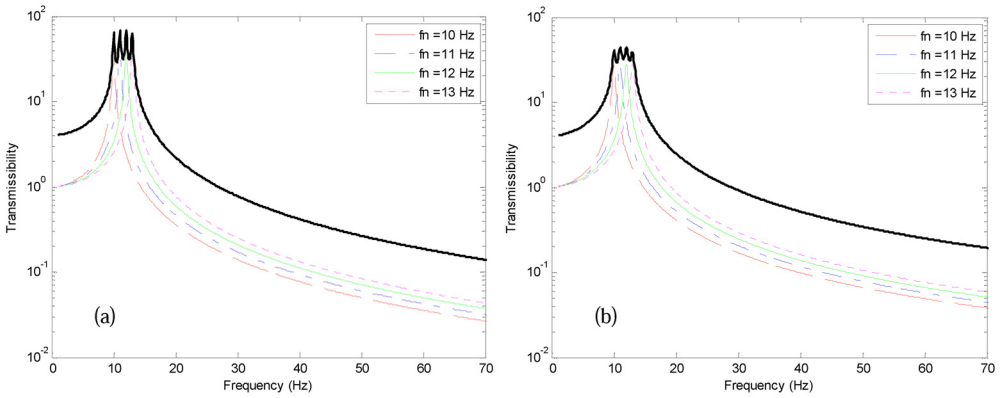

Figure 3: Transmissibility of SDOF equivalents of 4 cantilevered beams of fundamental resonance frequencies 10, 11, 12 and 13 Hz for damping ratios of (a) 0.01, (b) 0.02

Figure 3 shows a comparison of the transmissibility amplitudes of the 4 cantilevered beams for Case 1 for which the fundamental natural frequencies of the beams are 10, 11, 12 and 13 Hz. Figure 3(a) applies to a viscous damping ratio of 0.01 while Figure 3(b) is for a viscous damping ratio of 0.02. The thin curves are the transmissibility response curves for each beam while the thick curve is the theoretical sum of the 4 transmissibility curves. It is seen that an individual transmissibility curve has a sharp peak and a very narrow frequency band over which the transmissibility is greater than a factor of say 10. However, by using a combination of the 4 beams simultaneously and summing their amplitudes, the frequency range over which the

transmissibility is greater than a factor of 10 is significantly extended. Increasing the damping ratio from 0.01 to 0.02 causes the peak amplitudes of the individual and sum transmissibility curves to reduce.

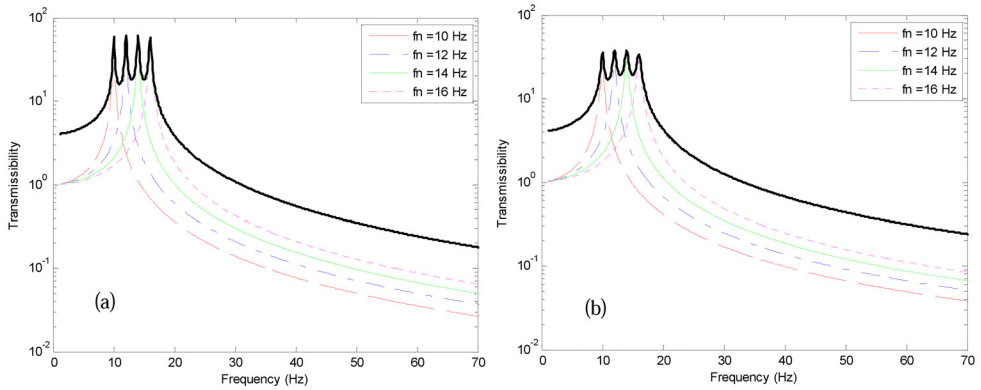

Figure 4: Transmissibility of SDOF equivalents of 4 cantilevered beams of fundamental resonance frequencies 10, 12, 14 and 16 Hz for damping ratios of (a) 0.01, (b) 0.02

The individual and sum transmissibility curves for Case 2, for which the fundamental natural frequencies of the beams are 10, 12, 14 and 16 Hz, are shown in Figure 4(a) for viscous damping ratio of 0.01, and in Figure 4(b) for viscous damping ratio of 0.02. It is seen that by increasing the maximum difference of the fundamental natural frequencies from 3 Hz in Case1 to 6 Hz in Case 2, the frequency range over which the transmissibility is greater than a factor of 10 has been increased from about 6 Hz to about 9 Hz. Similarly to the observation made for Case 1 (Figure 3), increasing the damping ratio from 0.01 to 0.02 causes the peak amplitudes of the individual and sum transmissibility curves to reduce. Also, the frequency range over which the transmissibility is greater than a factor of 10 is not affected by the increase in the viscous damping ratio.

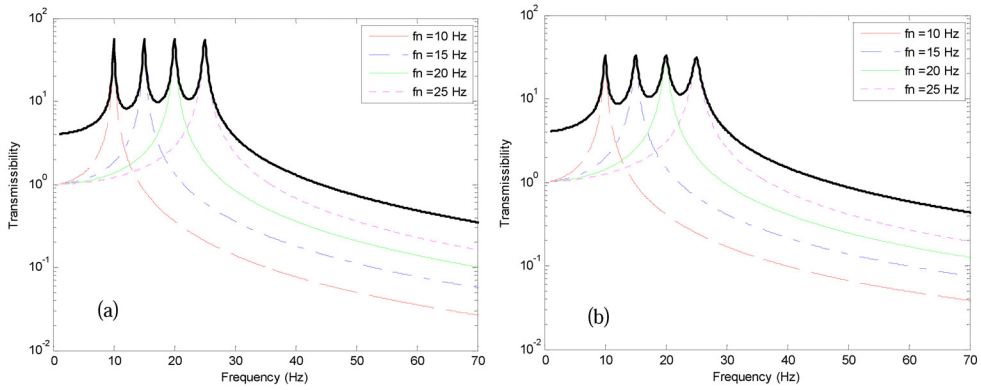

Figure 5: Transmissibility of SDOF equivalents of 4 cantilevered beams of fundamental resonance frequencies 10, 15, 20 and 25 Hz for damping ratios of (a) 0.01, (b) 0.02

The predicted transmissibility curves for Case 3, when the fundamental natural frequencies of the beams are 10, 15, 20 and 25 Hz, are shown in Figures 5(a) and 5(b) for viscous damping ratios of 0.01 and 0.02 respectively. Comparing Figures 5(a) and 5(b) with Figures 3(a) and 3(b) and with Figures 4(a) and 4(b), respectively, it can be seen that the peak levels of the individual and sum transmissibility curves are approximately the same. However, the troughs of the sum transmissibility curves decrease as the difference between the individual natural frequencies of the beams increases. It can be observed from Figures 5(a) that the first trough has a transmissibility amplitude of about 8 (i.e. less than a factor of 10). However, the transmissibility amplitude is greater than a factor of 8 over a frequency range of about 17 Hz compared to a range of about 10 Hz in Case 2. A detailed comparison of Figures 5(a) and 5(b) shows that by increasing the viscous damping ratio from 0.01 to

0.02, the peak transmissibility amplitudes are reduced while the transmissibility amplitudes of the troughs are increased. These results show that increasing the difference between the individual fundamental natural frequencies of the beams can limit the frequency range over which the transmissibility amplitude of the sum curve is continuously above a specified value.

Figures 6(a) and 6(b) show the comparisons between the individual and sum transmissibility curves of the 4 cantilevered beams for Case 4 for which the fundamental natural frequencies of the beams are 10, 20, 30 and 40 Hz and for damping ratios of 0.01 and 0.02 respectively. The figures show that the individual transmissibility curves have variable frequency bands over which the transmissibility is greater than a factor of 10. The frequency band ranges from about 1 Hz for Beam 1 (f =10 Hz) to about 4 Hz for Beam 4 (f = 40 Hz). Also, both figures show that the transmissibility amplitudes of the three troughs are less than 10. For a damping ratio of 0.01, Figure 5(a) shows that the transmissibility amplitudes of troughs 1, 2 and 3 are about 5.5, 6.0 and 8.0 respectively. But when the damping ratio is increased to 0.02, Figure 5(b) shows that the transmissibility amplitudes of troughs 1, 2 and 3 are slightly increased to about 6.0, 7.3 and 8.3 respectively. From these results, it can be concluded that increasing the difference between the individual fundamental natural frequencies of the beams can severely limit the frequency range over which the transmissibility amplitude of the sum curve is continuously above a specified value.

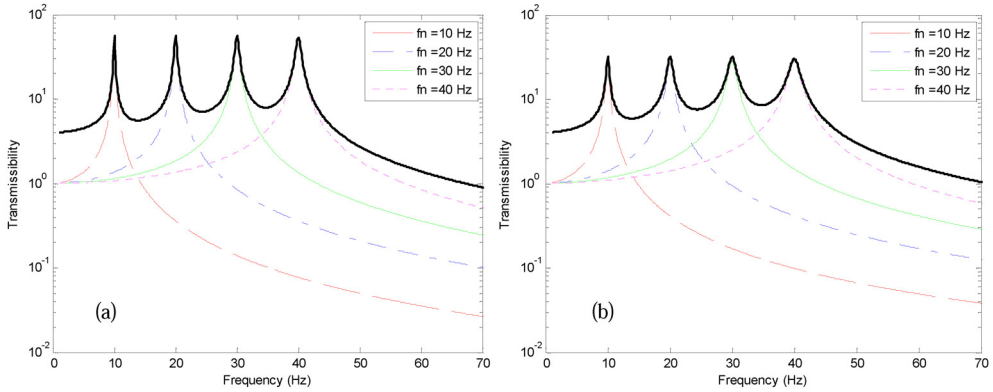

Figure 6: Transmissibility of SDOF equivalents of 4 cantilevered beams of fundamental resonance frequencies 10, 20, 30 and 40 Hz for damping ratios of (a) 0.01, (b) 0.02

Comparing Figures 3 to 6, it can be seen that the difference in the fundamental natural frequencies of the cantilevered beams has a more pronounced effect on the frequency range over which the transmissibility amplitude of the sum curve is continuously above a specified value. The value of the viscous damping ratio has a relatively less pronounced effect. To maximise the frequency range over which the transmissibility amplitude of the sum curve is continuously above a threshold value T_{sum}, the difference in fundamental natural frequency (Δf) should be large when T_{sum} is less than 10 but small when T_{sum} is equal to or greater than 10. For example, when T_{sum} = 5, Figure 6 shows that Δf =10 Hz gives a frequency range of about 40 Hz compared to 17 Hz for Δf =5 Hz (Figure 5), 8 Hz for Δf =2 Hz (Figure 4) and 6 Hz for Δf =1 Hz (Figure 3). But when T_{sum} = 10, Figure 6 shows that Δf =10 Hz gives a maximum continuous frequency range of about 5 Hz compared to 13 Hz for Δf =5 Hz (Figure 5), 8 Hz for Δf =2 Hz (Figure 4) and 6 Hz for Δf =1 Hz (Figure 3).

4 INITIAL EXPERIMENTAL TEST RESULTS

Initial transmissibility tests are carried out on 4 piezoelectric fibre composite (PFC) cantilevered beams. Each PFC beam has a total length of 135 mm, width of 13 mm and a total thickness (including thickness of steel shim and top and bottom piezoelectric fibre electrodes) of about 1.25 mm. One end of each beam is clamped in a box while a tip mass is attached to its free end as shown in Figure 7. The magnitudes of the tip masses used are 8.5, 15, 21 and 30 grams. The box containing the 4 PFC cantilevered beams is mounted on top of an electromagnetic vibrator which is driven from a power amplifier that is connected to a frequency response analyser. An accelerometer is mounted on the base of the box while a very small accelerometer is attached to the tip of each PFC cantilevered beam. The beams are excited sinusoidally over a frequency range from 0 to 50 Hz. The frequency response analyser acquired the tip responses of the PFC beams as well as the base excitation applied. From these measurements, the transmissibility amplitude data for each beam is produced in the frequency domain as the ratio of the output response to the input excitation.

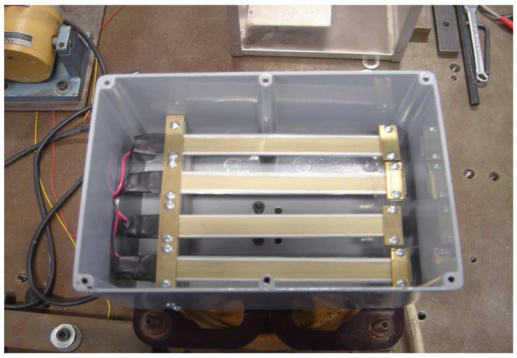

Figure 7. Multiple cantilevered PFC beams vibration energy harvester

Figure 8 shows the plots of the transmissibility amplitudes versus excitation frequency for the 4 cantilevered PFC beams. It can be deduced that the beams have different resonance frequencies of 10.9, 11.8, 13.2 and 15.9 Hz. For each beam, Figure 8 shows that the maximum vibration energy occurs at its peak amplitude which is at its resonance frequency. Away from resonance, it is seen that the amplitude and, hence, the vibration energy rapidly decreases. Thus, for a single cantilevered PFC vibration energy harvesting beam with tip mass, the frequency band of significant energy harvesting is small. However, when the 4 beams are used simultaneously, the resultant response amplitude can potentially be the sum of the individual amplitudes. Consequently, the magnitude and the frequency band of the vibration energy that can be harvested in the resonant region of the 4 beams will be greater than that of a singe beam as was demonstrated in Figures 3 to 6.

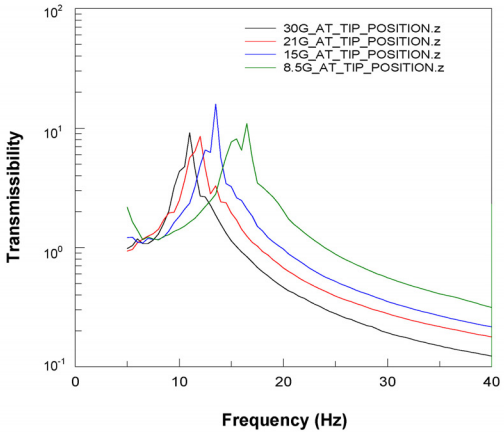

Figure 8. Transmissibility response of multiple cantilevered PFC beams

Comparing the measured and predicted transmissibility responses, it can be seen that the measured resonance frequencies of 10.9, 11.8, 13.2 and 15.9 Hz for the 4 PFC beams are close to those of Case 2 of the theoretical predictions, namely: 10, 12, 14 and 16 Hz. It can be seen that the measured individual transmissibility curves shown in Figure 8 compare fairly well with those predicted for Case 2 which are shown in Figure 4. Consequently, it would be expected that the experimental sum transmissibility curve will also compare fairly well with the predicted sum transmissibility curve shown in Figure 4. The challenge is to build an electronic circuit that will enable this to be done effectively with minimal power losses. The experimental transmissibility measurements need to be improved in quality, especially around the resonance frequencies, by decreasing the frequency step of the excitation around the resonance frequencies.

5 CONCLUSIONS

A theoretical basis for analysing the vibration transmissibility responses of single cantilevered piezoelectric beam and of the single degree-of-freedom idealisation has been presented. This model has been used to predict the transmissibility responses of cantilevered PFC beams subjected to sinusoidal vibration. It has been shown that the difference in the fundamental natural frequencies of the cantilevered beams has a more pronounced effect on the frequency range over which the transmissibility amplitude of the sum curve is continuously above a specified value, and that the value of the viscous damping ratio has a relatively less pronounced effect. It has also been shown that the multiple cantilevered PFC beams vibration energy harvester can harvest energy from ambient vibrations more effectively than a single cantilevered PFC beam vibration energy harvester as it provides a wider frequency range over which the transmissibility level and, hence, the strain levels induced in the beams, continuously exceed a threshold level for effective vibration energy harvesting.

6 REFERENCES

1. Anton SR & Sodano HA. (2007) A review of power harvesting using piezoelectric materials (2003–2006) Smart Materials and Structures 16, R1–R21
2. Sodano HA, Inman DJ & Park G. (2004) A review of power harvesting from vibration using piezoelectric materials, The Shock and Vibration Digest 36:197–205
3. Beeby SP, Tudor MJ & White NM. (2006) Energy harvesting vibration sources for microsystems applications, Measurement Science and Technology 13, 175–195
4. Cook-Chennault KA, Thambi N & Sastry AM. (2008) Powering MEMS portable devices – a review of non-regenerative and regenerative power supply systems with emphasis on piezoelectric energy harvesting systems, Smart Materials and Structures 17, 043001, 1–33
5. Priya S. (2007) Advances in energy harvesting using low profile piezoelectric transducers, Journal of Electroceramics 19, 167–184
6. Arnold D. (2007) Review of microscale magnetic power generation IEEE Transactions on Magnetics 43, 3940–3951
7. Glynne-Jones P, Tudor MJ, Beeby SP & White NM. (2004) An electromagnetic, vibration powered generator for intelligent sensor systems, Sensors and Actuators A 110, 344–349
8. Williams CB & Yates RB. (1996) Analysis of a micro-electric generator for microsystems, Sensors and Actuators A 52, 8–11
9. Mitcheson P, Miao P, Start B, Yeatman E, Holmes A & Green T. (2004) MEMS electrostatic micro-power generator for low frequency operation, Sensors and Actuators A 115, 523–529
10. Roundy S, Wright PK & Rabaey J. (2003) A study of low level vibrations as a power source for wireless sensor nodes, Computer Communications 26:1131–1144
11. Roundy S, Wright PK & Rabaey J. (2002) Micro-electrostatic vibration-to-electricity converters Proceedings of the ASME 2002 International Mechanical Engineering Congress and Exposition
12. Sodano H, Inman D & Park G. (2005) Generation and storage of electricity from power harvesting devices, Journal of Intelligent Material Systems and Structures 16, 67–75
13. Sodano HA, Park G & Inman DJ. (2004) Estimation of electric charge output for piezoelectric energy harvesting, Strain 40, 49–58
14. Jeon YB, Sood R, Jeong JH & Kim S. (2005) MEMS power generator with transverse mode thin film PZT, Sensors & Actuators A 122, 16–22
15. Erturk A and Inman D J 2008a On mechanical modeling of cantilevered piezoelectric vibration energy harvesters, Journal of Intelligent Material Systems and Structures 19:1311–1325
16. Erturk, A & Inman, DJ. (2007) Mechanical Considerations for Modeling of Vibration-Based Energy Harvesters, Proceedings of the ASME IDETC 21st Biennial Conference on Mechanical Vibration and Noise.
17. Blevins, RD. (1979) Formulas for Natural Frequency and Mode Shape, Van Nostrand Reinhold, New York.

Acknowledgments

The funding received for this work from the EU under the FP6 programme for the DYNAMITE project is gratefully acknowledged.

Appendix H:

Reprint -

Self-powered Intelligent Wireless Disposable Micro-sensors

Author:

S. O. Oyadiji, Z. Zhu, R. Sun, R. Pietruszkiewicz, P. Charles, S. Qi, R. Shuttleworth

Publisher:

Wireless Sensing Demonstrator Showcase, National Physical Laboratory, *UK*, 2009

Self-powered Intelligent Wireless Disposable Micro-sensors

S. Olutunde Oyadiji[1], Zhenhuan Zhu[1], Rongqiang Sun[1], Robert Pietruszkiewicz[1], Peter Charles[1], Shaofan Qi[2] and Roger Shuttleworth[2]
[1]School of Mechanical, Aerospace and Civil Engineering,
[2]School of Electrical and Electronic Engineering,
University of Manchester,
Manchester M60 1QD
Tel. 0161 275 4348, Email: s.o.oyadiji@manchester.ac.uk

Abstract: Intelligent sensors are vital for an efficient e-maintenance system with distributed architecture. This paper presents and demonstrates the achievements that were made at the University of Manchester as part of the EU FP6 DYNAMITE research project. The role of the University of Manchester in the project was to develop cheap, self-powered, intelligent, wireless and disposable micro-sensors to monitor system variables in engineering assets including vibration, temperature and pressure. This has involved the developments of wireless sensor systems, energy harvesting devices, and MIMOSA Database communication link.

1. INTRODUCTION

This paper is based on research work carried out as part of an EU research project codenamed DYNAMITE which stands for Dynamic Decisions in Maintenance. The project was an integrated project and was executed by a consortium of 18 partners drawn from several European countries. The objectives of the project were to produce an infrastructure for global e-maintenance in order to enable mobile and wireless condition monitoring of machinery and processes. This involved the development and integration of hardware and software including mobile wireless devices for accessing and reporting from the e-maintenance infrastructure. Analytical methods and tools were also developed to enable cost-effective applications of maintenance technologies for the continuous enhancement of the profitability and competitiveness of companies. The role of the University of Manchester in the project was to develop cheap, self-powered, intelligent, wireless and disposable micro-sensors to monitor system variables in engineering assets including vibration, temperature and pressure. This was achieved via the execution of the following three major tasks: development of (1) wireless sensor systems; (2) energy harvesting devices; (3) MIMOSA Database communication link.

Intelligent sensors play a leading role in the design of an efficient e-maintenance system with distributed architecture. They are required to possess a number of capabilities including: self-calibration, ability to analyse, make decisions and to correct a process, changing of software parameters, detection and isolation of faults, cooperation with the top acquisition supervisory stations, communication with the supervisory condition monitoring systems, performing requested tests and sending data to the condition maintenance system. The processing unit of a sensor node, which is generally associated with a small storage unit, manages the procedures that make the sensor node collaborate with the other nodes to carry out the assigned sensing tasks.

There are many processors available that meet the power and cost targets as well as data processing requirements. In a given network, thousands of sensors could be continuously reporting data, creating heavy data flow. Thus, the overall system is memory constrained, but this characteristic is a common design challenge in any wireless sensor network. Expansion of the functionality of the sensor node by implementing additional processing unit comes at a price, as the additional processing power adds energy consumption. Also data pre-processing requires additional control over the data and settings of the system. The control over the measured values has to be done in the device bringing additional control over the sensor itself. Data transmission is made at specified intervals of time. This intermittent measurement and transmission of data gives the potential for the development and integration of energy harvesting devices in order to provide the sensors with self-powering capability. Energy could be harvested from ambient sources such as vibration, light and heat.

The wireless sensor system developed consists of Crossbow Imote2 sensor platforms, MEMS accelerometers, pressure sensors and thermistor temperature sensors. The MEMS accelerometers were made in-house using ADXL202E and ADXL311JE two-axis accelerometers which were mounted on tiny circuit boards and encased. The wireless intelligent sensor platforms were designed to perform advanced operations internally before the measured data are transmitted.

In order to achieve self-powering capability for the sensor platforms, an energy harvesting system was developed. This consists of an in-house developed multiple cantilevered piezoelectric fibre composite (PFC) beams vibration energy harvester and a solar panel which are connected to an electronics power management board (PMB) middleware. The harvested energy is stored on a supercapacitor on the PMB and use to recharge two sets of three AAA rechargeable batteries.

The MIMOSA standard for asset management data exchange was chosen by the Dynamite project partners to be used for data exchange, as the absence of a standard for asset management data exchange was the motivating factor during the foundation of MIMOSA. The final part of the paper is on the integration of the OSA-EAI MIMOSA standard into the wireless sensor platform developed for data transmission to the MIMOSA Database.

2. WIRELESS SENSOR SYSTEMS

The wireless sensor system development was based on the Imote2 wireless sensor node platforms ITS400 which are produced by the Crossbow Technology, Inc., USA. External sensors, comprising MEMS accelerometers, pressure and temperature sensors, were integrated with the Imote2 wireless sensor platforms. The system has been developed to be able to add intelligence to measurement, communications and control functions. The system specification includes:

- Measurement and sampling of data from the sensors at predefined intervals,
- Data logging and diagnostics such as comparison with programmed thresholds, with event triggering;
- Receiving of instructions from a base station including changes to logging and diagnostic functions;
- Transmission of data packages at required intervals and events;
- Management of system start-up.

2.1 Hardware description & implementation

Imote2 sensor node platforms

The Imote2 is produced by Crossbow Technology, Inc., USA. It is an advanced wireless sensor node platform which is based on the low power PXA271 XScale CPU [1]. It is of modular and stackable design with interface connectors for expansion boards on both the top and bottom sides. The top connectors provide a standard set of I/O signals for basic expansion boards. The bottom connectors provide additional high-speed interfaces for application specific I/O. It has a main board and a power supply battery board. The main board incorporates a central processing function and a communications function that is based on the CC2420 IEEE 802.15.4 radio transceiver, from Texas Instruments, which supports a 250kb/s data rate with 16 channels in the 2.4GHz band. The Imote2 platform also integrates a 2.4GHz surface mount antenna which provides a nominal range of about 30 meters [1].

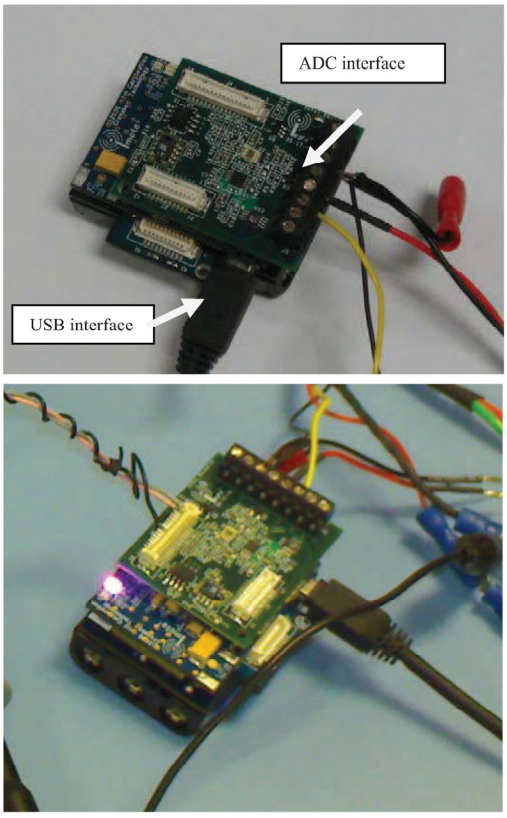

Fig. 1. Configuration of the Imote2 sensor node

An ITS400 sensor board is also integrated with the Imote2 for data acquisition (DAQ) functions. The ITS400 was developed by Intel Research Lab and was licensed to Crossbow, and is designed to interface with the Imote2 platform. It contains a three-axis accelerometer, an advanced temperature/humidity sensor, a light sensor and a 4 channel A/D converter. The ITS400 allows stacking with other extension boards and it provides multiple sensing capabilities for the Imote2 sensor node [2].

Fig. 1 shows multi-sensing with the Crossbow devices. In this example, there are two external sensors (not shown): a thermistor and an accelerometer. These sensors are connected to the ADC of the ITS400 DAQ module. The DAQ module is making measurements and the wireless (comms) module is transmitting the data to the coordinator (wireless receiver) connected to a PC which runs a remote monitoring software.

Temperature sensors

The temperature sensor used is a thermistor whose resistance varies inversely with temperature. Thus, it has a negative temperature coefficient e.g. at -15C° resistance is 72875Ω and at 85C° is 1070.58Ω. Its voltage-temperature characteristic is almost a negatively sloping line. Fig. 2 shows the thermistor and the cable connecting it to a power output and ADC input on the Imote2 sensor node. The thermistor is calibrated to send voltage measurements in the range between 0V and 2.8V which is the voltage limit of the ADC.

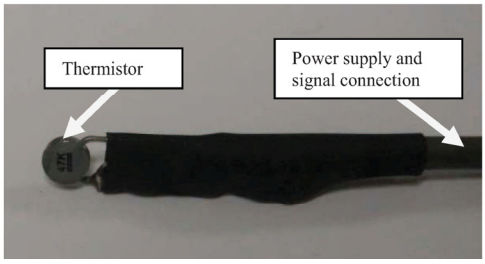

Fig. 2. Configuration of temperature sensor

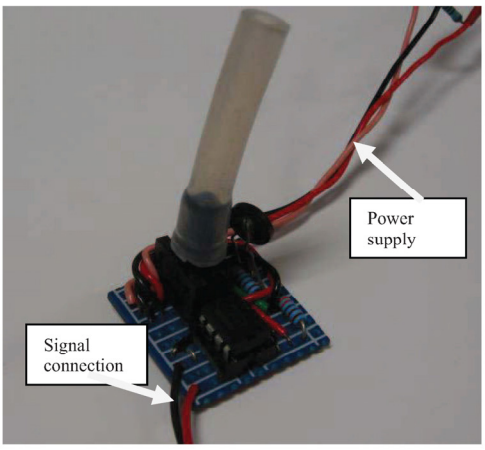

Fig. 3. Configuration of pressure sensor

Pressure sensors

The main element of the pressure sensor used is the 40PC Series miniature pressure sensors made by Honeywell [3]. It is a fully compensated and fully signal conditioned and amplified sensor of monolithic design made using silicon piezoresistive technology. It has an operating temperature range from -45 C° to +125 C°, an analog output voltage signal of 0.5 V to 4.5 V which is linearly proportional to input pressure, and an accuracy of 0.2%. The miniature package mounts easily on printed circuit boards [3]. The electrical output characteristics of this sensor was experimentally tested and found to be 4.5 V at maximum pressure of 15 psi. But the maximum output voltage was stepped down to 2.5 volts in order to match the maximum dynamic input limit of the data acquisition unit (ADC) of the sensor node. Fig. 3 shows the pressure sensor and the cables connecting it to the power output and ADC of the Imote2 sensor node.

Accelerometers

Cheap MEMS accelerometers were made in-house using small ADXL202E and ADXL311JE two-axis accelerometers from Analog Devices, Inc. The ADXL202E and ADXL311JE are low-cost, low-power, complete 2-axis accelerometers with signal conditioned digital voltage outputs, all on a single monolithic IC (integrated circuit) chip [4,5]. They can measure both dynamic acceleration (e.g., vibration) and static acceleration (e.g., gravity) with a full-scale range of 2 g. The outputs are analog voltages or digital signals whose duty cycles (ratio of pulse-width to period) are proportional to acceleration [4,5].

Each of the ADXL202E and ADXL311JE chips was mounted, along with some solid-state components, on a tiny circuit board which was encased in a cylindrical casing using elastomeric or epoxy material. The resulting cheap MEMs accelerometer for vibration condition monitoring is shown in Fig. 4.

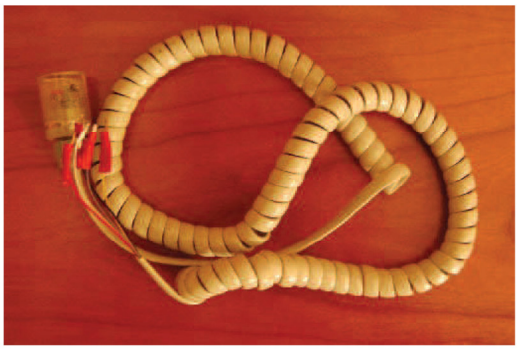

Fig. 4. Configuration of ADXL202E and ADXL311JE MEMs accelerometers

2.2 Sensor Calibration

The calibration of the temperature and pressure sensors has been briefly described above. The calibration of the frequency response characteristics of the MEMs accelerometers and of the ADC of the data acquisition unit is described here.

Calibration of MEMS accelerometers

The MEMs accelerometers were calibrated by reference to a commercial PCB 352C22 accelerometer. Both sets of accelerometer were mounted on an electromagnetic exciter and the time histories of their responses were sampled and transformed into the frequency domain using the Fast Fourier Transform (FFT) algorithm. Fig. 5 shows that the MEMs accelerometer, whose production cost is less than 10% of the price of the PCB accelerometer, manifests vibration characteristics that are similar to those of the PCB accelerometer.

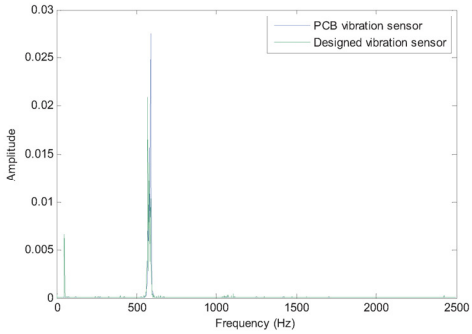

Fig. 5: Comparison of MEMs and PCB accelerometers

Calibration of ADC of ITS400 board

The sampling accuracy of the ADC of the ITS400 board was tested via back-to-back calibration against a commercial National Instruments (NI) data acquisition card. Both cards were used to sample sinusoidal waves of varying frequencies and the FFT of the sampled signals were compared. It was found that the FFT of the data acquired using the ITS board compared fairly well with the FFT of the data acquired using the NI card up to a frequency of 2200 Hz as shown in Fig. 6.

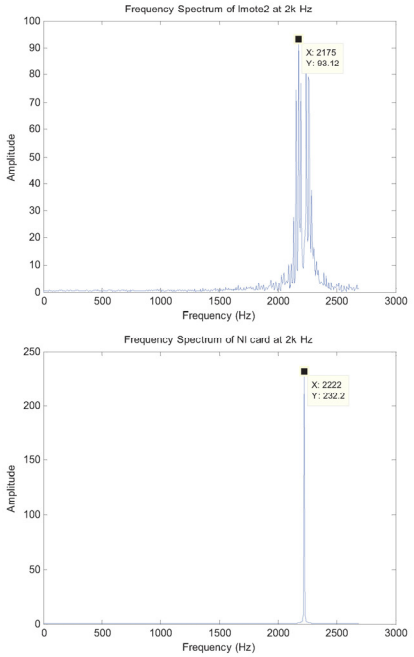

Fig. 6: Comparison of frequency spectrum of vibration data acquired using (a) ITS400 board, (b) NI card at 2 kHz

At lower frequencies, the FFT of the ITS400 board data is less noisy and correlates much more closely to the FFT of the NI card data. Above 2200 Hz, the ITS400 board signal becomes noisier and less accurate. The ITS400 board gives satisfactorily accurate vibration measurements up to about 1000 Hz.

2.3 Data sampling, processing and transfer

One of the Imote2 sensor node functions is to record vibration data samples that might be large in size compared to the data frame available in the ZigBee transmission protocol. To enable the sensor node to transfer the raw data sample, the recorded files, which are a string of data values, have to be divided into manageable segments. Each data frame has 60 bytes of sampled data to be fitted into the data frame. The data sample is divided into N segments. These segments are transferred one by one in the data frame of the message as shown in Fig. 7. The highlighted segment of the data symbolises the segment of the vibration data that will be transferred in the data-packet N times.

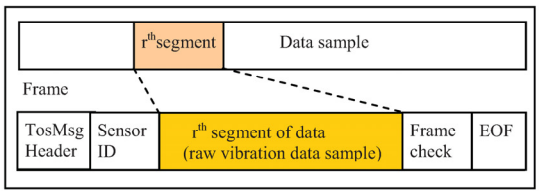

Fig. 7. Organisation of data transfer

The raw condition monitoring data acquired from a location on an asset is not often useful for the rest of the asset. It is the information about the condition of the asset produced from the data during the processing which is valuable. The need to reduce the amount of data was achieved by analysing data locally on-board the sensor node. Raw data is converted into information of reduced size and standard format and, thus, it is directly usable for the other stations. To enable this data reduction, the conversion of data into information must be performed directly at the source of the data. The intelligent sensor node has an embedded FFT algorithm and is, therefore, able to pre-process and assess the data. Based on the set thresholds, it automatically decides if the data is within the limits thereby allowing normal functioning to continue. If the results from the data suggest abnormality, a decision about the severity of the fault should follow. In the case of the detection of a faulty situation, the system should take a decision on what to do next. This decision is based on the automated reasoning.

Decision making and reasoning are part of the advanced embedded software designed to operate the prototypes of the intelligent sensor nodes. These functions are an essential part of the intelligent sensor and the DYNAMITE system. In the example shown in Fig. 8, three sensor nodes 1, 2 and 3 are continuously sensing the temperature (T), pressure (P) and vibration (V) and simultaneously assessing the values of the measurements. The values are analysed by the wireless sensor node which decides on the condition of the parameter by comparing it to the value of the thresholds set for it. If the parameters exceed the limit it will prompt an alarm for the monitoring station which can have a different set of limits for the internal alarms, so an alarm from the sensor can be triggered and either they are activated or ignored. Fig. 8 shows the screen shot from the monitoring software. The screen shows the three sensor nodes monitoring simultaneously the three parameters.

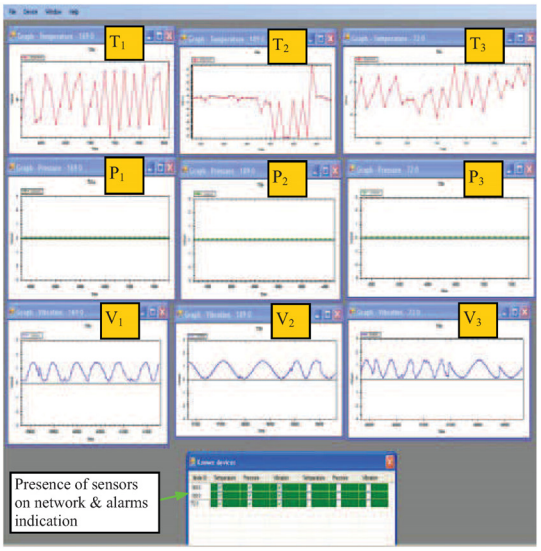

Fig. 8. Screen shot from monitoring software for 3 sensor nodes monitoring temperature, pressure and vibration

3. ENERGY HARVESTING

The Imote2 sensor platforms are currently powered by a set of three AAA rechargeable batteries. This limits the life span of the sensor nodes as they will stop functioning when the batteries are drained of electrical power. To keep them functioning all the time, there is the nuisance factor of constantly checking their power level. Of course, one can conceive the design and embedment of a voltage sensor and algorithm to constantly monitor the voltage level of the sensor node which must lie between 3.5V and 4.2V while the current requirement is about 200 mA. However, such additional sensor will further drain power from the batteries.

In order to achieve self-powering capability for the sensor platforms, there was the need to consider harvesting energy from ambient sources, such as vibration, light and heat, in order to supply the electrical power requirements. Thus, there will be no need to replace the batteries that are currently used to power wireless sensor nodes. The long-term goal is to make wireless sensor nodes truly battery-free. However, the energy harvested from the indoor environment is not matched with the power requirement of wireless sensor nodes, as it is very small and random. In order to solve this problem, an energy harvesting system which incorporated a middleware for dynamic power management, was developed. The system consists of an in-house developed multiple cantilevered piezoelectric fibre composite (PFC) beams vibration energy harvester (VEH) and a solar panel which are connected to an electronics power management board (PMB) middleware. The development of this integrated energy harvesting system is presented in this section.

3.1 Multiple cantilevered PFC beams VEH

Mechanical vibration is one of the main sources of ambient energy. Harvesting of vibration energy has been achieved using electromagnetic, electrostatic and piezoelectric devices. The focus of the current work has been on the development of piezoelectric vibration energy harvesters (VEHs). One of the most commonly used piezoelectric materials is piezoelectric fibre composite (PFC). It enables realistic applications which require highly distributed actuation and sensing, maintains the majority of the stiffness and bandwidth of monolithic piezoelectric ceramics. Typically, piezoelectric vibration energy harvesters have been designed as a cantilevered beam consisting of one or two piezoelectric material layers bonded to the top and bottom surfaces of usually a metallic base structure. The beam may have a tip mass whose magnitude and location along the length of the beam may be adjusted in order to obtain a resonance frequency which coincides with the dominant frequency of the ambient vibration energy. This enables significant amounts of energy to be harvested at the resonance peak of the PFC-mass vibration system. However, off the resonance peak, the harvested vibration energy is relatively too small and, consequently, the bandwidth of reasonable energy harvesting is too small. To overcome this problem, a vibration energy harvesting device, consisting of four PFC beams with tip masses, was developed.

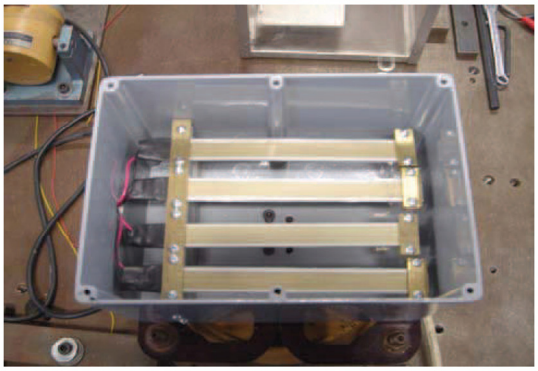

Fig. 9. Multiple cantilevered PFC beams vibration energy harvester (VEH)

The multiple cantilevered PFC beams vibration energy harvester developed is shown in Fig. 9. It consists of 4 cantilevered beams with different tip masses. Fig. 10 shows the frequency spectrum of the 4 cantilevered beams. It is seen that the beams have different resonance frequencies. For each beam, Fig. 10 shows that the maximum vibration energy occurs at its peak amplitude which is at its resonance frequency. Away from resonance, it is seen that the amplitude and, hence, the vibration energy rapidly decreases. Thus, for a single cantilevered PFC VEH beam with tip mass, the frequency band of significant energy harvesting is small. However, when the 4 beams are used simultaneously, the resultant response amplitude will be the sum of the vectorial sum of the individual amplitudes. Consequently, the magnitude and the frequency band of the vibration energy that can be harvested in the resonant region of the 4 beams will be greater than that of a singe beam.

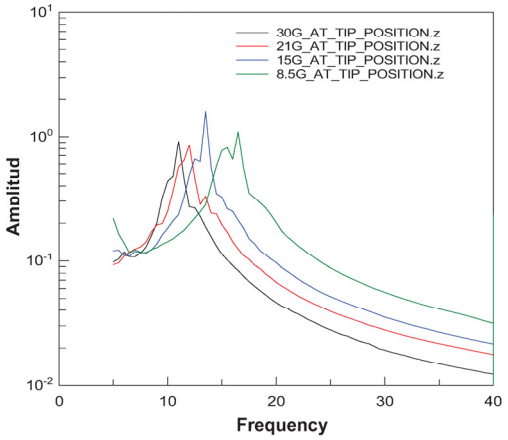

Fig. 10. Frequency spectrum of multiple cantilevered PFC beams vibration energy harvester (VEH)

3.2 Development of Middleware

An electronics power management board (PMB) middleware was designed and developed in-house. Fig. 11 shows the layout of the electronic components while Fig. 12 shows the prototype PMB that was fabricated. The multiple cantilevered PFC beams vibration energy harvester and a solar panel are connected to the power input side of the PMB. The harvested energy is stored on a supercapacitor on the PMB middleware which also houses two sets of three AAA rechargeable batteries. While one set is being recharged with the harvested energy stored in the supercapacitor, the other set, which is already fully-charged, is used to power the Imote2 sensor platform. The PMB middleware has a controller for monitoring the charge states of the battery sets and for switching one set to charge and the other to power the sensor node and vice versa.

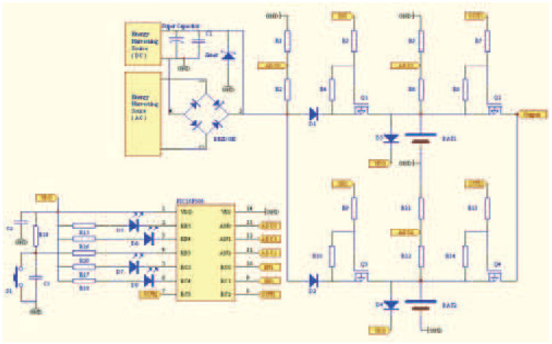

Fig. 11. Configuration of middleware

The middle was evaluated via experimental tests which involved checking the voltage states at different check points on the PMB. The measured voltage-time waveforms showed the voltage level in the battery set being charged increasing exponentially, while that of the battery set powering the sensor node decreases exponentially in value. They also show the rapid dumping of electrical power from the supercapacitor to the battery set under charge.

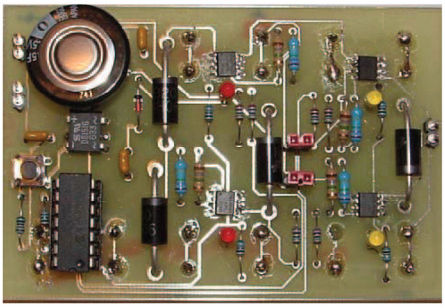

Fig. 12. Prototype of middleware

4. MIMOSA DATABASE COMMUNICATION LINK

The MIMOSA standard for asset management data exchange was chosen by the Dynamite project partners to be used for data exchange, as the absence of a standard for asset management data exchange was the motivating factor during the foundation of MIMOSA. The process of data integration is complex as several asset management systems offered by different suppliers have their individual data exchange interfaces. Different integration methods have their own advantages and disadvantages. The OSA-EAI MIMOSA standard provides an open data exchange standard in a number of key asset management areas. This can be the asset register and work management, the diagnostic and the prognostic assessment, as well as vibration, sound, oil, fluid, gas and thermographic data. A relational model named Common Relational Information Schema (CRIS) defines these areas [6]. The CRIS defines relationships between entities and also asset management entities, their attributes and associated types. However, the OSA-EAI MIMOSA standard was chosen by the Dynamite project partners to be the standard used for data integration and exchange in this research project.

The communication link developed for controlling sensor measurements and communicating with the MIMOSA database is presented. The functionality and key capabilities of the developed link are: Connection to a global or local database, SQL Communication Control, Sensor control, University of Manchester's CRIS table definitions, Location of MAN Wireless-Sensor System, Dynamite MIMOSA Table Definitions and MAN Flowchart. Using an SQL-GUI software interface that was developed, the CRIS (Common Relational Information Schema) table definitions for the University of Manchester have been effected. Firstly, by identifying the functions of the system and data required for the database, the minimum numbers of tables in the database have been chosen. Secondly, unwanted columns in the data tables have been identified.

Fig. 13 gives a brief overview of how the intelligent wireless sensor platform communicates with the MIMOSA database. The yellow boxes (on the right) represent the enterprise MIMOSA description. The enterprise table contains the information where the wireless sensor platform belongs to, the site table where it is situated in, the asset table describes the sensor itself and its transducers and the meas_location table where the sensor operates at. On the other hand the red boxes (on the left) represent the data process information. The meas_event table stores a measurement event, the mevent_num_data table stores sample data, like the temperature and the vibration and the sp_time_data stores BLOB (Binary Large Object) values, such as the high sampling rate vibration data. All tables have generally their own keys and are connected to each other.

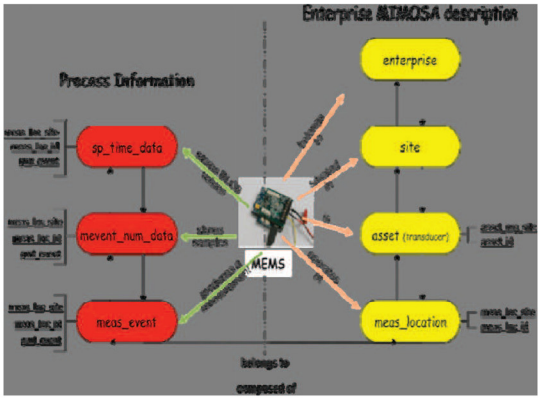

Fig. 13. Various sensing options

5. CONCLUSIONS

The three major tasks executed at the University of Manchester, namely: the wireless sensor system, the energy harvesting system, and the MIMOSA Database communication link have been presented and demonstrated. It has been shown that the multiple cantilevered PFC beams vibration energy harvester has the potential to harvest energy from ambient vibrations more effectively and efficiently and over a wider frequency band than a single cantilevered PFC beam vibration energy harvester. It was found that the PMB and the MIMOSA Database communication link performed very well.

ACKNOWLEDGMENT

The funding received for this work from the EU under the FP6 programme for the DYNAMITE project is gratefully acknowledged.

REFERENCES

[1] Crossbow Technology, Inc., 2009, Imote2: High-performance Wireless Sensor Network Node, www.xbow.com.

[2] Crossbow Technology, Inc., 2009, ITS400: IMOTE2 Basic Sensor Board, www.xbow.com.

[3] Honeywell, 2003, Installation Instructions for the 40PC Series Miniature Signal Conditioned Pressure Sensors, Issue 8, PK 88820, www.honeywell.com/sensing.

[4] Analog Devices, Inc., 2000, ADXL202E: Low-Cost ±2 g Dual-Axis Accelerometer with Duty Cycle Output.

[5] Analog Devices, Inc., 2003, ADXL311JE: Low-Cost, Ultracompact ±2 g Dual-Axis Accelerometer.

[6] K. D. Bever, Common Related Information Schema (CRIS) Version 3.2.1 Specification, Production Release, MIMOSA December 31, 2008